Title

LOW-FREQUENCY WAVES, STABILIZATION, AND ENHANCED TRANSPORT IN THE PLASMA SURROUNDING A HOLLOW CATHODE DISCHARGE

Author

Wheeler, George Macgregor.

Publication Date

1972

LOW-FREQUENCY WAVES, STABILIZATION, AND ENHANCED TRANSPORT IN THE PLASMA SURROUNDING A HOLLOW CATHODE DISCHARGE

George MacGregor Wheeler
(Ph. D. Thesis)

January 1972

AEC Contract No. W-7405-eng-48

DISCLAIMER

Contents

LOW-FREQUENCY WAVES, STABILIZATION, AND ENHANCED TRANSPORT IN THE PLASMA SURROUNDING A HOLLOW CATHODE DISCHARGE

George MacGregor Wheeler

Lawrence Berkeley Laboratory
University of California
Berkeley, California

January 6, 1972

ABSTRACT

Low-frequency waves, particle transport, and stabilization are studied in the secondary plasma of a hollow cathode arc discharge. Plasma is transported across and along an axial magnetic field of B = 580 to 1160 gauss by diffusion in a partially ionized plasma, by mobility in the radial electric field, and by wave enhanced convection. The latter is often the dominant transport mechanism, and is certainly the least understood.

The resulting radial profile parameters are functions of the arc operating conditions, the transport mechanisms, and the boundary conditions. The ion density falls from $\sim 10^{13}$ cm^{-3} near the central arc column to $\sim 10^{10}$ cm^{-3} near the wall of the 20 cm diameter diffusion chamber. The electron temperature falls from ~5 eV near the arc column to ~0.3 eV near the wall. Neutral gas pressure is varied between p_t = 0.2 and 3.0 mtorr of argon or helium.

The axial boundaries consist of five concentric end-ring electrodes at both ends of the system. Independent biasing allows some control over the axial and radial boundary conditions. The inner two end-rings are quartered, providing information on azimuthal symmetry and

wave propagation. The end-rings also serve as suitable suppressor electrodes for three wave-stabilization techniques.

Langmuir probes are used to measure plasma and wave profiles. A directional Langmuir probe (DLP) is used to measure azimuthal and axial streaming directly. Six experimental checks are made on the functioning of the DLP as a simple probe, and as a tool to determine streaming velocities directly. In particular, the streaming velocity was determined by measuring directional ion currents in a microwave plasma device, with a known streaming velocity. The streaming velocity was determined independently by measuring the difference in the propagation speeds of sound waves, launched in the upstream and downstream directions. Good agreement between the two methods is obtained.

The present work adds new information regarding plasma stability based on simultaneous consideration of most of the effects considered important in an HCD. "Drift wave" theory seems inappropriate for experimental flute instabilities. And E x B neutral drag theory seems incomplete in not including diamagnetic and centrifugal gravity drifts.

We develop a single-fluid instability theory, which includes the effects of density gradient, centrifugal and Coriolis forces due to plasma rotation in a radial electric field, collisions with cold neutrals, fluid compressibility, finite gyroradius, ion inertia, and an ion sink term. A simple quadratic dispersion relation results for low-frequency ($\omega/\Omega_i \ll 1$) waves. The solution explains the behavior of two low-frequency experimental flute instabilities on

five points of comparison: (1) spatial location; (2) frequency; (3) direction of propagation; (4) parallel wavelength; and (5) growth rate, γ/Ω_r, where $\omega = \Omega_r + i\gamma$.

The lower-frequency experimental wave (LF $\approx$ 2.0 kHz) is localized at large radii in the region of large positive radial electric field, and propagates in the ion-diamagnetic direction. The higher-frequency wave (HF $\approx$ 30 kHz) is localized at small radii in the region of large negative electric field and density gradient, and propagates in the electron-diamagnetic direction.

Enhanced convection due to low-frequency, coherent oscillations is expressed in terms of the correlation between the density and potential fluctuations, which in the case of a single coherent mode can be written as, $\langle n_1 v_{1r} \rangle_{conv} = (k_\perp n_1 \varphi_1 c/2B) \sin \psi$, where ψ is the phase between the density and potential fluctuations. By inferring an enhanced diffusion coefficient, $-D_{enh} \nabla n \equiv \langle n_1 v_{1r} \rangle_{conv}$, which is used in a simple diffusion theory, we calculate semi-quantitatively a radial density shape which agrees well with the measured profile. Enhanced diffusion at large radii is several orders of magnitude larger than classical diffusion, and is comparable in magnitude to Bohm diffusion.

Three wave-stabilization techniques are attempted which effectively stabilize the lower-frequency (LF $\approx$ 2.0 kHz) wave. A linear feedback loop is used to phase-shift and amplify a reference wave signal, which is sensed on a Langmuir probe. The resulting feedback signal is returned to the plasma on one quarter of the second axial end-ring, which is used as a suppressor electrode. Wave amplitude is

observed to decrease with increasing negative feedback power until an optimum is reached, with feedback power of ~0.5 watt required to decrease the wave amplitude by an order of magnitude. The effect of linear feedback on the theoretical growth rate is explained by means of an effective ion sink term in the equation of continuity.

New information is also obtained in the present experiment by investigating wave stabilization and wave enhanced transport by controlling the axial boundaries. When various end-rings are floated electrically, or positively DC biased, the radial electric field at large radii ($R \gtrsim 3$ cm) can be reduced or eliminated. The wave at large radii, which is driven by the radial electric field, is stabilized in this manner by "DC stabilization," with power levels ~1.0 watt. When the wave is stabilized ($\tilde{n} \lesssim 0.01$), there is negligible enhanced convection. The density profile steepens at large radii, in agreement with our calculations based on simple diffusion theory. Density increases at small radii are difficult to determine experimentally, due to large density gradients. By floating certain end-rings, the radial electric field can be reduced or eliminated, and the LF wave can be stabilized, with no external power required.

An "AC stabilization" technique is attempted to see if wave amplitude reduction, and reduced transverse particle transport, could be attained at lower power levels. AC stabilization means the application of a rectangular pulse signal to the suppressor electrode, where the pulse frequency, duty ratio, and power can be varied. We find that similar power levels are required as for DC stabilization.

Two experimental techniques are investigated which measure the instability growth rate directly. The first method employs linear feedback at a given azimuthal position. By monitoring the wave amplitude as a function of azimuthal position after feedback, the growth or decay rate can be measured directly. The second method involves measuring the wave growth or decay rate as a function of time after a stabilizing voltage is turned off or on, respectively. Agreement between theory and experiment suggest consideration of both techniques for future diagnostics.

I. INTRODUCTION

Plasma transport across and along magnetic fields is a subject under intensive study, motivated in large part by the requirements of controlled thermonuclear fusion research. "Classical" transport rates have been calculated for most magnetic field geometries, but are rarely observed. The subject of "enhanced" or "anomalous" transport, caused by plasma waves, is often discussed regarding plasma confinement, and is reported in most plasma devices. "Enhanced transport" includes several explanations and models, but is still not clearly understood. In some cases, the theory is unsatisfactory; and in others, information on the plasma and/or fluctuation parameters is insufficient.

Information about waves and enhanced transport can be obtained from several experimental plasma devices. For example, several authors have studied the spatial dependence of the plasma surrounding the hollow cathode discharge, HCD, as a function of measurable plasma and wave parameters. Some of these have found agreement with some form of classical theory.[1,2] Others report anomalous or enhanced transport as much as two orders of magnitude larger than predicted classically.[3-9] Previous work on understanding transport in HCD's is discussed in Section II. A. The present work is a theoretical and experimental study of coherent low-frequency instabilities, particle transport, and wave stabilization in the secondary plasma surrounding an HCD.

The primary arc discharge is treated as a magnetically and mechanically collimated line plasma source, on the axis of a 20-cm diameter diffusion chamber. The plasma is transported across and along

an axial magnetic field of B = 580 to 1160 gauss to form the partially ionized plasma studied in this experiment.

The arc runs into a differentially pumped diffusion region. Diffusion region neutral pressure is varied from 0.2 to 3 microns argon or helium. Typical particle densities fall from $\sim 10^{13}$ cm^{-3} in the central arc column to $\sim 10^{10}$ cm^{-3} near the walls of the 20-cm diameter diffusion region. The axial density profile is nearly cosinusoidal. Electron temperature ranges from ~5 eV in the central column to ~0.3 eV near the walls. The diffusion region is 58.2 cm long and terminates on end plates consisting of five concentric conducting rings, allowing some control over axial and radial boundary conditions. The inner two end-rings are quartered to provide information regarding azimuthal symmetry and azimuthal wave propagation. All rings, the diffusion region tank, and the anode are independently biasable.

Profile measurements of the saturated ion current, floating potential, and electron temperature are made radially along five different azimuths, as well as axially, using Langmuir probes. A directional Langmuir probe (DLP) is also employed to measure the azimuthal and axial streaming directly, as well as to provide an independent check on the radial electric field.[6,7,10] Density and potential fluctuations are determined from probe signals using a phase-sensitive differential amplifier and a Tektronix spectrum analyzer. Typical experimental plasma parameters are presented in Section VI.A.

An expression for enhanced convection is easily obtained for the case of coherent low-frequency waves. The time-averaged expression for

enhanced convection can be written $\langle nv_r \rangle_{conv} \equiv \frac{1}{2\tau}\int_{-\tau}^{\tau} n(t)v_r(t)dt$. In the absence of zero-order drifts, enhanced convection can be expressed as $\langle nv_r \rangle_{conv} = (n_1 v_{1r}/2) \cos \Delta$, where Δ is the phase between the density, n_1, and velocity, v_{1r}, fluctuations. The radial velocity fluctuation, v_{1r}, is not readily measurable. However, if we assume that v_{1r} is due to an azimuthal electrostatic electric field,

$$v_{1r} = \frac{E_{1\theta}\, c}{B} = - \frac{i\, k_\perp\, \varphi_1 c}{B}$$

then we have the expression[11,12]

$$\langle nv_r \rangle_{conv} = \frac{k_\perp n_1 \varphi_1 c}{2B} \sin \Psi$$

The density, n_1, and potential, φ_1, fluctuations, separated by the phase, Ψ , can be readily measured; and we have a useful expression with which to estimate the magnitude of enhanced convection.

Several low-frequency instabilities have been reported in previous experiments on HCD's. A survey and discussion of low-frequency instabilities which might occur in an HCD is presented in Chapter IV. Two coherent low-frequency oscillations are observed in the present experiment.

A large nonambipolar radial electric field exists. The electric field is large and negative for small radii near the central arc column, and large and positive at large radii, causing plasma rotation in the electron- and ion-diamagnetic directions, respectively. Two experimental low-frequency instabilities are observed as density and

potential oscillations in regions of large radial electric field and large plasma rotation. The higher-frequency (HF $\approx$ 30 kHz) wave amplitude maximizes at small radii in the region of large negative electric field; and the lower-frequency wave (LF $\approx$ 2 kHz) at large radii in the region of large positive electric field.

First we would like to "identify" two low-frequency experimental instabilities, in order to better understand their properties. The nonequilibrium plasma surrounding an HCD contains several free energy sources available to drive an instability. Near the primary arc column, at small radii, expansion of the plasma in large density and temperature gradients drives diamagnetic drift currents. The resistive drift wave may be unstable in this region.[12-14] However, a finite parallel wavelength is required, but not observed.

The E x B neutral drag instability may occur in the regions of large electric field, since collisions with neutrals cause the ions to drift slower than the electrons.[15-17]

Centrifugal and Coriolis forces arise in rotating systems. The centrifugal force can be treated as an effective gravity, which leads to the plasma analog of the fluid gravitational instability in the presence of a density gradient.[18-20] The Coriolis force can be either stabilizing or destabilizing, depending on the magnitude and direction of the plasma rotation.[21-22]

The Kelvin-Helmholtz instability should be considered in the region where the radial electric field changes sign.[20, 23-26] This region of strong azimuthal velocity-shear might be unstable under interchange of adjacent fluid elements. These, and other instabilities are

discussed in more detail in Chapter IV.

A single-fluid model, including the effects of density gradient, centrifugal and Coriolis forces due to plasma rotation in a radial electric field, collisions with cold neutrals, fluid compressibility, finite gyroradius, and ion inertia, is developed in Section V.A. under the name "rotational instability." The two experimental instabilities are explained well by this theory on five points of comparison.

Next, we would like to predict the radial density distribution, which depends strongly on the magnitudes of the various transport mechanisms, including enhanced transport. In fact, the shape of the radial density profile, characterized by a radial scale length $q = -(\nabla \ln n)^{-1}$, can be calculated from a simple transport theory.[2, 27-31] Observations of the magnitude and parametric dependence of the experimental scale length may yield information on the magnitude and type of transport mechanisms present.[9,32] When the expression for enhanced convection is included in a simple diffusion theory, a radial density scale length is calculated, which explains semi-quantitatively the observed steepening of the density profile when the wave is stabilized. Transport theory is discussed in Appendix B, and summarized in Section V.B.

Finally, we would like to study the effect of wave stabilization on enhanced transport and the density profile. Three techniques of wave stabilization are attempted. A linear feedback loop is applied to one quarter of the second end-ring as a suppressor electrode.[11, 33-35] A DC, or floating, bias is applied to several end-ring electrode configurations. An AC stabilization method is also

attempted, where a rectangular positive, or floating-voltage signal, the duration and repetition rate of which can be varied, is applied to an end-ring suppressor electrode. Previous experiments on wave stabilization techniques are discussed in Section II. B.

All three techniques are found to be effective in stabilizing the lower-frequency (LF $\approx$ 2 kHz) wave. The stabilization is observed to agree semi-quantitatively with the steepening of the density profile, indicating reduced cross-field transport. The resulting density profile is in agreement with that calculated classically for a quiescent plasma. The higher-frequency wave (HF $\approx$ 30 kHz), localized at small radii, could not be stabilized. The large negative electric field, which we believe drives the HF wave, is characteristic of arc discharges and cannot be eliminated. Fortunately, the HF wave does not contribute significantly to enhanced transport.

Previous work on the HCD is discussed in Chapter II. The experimental arrangement is presented in Chapter III. Chapter IV is a survey of low-frequency instabilities which may be present in an HCD. Transport and wave theory is discussed in Chapter V, and the experimental results are presented and discussed in Chapter VI.

II. PREVIOUS WORK ON THE HCD.

A. Understanding Transport.

The HCD is a good experimental device in which to study plasma transport processes. The secondary plasma surrounding the central arc column may exhibit large density and temperature gradients and strong radial electric fields. Several coherent, low-frequency instabilities have been reported, which are associated with "enhanced" transport.

One of the earliest studies, presented in 1949, on a small rectangular argon arc is discussed by Bohm, Burhop, Massey, and Williams.[36] They argued that an ambipolar electric field is necessary for charge neutrality. However their experiment indicated a diffusion rate two orders of magnitude larger than the predicted ambipolar rate. They concluded that an enhanced "drain diffusion" mechanism caused the discrepancy, and proposed what has come to be known as Bohm diffusion.

In 1955, Simon and Neidigh[2,27] proposed an alternate solution to the "drain diffusion" of Bohm et. al.[36] They claimed that unrestrained ion collisional diffusion is sufficient to explain the observed transport rate, due to the fact that the ambipolar electric field is "short-circuited" by conducting end plates. The ions are then transported across the magnetic field at the classical ion-neutral collisional rate, unrestrained by ambipolar fields due to the slower electron-neutral transport rate.

In 1960, Zharinov[28] proposed a model of electron trapping along the magnetic field lines in the potential well between the end sheaths. The electrons were assumed to be in Maxwell-Boltzmann equilibrium. Tonks[29]

generalized further, assuming arbitrary trapping at the end sheaths, characterized by the relation, $\langle nv_{\parallel} \rangle^{e}_{wall} = \beta \langle nv_{\parallel} \rangle^{i}_{wall}$. His results reduce to those of Zharinov for electron trapping with $\beta = 0$, and to those for insulating end plates with $\beta = 1$.

In 1962, Yoshikawa and Rose[9] studied the transport mechanisms in an HCD. They measured the current to an annular ring as a function of voltage, for various neutral gas pressures, p_t , and magnetic field strengths, B. They expected to see the transverse current scale as p_t/B for enhanced diffusion, and as p_t^2/B^2 for collisional diffusion. Their results lay somewhere between the two.

Also in 1962, Rothleder[37] studied transport in an HCD in argon. He used a set of concentric end-ring segmented electrodes, and found that when grounded, the inner ring draws a net electron current, while the outer rings draw a net ion current in agreement with our results. He had some difficulty calculating a good theoretical fit for the observed density profile for the case of conducting end-ring electrodes. However, his experiments were among the first to investigate the axial as well as radial plasma profiles, and to investigate the effects of axial and radial boundary conditions.

In 1963, Berkner et. al.[1] measured the axial and radial dependence of an argon HCD plasma. Conducting end plates were used, and the axial density profile was measured to be roughly cosinusiodal. Order of magnitude agreement with the axial electron trapping model of Zharinov and Tonks was obtained.

In 1968, Warren[5] presented a more consistent study of transport in a helium HCD, by including enhanced transport when a "drift-type" instability was present. Five concentric end-ring electrodes were

employed in the 20 cm diameter diffusion region, by which control over the axial and radial boundary conditions was studied. The magnitude of enhanced transport was estimated by measuring the phase, ψ, between the density, n_1, and potential, φ_1, fluctuations, $\langle nv_r \rangle_{conv} = (k_1 n_1 \varphi_1 c / 2B) \sin \psi$.[11, 12] Often enhanced convection was the dominant transport mechanism. The calculated density profile shape agreed well with the measured value, when enhanced transport was negligible. Particle balances for the ions and electrons were satisfied by the experimental radial and axial particle currents.

In 1969, Hudis[6] measured ion streaming directly in an argon HCD, using a directional Langmuir probe, DLP. He identified one low-frequency instability as the Rayleigh-Taylor, R-T, centrifugal flute, and partially identified another as the transverse Kelvin-Helmholtz, K-H, velocity-shear-driven flute. By using the DLP, he was able to measure ion streaming directly in the axial, azimuthal, and radial directions. He measured enhanced cross-field transport associated with the presence of the Rayleigh-Taylor waves, but independent of the presence of the K-H wave. This agrees with the predictions of a non-linear computer model by Byers.[38] Byers showed that large amplitude R-T waves transport plasma to the vacuum wall, whereas the K-H wave remains localized in convective cells.

Hudis was not able to estimate enhanced convection by the method of phase correlation between the density and potential oscillations. Nonlinear coupling of large-amplitude co-existing waves left him no meaningful determination of the fluctuating electric field. However, a simple expression from fluid theory was used to calculate an enhanced cross-field velocity, in semi-quantitative agreement with

the measured value.

In a later work, Hudis and Lidsky[7] used numerical methods on a normal mode stability condition, derived by Perkins and Jassby.[26] By averaging over radial plasma and wave profiles, they were able to infer that normal mode R-T and K-H waves could be destabilized by the radial electric field profile. This work was an improvement over the previous work, based only on a local approximation.

In the present experiment, the secondary plasma of an HCD in Argon and helium is studied. Five concentric end-ring electrodes are employed, with which the axial and radial boundary conditions are varied. The inner two end-rings are quartered in order to study azimuthal properties. Coherent waves, enhanced transport, and wave stabilization are studied. A DLP is employed to measure ion streaming in the azimuthal and axial directions directly.

B. Wave Stabilization.

Plasma instabilities are often associated with enhanced plasma loss.[3-9] Furthermore, our success in attaining a self-sustaining, thermonuclear reactor may depend on our ability to understand and control enhanced plasma losses. For example, several recent experiments have shown improved plasma confinement when certain coherent plasma waves are stabilized. Some of these experiments will be discussed further in this section, with the help of a recent review article by Thomassen.[39]

Several techniques have been attempted in order to make plasmas quieter, such as minimum-B geometry, magnetic shear, and more recently, linear feedback stabilization.[11, 33-35] Linear feedback means that a signal proportional to the plasma wave is phase shifted, amplified, and returned to the plasma in order to reduce the signal amplitude. Several methods of sensing the signal and coupling feedback power to the plasma will be discussed here.

Under certain conditions, some linear feedback schemes are predicted to be ineffective in stabilizing flutes. For example, in a torus net linear feedback should vanish due to averaging over azimuthal and axial periodicities.[40,41] A nonlinear feedback technique is proposed to overcome this obstacle.[40-42] A corrective force is applied whenever the wave amplitude exceeds a chosen value and is removed when the wave subsides. Hendel and Chu report the only experiment we could find using this method, with results comparable in effectiveness and power requirements with linear feedback.[42]

Dynamic stabilization is another method, which is reportedly successful in stabilizing single-mode, multimode, or turbulent regimes

simultaneously. A high frequency signal is applied to the plasma which stabilizes lower-frequency instabilities by suspending the electrons in a new "dynamic" equilibrium.

1. Linear Feedback

Arsenin and Chuyanov first suggested feedback stabilization of gravitational flutes using linear feedback applied to suppressor plates, external to the plasma.[43] The potential applied to the suppressor electrodes is proportional to a signal sensed at the plasma edge. In this case, the electric field between the suppressor plates opposes the electric field of the wave for negative feedback. Theory includes the suppressor electrode potentials as boundary conditions to the solutions of Poisson's equation. Success of this technique was subsequently reported on the Ogra-II device,[44] and on the Phoenix II device,[45] operating as a simple mirror. Wave amplitudes were reduced an order of magnitude, and density was reported to increase by factors of 2 to 4.5.

Arsenin and Chuyanov also suggested stabilization of the collisionless drift instability by linear feedback similar to that proposed for the gravitational flute.[46] Since then, voluminous work on the feedback stabilization of drift waves in Q-machines has appeared in the literature. Wong, Baker, and Booth[47] and Lindgren and Birsdall[34] reported suppression of the collisionless drift wave using suppressor electrodes immersed in the plasma. Lindgren and Birdsall simultaneously suppressed the m = 2, 3, and 4 modes by using filters and three independent feedback loops. The phase shifts required for the three modes were different, indicating that simultaneous suppression was not possible with a single loop. Hendel et. al.[11, 12, 33] and Furth

and Rutherford[35] reported suppression of the collisional drift wave, in agreement with a theory which includes an electron sink term in the continuity equation. Density increases up to 30°/o were reported.

Prater observed that density increases due to wave suppression are to some degree offset by currents to suppressor electrodes, acting as electron sinks.[48] He reported suppression of a mirror instability by injection of a low-energy electron beam, modulated by a signal proportional to the density perturbation, as an electron source. Preliminary results are similar to those of electron sink feedback, indicating that the stabilization mechanism is actually charge feedback.

Another method of coupling feedback power to the plasma is a low-frequency modulation of microwaves at the upper hybrid frequency. WKB theory shows that there is high absorption of microwaves at the upper hybrid frequency.[39] This technique also has the advantage that no electrodes are immersed in the plasma, and is therefore more suitable for fusion plasmas. Hendel, Chu, Perkins, and Simonen reported stabilization of the collisional drift wave using microwaves, in agreement with a theory which includes a feedback controlled heat sink in the electron heat flux equation.[49] Wong, Baker, and Booth explained similar stabilization of the collisionless drift wave by microwave coupling to the electron orbits.[47]

Chen and Furth proposed another interesting remote technique of coupling feedback power to the plasma.[50] They suggested low-frequency modulation of a neutral beam being injected into the plasma. When appropriate volume plasma and momentum sources were included in the two-fluid equations, they were able to show stabilization of the resistive drift wave, for example, as a function of modulation gain

and phase. Three physical explanations were discussed: (1) Density smoothing--filling in the wave troughs at low beam energies; (2) simulation of minimum-B--the pressure of the neutral beam may have an effect similar to favorable gradients in the magnetic field; and (3) de-energization of the wave--the neutral beam pressure works against plasma motion. In practice, all three mechanisms may be working simultaneously, which determines the net phase and gain required for feedback.

Since low-frequency modulation of high-energy neutral beams may be difficult, Chen proposed modulation of infrared laser beams for fusion plasmas.[51] Coupling power to the plasma was explained by means of local radiation pressure acting on the ions, or quasi-linear drift of electrons along the density gradient. Theoretical stabilization of drift and flute modes was shown. Recent work implies that laser power can be coupled to the plasma, in both the ordinary and extraordinary modes.[52]

Success of linear feedback techniques has also been reported in arc discharges. Parker and Thomassen reported feedback stabilization of "drift-type" waves in a hydrogen reflex arc.[53] Two suppressor electrodes extending the length of the system created an azimuthal electric field which opposed the wave field for negative feedback, as suggested by Arsenin and Chuyanov.[43,46]

Keen and Aldridge reported suppression of a collisional drift wave in an argon HCD.[54,55] A suppressor plate electrode was immersed in the plasma. The experimental results were explained well by treating the system as a classical Van der Pol oscillator, which included linear growth rates and nonlinear saturation coefficients to determine

the limiting wave amplitudes.[56,57] Good agreement between theory and experiment was obtained when a feedback controlled ion source was included to account for the effect of feedback.

Stufflebeam et. al. have also reported successful feedback stabilization of the rotationally convected drift instability in an argon HCD.[58] However, the optimum phase for feedback is shifted from measurements by Keen using solutions of the Van der Pol equation.[56,57]

2. Nonlinear Feedback

Millner and Parker[40] and Melcher[41] considered theoretical suppression of flute instabilities by means of external currents, providing vacuum magnetic fields perpendicular to an axial magnetic field. This method has the advantage that no electrodes are immersed in the plasma, and therefore may be more suitable for fusion plasmas. However, they calculated that linear feedback is ineffective for a system with axial periodicity, such as a torus, since integrals over axial and azimuthal periodicities vanish. A method of nonlinear feedback was proposed for stabilizing flutes. Local plasma surface displacements trigger currents applied to external conducting straps. The increased "magnetic pressure" is maintained until the surface displacement subsides below the trigger level.

Hendel and Chu report successful stabilization of the collisional and collisionless drift wave using a nonlinear feedback technique.[42] A corrective pulse signal was applied to a Langmuir probe, acting as a current sink, whenever the wave amplitude was positive. The duration, phase, and amplitude of the rectangular suppressor signal

were varied. Results showed phase and power requirements similar to those for linear feedback. When the nonlinear pulse was applied only every second wave cycle, the feedback voltage requirements rose so that the feedback power was approximately the same. They observed, however, that in regions where several modes may be simultaneously unstable, such as for the collisionless drift wave, nonlinear feedback suppression may excite higher modes and harmonics more readily.

3. Dynamic Stabilization

Dynamic stabilization at frequencies much larger than instability frequencies can be used in the single-mode, multimode, or even turbulent regimes.

In an early experiment, Rugge[59] suppressed the helical instability[60] in a positive column, by the application of an ac axial electric field. Since the instability grows by drifting in a "kinked" axial electric field and an axial magnetic field, Rugge found that the instability could be suppressed by reversing the axial electric field at frequencies greater than the instability growth rate.

Keen and Scott reported stabilization of the drift dissipative instability in a hydrogen afterglow, by applying either an ac azimuthal magnetic field or an axial electric field.[57,61]

Hendel and Chu applied rf radial or axial electric fields on one or two electron-emitting ring probes in a Q-machine.[42] Stabilization of the drift instability was reported for the entire unstable regime--single-mode, multimode, and turbulent. The transverse Kelvin-Helmholtz "edge oscillation" was similarly stabilized. However, higher power levels were required to maintain the dynamic equilibrium. Interpreta-

tion of results was also more difficult, since the plasma parameters were changed.

4. Feedback as a Diagnostic Tool

Feedback can also be used as a diagnostic tool. For example, one can measure the density profile as a function of wave amplitude by varying the feedback gain. From the shape of the density profile, one can infer the effect of enhanced transport as a function of wave amplitude. Hudis measured enhanced transport directly with a directional Langmuir probe.[6,7,10]

Another diagnostic application was first suggested by Wong and Hai.[62] They measured the linear growth rates and nonlinear saturation coefficients for drift waves in a Q-machine. Linear feedback was suddenly removed. Curve fitting between the plasma response and a power series expansion for the wave energy yielded the desired coefficients. Keen used this method to measure the linear growth rate directly, by comparing plasma response with a solution of a Van der Pol-type equation.[56,57] By gating the feedback amplifier, Hendel, Chu, and Simonen measured the nonlinear growth rate of the collisional drift wave to be much smaller than the linear growth rate.[63]

5. Other Interesting Experiments: Stabilization

In other interesting experiments, Scott, Little, and Burt reported stabilization of the Q-machine collisionless drift wave by dc magnetic shear stabilization, using external stellarator-type $\ell = 3$ windings.[64] Hartman, Hendel, and Munger reported suppression of balloning-type drift modes in a toroidal stellarator by magnetic shear from $\ell = 2$ helical windings.[65] Chen and Rogers reported minimum-B stabilization of drift waves in a Q-machine by adding internal solenoidal reverse

coils which created a minimum-B configuration.[66] They proposed minimum-B stabilization of long wavelength instabilities in tori in this manner. Chu et. al. have suppressed the Kelvin-Helmholtz "edge-oscillations" in the Q-machine, comparing with an electron-sink theory.[67] In the earliest reported feedback experiment, Arsenin et. al. stabilized the resonant ion-cyclotron instability.[68] Keen and Fletcher used a photo-sensing technique, coupled through the feedback loop to the electrons by means of the electron-cyclotron resonance, to stabilize the ion sound wave.[69] Ionization waves were studied using feedback on a positive column by Garscadden and Bletzinger.[70]

Finally, Lindman has proposed an interesting technique of passive stabilization by applying passive RC networks to a segmented plasma boundary.[71] Theoretical success was shown by numerical integration of Kent, Jen, and Chen's radial wave equation, including passive RC circuitry as boundary conditions.[23] Preliminary experimental results by Carlyle on the Texas Q-machine have confirmed Lindman's theory.[72]

In summary, wave stabilization has been shown to reduce enhanced transport, often reported to be several orders of magnitude larger than predicted classically. Wave amplitudes are reduced more than an order of magnitude, with resulting density increases of up to 30%. And several remote techniques of coupling feedback power to the plasma have been proposed and tested. We expect to see some of these techniques used to stabilize fusion reactor plasmas.

6. The Present Experiment.

In the present experiment, we intend to explore three wave stabilization techniques. Suppressor electrodes are the five concentric end-rings, located at each end of the system. The inner two end-

rings are quartered to provide good electrical contact with the plasma, for linear feedback electrodes. Linear feedback is treated semi-quantitatively as a controlled ion sink in the equation of continuity (see Section V. A.).

Also, by applying dc potentials to various end-ring configurations, we can affect the radial and axial boundary conditions. We will see that one low-frequency instability can be stabilized in this manner, in part at least, by eliminating the radial electric field, which we believe drives the instability. A "passive" stabilization technique is also successful, in which given end-ring electrodes are floated, while others remain at ground.

An AC stabilization technique is also attempted, by applying a rectangular pulse signal to a given end-ring electrode configuration. Pulse frequencies greater than wave frequencies are required, since the growth rate is comparable to the frequency. We want to investigate power requirements and plasma parameter changes, the radial electric field in particular, when a pulse signal is applied.

Wave stabilization is also used as a diagnostic technique. We use stabilization to study the effect of coherent low-frequency plasma waves on enhanced transport rates and on the density profile, as a function of power and wave amplitude. We also use stabilization to measure instability growth and decay rates directly, using two independent techniques. However, care must be taken in the interpretation of results when the plasma parameters are changed by stabilization techniques. The three stabilization techniques are discussed in Sections VI. C, D, and E, respectively. Use of linear feedback and AC stabilization to measure the growth rate directly is discussed in Section VI.G.

III. EXPERIMENTAL ARRANGEMENT

The experiment was conducted in the secondary plasma of an HCD. The primary discharge is treated as a magnetically and mechanically collimated line plasma source, on the axis of the diffusion chamber. The plasma expands, diffuses, and drifts across and along the magnetic field to form the partially ionized plasma studied in this experiment.

A. The Hollow-Cathode Discharge

Properties of the hollow-cathode discharge are discussed in detail in the literature.[3-6,73,74] The experimental arrangement is shown in fig. III.1. An axial magnetic field of B = 580 to 1160 gauss is created by six modular coils, as shown. Neutral gas is fed through the cathode, which is a tungsten tube, 0.476 cm in diameter with a 0.076 cm wall. The arc is ignited by a commercial welding starter which applies rf to the cathode. The hot ions return to the cathode. When the cathode reaches electron emission temperatures of $\sim 2700^{\circ}K$, the arc is self-sustaining, and the rf is stopped. Cathode gas flow rates of 3 to 30 cm^3/min, STP, of argon and helium are used in this experiment, with a gas pressure of 3 to 10 mtorr in the cathode region.

This experiment uses a bare cathode, without the anode assembly A_I shown in fig. III.1. Limiting apertures with a diameter of 0.5 in. are used in both the cathode and anode ends. Arc currents of 5 to 40 amperes were possible; however, long cathode life and a highly ionized arc column is obtained for $I_{CI} = 20$ A. Cathode voltage with respect to ground is typically -40 V to -70 V in

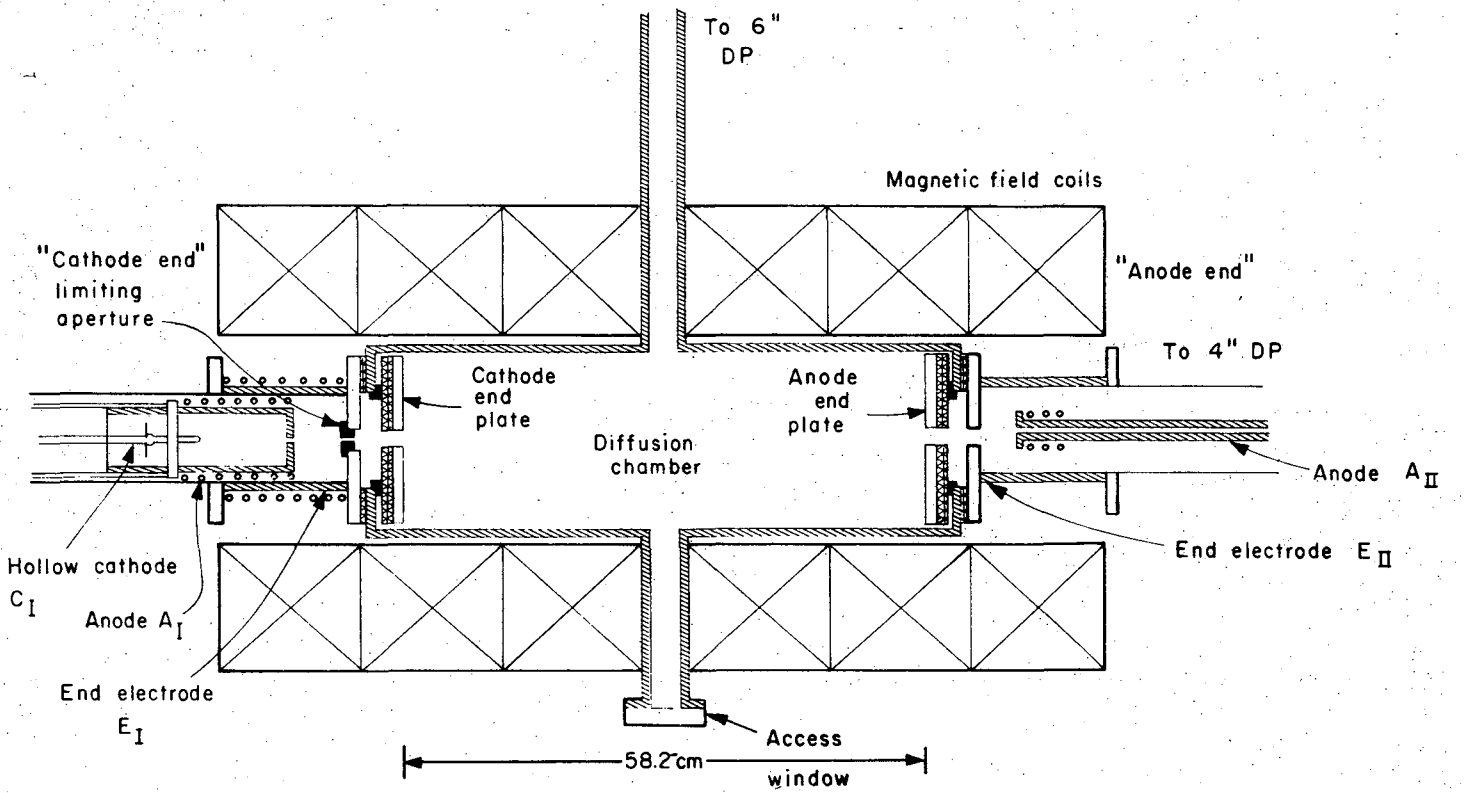

Fig. III.1. Hollow cathode arc discharge experiment.

XBL676-3255

argon and -70 V to -100 V in helium.

The arc runs from the cathode to several electrodes, E_I, A_{II}, and E_{II}, which are generally at ground, but can be independently biased. Typically ~ 75% of the arc current goes to electrode E_I, another 20% goes rather evenly to the anode end electrodes, E_{II} and A_{II}, and the remaining 5% goes to the end-ring electrodes and the tank. Independent biasing of the anode A_{II} from +40 V to -40 V was attempted in order to change the shape of the radial electric field, as reported by Hudis.[6] Little effect was observed, except on broad-band noise, which we believe is due to the fact that only 10% of the current is received by A_{II}.

The axial magnetic field is produced by six modular coils, 22.9 cm i.d. x 50.8 cm o.d. x 15.6 cm deep. The coil positions and currents were adjusted so that the field was measured to be uniform within 5% over the 60-cm length of the diffusion chamber. Care was taken so that the axial alignment of the magnetic and mechanical axes is good to within 0.05 cm over the 64.7-cm length of the diffusion chamber.[5] The cathode and anode are then aligned on the mechanical axis using a cathetometer telescope.

Differential pressures are obtained by the following pumping and gas inlet configuration. The cathode and anode ends of the system are each pumped by a 200-liter/sec, 4-in., liquid-nitrogen-trapped mercury diffusion pump. The diffusion chamber is pumped from the rear access port by a 1400-liter/sec, 6-in., water-trapped oil diffusion pump. The pumping speeds of all three diffusion pumps can be "throttled" by use of manual gate valves. Gas can be

introduced independently into the diffusion and anode regions, controlled by needle valves. Base pressures are typically 5×10^{-6} torr.

The properties of the plasma in the diffusion region are summarized in Table VI.1, while typical radial profiles are presented in Sec. VI. A. Our measurements agree with those of previous experiments.[1,5,73,74] The diffusion chamber is an aluminum cylinder, 64.7 cm long and 20 cm in diameter. At the axial midplane of the diffusion region are front and rear access ports, 3.6 x 22 cm. At the front port is a lucite window, through which 3 probes are inserted, neutral gas can be introduced, and visual and spectrosopic observations can be made. The rear port goes to the 6-in. diffusion pump, as well as to a lucite window, through which another probe is inserted.

At each end of the diffusion chamber, the axial boundaries consist of 5 concentric end-ring electrodes, mounted on an alumina insulating plate (fig. III.2). The inner two end-rings are quartered to provide information on azimuthal symmetry, as well as to provide suitable suppressor electrodes for the application of linear feedback. The electrical connections to the end-rings leave the diffusion region through an epoxy seal, and terminate on a banana-plug panel. Each electrode can be independently biased and monitored. The system length with the end-rings in place is reduced to L = 58.2 cm.

Reference to any end-ring electrode includes the correspond-

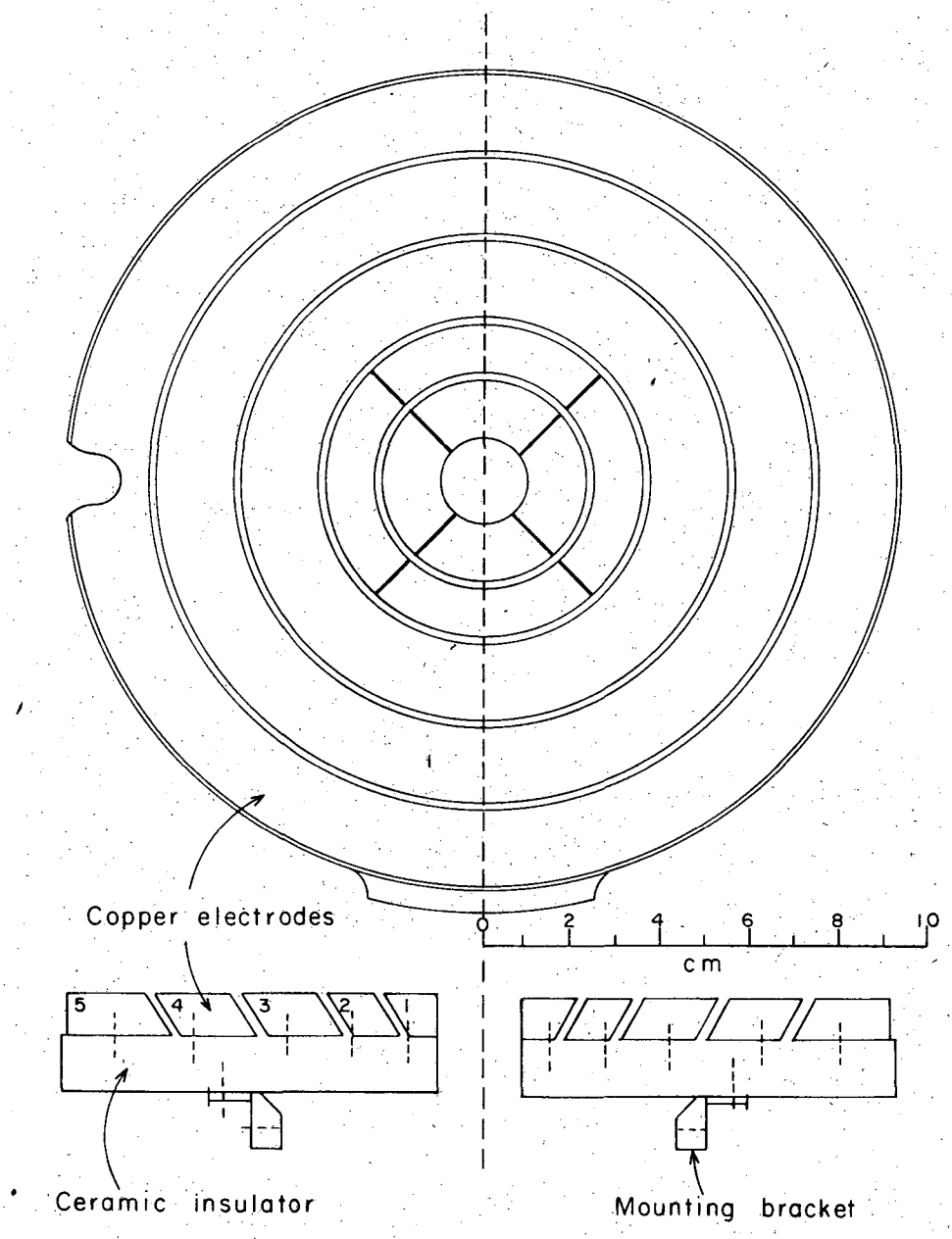

XBL689-6839

Fig. III.2. Concentric end-ring electrode configuration. Inner two tantalum end-rings are quartered; outer three end-rings are copper.

ing electrode at both the cathode and anode ends. For example, reference to the third end-ring implies the third end-ring at each end, tied together electrically.

The effect of the end-ring electrodes on the radial plasma profiles is discussed in Sec. VI. C. (DC stabilization). The effect of using the upper quarter of the second end-ring as a suppressor electrode for linear feedback is discussed in Sec. VI. D. And the effect of using the second and third end-rings as suppressor electrodes for AC stabilization is discussed in Sec. VI. E.

B. Langmuir Probe Configuration

Langmuir probes are used as the primary diagnostic tool. Probe theory, as discussed in Appendix C, is summarized in Sec. V. C. Physically the probe tips are 0.020-in. tungsten wire, extending 2 mm beyond a 3-mm o.d. quartz sleeve. The probe shank is 6-mm o.d. quartz or Pyrex tubing, which leaves the vacuum through a 0.25-in. sliding Wilson seal. The tungsten tip passes through a quartz-to-Pyrex graded seal to a coaxial cable, which runs to the probe circuitry. The saturated ion current, I_{si}, is measured by applying a -45 V bias to the probe and monitoring the current through a 1K resistor to ground. The floating potential, φ_f, is measured directly with a high impedance digital voltmeter. Fluctuations on I_{si} and φ_f are measured on a Tektronix Model 1L5 spectrum analyzer, or on a phase-sensitive lock-in amplifier Princeton Applied Research Model HR-8. The measurement equipment can be further isolated from the plasma by inserting an integrated circuit voltage-follower.

The physical probe arrangement at the axial midplane is shown in fig. III.3. Five radial probe ports exist, A through E. An axial probe, X, can be moved the length of the system, as well as rotated to various radii and azimuths. When the axial probe is removed beyond the midplane, the radial probe A can be inserted from the rear access port. In the figure, probe C is a suppressor probe, a 2 cm-long-probe tip, which can be aligned along B to provide larger plasma contact when applying linear feedback. Probe E is the directional Langmuir probe (DLP).

The probe characteristic (V-I plot) is obtained by using the Langmuir probe sweep chassis, shown schematically in fig. III.4. A low-impedance (R_{emf} = 50 ohm) voltage ramp is applied to the probe, and the current is measured through a 1K resistor R_I. The probe voltage can be measured through a 100 megohm resistor, as shown. This gives a 100:1 voltage reduction at the oscilloscope, as well as increasing the input impedance of the monitoring equipment. In practice, the 100 megohm resistor was replaced by an integrated circuit voltage-follower, giving higher input impedance, and no voltage divider. The probe characteristic is displayed on a Tektronix Model 502A oscilloscope where it can be photographed, or on a storage oscilloscope to save camera film, or on an X-Y recorder. The electron temperature can be obtained from the logarithmic derivative of the probe characteristic, as discussed in Appendix C.

C. Directional Langmuir Probe (DLP) Construction

A directional Langmuir probe, DLP, is used in the present

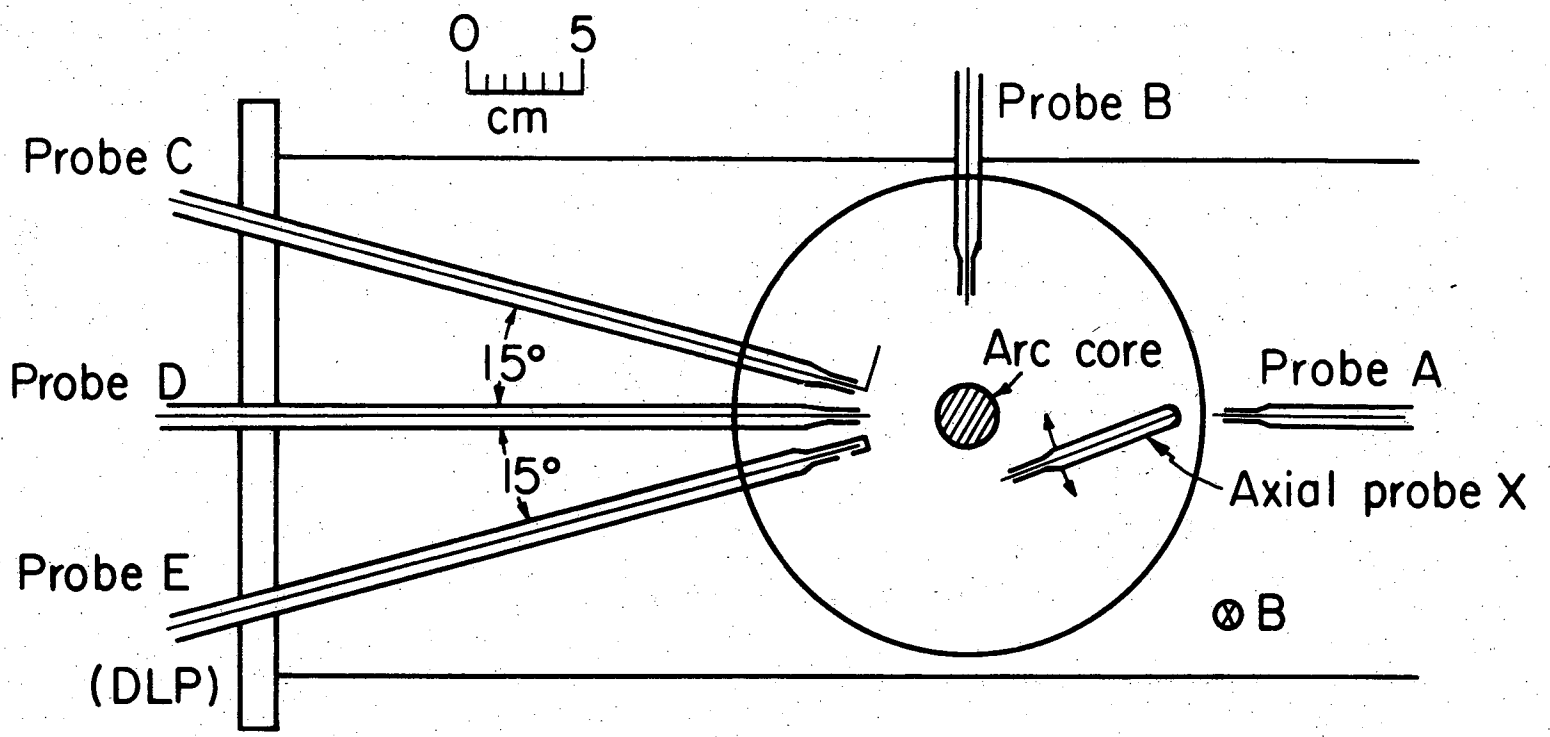

XBL 7112-4892

Fig. III. 3. Probe arrangement at the midplane of the diffusion chamber looking toward the "cathode end." The axial probe, X, can be rotated on its support rod. Probe E is the directional Langmuir probe (see Fig. III.5). Probe C has a 2-cm-long probe tip aligned along the magnetic field, to serve as a controlled electron sink for linear feedback experiments.

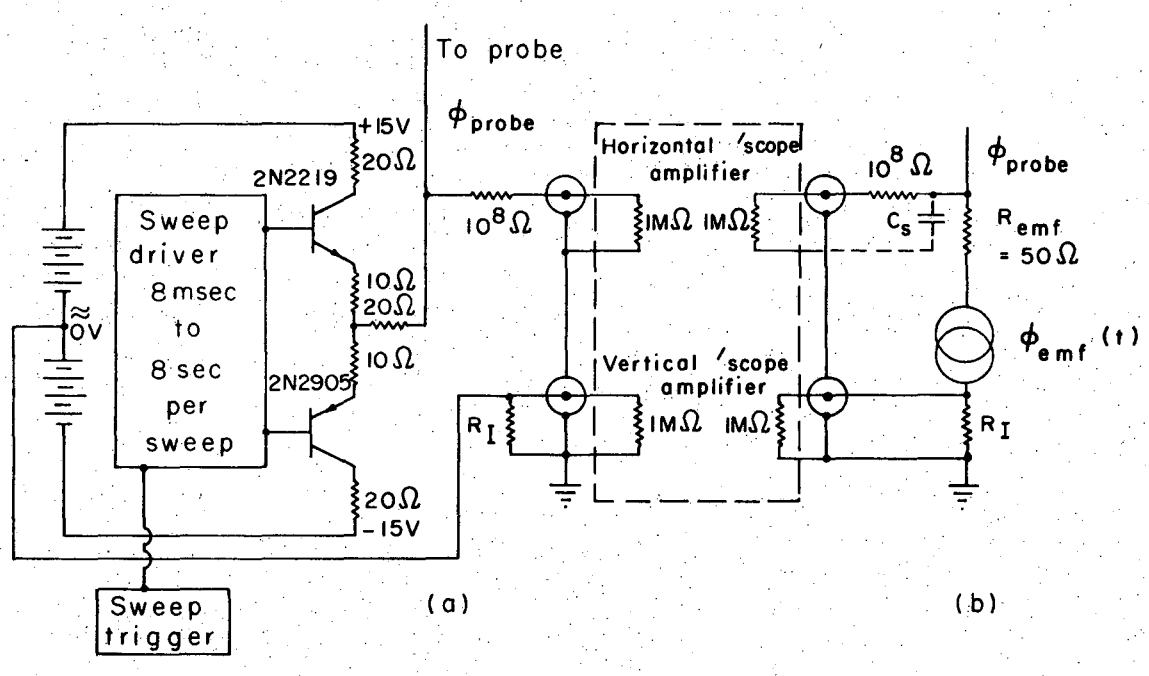

Fig. III.4. Langmuir probe sweep chassis. (a) Schematic; (b) equivalent circuit.

experiment to measure ion currents in the azimuthal and axial directions. Using simple probe theory, we derive an expression for the streaming velocity as a function of measured directional ion currents. Theory and six experimental checks on the operation of the DLP are discussed in Appendix D. In particular, the DLP is found to operate correctly as a simple Langmuir probe, and to correctly measure a known plasma drift velocity.

A DLP was constructed, as discussed by Hudis and Lidsky,[6,7,10] so that simple probe theory should be valid. The construction we use is presented in fig. III.5. A flat slot was milled in the 0.040-in. tungsten rod so that a planar collection surface is obtained. The remainder of the tungsten rod was shielded from the plasma by an insulating sleeve of alumina. An alumina plug was inserted in the end of the alumina tube, and bonded with a ceramic cement. The epoxy vacuum seal was made 12 cm from the probe tip, outside the plasma region. The alumina sleeve was broken about 1 in. inside the 0.25-in. o.d. x 0.065 in. wall stainless steel support tube, so that an epoxy vacuum seal could be made. The alumina sleeve was then epoxied to the stainless steel tube. The tungsten rod runs the entire length of the probe. It is silver-soldered to coaxial cable at the end, and the grounded coaxial shield is connected to the stainless steel support tube.

The DLP is biased -45 V negative, and the saturated ion current is measured through a 1K resistor to ground. The stainless steel support tube leaves the front access port E, through a

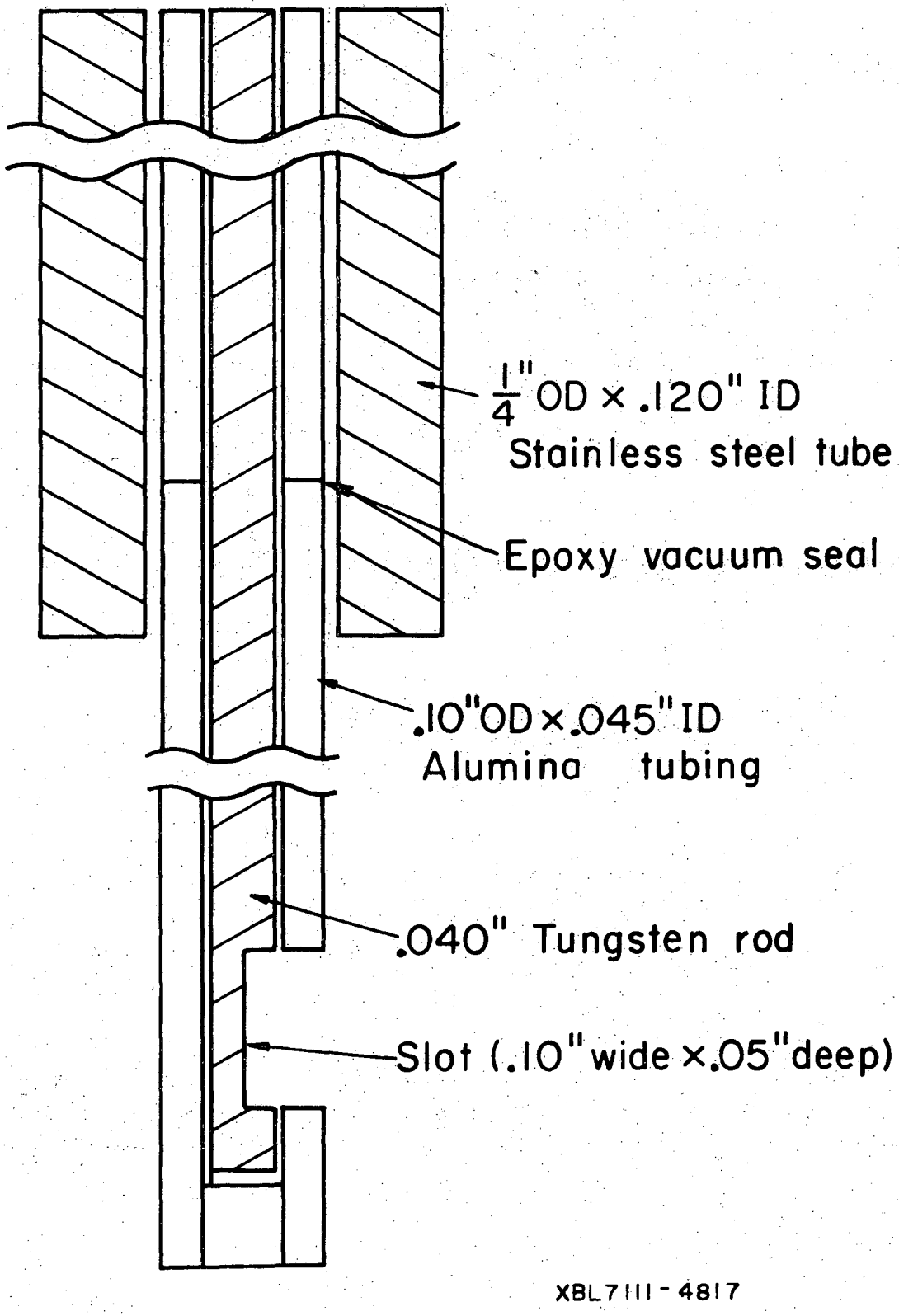

Fig. III.5. Directional Langmuir probe construction.

sliding Wilson seal. Particle currents can be measured in the axial and azimuthal directions at all radii. The difference in the azimuthal particle currents is typically 10 to 50%, which can be observed on a digital voltmeter, so that no sophisticated equipment is required.

D. Linear Feedback Circuitry

The linear feedback loop we use to stabilize a low-frequency instability is shown schematically in fig. III.6. Experimental feedback results are discussed in Sec. VI. D. The rear radial probe is generally used as the sensor probe, monitoring a reference fluctuation on I_{si} or Φ_f for the lower-frequency (LF $\approx$ 2 kHz) wave. The signal is then filtered so that we only affect the m = 1 mode of the LF wave. Then the signal is phase-shifted 0 to 360 deg by an active RC circuit. The signal is amplified and fed into the 8 ohm impedance terminals of two voice-to-line transformers in series. The transformers were used for two reasons: (1) so we could more nearly match the plasma impedance at low feedback power levels, as well as protect the amplifier; and (2) so we could electrically float, or dc bias, the feedback signal with respect to ground.

Feedback current is measured through a 10 ohm resistor. The complex loop frequency response is measured from the input at the sensor probe, to the output at the suppressor electrode, so that the actual loop gain and phase shift is measured.

Linear feedback was attempted on one or more quarters of the inner two end-ring electrodes (fig. III.2). The signal on a

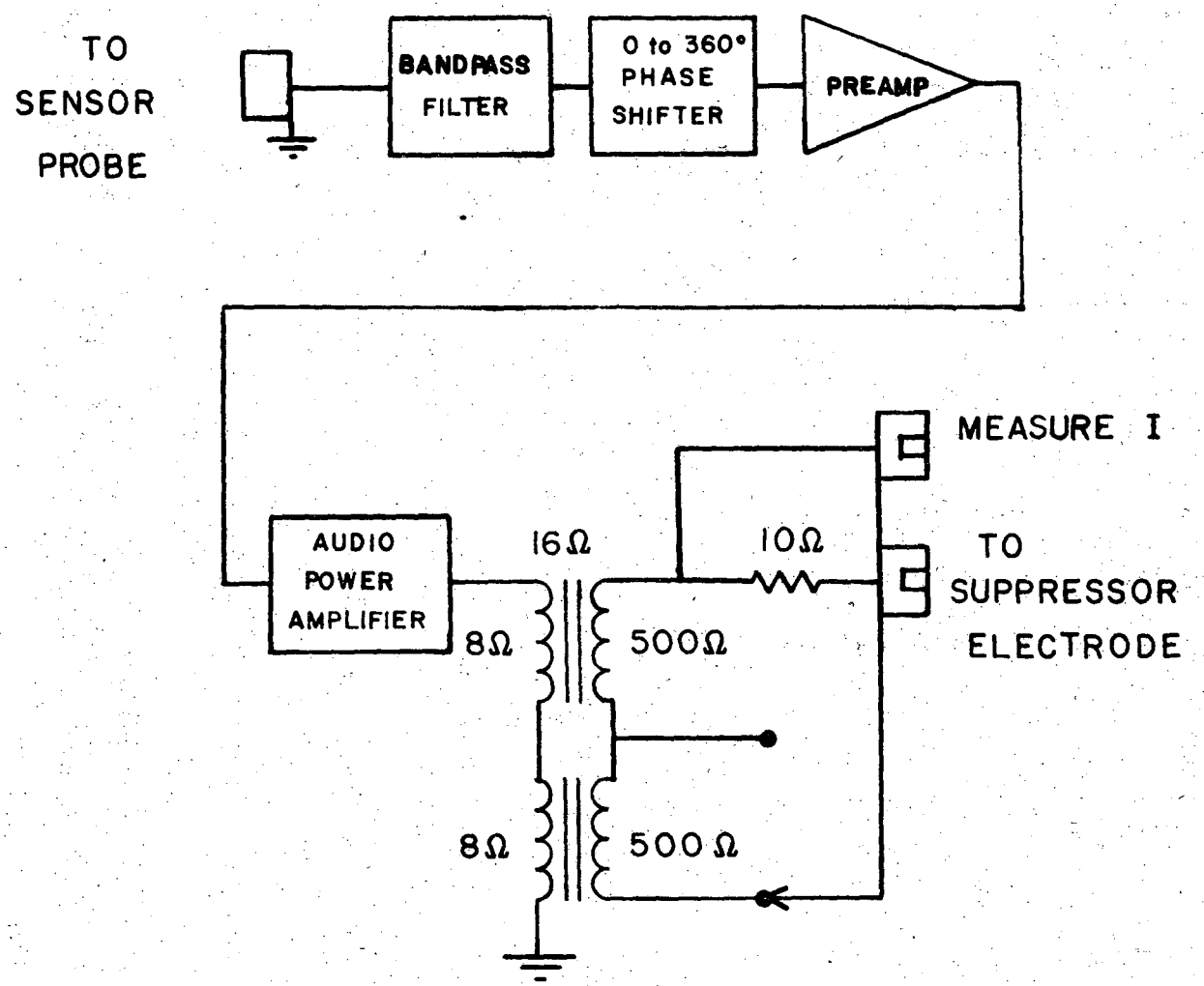

XBL 7112-1820

Fig. III.6. Linear feedback loop schematic.

given suppressor electrode was applied in a variety of configurations: (1) with respect to ground; (2) with respect to other electrodes at different azimuths; and (3) with respect to the corresponding electrode at the opposite end of the system. A typical case is presented in Sec. VI. D., when the feedback signal is applied to the upper quarter of the second end-ring electrode with respect to ground.

Feedback was also attempted on a modified Langmuir probe, probe C in fig. III.3 , described as a 2-cm-long, 0.020-in. diameter tungsten probe tip, aligned along B. This suppressor probe is much less effective than the end-ring electrodes, probably due to the small plasma contact area.

E. AC Stabilization Switching Circuit

AC stabilization is applied by pulsing a rectangular voltage signal on and off a chosen electrode. The necessary voltage switching circuit is presented in fig. III.7. A regulated dc power supply is applied to the DC INPUT connector. An amplified TRIGGER INPUT is used to switch the power transistor on and off. When the power transistor is on, the OUTPUT is grounded through the transistor. When the power transistor is off, the OUTPUT voltage is the power supply voltage minus the voltage drop through the 10 ohm resistor, through which the current is measured. Switching frequencies of up to 20 kHz were studied, with negligible deterioration of the OUTPUT pulse. AC stabilization is discussed in Sec. VI. E.

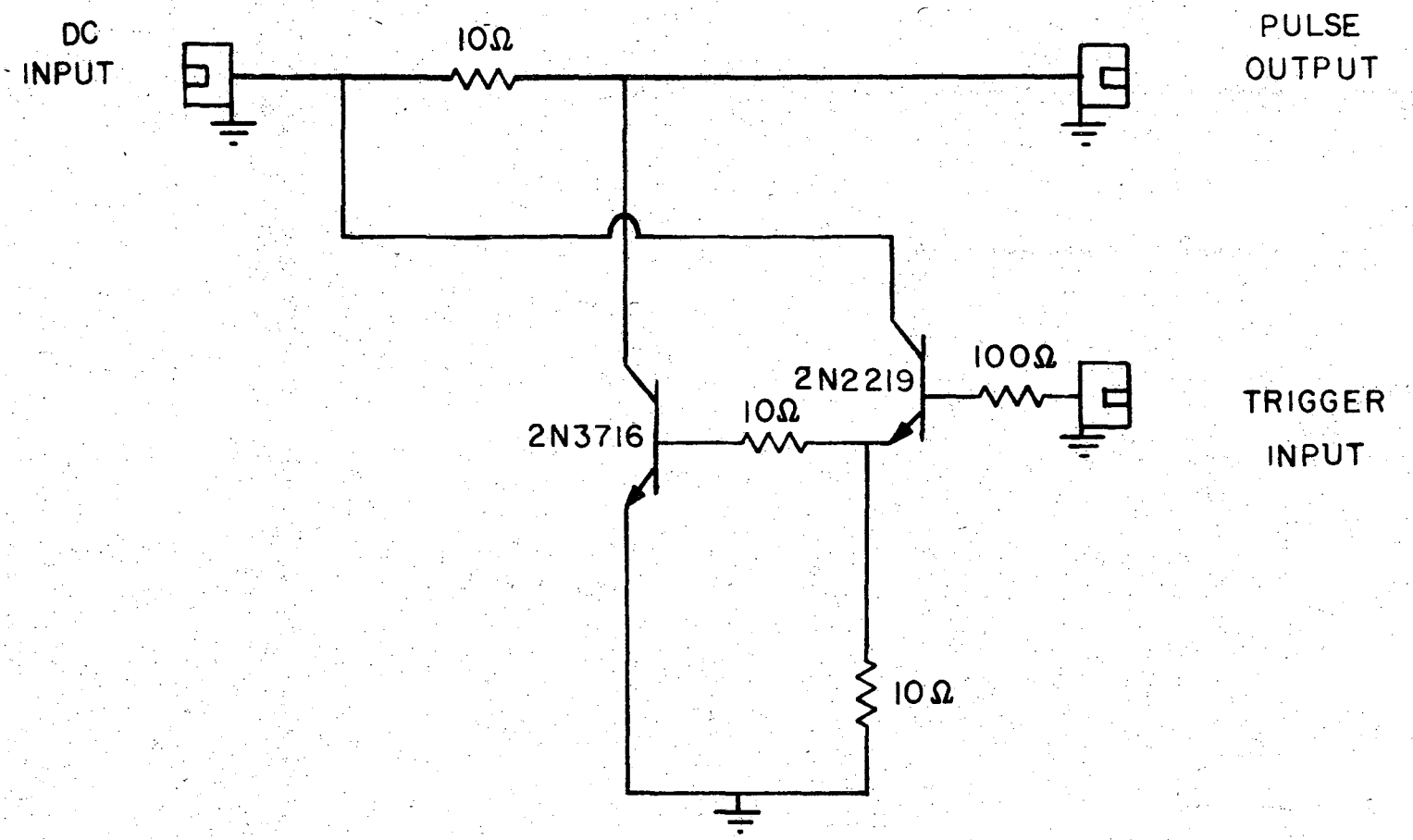

XBL 7112-1818

Fig. III.7. AC stabilization switching circuit.

IV. SURVEY OF LOW-FREQUENCY INSTABILITIES.

A. Introduction.

The secondary plasma of an HCD contains several free energy sources, which can drive instabilities. As a result, several different low-frequency instabilities have been "identified" in an HCD, which we summarize in Table IV.1. Several of these instabilities have similar properties, in that they are driven by plasma rotation in a nonuniform radial electric field. Also, large density and temperature gradients exist near the primary arc column, in addition to a large electric field. Collisional effects can also be important. In these circumstances, it is not surprising to observe waves which exhibit properties consistent with several driving mechanisms, simultaneously.

A theory which includes all of these effects simultaneously and self-consistently does not exist. Recently, however, computers have been used to treat more correct fluid models, and give solutions more consistent with experiment. We expect future work to include numerical integration of a radial wave equation,[78] using realistic experimental plasma profiles, and solving for normal mode behavior.

In this section we categorize and discuss some of the instabilities which might occur in an HCD with the aid of a review article by Lehnert.[79] We consider only electrostatic instabilities for our low $\beta \equiv p_i/(p_i + B^2/8\pi) \ll 1$, high density, $c_A^2/c^2 \ll 1$, plasma, since induced magnetic fields in the plasma are negligible compared to the applied axial field.

Table IV.1. Waves Identified in an HCD.

Wave	Author	Frequency (kHz)
1. Rayleigh-Taylor centrifugal flute	Hudis (1969)[6,7]	1 - 5
2. Kelvin-Helmholtz velocity-shear flute	Hudis (1969)[6,7]	12 - 17
3. Resistive drift	Chung and Rose (1967)[75]	10 - 20
	Aldridge and Keen (1970)[55]	15 - 20
	Gunshor, Noon, and Holt (1968)[76]	8
	Kambic, Noon, and Jennings (1971)[77]	
	Stufflebeam, Reinovsky, Noon and Jennings (1971)[58]	
4. E x B drag	Morse (1965)[17]	2
5. Electrostatic ion cyclotron	Chung and Rose (1967)[75]	50 - 80
6. Ion-acoustic	Gunshor, Noon, and Holt (1968)[76]	4 - 20

B. Classification of Instabilities.

1. MHD.

This class of instability is driven by the kinetic and potential energy of the macroscopic fluid. For example, available energy is associated with plasma rotation, shear in the mass flow velocity, and an effective gravitational or electric potential. This is generally a large source of energy. Fluid instabilities can be derived from the well-known MHD equations. The following MHD instabilities will be considered:

a. Rayleigh-Taylor flute instability[18-22]

b. Rotational flute instability

c. Velocity shear

   i. Kelvin-Helmholtz[20,23-26]

   ii. Diocotron[80]

d. E x B neutral drag[15-17]

e. Screw[60]

f. Ion-acoustic[81]

2. Drift.

Drift instabilities are driven by the expansion energy of the plasma, while charge separation is maintained by the relative drifting of the ions and electrons. Drift instabilities can often be derived from the fluid equations, when appropriate assumptions are made. Instability requires finite parallel wavelength. The following drift waves will be considered:

a. Resistive drift[12-14,82]

b. Current convective[83]

c. Drift cyclotron[83-85]

3. Micro-Instabilities.

The available energy is contained in deviations from the Maxwellian velocity distribution, and is generally released by resonant interaction with high-frequency waves. These kinetic instabilities must be derived from the more complex Vlasov-Maxwell equations. The available energy, and enhanced transport rates are generally small, however, and micro--instabilities will not be included in our survey of low-frequency (LF $\lesssim \Omega_i$) instabilities.

C. Experimental Evidence for Wave Identification.

In practice a wave can be characterized by certain experimentally measurable properties. For example, we consider the five following experimental parameters:

(a) Spatial location

(b) Frequency

(c) Direction of Propagation

(d) Parallel wavelength

(e) Growth rate

Many of the instabilities mentioned in section IV. B. have markedly different characteristics. Some however, have similar properties on all five points. We summarize the properties of the instabilities mentioned in section IV. B, as well as two experimental instabilities, in Table IV.2. The waves are discussed in section IV. D, from which we conclude that both experimental waves have properties similar to the centrifugal flute and the E x B drag instabilities. A theory which includes density gradient, centrifugal and Coriolis forces due to plasma rotation in a radial electric field, and

Table IV.2. Survey of Low-frequency Instabilities.

WAVE	FREQUENCY	DIRECTION OF PROPAGATION	LOCATION	$k_\parallel$
Rayleigh-Taylor	$k_y g/2\Omega_i$ ($\lesssim$ 5 kHz)	ion diamagnetic	E_r (max)	$k_\parallel = 0$
Rotational Flute	$k_y g/2\Omega_i - 2\Omega_0\delta/k_y$ ($\lesssim$ 50 kHz)	either	E_r (max)	$k_\parallel = 0$
Kelvin-Helmholtz	$k_y (Ec/B)$ ($\lesssim$ 50 kHz)	either	d ln E_r/dr (max)	$k_\parallel = 0$
Diocotron	ω_{pi}^2/Ω_i ($\gg \Omega_i$)	either	d ln E_r/dr (max)	$k_\parallel = 0$
E x B neutral drag	k_y Ec/B ($\lesssim$ 50 kHz)	either	E_r (max)	$k_\parallel = 0$
Screw	$k_z U_{z0}$	electron diamagnetic		
Ion Acoustic	$k_z c_s$	z		
Resistive Drift	$k_y kT_e c\delta/eB$ ($\lesssim$ 50 kHz)	electron diamagnetic	$\nabla n/n$ (max)	$k_\parallel/k_\perp > 4 \times 10^{-2}$
Current Convective	$k_y kT_e c\delta/eB$ ($\lesssim$ 50 kHz)	electron diamagnetic	$\nabla n/n$ (max)	$10^{-4} \ll k_\parallel/k_\perp \ll 1$
Drift Cyclotron	$n\Omega_i$; n = 1, 2 (25 to 50 kHz)	electron diamagnetic	$\nabla n/n$ (max)	$10^{-4} \ll k_\parallel/k_\perp \ll 1$
Experimental LF	2 kHz	ion diamagnetic	E_r (max) (R = 5.0 cm)	$k_\parallel = 0$
Experimental HF	30 kHz	electron diamagnetic	$-E_r$(max), $\nabla n/n$(max) (R = 1.0 cm)	$k_\parallel = 0$

collisions with a cold neutral background gas is developed in section V.A under the name "rotational instability."

D. Discussion of Possible Waves

I. MHD.

a. Rayleigh-Taylor Flute Instability The centrifugal force due to plasma rotation in a radial electric field, acting in the direction of decreasing density, will be shown in section V.A to be an important destabilizing influence in the HCD. Hudis identified one low-frequency instability in an HCD as the Rayleigh-Taylor centrifugal flute.[6,7] However, Rayleigh-Taylor theory as derived in the literature neglects the important rotational effect of the Coriolis force, as well as collisions with neutrals. These latter effects cannot be ignored in the HCD. The Rayleigh-Taylor theory will be modified to include Coriolis and collisional effects, under the new name, rotational instability.

b. Rotational Flute Instability. This instability includes most of the important effects present in the HCD, and provides a good explanation of the experimental results. See section V.A. for the derivation and discussion.

c.(i) Kelvin-Helmholtz Instability. The K-H instability is driven by the free energy stored in the relative motion of adjacent fluid elements. Chandrasekhar derived the dispersion relation from the high density ($c_A^2 / c^2 << 1$) fluid equations, assuming a 2-region discontinuity in the density and velocity profiles.[25] He presented a good physical discussion.

In 1965, Rosenbluth and Simon derived a "radial wave equation"

which is the starting point for much later work.[78] It was derived by a finite gyroradius (FGR) ordering of the Vlasov equation. The radial displacement eigenfunction is complex, and usefulness is limited to special cases.

Stringer and Schmidt generalized the work of Rosenbluth and Simon[24] by making no initial ordering assumptions on the Vlasov equation. By making the ordering assumptions of FGR, low density, and high density, their results reduce to those of Rosenbluth and Simon,[78] Damm et. al.,[86] and Chandrasekhar,[25] respectively.

In 1968, Hans presented a simple derivation, beginning with the incompressible single-fluid equations.[20] He included finite gyroradius effects(FGRE) in the pressure tensor and collisions with neutrals,and assumed a 2-region discontinuity in the velocity to obtain a quartic dispersion relation. A parametric plot of the results of numerical integration shows that FGRE are stabilizing, while collisions with neutrals are stabilizing for low collision frequencies and destabilizing for large collision frequencies.

In 1969, Kent, Jen, and Chen identified the edge oscillation the Q-machine as a K-H flute.[23] They begin with Rosenbluth and Simon's radial wave equation. A 3-region solution yielded good agreement with theory and experiment for frequencies from 5 to 17 kHz. Also, measured wave amplitudes correlated with calculated growth rates for azimuthal mode numbers m = 3,4,5. They suggested future improvements: (1) solve the full quartic dispersion relation instead of simplifying to a quadratic; (2) include finite parallel resistivity, $k_{\parallel} \neq 0$; and (3) numerically integrate more realistic profiles which would contain FGRE, and density gradient drifts.

In 1970, Perkins and Jassby looked for normal mode solutions of the radial wave equation.[26] The effects of finite $k_{\parallel}$, finite resistivity, gravity, density gradient, finite gyroradius (FGR), ion viscosity, and velocity shear were included. They derived analytic integral expressions for the thin shear-layer case, by assuming a jet velocity profile. These analytic results yielded good agreement with numerical integration of the radial wave equation, using experimental electric field and density profiles. Comparison of theory and experiment yielded a convincing identification of the Q-machine edge-oscillations of Enriques, Levine, and Righetti[87] as the K-H instability. It is interesting to observe how the K-H flute goes over to a resistive drift wave as $k_{\parallel}$ is increased.

Hudis and Lidsky used the results of Perkins and Jassby, and of Kent, Jen, and Chen to help identify a K-H instability in an HCD.[7] By numerical averaging over radial plasma and wave profiles, they were able to conclude that shear in the radial electric field profile was sufficient to destabilize a normal mode K-H wave.

In the present experiment, the frequency, rotation direction, and flute-like structure of the K-H instability are compatible with both experimental waves. However, the Kelvin-Helmholtz instability will be eliminated from consideration here, since both experimental waves occur in regions of large centrifugal force, and low velocity-shear.

c.(ii) Diocotron. The Diocotron instability is applicable to the case of low-density ($\omega_{pe} \ll \Omega_e$) velocity-shear, when eddy currents form. The Diocotron instability will be eliminated because

it is applicable to lower density plasmas, and the predicted frequency is much higher than those observed.

d. E x B neutral drag. In 1963, Simon considered a partially ionized plasma in crossed electric and magnetic fields.[15] He used a 3-fluid slab model and showed that electrons and ions drift at different rates due to collisions, $v_y = (E_x c / B) \left[\Omega_i^2 \tau_{in}^2 / (1 + \Omega_i^2 \tau_{in}^2) \right]$. Instability was shown by means of the "Rosenbluth-Longmire" picture only if $\underline{E} \cdot \nabla n > 0$.[88] Other mechanisms which caused differential drifting of the ions and electrons, such as diamagnetic drift and effective gravity, were not considered.

Hoh included these Hall drifts in a 3-fluid treatment, but could not get an analytic solution.[16] A dispersion relation was obtained by dimensional analysis.

In 1965, Morse modified the E x B neutral drag theory by introducing a "corrected" electric field, which included density and plasma potential gradients, $\underline{E}_c = \underline{E}_o + \frac{\nabla n}{n} \left[(\Omega_i \tau_{in} / \Omega_e \tau_{en}) T_e - T_i \right]$, where $\tau_{\alpha n}$ is the neutral collision time for species α.[17] Instability can now occur even for $\underline{E} \cdot \nabla n < 0$, a fact Morse used to identify a 2 kHz oscillation in an HCD.

The predictions of E x B neutral drag theory agree with experimental data, at least qualitatively. However, ignored are rotational effects such as centrifugal and Coriolis forces, which are important in the present experiment. Since numerical solutions are required in either case, we will attempt a more complete theory in order to include several effects simultaneously. Although the E x B Drag theory contains some of the physics involved in the present experiment, it is incomplete. Hence, the E x B neutral drag instability

will be replaced with a theory which includes diamagnetic and gravitational drifts as well as rotational effects.

e. Screw. The Screw instability will be eliminated. since there is no evidence in support of a finite parallel wavelength, or any screw-like structure.

f. Ion-Acoustic. Gunshor, Noon, and Holt reported an ion-acoustic wave in an HCD, with a frequency range 4 to 20 kHz.[76] The wave propagated at an angle with respect to the axial magnetic field, and was observed to be a standing wave in the axial direction. Identification was obtained by studying frequency dependence of the wave on the system length and the atomic mass. The ion-acoustic instability will be eliminated here since there is no measurable travelling or standing wave along the magnetic field.

2. Drift Waves.

Drift waves are considered as a possible explanation for the higher-frequency (HF) wave, which is located at small radii, in a large density gradient.

(a) **Resistive Drift.** The resistive drift wave is driven by the expansion energy in a density gradient, and is destabilized by finite parallel resistivity. The resistive drift wave was reported in and HCD by Chung and Rose,[75] Aldridge and Keen,[55] and Gunshor, Noon, and Holt.[76]

Hendel et. al. showed that ion-ion collisions are stabilizing.[82] Chen showed that small amounts of axial current (~ 10 amps) localized on the axis of a cylindrical chamber, such as the primary arc of an HCD, can provide sufficient magnetic shear to stabilize

certain localized drift modes.[21]

Resistive drift theory is incomplete in its application to an HCD, since important differential drifting mechanisms such as centrifugal gravity and collisions with neutrals are neglected. We eliminate the resistive drift wave here, since there is no experimental evidence for finite parallel wavelength, and present a more relevant theory including rotational and collisional effects.

(b) Current-Convective Instability. The current-convective instability is similar to the resistive drift instability, but is destabilized by parallel streaming, such as in the primary arc column in an HCD. However, Landau growth should not be expected where collisions are important.[14] We eliminate the current-convective instability on the grounds of parallel wavelength and collisional effects.

(c) Drift Cyclotron. The drift cyclotron instability is also destabilized by parallel streaming. Chung and Rose identified an electrostatic ion-cyclotron instability at frequencies of 50 to 80 kHz in an HCD.[75] However, we eliminate the drift cyclotron instability since the measured frequency is too low, and not a multiple of Ω_i.

3. Summary.

We conclude that the two experimental waves are most consistent with the Rayleigh-Taylor centrifugal flute theory, and with the $E \times B$ neutral drag instability, which are both driven by plasma rotation in a radial electric field. In section V.A. we develop a theory for the "rotational" flute instability, which includes the effects of

density gradient, centrifugal and Coriolis forces due to plasma rotation in a radial electric field, and collisions with neutrals.

V. THEORY

A. Rotational Flute Instability

1. Introduction

The plasma in the diffusion region of the hollow cathode discharge (HCD) is rotating in the presence of a nonuniform, nonambipolar, radial electric field, which is discussed in section VI.A.4. Under such conditions, with the centrifugal force treated as an effective gravity, $\underline{g}$, opposing the density gradient, $\underline{g}\cdot\nabla n < 0$, the plasma may be unstable to the Rayleigh-Taylor centrifugal flute instability. As will be shown, the plasma may be unstable even for $\underline{g}\cdot\nabla n > 0$, if the radial-velocity shear is sufficient.

A comprehensive and analytically useful theory including simultaneously the effects of 2-fluid compressibility, finite gyroradius (FGR), ion inertia, collisions, and Coriolis force does not exist. However, most of these effects have been treated by various authors, and will be discussed here. A useful and simple derivation by Roberts and Taylor (1962) will be modified in section V. A. 2 to include the Coriolis force, collisions with neutrals, and an ion sink term.[18] The remainder of this section is devoted to a historical and conceptual survey of recent work.

In 1954, Kruskal and Schwarzschild presented one of the earliest derivations of the graviational instability, which is sometimes named after them.[89] In 1957, Rosenbluth and Longmire treated a noncompressible, infinitely conducting fluid model, with a sharp fluid-vacuum interface,[88] and calculated a purely growing wave with the growth rate $\gamma = (gk)^{1/2}$.

In 1961, Lehnert extended the work of Rosenbluth and Longmire

to arbitrary density steps at the interface.[90] His results show that plasma stability can be maintained for $\underline{g}\cdot\nabla n < 0$, provided the density gradient is sufficiently small. FGR stabilization is also calculated, but incorrectly.

Rosenbluth, Krall, and Rostoker correctly treated FGRE beginning with a small gyroradius ordering of the Vlasov equation.[90] They worked in the zero electric field frame. However, we can translate to the more useful drift frame by adding the Doppler shift $V_D = E/B = 2\nu\delta + g/\Omega_i$.[18] In this frame for a slab model, their dispersion relation is equivalent to $\omega^2 + (2\nu\delta k + gk/\Omega_i)\omega + g\delta = 0$, with solution for the frequency $\Omega_r = \frac{1}{2}(2\nu\delta k + gk/\Omega_i)$, and growth rate $\gamma = (g\delta - \Omega_r^2)^{1/2}$. In the above, $\nu = \frac{1}{2} a_i^2 \Omega_i$ is a collisionless viscosity; the inverse density scale length, $\delta \equiv -\nabla n/n > 0$; $a_i \equiv v_{th}^i/\Omega_i$ is the ion gyroradius; $g \equiv V_\theta^2/R$ is the centrifugal gravity; and k is the perpendicular wave number. The first term in the coefficient of ω in the dispersion relation is the FGR term, while the second is the 2-fluid gravitational effect. The fact that the growth rate γ is reduced from that of earlier calculations is also apparent, showing FGR stabilization. Application to cylindrical geometry results in Whittaker's equation.[92] The solution is quantized, and is only briefly discussed.

Subsequently, Lehnert[19] has cast doubt on the treatment of Rosenbluth, Krall, and Rostoker. He used a 2-fluid model and included compressibility in the equations of continuity (FGRE), but inconsistently ignored off-diagonal elements of the pressure tensor. A term exactly cancels the FGR stabilization reported by

Rosenbluth, Krall, and Rostoker, leaving a residual stabilizing term reported earlier by Lehnert.[90]

In 1962, Roberts and Taylor used a one-fluid model to vindicate Rosenbluth, Krall, and Rostoker.[18] They showed that Lehnert's work was equivalent to including FGR compressible effects in Ohm's law.[19] However, they included FGRE in the ion pressure tensor, as calculated by Thompson.[93] The results are in agreement with Rosenbluth, Krall, and Rostoker. Lehnert's result can be obtained by setting the viscosity $\nu = 0$.

Lehnert introduced the Coriolis force in the fluid equations and obtained the following solution:[22] $\omega = -\frac{1}{2} m\Omega_0 K \pm \frac{1}{2}\Omega_0(m^2K^2 + 4\lambda)^{1/2}$, where m is the azimuthal mode number, $\Omega_0 = V_\theta/R$ is the angular fluid rotation, $\lambda \equiv (1 + 2\Omega_0/\Omega_i)R\nabla n/n < 0$, and $K \equiv \Omega_0/\Omega_i + 2\lambda/m^2$. The first term in K is the usual 2-fluid gravitational effect, independent of the direction of rotation, while the second term contains the Coriolis effect. For small rotations the frequency is increased, and the growth rate reduced for $\Omega_0 < 0$ (ion-diamagnetic direction); and the frequency is reduced and the growth rate increased for $\Omega_0 > 0$. The Coriolis force contribution is proportional to the density gradient.

Lehnert made an interesting comment based on the form of the ion momentum equation, $nM\frac{dv}{dt} = nq(\underline{E} + v \times \underline{B}) + nM\Omega_0^2\underline{R} + 2nM\underline{v} \times \underline{\Omega}_0$

He remarked that the Coriolis force term, last term, can be combined with the Lorentz force term to yield an effective magnetic field for the ions, $\underline{B}^{*} = \underline{B} + 2M\underline{\omega}_0/e$. This causes an additional ion drift, and hence charge separation. As in previous work, Lehnert treated FGRE incorrectly.

In 1965, Rosenbluth and Simon showed the validity of Roberts and Taylor's method by developing a set of single-fluid equations from the FGR expansion of the Vlasov equation.[78] The resulting equations are identical to those used by Roberts and Taylor, except for a term involving the divergence of the diamagnetic drift velocity, which vanishes for uniform temperature, kT_e, and density gradient, $\delta = -\nabla n/n$. A radial wave equation was developed, from which a quadratic integral expression for the complex eigenfrequencies results. However, the radial displacement eigenfunction is in general complex, so that direct application is limited to special cases.

A suggestion is mentioned by Bogdanov et al., conjecturing FGR stabilization of the gravitational flute by fixing the potential on various radial end-rings.[94] Since an ion will drift at a reduced velocity,

$$\underline{v}_i = \frac{\underline{E}_o \times \underline{B}}{B^2} c + \frac{1}{2} \frac{a_i^2}{B^2} \frac{d^2 \underline{E}_o}{dx^2} \times \underline{B}c ,$$

due to FGRE, choosing $d^2\underline{E}_o/dx^2$ properly can reduce the effect of rotation.

Chen presented a physical picture showing clearly the effects

of ion-inertia, FGR, gravity, parallel wavelength, and density gradient.[95] In particular he showed that for an unstable gravitational flute, the density leads the potential fluctuations by the phase ψ = 180 to 270 deg, whereas for a resistive drift wave, ψ = 0 to 90 deg. This picture does not include neutral collisions or the Coriolis force, which we show in Sec. V. A. 3 can cause phase shifts ~ 90 deg. The resulting ψ = 90 to 180 deg is in better agreement with the phases measured for both experimental waves.

In 1966, Chen extended the work of Rosenbluth, Krall, and Rostoker to larger E_r, finite $k_\parallel$, finite resistivity, and arbitrary T_i/T_e.[21] He considered the 2-fluid equations in cylindrical geometry. The presence of a radial electric field, E_r, produces centrifugal and Coriolis forces, and they are not introduced externally, as in most previous calculations in slab geometries. On transforming variables, he obtained Whittaker's equation.[92] The solution for $k_\parallel = 0$, small rotations, and $T_i = T_e$ agrees with the results of Rosenbluth, Krall, and Rostoker.[91] The solution is difficult to interpret due to quantization of the radial mode number, but some insight is gleaned. For instance, Chen observed that the sign of the Coriolis force causes an asymmetry in the frequency and stability condition, whereas the centrifugal force is independent of the direction of rotation, as mentioned earlier in Lehnert's work.[22] He also showed that the Coriolis force is important for small radial mode numbers, whereas FGRE are more important for large radial mode numbers. The radial dependence

becomes quantized in the solution of Whittaker's equation, and determining what radial mode number to use limits present application of his results. It does appear to be closest to simultaneous consideration of FGR and cylindrical effects.

Byers added new information by using a nonlinear, two-dimensional, 2-fluid computer model.[38] The parameter ω_g/γ is considered, where $\omega_g = gk/2\Omega_i$ is the 2-fluid differential drift frequency, and $\gamma = (g\delta)^{1/2}$ is the simple growth rate. Linear theory predicts stability for $\omega_g > \gamma$. Physically this means that the differential drift of ions and electrons causes the density and velocity fluctuations to drift out of phase and stabilize the wave, before the wave can grow large on the γ time-scale. In particular, Byers showed that for $\omega_g^2/\gamma^2 = 1/4$, the Rayleigh-Taylor wave grew unbounded to the walls, but for $\omega_g^2/\gamma^2 = 1/2$, the wave saturated at finite amplitude, after initial growth. It would be meaningless to infer a sharp cutoff for nonconfinement of the R-T wave around $\omega_g^2/\gamma^2 \approx 1/2$, but based on this simple model we predict a large amplitude, nonconfined R-T instability at large radii. In the present work we include the effects of plasma rotation, collisions with neutrals, FGR, and ion inertia to calculate a more relevant stability ratio, γ/Ω_r, of the order unity at large radii, where the complex frequency $\omega = \Omega_r + i\gamma$.

In 1967, Stringer and Schmidt[24] generalized the work of Rosenbluth and Simon[78] and Chandrasekhar.[25] They derived a set of guiding-center equations in the presence of a nonuniform electric field, making no initial ordering assumptions. The usual FGR

ordering then reduces their result to the previous result of Rosenbluth and Simon.[78] Reordering for the high density case, $c_A^2/c^2 \ll 1$, yields the results of Chandrasekhar.[25] In particular, from their wave equation they found that a necessary, but not sufficient, condition for instability is that the "Richardson number" $J \equiv (g\nabla n/n)/(dV/dx)^2 < 1/4$. Note that instability is predicted for $\underline{g}\cdot\nabla n < 0$, the usual case for gravitational instability, and that instability may also occur for $\underline{g}\cdot\nabla n > 0$, for sufficiently large velocity shear, dV/dx.

Chandrasekhar derived the Richardson criterion physically by using an energy variational principle applied to the interchange of two adjacent fluid elements $\delta\rho$, located at x and $x + \delta x$, with velocities V and $V + \delta V$.[25] The work required to effect such an interchange is $\delta W = (-\, g\, \delta\rho\, \delta x)$, while the change in kinetic energy is $\delta E = \frac{1}{2}\rho\left[V^2 + (V + \delta V)^2 - \frac{1}{2}(V + V + \delta V)^2\right] = \frac{1}{4}\rho(\delta V)^2$. A necessary instability condition, based on simple energetics is $\delta E > \delta W$, or $J = (gn_0'/n_0)/(dV/dx)^2 < \frac{1}{4}$. This can be put in a simpler form, by using the scale lengths $L_v^{-1} \equiv \frac{1}{V}\frac{dV}{dx}$ and $L_n^{-1} = \frac{1}{n}\frac{dn}{dx}$, and the fact that the centrifugal gravity $g = V^2/R$. The resulting instability condition is $J = L_v^2/L_n R < \frac{1}{4}$, which will be another useful parameter for wave identification. Note that the Richardson number is the ratio of gravitational energy to velocity shear energy, available to drive an instability.

In 1968, Hans included collisions with neutrals in a "dusty" fluid model.[20] By assuming a density discontinuity in a uniform gravity and magnetic field, and matching solutions at the interface,

he obtained a cubic dispersion relation. FGRE are included in the pressure tensor, although the fluid is inconsistently considered to be incompressible. Numerical integration of the cubic dispersion relation shows that neutral collisions are stabilizing in a R-T configuration.

Bhatia extended the work of Hans to include a "stratified" density, $\rho(z) = \rho_0 e^{\beta z}$,[96] and magnetic field, $B^2(z) = B_1^2 e^{\beta z}$. Collisions with neutrals are found to be stabilizing for propagation transverse to B, while parallel propagation is unaffected.

In 1970, Ariel and Bhatia considered the effects of FGR and the Coriolis force on a slab fluid model.[97] The Coriolis force was introduced in the equation of motion, as suggested by Lehnert.[22] Numerical results show that FGRE are stabilizing, in agreement with earlier predictions, while the Coriolis force can be either stabilizing or destabilizing, depending on the magnitude and direction of plasma rotation.

In Sec. V. A. 2, we develop a single-fluid slab theory which includes many of the effects which we consider important in an HCD. An arbitrary density gradient is included, which corresponds to the actual measured profile. A centrifugal gravity due to plasma rotation is included, and the Coriolis force is introduced according to Lehnert,[22] and Ariel and Bhatia.[97] FGRE are included in the pressure tensor, consistent with allowing FGR compressible effects in Ohm's law, as pointed out by Roberts and Taylor.[18] We also include ion-inertia and collisions with neutrals.

2. The Fluid Equations

We write down a familiar form of the single-fluid equations:

$$\rho \frac{d\underline{v}}{dt} \equiv \rho \dot{\underline{v}} = \rho_e \underline{E} + \underline{j} \times \underline{B} - \nabla p - \nabla \cdot \underline{\underline{P}} + \underline{F} - \rho \nu_{in} \underline{v} \qquad (5.1)$$

$$\frac{\partial \rho}{\partial t} + \nabla \cdot (\rho \underline{v}) = S \qquad (5.2)$$

$$\frac{m}{ne^2} \frac{d\underline{j}}{dt} = \underline{E} + (\underline{v} - \underline{j}/ne) \times \underline{B} + \frac{\nabla p_e}{ne} - \eta \underline{j} \qquad (5.3)$$

This set will be closed in subsequent approximations.

a. The Drift Approximation. These equations reduce to those used by Chen[14] to derive the resistive "universal" overstability if we assume: (1) quasi-neutrality, $\rho_e \approx 0$; (2) no ion sink, $S \approx 0$; (3) low frequency, $\omega/\Omega_i \ll 1$, neglect electron inertia, $d\underline{j}/dt = d\underline{E}/dt = 0$; (4) cold ions, neglect viscosity. $\underline{\underline{P}} = 0$; (5) fully ionized, $\nu_{in} = 0$; (6) no additional body forces, $\underline{F} = 0$; (7) no zero-order electric field, $\underline{E}_0 = 0$; and (8) nearly perpendicular propagation, $k_\parallel^2/k_\perp^2 \ll 1$.

b. The Gravitational, Kelvin-Helmholtz Approximation. With different assumptions, the fluid equations reduce nearly to those used by Hans[20] in deriving the K-H and R-T instabilities. In this case we assume: (1) quasi-neutrality, $\rho_e \approx 0$; (2) no ion sink, $S = 0$; (3) low-frequency, $\omega/\Omega_i \ll 1$, neglect electron inertia, $d\underline{j}/dt = d\underline{E}/dt = 0$; (4) FGRE included in pressure tensor, $\nabla \cdot \underline{\underline{P}}$; (5) Coulomb collisions neglected, $\eta = 0$; (6) an effective gravity, $\underline{F} = \rho \underline{g}$; and (7) incompressible fluid, $\nabla \cdot \underline{v}_1 = 0$.

The difference between our equations and those of Hans is that we have assumed cold neutrals, and that we allow a compressible fluid. Hans solved for the K-H and R-T configurations by assuming

a discontinuity in the fluid velocity and plasma density, respectively. Solutions were matched at the interface to yield the dispersion relation.

c. The Rotational Approximation and Solution. Now the derivation of the expressions for the rotational instability which we will use is presented. FGRE and gravity will be included following the mathematics as presented by Roberts and Taylor.[18] However, the Coriolis force due to uniform rotation will be introduced in a slab model, as in Eq. (1) of Lehnert.[22]

An effective source term, S, is included in the continuity equation to show theoretically the effect of linear feedback.[33-35] In practice however, linear feedback applied to the end-ring electrodes changes the axial boundary conditions.[98-100] The potential changes due to linear feedback are shown to be equivalent to an ion-source in the continuity equation, thereby greatly simplifying the mathematics.

Prater[99] and Kunkel and Guillory[100] included a source term in the linearized particle continuity equations due to currents to the axial boundaries, $\langle \nabla_{\parallel} \cdot n\underline{v}_{\parallel} \rangle$ V, where the brackets indicate averaging over the flux tube volume, V. Following Chen,[98] they found the axial boundary currents as a function of density and potential variations, and used Poisson's equation to obtain a local dispersion relation. For a highly conducting sheath, stabilization of the interchange instability is shown theoretically and experimentally, as charge drains out the ends faster than it accumulates due to the instability.

In the present experiment, where transverse ion transport dominates electron transport, current to the axial boundaries must be balanced by transverse ion currents due to changes in potential. Charge con-

servation requires, $q^\alpha \nabla_\parallel \cdot n\underline{v}^\alpha_\parallel + e \nabla_\perp \cdot n\underline{v}^i_\perp = 0$. The resulting ion source term is approximated by,

$$S = M_i\langle \nabla_\perp \cdot n\underline{v}^i_\perp \rangle_V = -\frac{M_i q^\alpha}{e}\langle \nabla_\parallel \cdot n\underline{v}^\alpha_\parallel \rangle_V = -\frac{M_i q^\alpha}{eV}\int_{wall} d\underline{S}_\parallel \cdot n\underline{v}^\alpha_\parallel = -\frac{M_i q^\alpha}{e^2 V} I_\parallel ,$$

where $I_\parallel$ is the actual feedback-controlled current to the wall.

Assume:

(1) Quasi-neutrality, $\rho_e \approx 0$;

(2) Low-frequency, ω/Ω_i, $\omega/\omega_{pe} \ll 1$, neglect electron inertia, $d\underline{j}/dt = d\underline{E}/dt = 0$;

(3) Low $\beta \lesssim (m/M)^{1/2} \rightarrow \underline{B} = B_0\hat{z}$ uniform, $\nabla \times \underline{E} = 0$;

(4) resistivity negligible, $\eta = 0$;

(5) $\delta \equiv -\nabla n(x)/n(x) =$ constant;

(6) High density, $c_A^2/c^2 \ll 1$;

(7) δa_i, $ka_i \ll 1$;

(8) No z-dependence;

(9) $\nabla \cdot \underline{\underline{P}} \equiv -\nu\underline{\lambda}$, according to Thompson;[92]

(10) Centrifugal and Coriolis forces, $\underline{F} = \rho\underline{g} + 2\rho\underline{v} \times \underline{\Omega}_0$;

(11) Linear feedback electron sink, $S \equiv \sigma\rho_i$;

(12) Negligible temperature gradient effects, $\dfrac{\nabla \ln T}{\nabla \ln n} \ll 1$

where

$\nu \equiv \frac{1}{4} a_i^2 \Omega_i$ is the collisionless viscosity,

$a_i \equiv v^i_{th}/\Omega_i$ is the ion gyroradius,

$\nu\underline{\lambda} \equiv -\nabla \cdot \underline{\underline{P}}$ is the divergence of the collisionless pressure tensor

$p = n(kT_e + kT_i)$ is the scalar pressure,

$\underline{\Omega}_0 \equiv \Omega_o\hat{z}$ is the uniform rotation frequency,

$\underline{g} = g\hat{x} =$ const. is the effective centrifugal gravity,

$\dot{\underline{A}} \equiv (\partial/\partial t + \underline{v}\cdot\nabla)\underline{A}$

$$\lambda_x = \partial/\partial x \left[\rho(\partial v_y/\partial x + \partial v_x/\partial y) \right] - \partial/\partial y \left[\rho(\partial v_x/\partial x - \partial v_y/\partial y) \right]$$

$$\lambda_y = -\partial/\partial y \left[\rho(\partial v_y/\partial x + \partial v_x/\partial y) \right] - \partial/\partial x \left[\rho(\partial v_x/\partial x - \partial v_y/\partial y) \right]$$

The MHD fluid equations reduce to:

$$\rho \dot{\underline{v}} = \underline{j} \times \underline{B} - \nabla p + \nu \underline{\lambda} + \rho \underline{g} + 2\rho \underline{v} \times \underline{\Omega}_0 - \rho \nu_{in} \underline{v} \qquad (5.4)$$

$$\frac{\partial \rho}{\partial t} + \nabla \cdot (\rho \underline{v}) = S \qquad (5.5)$$

$$\underline{E} + \underline{v} \times B = \underline{j}/ne \times \underline{B} + \eta \underline{j} - \frac{\nabla p_e}{ne} . \qquad (5.6)$$

We will also need one of Maxwell's equations:

$$\nabla \times \underline{B} = 4\pi \underline{j} + \frac{\partial \underline{E}}{\partial t} . \qquad (5.7)$$

Substitute Eq. (5.7) in Eq. (5.4) for $\underline{j}$:

$$\rho \dot{\underline{v}}' = - \nabla(p + B^2/8\pi) + \rho \underline{g} + \nu \underline{\lambda} + 2\rho \underline{v} \times \underline{\Omega}_0, \qquad (5.8)$$

where

$$\dot{\underline{v}}' \equiv \dot{\underline{v}} + \nu_{in} \underline{v}.$$

Substitute Eq. (5.4) in Eq. (5.6) for $\underline{j} \times \underline{B}$:

$$\underline{E} + \underline{v} \times \underline{B} = \frac{\rho}{ne} \dot{\underline{v}}' + \frac{1}{ne} \nabla p_i - \frac{\rho \underline{g}}{ne} - \frac{\nu}{ne} \underline{\lambda} - \frac{2\rho}{ne} (\underline{v} \times \underline{\Omega}_0). \qquad (5.9)$$

Roberts and Taylor claimed that keeping the $\nabla p_i/ne$ term and the $\underline{\lambda}/ne$ term in Eq. (5.9) leads to a negligible correction in the result. The $\nabla p_i/ne$ term is negligible for $v_{Di} \equiv (kT_i c/eB)\,\delta \ll g/\Omega_i \equiv v_g$, which is a good approximation in the present experiment, except near the region where the radial electric field changes sign. However, no wave is localized in this region of small plasma rotation, so the neglect of $\nabla p_i/ne$ term should still be valid. The $\nu\underline{\lambda}/ne$ term leads to terms $\sim \mathcal{O}(a_i^4/L^4)$, which we neglect.

Take the curl of Eq. (5.9),

$$\nabla \times \underline{E} - \underline{B}\nabla\cdot\underline{v} = \frac{\rho}{ne} \nabla \times \dot{\underline{v}}' - \frac{\rho}{ne} \nabla \times \underline{g} + \frac{2\rho}{ne} \underline{\Omega}_0(\nabla\cdot\underline{v}).$$

Define an effective magnetic field,

$$\underline{B}^* \equiv \underline{B} + \frac{2\rho\underline{\Omega}_0}{ne} = \underline{B}\left(1 + \frac{2\Omega_0}{\Omega_i}\right) \equiv \underline{B}\Lambda,$$

due to the Coriolis force as does Lehnert,[22] and rewrite:

$$\hat{z}(\nabla\cdot\underline{v}) = - \frac{\rho}{neB^*} \nabla \times \dot{\underline{v}}' \equiv - \frac{1}{\Omega^*} \nabla \times \dot{\underline{v}}'. \tag{5.10}$$

Note, had we neglected compressible effects in Ohm's law, Eq. (5.9), we would now have an incompressible fluid, $\nabla\cdot\underline{v} = 0$.

Take the curl of Eq. (5.8):

$$\nabla \times (\rho\dot{\underline{v}}') = \rho(\nabla \times \dot{\underline{v}}') + \nabla\rho \times \dot{\underline{v}}' = \nabla\rho \times \underline{g} + \nu\nabla \times \underline{\lambda} - 2\underline{\Omega}_0\nabla\cdot(\rho\underline{v}) \tag{5.11}$$

Now, assume perturbations of the form $f_1 = f_1 \exp\left[i(ky - \omega t)\right]$ and linearize Eqs. (5.5), (5.10), and (5.11) about equilibrium:

Eq. (5.5) becomes,

$$(-i\omega - \sigma)\rho_1 - \delta\rho_1 v_{1x} + ik\rho_0 v_{iy} + ik\rho_1 V_{0y} = 0. \tag{5.12}$$

We can take $V_{0y} = 0$ by a Galilean transformation to the drifting frame.

Eq. (5.10) becomes,

$$ikv_{iy} = \frac{\omega' k}{\Omega^*} v_{1x}, \quad \text{or} \quad v_{1y} = -i \frac{\omega'}{\Omega^*} v_{1x} \tag{5.13}$$

Eq. (5.11) becomes,

$$i\omega'\delta\rho_0 v_{iy} - \omega' k\rho_o v_{1x} = -ik\rho_1 g - ik\nu\lambda_{1x} - \delta\nu\lambda_{1y} - 2(i\omega' + \sigma')\Omega_0\rho_1 \tag{5.14}$$

where $\omega' \equiv \omega + i\nu_{in}$, and $\sigma' \equiv \sigma + \nu_{in}$.

We now need:

$$\lambda_{1x} = - ik\delta\rho_0 v_{1x} - k^2\rho_o v_{1y} \tag{5.15}$$

$$\lambda_{1y} = k^2\rho_o v_{1x} - ik\delta\rho_0 v_{1y}. \tag{5.16}$$

Substituting Eqs. (5.15) and (5.16) into (5.14) and collecting terms:

$$\left[kg + 2\Omega_0(\omega' - i\sigma')\right] \frac{\rho_1}{\rho_0} + i(\omega' k - 2\nu\delta k^2)\, v_{1x} + \left[\omega'\delta - \nu k(k^2 + \delta^2)\right] v_{1y} = 0. \tag{5.17}$$

The last term in Eq. (5.17) is $\sim \mathcal{O}(k^2 a_i^2,\ \delta^2 a_i^2)$ and is negligible for small gyroradius.

The coefficient determinant of the set of Eqs. (5.12), (5.13), and (5.17) must vanish, yielding the following dispersion relation:

$$\omega'^3\left(\frac{\delta}{k\Omega_i}\right) - \omega'^2\left(1 + i\,\frac{\sigma'\delta}{k\Omega_i}\right) + \omega'\left(\frac{kg}{\Omega_i} + 2\nu\delta k\Lambda - \frac{2\Omega_0\delta\Lambda}{k} + i\sigma'\right) - g\delta\Lambda - i\sigma'\Lambda(2\nu\delta k - 2\Omega_0\delta/k) = 0. \tag{5.18}$$

The cubic term is $\sim\mathcal{O}(\omega/\Omega_i)$ and may be neglected for low frequencies ($\omega/\Omega_i \ll 1$) in order to compare our results with earlier work. If we also set $\nu_{in} = \sigma = 0$, we get

$$\omega^2 - \omega\left(\frac{kg}{\Omega_i} + 2\nu\delta k\Lambda - \frac{2\Omega_0\delta\Lambda}{k}\right) + g\delta\Lambda = 0 \tag{5.19}$$

The first term in the coefficient of ω is the 2-fluid gravitational effect, the second term shows the effect of finite gyroradius, and

the third term is the contribution due to the Coriolis force.

This is exactly the result of Roberts and Taylor for $\Omega_0 = 0$.[18] For $\nu = \Omega_0 = 0$, our dispersion relation reduces to the earlier work of Lehnert.[19] And in the limit $\nu = 0$, our result reduces to Lehnert's work with the Coriolis force included.[22] The present dispersion relation is consistent with previous work in the appropriate limits, leading us to believe that the effects of FGR, ion inertia, fluid compressibility, and the Coriolis force are consistently included.

In the present work, the cubic dispersion relation, Eq. (5.18), will be solved numerically using Newton's method for the wave frequency and growth rate.

3. Calculated Phase Relations

In order to derive an expression for enhanced convection due to coherent low-frequency waves, we will see in Sec. V. B that certain phase information is required. Readily measurable is the phase, ψ, between the density, n_1, and potential, φ_1, fluctuations. What is needed is the phase, Δ, between the density, n_1, and velocity, v_{1r}, fluctuations. If the velocity is due to a fluctuating azimuthal electric field, $v_{1r} = E_{1\theta}c/B = - ik_\perp \varphi_1 c/B$, then the phase relation is simply $\psi = \Delta \pm \pi/2$.

In practice, the velocity fluctuation may be strongly affected by collisions and the Coriolis force. In this case, the phase, ψ, is no longer meaningful in terms of calculating an expression for enhanced convection, since the radial velocity is no longer simply related to the potential fluctuation by $\pi/2$. The measured phase, ψ, is shifted from what we would predict from a simple physical

picture in the absence of collisions and Coriolis force. Therefore, in this section we calculate how much the phase, ψ, is shifted due to collisions and Coriolis force. Comparison with experiment is discussed in Sec. VI. A. 6.

We first calculate the phase, Δ, between the density $\tilde{n} \equiv n_1/n_0 = \rho_1/\rho_0$, and velocity, v_{1r}, fluctuations. Substituting Eq. (5.13) into Eq. (5.12), and collecting, we get

$$v_{1r} - \beta\tilde{n} = \alpha e^{i\Delta}\,\tilde{n} \tag{5.20}$$

where $\beta = (i\omega' + \sigma')/(k\omega'/\Omega^* - \delta)$, the magnitude $\alpha \equiv |\beta|$, and the phase $\Delta \equiv \tan^{-1}\left[\mathrm{Im}\ (\beta)/\mathrm{Re}\ (\beta)\right]$.

In order to calculate the phase, ψ, between the density and potential fluctuations, we must consider a two-fluid plasma model, including collisions with cold neutrals. Rather than solving the full two-fluid system, including Poisson's equation, we can simplify the mathematics considerably by using the solution of the single-fluid dispersion relation, Eq. (5.18). The two treatments are equivalent except for the use of different variables.

We now calculate an expression for the density in terms of the potential fluctuation using only the equations of motion and continuity for the ions. These we write down:

$$n_i M_i \dot{\underline{v}}_i = n_i e(\underline{E} + \underline{v}_i \times \underline{B}) - kT_i \nabla n_i + n_i M_i \underline{g} + 2n_i M_i \underline{v}_i \times \underline{\Omega}_0 - n_i M_i \nu_{im} \underline{v}_i \tag{5.21}$$

$$\dot{n}_i + \nabla\cdot(n_i \underline{v}_i) = 0 \tag{5.22}$$

where $\underline{\Omega}_0 = \Omega_0 \hat{z}$ is the azimuthal plasma rotation frequency.

We can combine the Coriolis force term with the Lorentz force term by defining an effective magnetic field, $B^* \equiv B\Lambda$, where the term, $\Lambda = 1 + 2\Omega_0/\Omega_i$, includes the Coriolis effect.[22]

Consider the zero-order, steady-state form of Eq. (5.21) in the drift frame, where $V_0 = 0$,

$$e\underline{E}_0 - kT_i \frac{\nabla n_0}{n_0} + M_i \underline{g} = 0. \tag{5.23}$$

We now want to linearize, assuming first-order perturbations of the form, exp i(ky - ωt). We assume $E_{1y} = -ik\varphi_1$, and define $\omega' \equiv \omega + i\nu_{in}$, $\delta = -(1/n)(dn/dx)$, and $\tilde{n} \equiv n_1/n_0$. Linearizing Eq. (5.21), we get

$$-i\omega' v_{1x} = \Lambda\Omega_i v_{1y} + \tilde{n}/M_i(eE_{0x} + kT_i\delta + M_i g), \tag{5.24}$$

where the last term vanishes according to Eq. (5.23). And,

$$-i\omega' v_{1y} = -i\frac{ke\varphi_1}{M_i} - \Lambda\Omega_i v_{1x}. \tag{5.25}$$

The equation of continuity yields,

$$-i\omega\tilde{n} + ikv_{1y} - \delta v_{1x} = 0. \tag{5.26}$$

We define $\alpha \equiv \omega'/\Lambda\Omega_i$, $\tilde{\varphi} \equiv e\varphi_1/kT_e$, $v_{De} \equiv kT_e\delta/eB$, and solve Eqs. (5.24), (5.25), and (5.26) to get

$$\frac{\tilde{n}}{\tilde{\varphi}} = \frac{kv_{De}}{\Lambda\omega}\frac{1 - \alpha k/\delta}{1 - \alpha^2}. \tag{5.27}$$

For low frequencies, growth rates, and collision frequencies

$\alpha \ll 1$, we get a simple relation

$$\frac{\tilde{n}}{\tilde{\varphi}} \rightarrow \frac{k v_{De}}{\Lambda \omega}, \qquad \alpha \ll 1. \tag{5.28}$$

We summarize the phase properties of Eq. (5.28) in Table V.1.

Table V. 1. Phase properties for no collisions.

Frequency	Growth Rate	Propagation Direction	Phase
>0	>0	electron-diamagnetic	0° to 90°
<0	>0	ion-diamagnetic	180° to 270°

These results are in agreement with those obtained by Chen from a simple physical picture.[95]

If, on the other hand, the collision frequency is so large that $\alpha = i\, \nu_{in}/\Omega_i \Lambda \gg 1$, then eq. 5.27 becomes,

$$\frac{\tilde{n}}{\tilde{\varphi}} = - i \frac{k\, v_{De}}{\omega} \frac{k}{\delta} \frac{\Omega_i}{\nu_{in}}, \quad \alpha \gg 1 \tag{5.29}$$

We observe that the phase is shifted 90° from the case in Table V.1, and present the phase properties of eq. 5.29 in Table V.2.

Table V.2. Phase properties for large collision frequencies.

Frequency	Growth Rate	Propagation Direction	Phase
>0	>0	electron-diamagnetic	90° to 180°
<0	>0	ion-diamagnetic	90° to 180°

The actual case lies somewhere between the two. The result is that we have an expression with which we can calculate a phase shift ψ, between the density, n_1, and potential, φ_1, fluctuations of up to 90°, due to collisions and the Coriolis force. Phase calculations using typical plasma parameters are discussed in section VI.A.6.

B. Transport theory - summary.

In the absence of local ionization and recombination, the radial plasma density profile is determined by the dominant transport mechanisms. The most important transverse transport mechanisms in an HCD are known to be weakly and fully ionized diffusion, mobility in the radial electric field, and enhanced convection.[5] (See Appendix A). The results of simple diffusion theory, as calculated in Appendix B, will be summarized here.

We find [Eq. (B.4)] that the enhanced convection due to a coherent low-frequency oscillation can be written as,

$$< n\, v_r >^{\alpha}_{conv} = \frac{n_1\, v_{1r}}{2} \cos \Delta \qquad (5.30)$$

where Δ is the phase between the density, n_1, and velocity, v_{1r}, fluctuations. If the radial velocity fluctuation is due to an azimuthal electric field, then [Eq. (B.5)],[11,12]

$$< n\, v_{1r} >^{\alpha}_{conv} = \frac{n_1\, \varphi_1\, c}{2\, B\, R} \sin \psi \qquad (5.31)$$

where ψ is the phase between the density, n_1 , and potential, φ_1 , fluctuations. We assume, as in [Eq. (B.6)], that an enhanced diffusion coefficient can be inferred,

$$D^{\alpha}_{enh} \nabla n_i = - < n v_r >^{\alpha}_{conv} \qquad 5.32$$

And if the radial electric field, E_r , is small, such as when a dc or floating potential is applied to the conducting end-rings, then ion mobility in E_r can be neglected. The ion currents can then be written:

$$n v_r = - D_{\perp eff} \partial n/\partial r$$

$$n v_z = - D_{\parallel in} (1 + T_e/T_i) \partial n/\partial z$$

where $D_{\perp eff} = D_{\perp in} + D_{\perp ei} + D_{enh}$. The transport coefficients are defined in Appendix B.

If we now assume a cosinusoidal axial density dependence, $n(r,z) = n(r) \cos (\pi z / L_{eff})$, in good agreement with experiment, and substitute the ion currents into the equation of continuity, we get the solution,

$$n(r) = AK_0(r/q) + BI_0(r/q),$$

where the radial scale length,

$$q^* \equiv \frac{L_{eff}}{\pi} \left[\frac{D_{\perp eff}}{D_{\parallel in}(1 + T_e/T_i)} \right]^{1/2} . \qquad (5.33)$$

For $q \ll r$, which is reasonably valid in an HCD at larger radii ($R \gtrsim 3$ cm) where the density gradient is not so steep, the Bessel functions of imaginary arguments can be approximated,

$$K_0(r/q) \approx (\pi q/2r)^{1/2} e^{-r/q}$$
$$I_0(r/q) \approx (q/2\pi r)^{1/2} e^{r/q}.$$

When $q \ll r$, a nearly exponential radial density profile is predicted with the scale length, q. We use Eqs. (5.30) and (5.31) to estimate wave enhanced convection. Equation (5.32) is used to infer an enhanced diffusion coefficient, and Eq. (5.33) is used to estimate semi-quantitatively the effect of enhanced transport on the radial density scale length, which is compared with the measured value.

C. Langmuir probe theory - summary.

Langmuir probes provide most of the data discussed in this experiment. Fortunately, we conclude in Appendix C that classical probe theory is valid in this experiment, so that simple expressions suffice to interpret probe data.[101]

In practice, this means that the axial magnetic field does not appreciably affect ion currents to the probe, since the ion gyroradius is much larger than the probe radius, $a_i/R_p \approx 14$.[102-104] And even though the electron gyroradius is much less than the probe radius, so that electron currents to the probe are diffusion limited,[102,103] we still obtain a good estimate of the electron temperature, T_e, from the high-energy tail of the Maxwellian electron distribution.[103]

The Debye length, which serves as a measure of how far the probe potential penetrates the plasma, is much smaller than the probe radius, $R_p/\lambda_{De} \approx 33$. Therefore, the particle collection area

can be taken to be the geometrical area of the probe tip, to good approximation.[105] Also the ion current should be negligibly reduced by trapped particle orbits.[106]

The validity of simple probe theory and the effect of fluctuations[5] on the probe characteristic (V - I plot) is discussed in Appendix C. In this section we summarize the useful expressions calculated from simple probe theory.

Application of a large negative bias to a probe results in ions being collected by the probe, but at the electron temperature. This effect is the Bohm sheath criterion, due to the penetration of the probe potential into the plasma. The ion density can then be calculated in terms of the saturated ion current, I_{si}, and the electron temperature, T_e, [Eq. (C.1)]

$$n_i = 1.13 \times 10^{12} \frac{I_{si}\ (mA)}{A_{probe}\ (mm^2)} \sqrt{\frac{A\ (amu)}{kT_e\ (eV)}}\ cm^{-3}. \qquad (5.34)$$

As the potential is raised from ion saturation, the probe begins to draw electrons, assumed to be in local thermal equilibrium. From the slope of a semi-log plot of the probe characteristic, the electron temperature can be calculated [Eq. (C.2)],

$$\frac{e}{kT_e} = \frac{d}{dV}\left\{ \ln\left[I(V) - I_{si}\right]\right\}. \qquad (5.35)$$

And by balancing the ion and electron currents to the probe at the floating potential, φ_f, we can calculate the plasma potential [Eq. (C.3)],

$$\varphi_p = \varphi_f + \gamma kT_e/e, \tag{5.36}$$

where [Eq. (C.4)],

$$\gamma = 1/2 \ln(M_i/m_e). \tag{5.37}$$

For argon, $\gamma = 5.6$, in agreement with the theory of Laframboise, which includes the effects of finite sheath thickness and trapped particle orbits.[102]

The radial electric field can be calculated,

$$E_r \equiv - \Delta\varphi_p/\Delta R. \tag{5.38}$$

The above expressions are used to calculate the T_e, n_i, φ_p, and E_r profiles from the directly measurable probe profiles, I_{si} and φ_f.

D. Directional Langmuir Probe (DLP)--Summary

The DLP can be used to measure particle currents directly and easily. A summary of the analysis in Appendix D will be presented here. The construction of our DLP is shown in Fig. III. 5. The probe is shielded so that particles strike the probe tip from a restricted solid angle only.

The results of a model presented by Hudis and Lidsky[6,10] will be summarized. We are interested in the saturated ion current only, and all the restrictions discussed in Appendix C for simple

probe theory apply and are satisfied here. If we consider a plasma drifting slower than the sound speed, $v_d^i \lesssim v_s$, then we expect that the sheath is not perturbed. However, the potential required to accelerate the ions to the sound speed at the sheath edge, the Bohm sheath criterion,[3] is dependent upon the direction of streaming. This change of probe potential penetration into the plasma changes the density at the sheath edge, at radius R_T, through the Boltzmann factor, e^{-eV/kT_e}, [Eq. (D.1)],

$$n_i(R_T) = n_\infty e^{-1/2} \exp(\pm 2 v_d^i v_{th}^i / v_s^2), \tag{5.39}$$

where $\pm v_d^i$ refers to particles drifting toward or away from the probe.

As a result, particle currents to the probe are a function of the drift velocity. If we define $\Delta I_{si} \equiv I_+ - I_-$ as the difference in I_{si} when the particles are streaming toward and away from the probe, we have

$$\Delta I_{si} = 4 I_{si} v_d^i v_{th}^i / v_s^2,$$

where we have used $v_d^i v_{th}^i \ll v_s^2$ to expand the exponential. We define $I_{si} \equiv \frac{1}{2}(I_+ + I_-)$ and solve for the drift velocity, [Eq. (D.2)],

$$v_d^i = \left(\frac{T_e}{T_i}\right)^{1/2} \frac{v_s}{4} \frac{\Delta I_{si}}{I_{si}}. \tag{5.40}$$

From the azimuthal drift velocity, $v_{d\theta}^i$, one can infer the plasma rotation frequency, $\Omega_0 = v_{d\theta}^i / R$. The centrifugal force,

$M\underline{g} = M\Omega_0^2\underline{R}$, and Coriolis force, $\underline{F}_c = 2M\underline{v} \times \underline{\Omega}_0$, result from plasma rotation. We assume that the plasma rotation is due to the radial electric field drift, the centrifugal drift, the ion-diamagnetic drift, and the effects of collisions, ν_{in}, and Coriolis force. The ion equation of motion can then be solved for the static radial electric field as a function of measurable quantities, [Eq. (D.4)],

$$E_r = -\frac{B}{c}\left[v_{d\theta}^i \Lambda\left(1 + \frac{\nu_{in}^2}{\Omega_i^2\Lambda^2}\right) + \frac{g}{\Omega_i} - \frac{kT_i c}{eB}\frac{\nabla n}{n}\right] \qquad (5.41)$$

where $\Lambda \equiv 1 + 2\Omega_0/\Omega_i$ includes the Coriolis effect. The Eqs. (5.40) and (5.41) are used to calculate the drift velocities and E_r, respectively.

In Appendix D, six checks on the experimental validity of the DLP are discussed. In particular, measurements of directional currents in a plasma device with a known streaming velocity indicate that Eq. (5.40) does give a correct expression for the streaming velocity. Also, the radial electric field, E_r, calculated from Eq. (5.41), is compared with an independent determination of E_r, from the gradient of the plasma potential. Good agreement between the two methods lends support to the validity of both. On the basis of theoretical inequalities being satisfied, and on six experimental checks, the DLP is concluded to correctly measure plasma streaming velocities directly.

E. The Ion Temperature

Ions are heated by collisions with the hotter electrons, and

cooled by collisions with the cold neutral background gas. The transverse ion mean-free-path is reduced to the gyroradius. Hence the ions experience many collisions before they are lost to the wall. Warren shows that ion-heating due to randomization of the drifting motion by collisions with neutrals is negligible.[5] Radiative processes will also be neglected.

If thermal convection is sufficiently slow, we can write down a local ion temperature relaxation equation,

$$\frac{dT_i}{dt} = \frac{m_e}{M_i} \nu_{ei}(T_e - T_i) + \nu_{in}(T_n - T_i), \qquad (5.42)$$

where $(m_e/M_i)\ \nu_{ei}$ is the Coulomb ion-electron relaxation frequency,[107] and ν_{in} is the ion-neutral collision frequency.[5,73,74,108]

Equation (5.42) can be solved for the steady-state ion temperature,

$$T_i = (\nu_{ei} \frac{m_e}{M_i} T_e + \nu_{in} T_n)/(\nu_{ei} \frac{m_e}{M_i} + \nu_{in}). \qquad (5.43)$$

The right-hand side of Eq. (5.43) is a weak function of T_i through the term $\nu_{in} = n_0 v_{th}^{i} \sigma_{in}$. As a first approximation we will take $T_i = T_e/10$ to calculate ν_{in}.[73,74] The neutrals are assumed to be in good thermal contact with the wall, and we take $T_n \approx 0.03$ eV. Successive iterations yield T_i to better approximation. However, as we see in Sec. VI. A. 3, $T_i \approx T_e/10$ to good approximation, and the first solution for T_i suffices.

EXPERIMENTAL RESULTS.

Experimental data will be labelled by the externally variable parameters, which can be readily fixed by buttons or knobs. The most important external parameters are the neutral gas pressure in the diffusion tank, p_t, the axial magnetic field, B, the arc current, I_{CI}, and the axial and radial boundary conditions. The resulting plasma profile parameters, such as the density, n_i, the radial electric field, E_r, the electron temperature, T_e, and stability are functions of the sheaths at the boundaries, the relative magnitudes of transport mechanisms operating, and even the mechanical and magnetic alignment of the system.

Directly measurable plasma parameters include the saturated ion current, I_{si}, the floating potential, ϕ_f, the Langmuir probe characteristic, and the ion currents to a directional Langmuir probe, DLP. Directly measurable wave parameters include the fluctuations on I_{si} or ϕ_f, as well as the phase of the fluctuations with respect to a fixed reference, determined by a phase-sensitive lock-in amplifier and/or a calibrated spectrum analyzer. From this data we can calculate T_e from the probe characteristic, E_r from the DLP data, the ion density, n_i, the plasma potential, $\phi_p = \phi_f + \gamma kT_e/e$, another value for $E_r = -\frac{\Delta\phi_p}{\Delta R}$, the normalized amplitudes, $\tilde{n} \equiv \frac{\Delta n}{n_i} = \frac{\Delta I_{si}}{I_{si}}$, $\tilde{\phi} \equiv \frac{e\,\Delta\phi_f}{kT_e}$, and the phase by which the density leads the potential fluctuations, ψ.

Data was taken over the ranges shown in Table VI.1. The data range shown was used as a partial parametric study of the arc parameters. However, since our primary interest is waves and wave enhanced transport, most of the data will be taken in a rather narrow range of parameters, where the signal-to-noise ratio is

Table VI.1. Range of Arc Parameters

Arc Parameters	Range
P_t (mtorr)	0.2 to 2.0, argon 2.0 to 3.0, helium
B (gauss, G)	580 to 1160 G.
n_{imax} (R = 1.0 cm)	3.0×10^{12} to 2.0×10^{13} cm^{-3}
n_{imax} (R = 10.0 cm)	9.0×10^{9} to 2.0×10^{11} cm^{-3}
T_{emax} (R = 1.0 cm)	1.5 to 3.2 eV
T_{emin} (R = 10.0 cm)	0.15 to 0.6 eV
E_{rmax}	0 to 1.6 V/cm
E_{rmin} (R = 1.0 cm)	-(0.6 to 3.2) V/cm
I_{CI} (amperes)	20.0 A

higher. Experimentally this means low neutral gas pressure, p_t, and low magnetic field, B. As the pressure is increased, the wave amplitude decreases. As B is increased above B = 870 G, the plasma becomes noisier.

A. Typical Experimental Results.

A set of data, corresponding to a typical case when two large-amplitude, low-frequency waves are present, is presented in figs. VI.1 to VI.9. p_t =0.25 mtorr argon, B = 580 gauss.

1. Normalized Wave Amplitudes and Radial Density Profile.

The ion density is calculated using Langmuir probe theory, Eq.(5.34), from the magnitude and shape of a probe characteristic, (V-I plot). The rms wave amplitudes on a Langmuir probe, are

measured using a Tektronix Model 1L5 spectrum analyzer, or a Princeton Applied Research Model HR-8 lock-in amplifier.

In fig. VI.1, the radial ion density profile, n_i, and the normalized wave amplitudes, $\tilde{n} \equiv \Delta n / n_i$, $\tilde{\phi} \equiv e\Delta\phi_f / kT_e$, are shown. Note that the lower-frequency wave (LF = -1.83 kHz, where negative frequencies refer to the ion-diamagnetic direction) has maximum amplitude near radius R = 5 cm, while the higher-frequency wave (HF = 36. kHz) has maximum wave amplitude near R = 1 cm. Phase information reveals that the LF wave propagates in the ion-diamagnetic direction, while the HF wave propagates in the electron-diamagnetic direction.

Fig. VI.2. shows typical frequency spectra of the wave amplitudes. Power supply current modulation is typically less than 1% at 360 Hz, the three-phase ac power line frequency. No power supply modulation is measurable at instability frequencies.

We also observe small amplitude "harmonics," which seem to be a real effect because harmonic amplitude does not scale with fundamental amplitude. The harmonics are observed at multiples of the fundamental frequency, as predicted for wave phase velocities, V_{ph}, significantly less than the plasma rotation velocity, V_θ. The frequency in the lab frame is $\omega_{lab} = m\dfrac{V_{ph,m} + V_\theta}{R}$ for azimuthal mode number m. From the dispersion relation Eq.(5.19) we can see that the phase velocity decreases for higher harmonics, $V_{ph,m} \sim A + B/m^2$, so that harmonics appear in the lab frame at near multiples of the plasma rotation frequency. There is negligible enhanced transport caused by the harmonics.

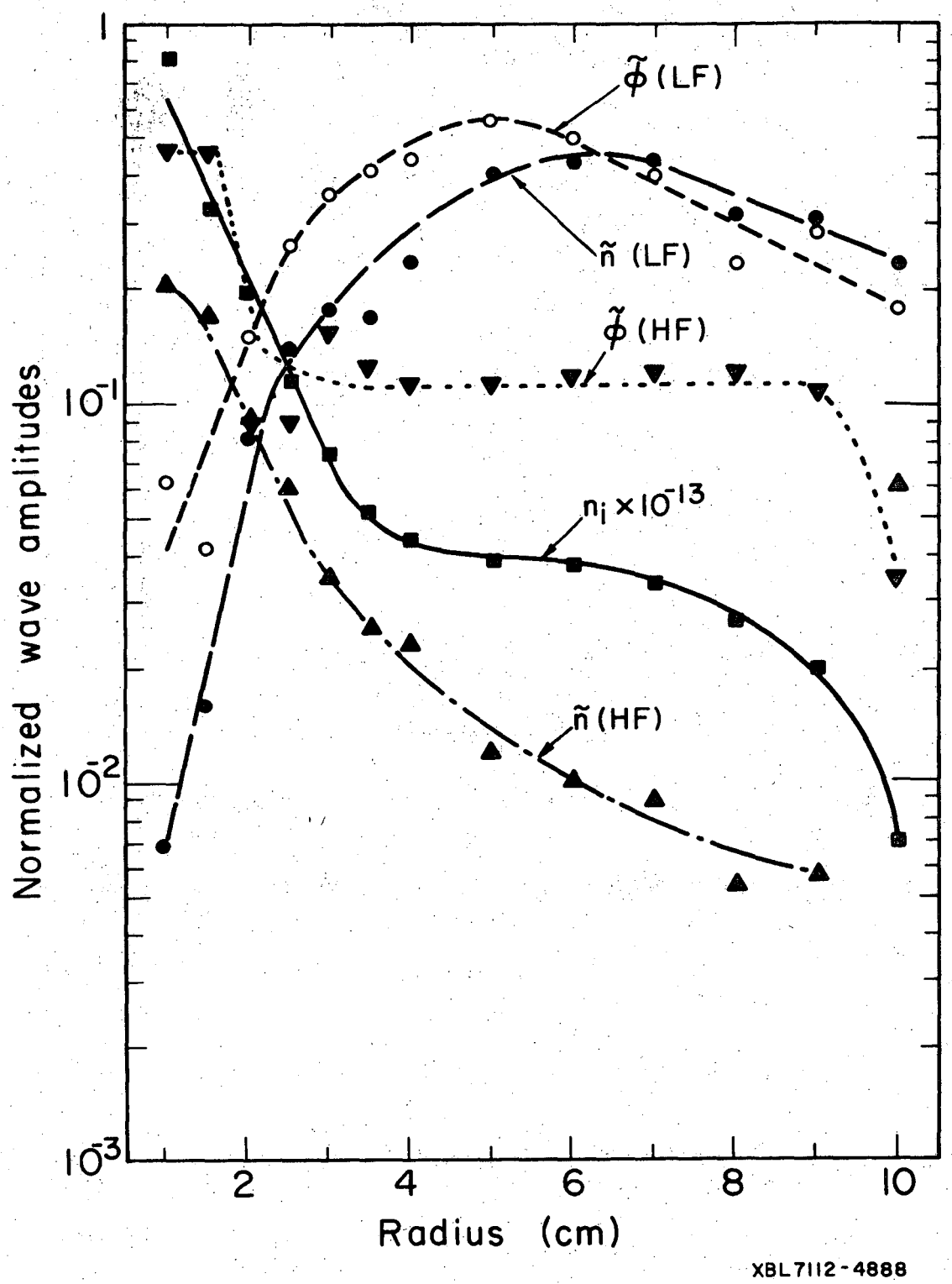

Fig. VI.1. Normalized wave amplitudes and density profile. ■, density, $n_i \times 10^{-13}$ cm^{-3}; ●, $\tilde{n}$ (LF wave, -1.83 kHz); O, $\tilde{\varphi}$ (LF wave); ▲, $\tilde{n}$ (HF wave, 36 kHz); ▼, $\tilde{\varphi}$ (HF wave). p_t = 0.25 mtorr Ar, B = 580 G, end-rings grounded.

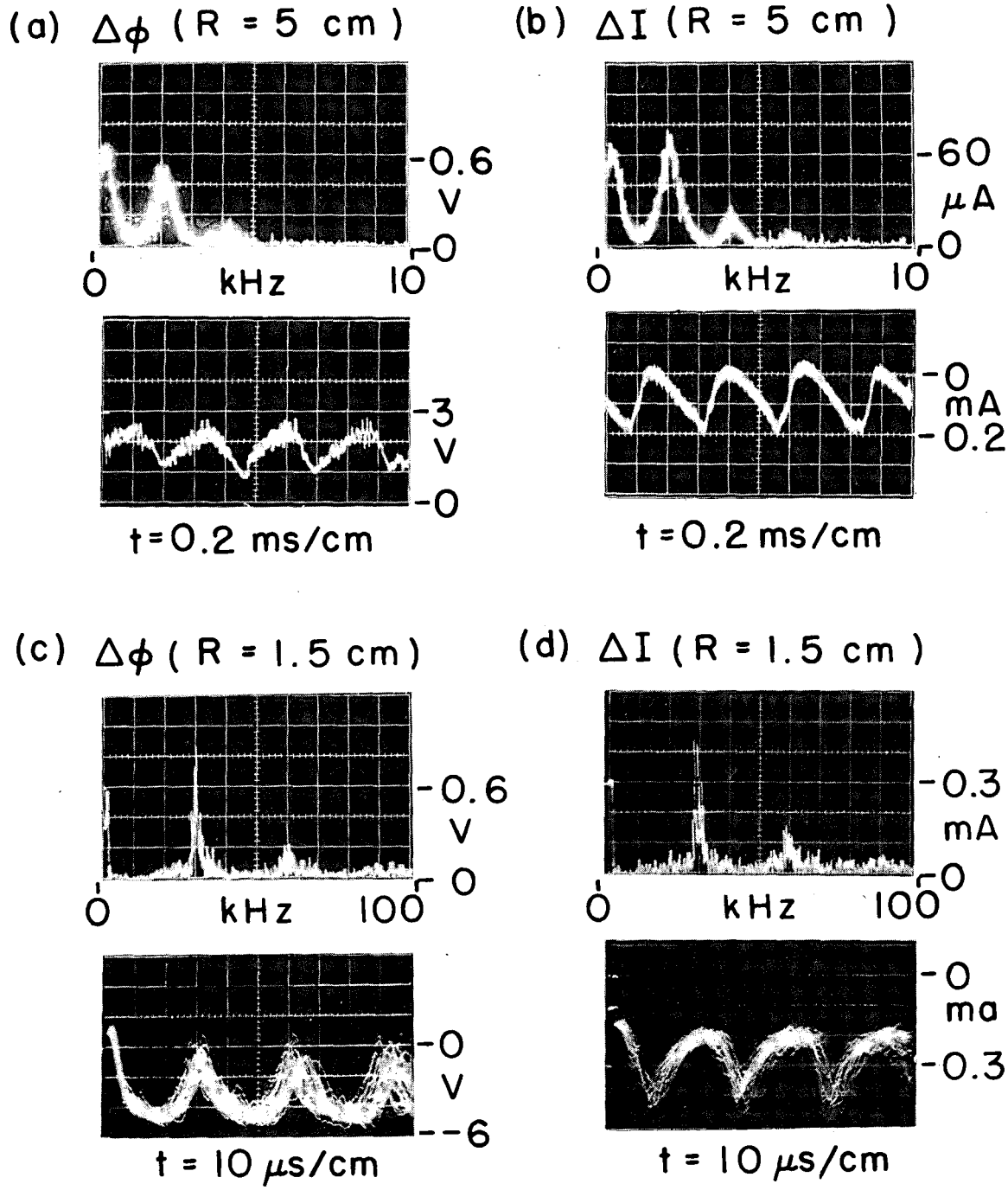

Fig. VI.2. Wave spectra. Upper trace is rms wave amplitude vs. frequency. Lower trace is DC coupled signal on a Langmuir probe. (a) $\Delta\phi$(R=5 cm); (b) ΔI(R=5 cm) (c) $\Delta\phi$(R=1.5 cm); and (d) ΔI(R=1.5 cm), showing waves at 2 kHz and 30 kHz. p_t=0.32 mtorr Ar, B=580 G, end-rings grounded.

2. Axial Profiles.

Axial plasma profile measurements are made using a Langmuir probe (probe X, fig. III.3), which can be rotated on its axis to vary the radial position. A typical axial profile is shown in fig. VI.3 at R = 6 cm. The measured axial density profile, n_i, normalized to unity at the midplane, is approximated well by the expression, $n(z) =$ $\cos(\pi z / L_{eff})$, where the effective length, $L_{eff} = L + 4/3\ \lambda_{eff} \simeq 120$ cm. The normalized rms density perturbations due to the LF wave, $\tilde{n}(LF)$, is also indicated in fig. VI.3. The electron temperature, T_e, and the floating potential, ϕ_f, are uniform axially, within our ability to measure them.

3. Electron and Ion Temperatures.

The electron temperature profile, T_e, determined from the shape of a probe characteristic, Eq. (5.35), is shown in fig. VI.4. A small error in T_e produces a magnified error in the plasma potential $\phi_p = \phi_f + \gamma kT_e/e$, since we calculated $\gamma = 5.6$ for argon in section V.C. A corresponding error would appear in $E_r = -\Delta\phi_p / \Delta R$. Since 10% errors in measuring T_e from Langmuir probe characteristics are common, we use a bi-exponential smoothing approximation on T_e before calculating ϕ_p. Bi-exponential means that a semi-log plot of T_e consists of two straight lines. An exponential choice was made since solutions of the diffusion equation and the heat flow equation are Bessel functions, which show nearly exponential behavior in the limit that the scale length is small compared to the radius, $q \ll r$.

A bi-exponential approximation to T_e is also drawn in fig VI.4. In order to see the effect of a small change

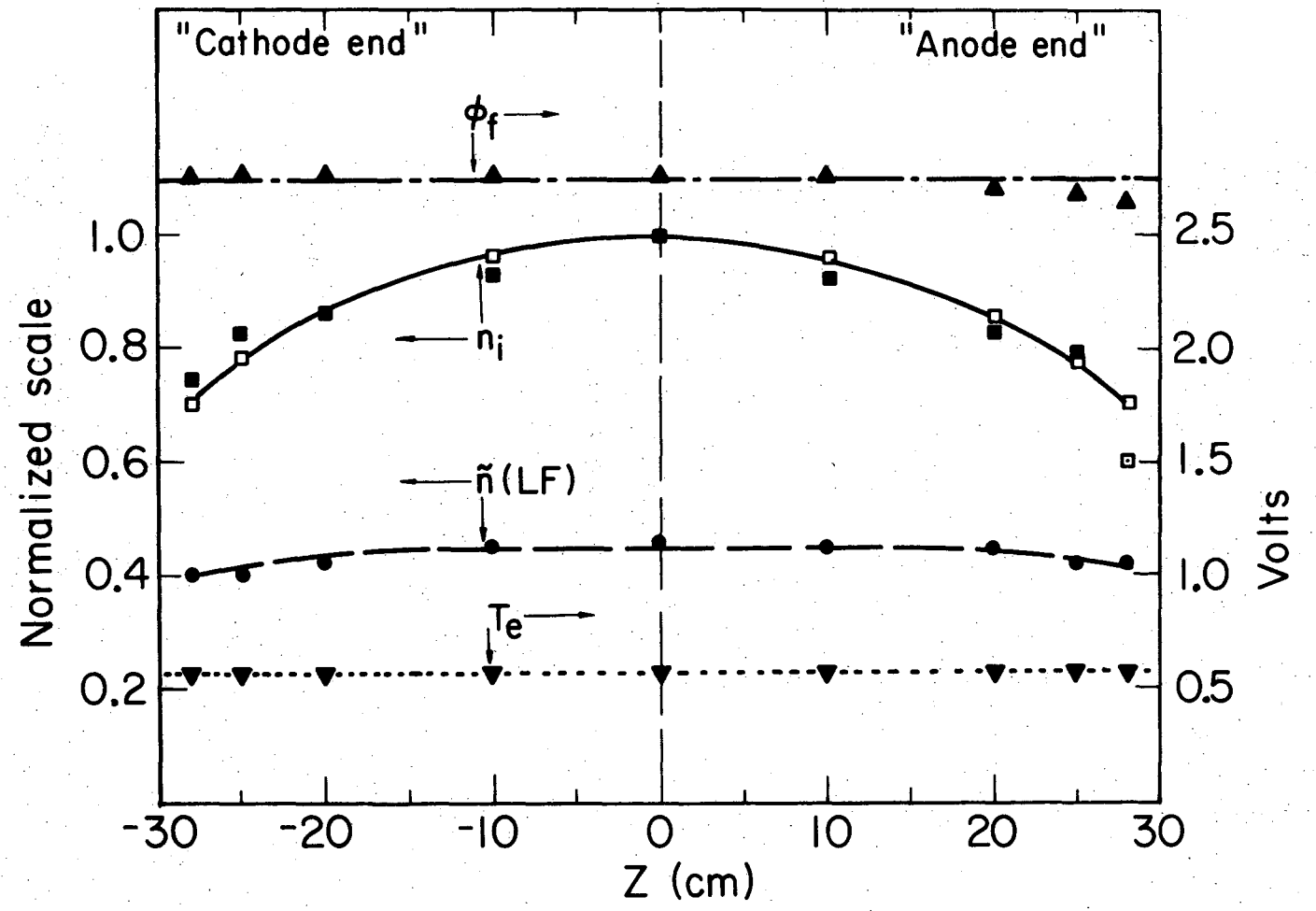

XBL7112-4887

Fig. VI.3. Axial profiles at R = 6 cm. ■, normalized density, n_i; □, $n(z) = \cos(\pi z/L_{eff})$ for L_{eff} = 120 cm; ●, normalized LF wave amplitude, $\tilde{n}$(LF); ▲, probe floating potential, φ_f; and ▼, electron temperature, T_e. p_t = 0.34 mtorr Ar, B = 580 G, end-rings grounded.

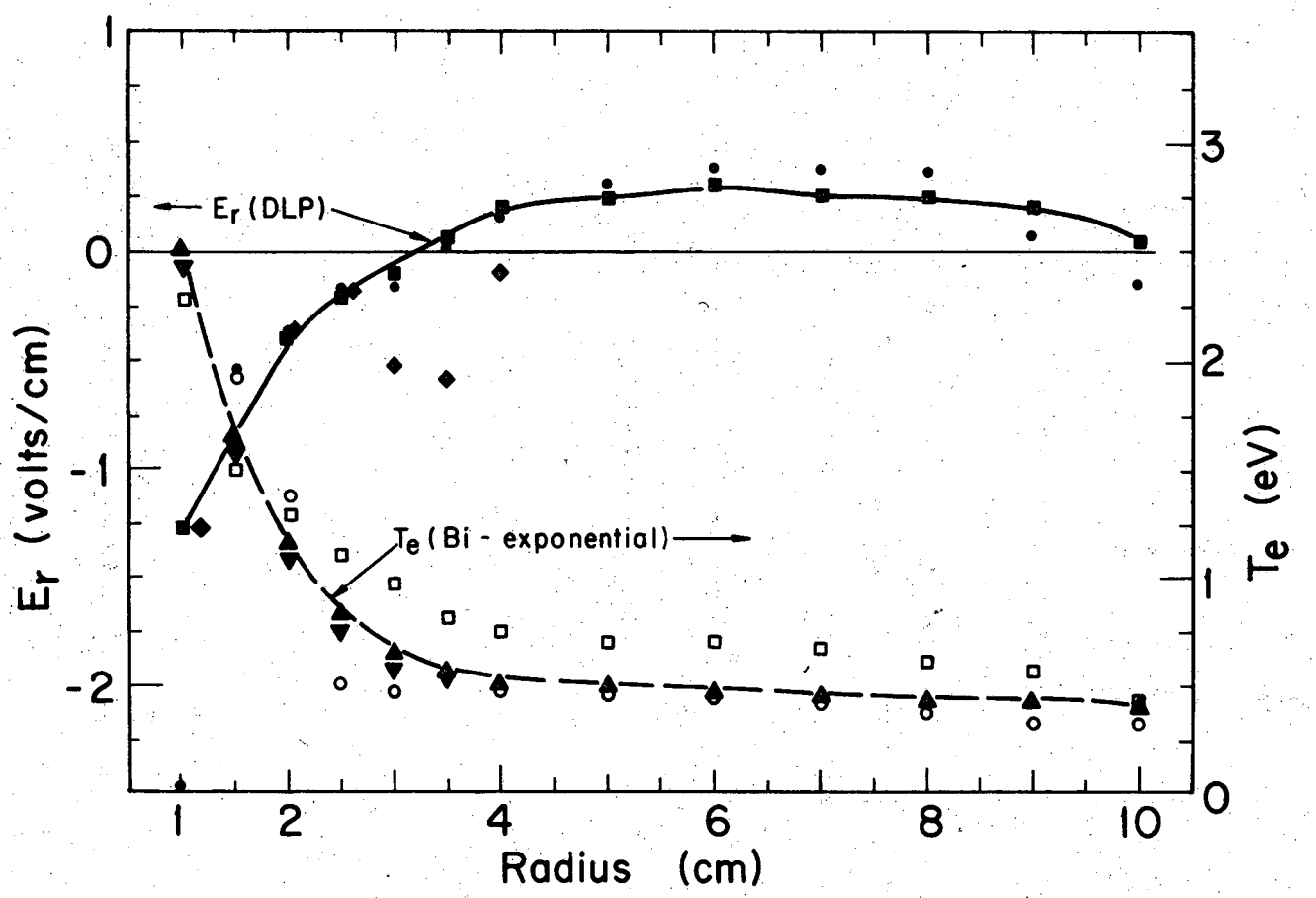

XBL 7111-4819

Fig. VI.4. Radial electric field and electron temperature profile. ■ , E_r (DLP); ●, $E_r(\varphi_p) = -\Delta\varphi_p/\Delta R$, in good agreement with E_r (DLP); ○, T_e (measured); ▲, T_e (bi-exponential approximation, smoothed); □ , 10 x T_i, [(see Eq. (5.43)] showing validity of $T_e/T_i \approx 10$ approximation; ▼, small change in T_e causes large change in $E_r(\varphi_p)$, ◆ , showing strong functional dependence on T_e. p_t = 0.25 mtorr Ar, B = 580 G, end-rings grounded.

in T_e on E_r, we denote a small change ($\lesssim$ 10%) in T_e by the symbol, ▼ . (Note, we have only changed T_e for small radii, $R \lesssim 4$cm.)

Finally, the squares, ■, in Fig VI.4 are 10x the ion temperature, T_i, as calculated from the temperature relaxation equation, Eq.(5.43). In all the calculations we have taken $T_i = T_e / 10$. Agreement between T_e and 10x T_i leads us to conclude that $T_i/T_e \simeq 0.1$, to good approximation.[73,74]

4. Radial Electric Field.

A large, nonuniform, nonambipolar, radial electric field exists for the case of grounded end-ring electrodes. Schwirzke claims that this field arises due to gradients in the electron temperature, T_e, and currents to the end sheaths.[109] The temperature gradient is due to collisional cooling. The resulting plasma potential gradient, for the grounded end-ring case, arises because the potential drop across the end sheaths is proportional to T_e.

However, when the end-rings are independently floated, the potentials adjust themselves so that negligible radial electric field exists for radii greater than a few centimeters from the arc column. A self-consistent solution for this case would be dominated by cross-field particle transport, with axial boundary conditions of equal electron and ion currents. Tonks solved a similarly formidable problem self-consistently for the density and potential distribution with conducting end-plates which could be floated or effectively grounded as a single unit.[29] However, a solution to the present problem is complicated by nonuniformity of the radial boundaries, since each end-ring can float independently. And the

coupled heat flow equation should also be solved self-consistently. We leave this calculation for future work, and accept the radial electric field empirically.

The radial electric field has been determined by two independent methods. The curve, ■, in fig. VI.4 shows E_r as calculated from the direct azimuthal streaming measurements using a DLP, Eq.(5.41). For comparison, $E_r = -\Delta\phi_p / \Delta R$ is shown, denoted by the dots, ● . This determination of E_r uses the bi-exponential T_e approximation. A slight change in T_e for small radii, $R \lesssim 4$ cm, causes a large change in $E_r(\phi_p)$.

Therefore, the DLP will be used to measure E_r since it is easier and more reliable to use. To substantiate this claim, we argue that this method of determining E_r has a weaker functional dependence on T_e. To get an estimate, we write $E_r \simeq (B/c)\, V^i_{d\theta}$, and $V^i_{d\theta} = \frac{V_s}{4}\sqrt{\frac{T_e}{T_i}}\ \frac{\Delta I_{si}}{I_{si}}$. If we use typical values, from Appendix A, and assume $\Delta I_{si}/I_{si} \simeq 20\%$, and $T_e/T_i \simeq 10 =$ constant, then we have approximately, $E_r \simeq \sqrt{T_e}$. Hence a small change in T_e causes a small change in E_r(DLP).

Experimentally, the DLP is found to give reproducible results to better than 10% in determining radial electric field profiles. Six independent experimental checks on the DLP, discussed in Appendix D, show that the DLP is also reliable in measuring ion streaming directly.

5. Radial Potential Profiles.

The floating potential of a Langmuir probe is obtained by measuring the probe voltage with a high impedance voltmeter, so

that negligible current is drawn. The plasma, or space, potential, ϕ_p, can then be determined from the floating potential and the electron temperature, $\phi_p = \phi_f + \gamma\, kT_e/e$, where $\gamma = 5.6$, Eq.(5.37).

The floating and plasma potentials are presented in fig. VI.5. The lower curve represents the magnitude of the Coriolis effect. The term $\Lambda = 1 + 2\ \Omega_o / \Omega_i$, where Ω_o is the measured plasma rotation frequency, appears often in the rotational instability theory of section V.A.2. From the graph we can see that the Coriolis effect is most important at small radii.

6. Phase Relations.

The phase by which a wave signal leads a fixed reference signal is measured using the phase sensitive, Princeton Applied Research Model HR-8 lock-in amplifier. Experimental phase accuracy is specified as $\pm 5^o$.

The phase, ψ, by which the density, n_1, leads the potential, ϕ_1, fluctuations is shown in fig. VI.6. Negative phases correspond to the density leading the potential fluctuations propagating in the electron-diamagnetic direction; and positive phases, the ion-diamagnetic direction. The LF wave, ψ (LF), propagates in the ion-diamagnetic direction; while the HF wave, ψ(HF), the electron-diamagnetic direction.

The phase, ψ_{calc}, is calculated from Eq. (5.27) using experimental plasma parameters and the solution of the cubic dispersion relation, Eq.(5.18). ψ_{calc} is shown is fig. VI.6 for comparison. We observe that at small radii, $\psi_{calc} = 0^o$ to 90^o in the electron-diamagnetic direction, and at large radii

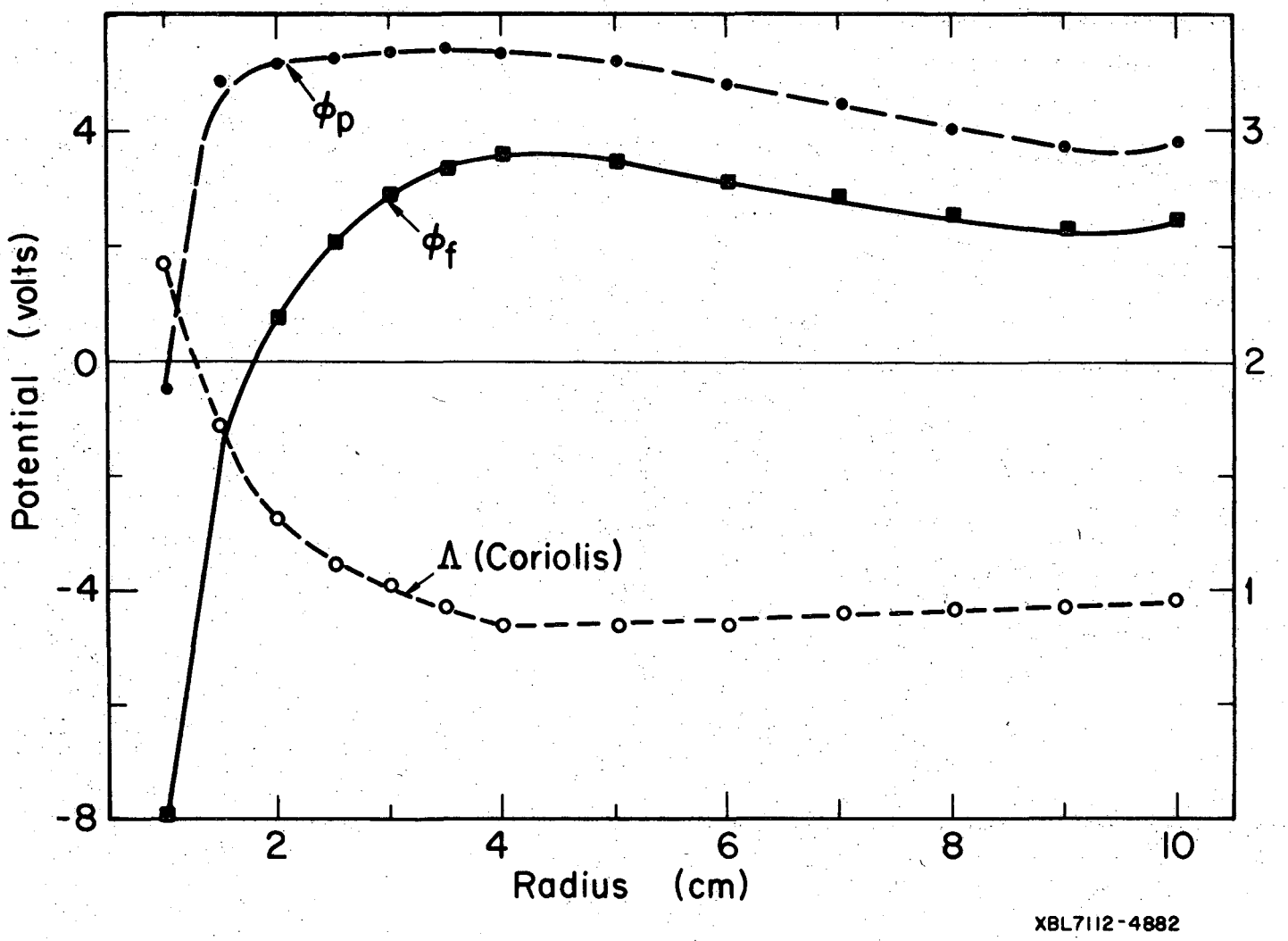

Fig. VI.5. Potential profiles and Coriolis effect. ■, floating potential, Φ_f; ●, plasma potential, Φ_p; and ○, Coriolis term, $\Lambda = 1 + 2\Omega_0/\Omega_i$. p_t = 0.25 mtorr Ar, B = 580 G, end-rings grounded.

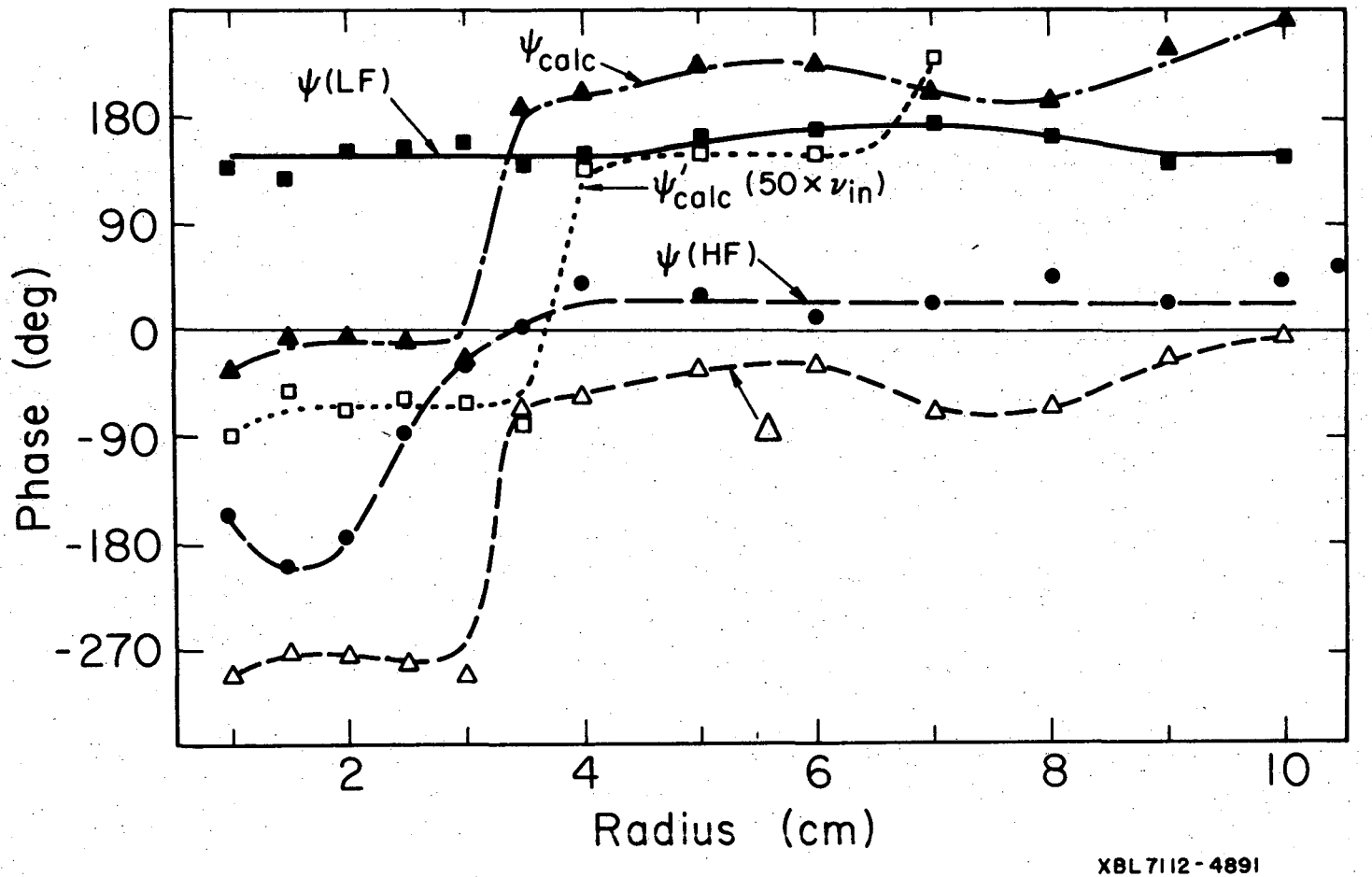

Fig. VI.6. Wave phase profiles. ■, ψ (LF), phase by which density leads potential fluctuation; ●, ψ (HF); ▲, ψ_{calc}, calculated phase [(see Eq. (5.27)]; □, $\psi'_{calc}(50 \times \nu_{in})$, phase calculated with collision frequency increased by a factor of 50; ▲, calculated phase, Δ, by which density lags velocity fluctuations. p_t = 0.25 mtorr Ar, B = 580 G, end-rings grounded.

$\psi_{calc} = 180^{\circ}$ to 270° in the ion-diamagnetic direction. This agrees with the results of a simple physical picture discussed by Chen,[95] and a simple calculation summarized in Table V.1. Agreement between measured and calculated phases is not too good.

The effect of neutral collisions on the phase has been discussed in section V.A.3, and summarized in Table V.2, indicating a 90° phase shift. We increase the collision frequency, ν_{in}, by an arbitrary factor of 50, recalculate the phase, ψ_{calc} $(50 \times \nu_{in})$, and show the result in fig. VI. 6, for comparison. A phase shift of nearly 90° is observed. Good agreement between measured ψ(LF) and calculated, $\psi'_{calc}(50 \times \nu_{in})$, phase is obtained at large radii where the LF wave is localized. And better agreement with ψ(HF) is obtained for small radii where the HF wave is localized. However, we have no good reason to believe that we have miscalculated ν_{in} by a factor of 50 in Appendix A.

Noon and Jennings claim that an effective collision frequency, $\nu_{eff} = \nu_{in} + \nu_{ei}$, due primarily to ion-electron collisions at small radii, explains a phase $\psi \simeq 180^{\circ}$ at small radii.[110] However, momentum is not conserved in their model.

We also show the phase, Δ, by which the density is calculated in Eq.(5.20)to lag the velocity fluctuations. The velocity leads the density fluctuation by $\Delta = 0^{\circ}$ to 90° in the direction of propagation, as required for an unstable wave. Note that $\psi_{calc} = \Delta \pm \pi/2$, as discussed in Appendix B, Eq.(B.5). This means that the radial velocity and azimuthal electric field are in phase, or $v_{1r} = E_{1\theta} c / B = -i k_{\perp} \phi_1 c / B$. However, as col-

lisions, the Coriolis force, and nonlinear effects become more important, this phase relation breaks down, and the velocity fluctuation is no longer simply related to the potential fluctuation.

To summarize the phase situation, we find that measured and calculated phases do not agree too well in the regions where the two experimental waves are localized. We have shown that collisions and the Coriolis force can shift the calculated phase $\sim 90^{\circ}$, obtaining better agreement with experiment. However, we do not believe that ion-neutral collisions and Coriolis effects are sufficient to explain the discrepancy.

Since we have included the effects considered to be most important in an HCD in our theory, we assume that the phase discrepancy is due to intrinsic weaknesses in the theoretical solution. First, using a linear solution, we have no good reason to expect agreement for an instability at nonlinear saturation amplitudes ($\tilde{n} \simeq 0.5$). Phase and growth rate, in particular, should be affected by nonlinear mechanisms in order for the wave amplitude to saturate. Second, a better solution would require integration over radial profiles to calculate normal mode behavior. Third, including the radial electric field and rotational effects self-consistently in cylindrical coordinates, rather than introducing rotational effects in a slab geometry, would also be an improvement, but we could not solve the cylindrical equations analytically. For these reasons we could not use the phase, ψ , to predict agreement for either experimental instability with theory.

Regarding phase relations for the determination of enhanced convection, we conclude that the experimental phase, ψ , is inconsistent with the radial velocity fluctuation being due solely to an azimuthal electric field. This assumption is explicit in the derivation of Eq. (5.31) for D_{enh}. We observe that $\psi_{calc} = \Delta \pm \pi/2$ is consistent with $v_{1r} = E_{1\theta} c/B = -ik_\perp \phi_1 c/B$, so that we expect ψ_{calc} to give a more reasonable estimate of D_{enh}. Alternate methods of determining enhanced convection will be compared in section VI. A.7.

7. Diffusion Coefficients.

First, let us compare various expressions for the enhanced diffusion coefficient, and choose the most reasonable. We begin with Eq. (5.30) for enhanced convection,

$$\langle nv_r \rangle_{conv} \equiv -D_{enh} \nabla n = \frac{n_1 v_{1r}}{2} \cos \Delta$$

where Δ is the phase between the density, n_1, and velocity, v_{1r} , fluctuations. If we use Eq. (5.20) to express v_{1r}, we get $D_{enh} = (\alpha \tilde{n}^2 / 2\delta) \cos \Delta$, where $\tilde{n} \equiv n_1/n_o$, $\delta \equiv - \nabla n_o/n_o$, and $\alpha e^{i\Delta} \equiv (i\omega' + \sigma') / (k \omega' / \Omega^* - \delta)$.

Alternatively, if we assume $v_{1r} = E_{1\theta} c /B = -i \phi_1 c / RB$, we get, as in Eq. (5.31), $D_{enh} = (\tilde{n} \phi_1 c / 2RB\delta) \sin \psi$, where ψ is the measured phase between the density, n_1, and potential, ϕ_1 , fluctuations. As discussed in section VI. A.6, we can also use a calculated value, ψ_{calc}, when the phase between the potential and velocity fluctuations is shifted by neutral collisions, Coriolis force, and

nonlinear effects. The following three expressions for the enhanced diffusion coefficient are presented in figs. VI.7 and VI.8 for the LF and HF waves, respectively;

■, $D_{enh(1)} = (\tilde{n}\ \phi_1 c\ /\ 2RB\delta\ )\ \sin\ \psi_{calc}$

o, $D_{enh(2)} = (\tilde{n}\ \phi_1 c\ /\ 2RB\delta\ )\ |\ \sin\ \psi|$

●, $D_{enh(3)} = (\ \alpha\ \tilde{n}^2\ /\ 2\delta\ \ )\ \cos\ \Delta$

Agreement between $D_{enh(1)}$ and $D_{enh(2)}$ is good, while $D_{enh(3)}$ is not so good in fig. VI.8. The third expression, $D_{enh(3)}$ is based on a linear calculation, while both experimental waves have reached nonlinear saturation.

As discussed in section VI. A.6, $\psi_{calc} = \Delta \pm \pi/2$, which is consistent with the radial velocity fluctuation being caused by an azimuthal electric field. This relation is explicit in the derivation of the first two expressions for D_{enh}. Whereas, this phase relation is violated by the measured phase, ψ, which we showed could be shifted due to collisions with neutrals, the Coriolis force, and even nonlinear mechanisms. Enhanced diffusion will henceforth be expressed as in the first expression above,

$D_{enh} = (\tilde{n}\ \phi_1 c\ /\ 2RB\delta\ )\ \sin\ \psi_{calc}$, using the measured density, n_1, and potential, ϕ_1, fluctuations, and the calculated phase, ψ_{calc}.

In fig. VI.9, all transverse diffusion coefficients are presented. Expressions for the diffusion coefficients appear in Appendix B. Note that enhanced diffusion due to the LF wave is

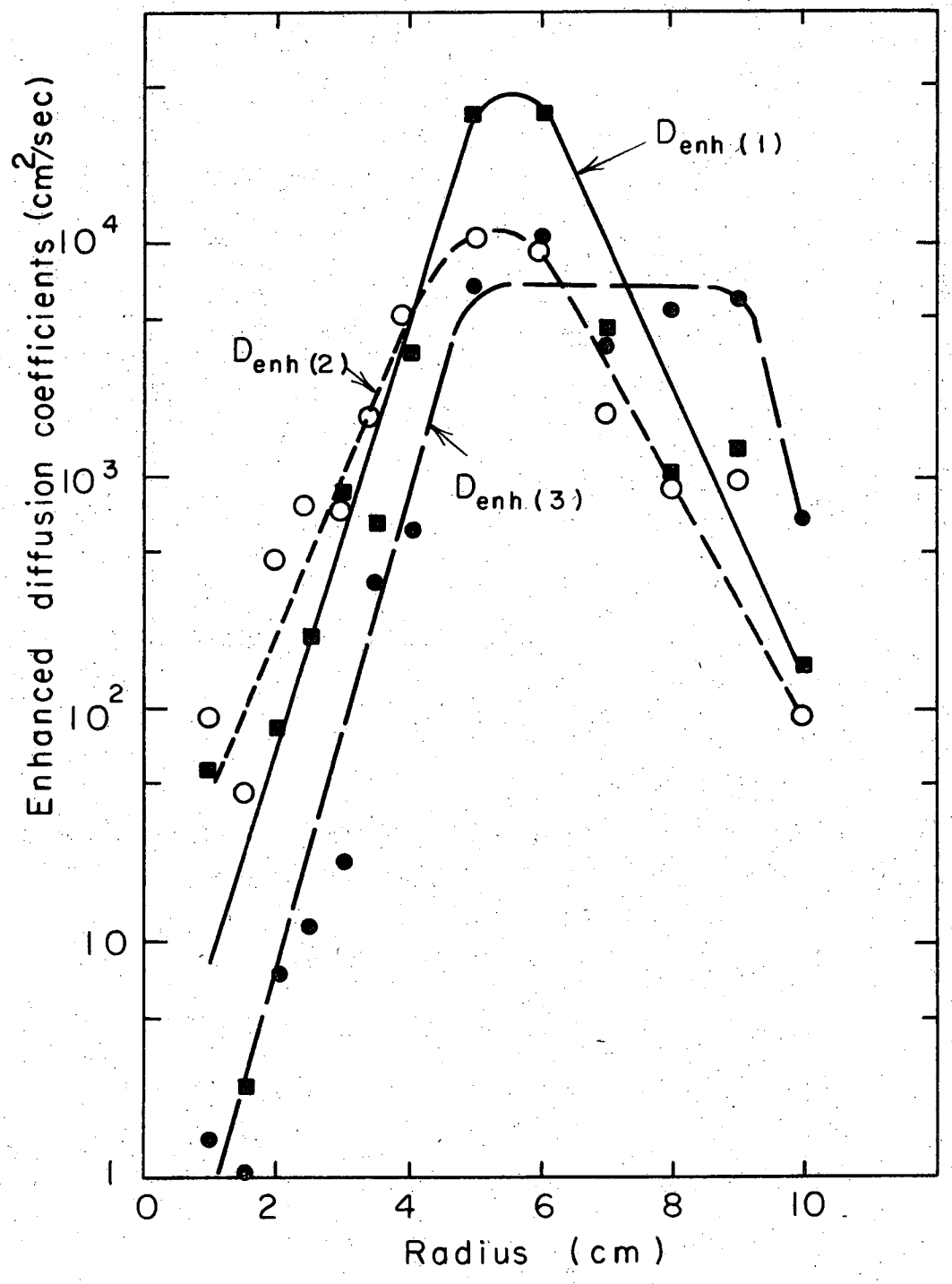

XBL7112 -4895

Fig. VI.7. Enhanced diffusion coefficients for the LF wave. ■, $D_{enh(1)}=(\tilde{n}\varphi_1 c/2Br\delta)\sin\psi_{calc}$; ○, $D_{enh(2)}=(\tilde{n}\varphi_1 c/2Br\delta)\sin\psi$; ●, $D_{enh(3)}=(\alpha\tilde{n}^2/2\delta)\cos\Delta$. p_t = 0.25 mtorr Ar, B = 530 G, end-rings grounded.

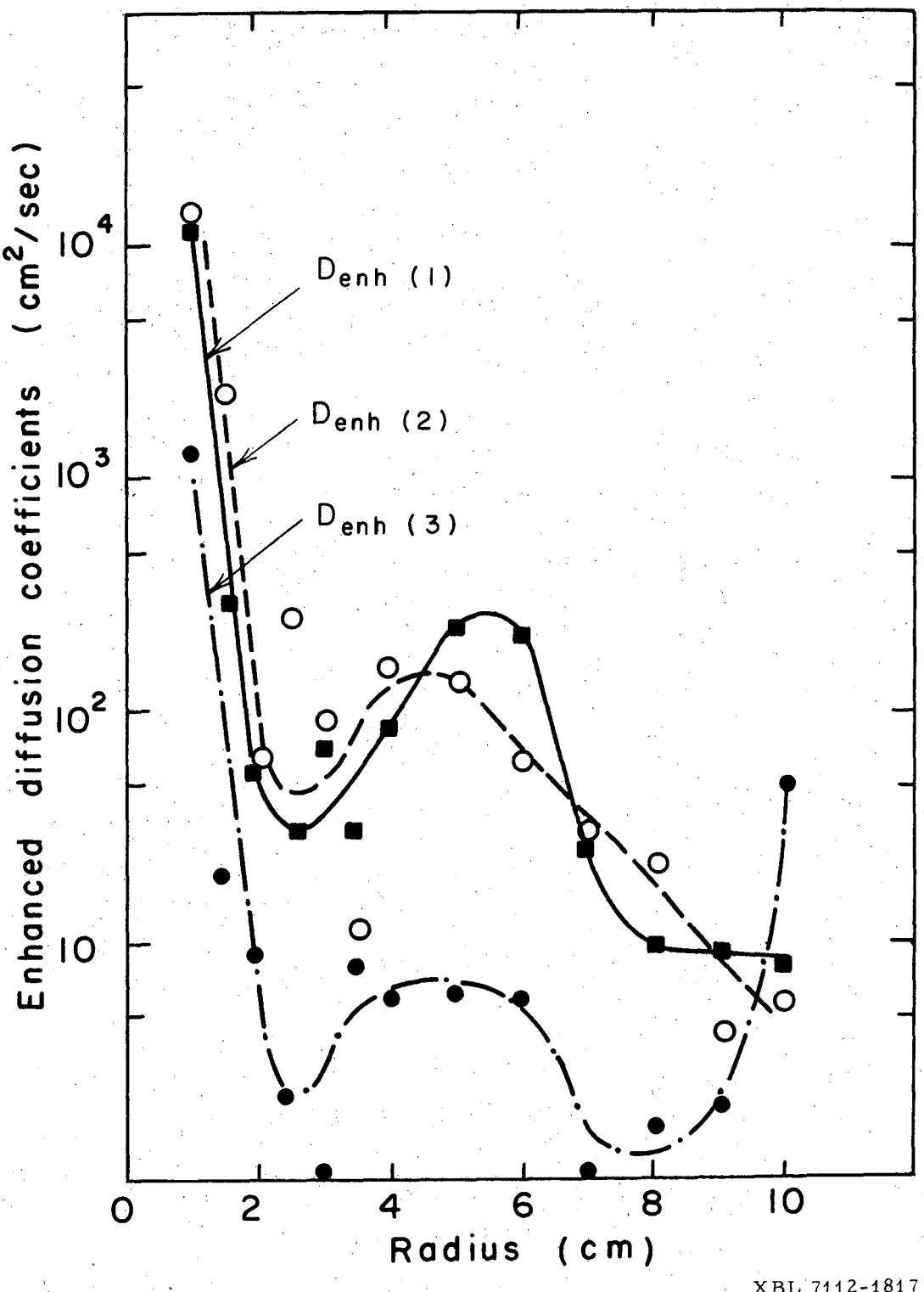

XBL 7112-1817

Fig. VI.8. Enhanced diffusion coefficient for the HF wave. ■, $D_{enh(1)}=(\tilde{n}\phi_1 c/2Br\delta)\sin\psi_{calc}$; ○, $D_{enh(2)}=(\tilde{n}\phi_1 c/2Br)\sin\psi$: ●, $D_{enh(3)}=(\alpha\tilde{n}^2/2\delta)\cos\Delta$. p_t=0.25 mtorr Ar, B=580 G, end-rings grounded.

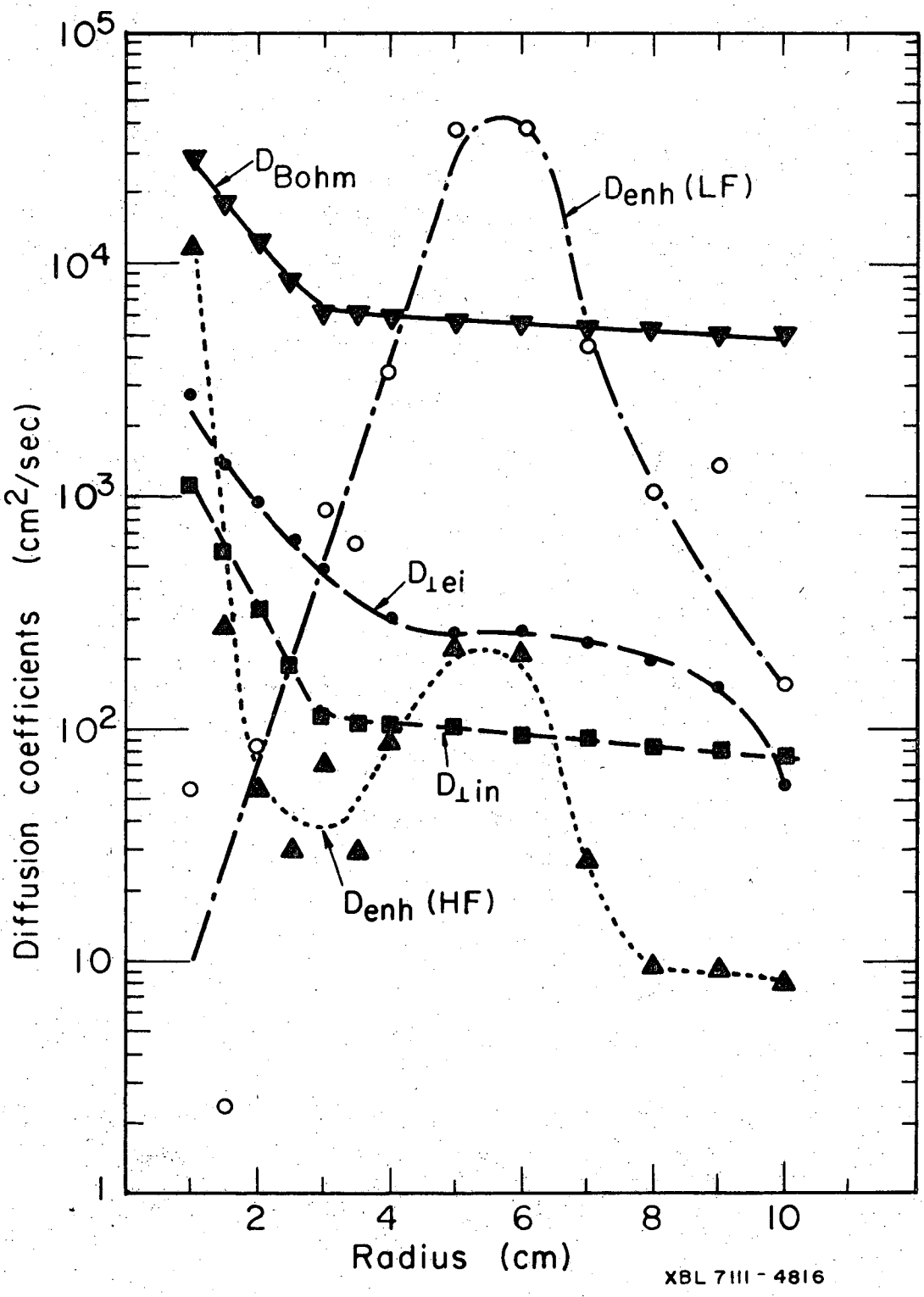

Fig. VI.9. Diffusion coefficients. ■, $D_{\perp in}$; ●, $D_{\perp ei}$; ○, D_{enh}(LF wave); ▲, D_{enh}(HF wave); and ▼, D_{Bohm}. p_t=0.25 mtorr Ar, B=580 G, end-rings grounded.

the dominant transport mechanism for $R \leq 4$ cm, and is comparable in magnitude to Bohm diffusion.

B. Wave "Identification".

The two low-frequency waves can be explained well by the theory for the rotational flute instability, which includes the effects of density gradient, plasma rotation, and collisions with neutrals. As mentioned in section IV. C, the experimental wave will be compared with theory on five counts: (1) Spatial location; (2) Frequency, Ω_r; (3) Direction of Propagation; (4) Parallel wavelength, $\lambda_\parallel$; and (5) Growth rate, γ/Ω_r.

1. Spatial Location.

In fig. VI. 10, the radial profile for the two wave amplitudes, $\tilde{n} \equiv n_1/n_o$, the Richardson number, $J \equiv L_v^2 / L_n R$, and the stability ratio of the calculated growth rate to frequency, γ / Ω_r, are shown. The Richardson number, discussed in section V.A.1, is the ratio of gravitational to velocity-shear energy. Hence, one would expect gravity to be the more important energy source for $|J| > 1/4$, while velocity-shear would be more important for $|J| < 1/4$. The ratio γ / Ω_r will serve as a calculated measure of instability.

Analysis of fig. VI. 10 shows that the LF wave amplitude, $\tilde{n}$ (LF), peaks near $R = 6$ cm, while the HF wave peaks near $R = 1$ cm. The Richardson number, $J \equiv L_v^2 / L_n R$, indicates that both waves peak in regions where centrifugal effects are more important than velocity-shear effects. Our neglecting of the Kelvin-Helmholtz velocity-shear wave therefore seems justified. The fact that the calculated stability parameter, γ/Ω_r, peaks near $R = 1$ cm

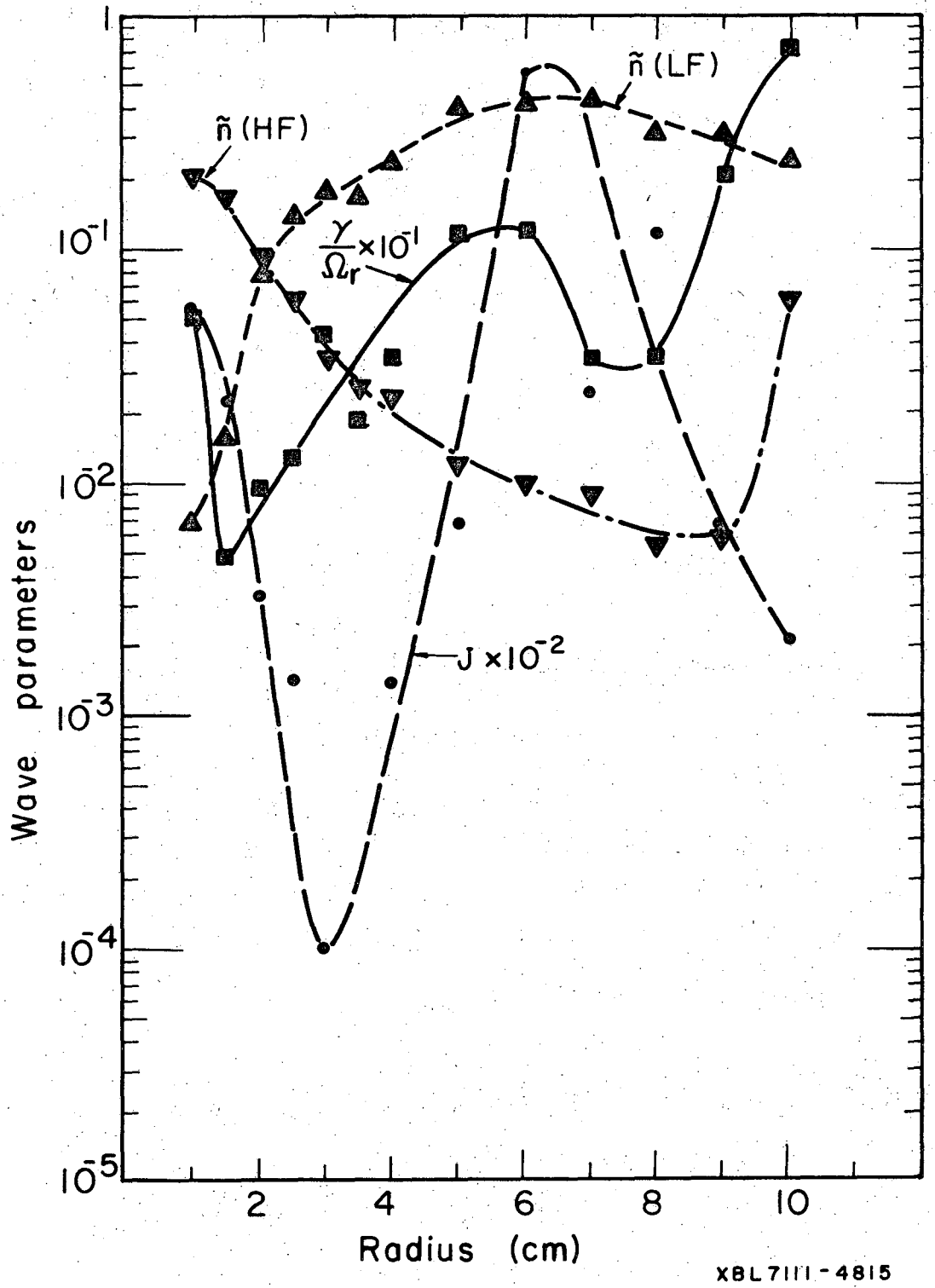

Fig. VI.10. Wave identification parameters. ■, $\gamma/\Omega_r \times 10^{-1}$, stability ratio; ●, $J \times 10^{-2}$, Richardson number, showing ratio of centrifugal to velocity-shear energy; ▲, $\tilde{n}$(LF wave); ▼, $\tilde{n}$(HF wave). p_t=0.25 mtorr Ar, B=580 G, end-rings grounded.

and R = 6 cm, and is of order unity there, gives further support for the rotational instability "identification".

In addition, if we consider fig. VI.4, we see that E_r is large and negative at R = 1 cm, and large and positive near R = 6 cm. This suggests that the wave may be destabilized by plasma rotation driven by E_r. We were not able to make significant changes in the radial positions of E_{rmax} and E_{rmin} over the range, B = 580 to 1160 G. We can, however, affect the magnitude of E_r at larger radii, by varying the neutral gas pressure, p_t, and the end-ring potentials. (For example, fig. VI. 40 shows the reduction of E_r at large radii due to increasing p_t, and fig VI.21 shows the reduction of E_r due to floating the third end-rings.) Furthermore in all cases where E_r was small at large radii, the LF wave was small or stable.

In summary, both waves occur consistently in regions of large radial electric field, in regions of large centrifugal effects as shown by the Richardson number, and where the rotational instability ratio, γ/Ω_r, is of order unity.

2. Frequency.

The radial frequency profiles calculated for the rotational flute, (Ω_r), including the Doppler shift due to plasma rotation, the electron-diamagnetic drift frequency (ω_{De}), the electric drift frequency (ω_E), the ion-diamagnetic drift frequency (ω_{Di}), and the gravitational drift frequency (ω_g) are presented in fig. VI. 11. The experimental wave frequencies are the dashed lines at LF = -1.83 kHz and HF = 36 kHz. Positive

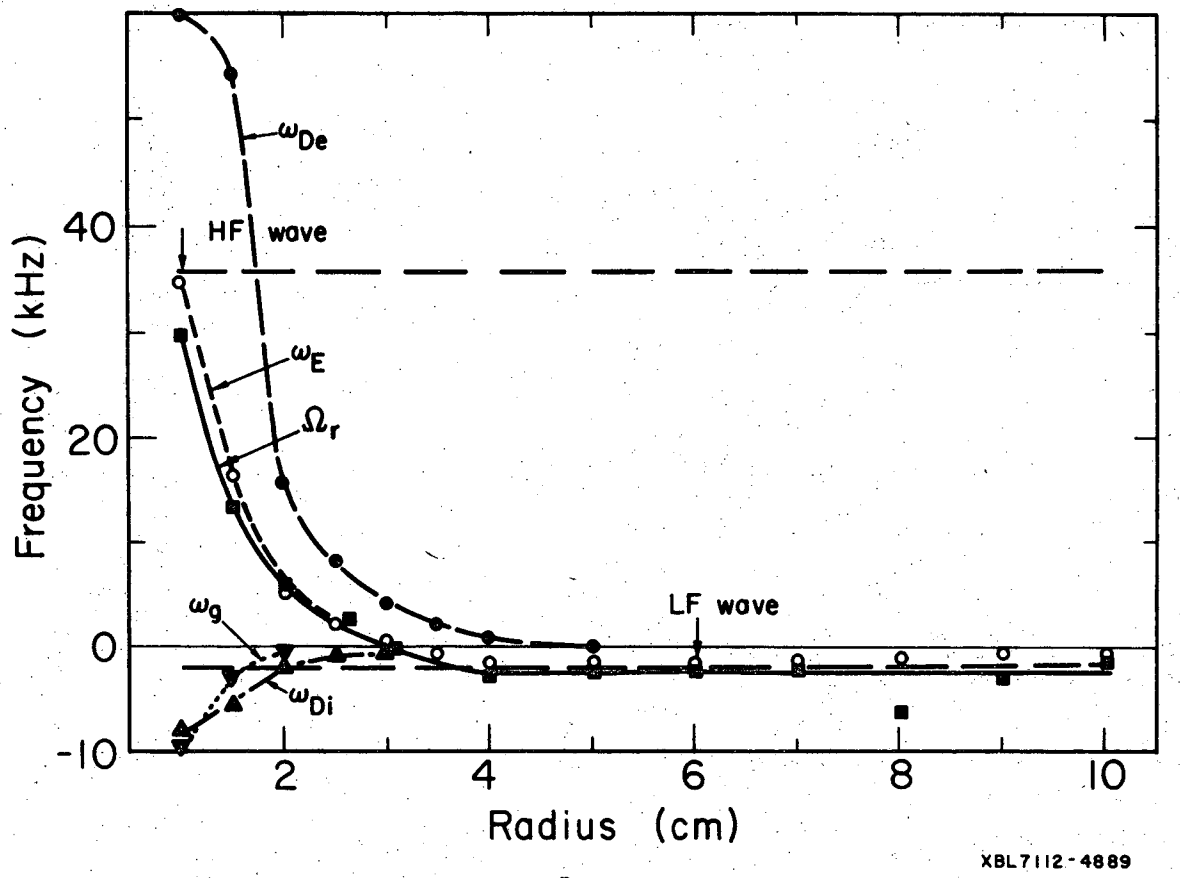

Fig. VI.11. Frequency profile. Positive frequencies correspond to the electron-diamagnetic direction. ■, Ω_r, calculated rotational instability frequency, including Doppler shift due to plasma rotation; ●, ω_{De}, electron-diamagnetic drift frequency; ○, ω_E, electric drift frequency; ▲, ω_{Di}, ion-diamagnetic drift frequency; ▼, ω_g, centrifugal gravity drift frequency. Two experimental wave frequencies are indicated by dashed lines. Arrows indicate radii of maximum wave amplitude. p_t = 0.25 mtorr Ar, B = 580 G, end-rings grounded.

frequency corresponds to propagation in the electron-diamagnetic direction.

We observe from fig. VI.11, that the frequency profile calculated for the rotational instability is very nearly the same as the E x B Drag instability frequency, ω_E . On this basis, also, it would be difficult to distinguish the two instabilities since they are very similar in being driven by E_r and collisions. However, the stability criteria should be different.

The two experimental instabilities are normal modes, since the frequency is independent of spatial position. We do not solve the radial wave equation for normal mode behavior, since numerical integration over the radial profile would be required. We calculate the wave parameters locally, and present the results as a function of radius. The local approximation is not too bad if the wave amplitude peaks in a rather narrow radial region.

The frequencies for the two waves are taken at the local positions where the wave amplitudes peak, as indicated by arrows, ↓ , in fig. VI.11. The measured frequency versus the local frequency approximation (including Doppler shift due to plasma rotation) is plotted in fig. VI.12 for the LF wave, and in fig. VI.13 for the HF wave. Points are plotted according to magnetic field, B = 580 to 1160 G, for argon and helium. The full range of operating conditions in Table VI.1 is represented in these two figures.

In summary, good agreement between measured and calculated frequencies confirms that the experimental frequencies for the two waves can be explained well by linear rotational instability theory.

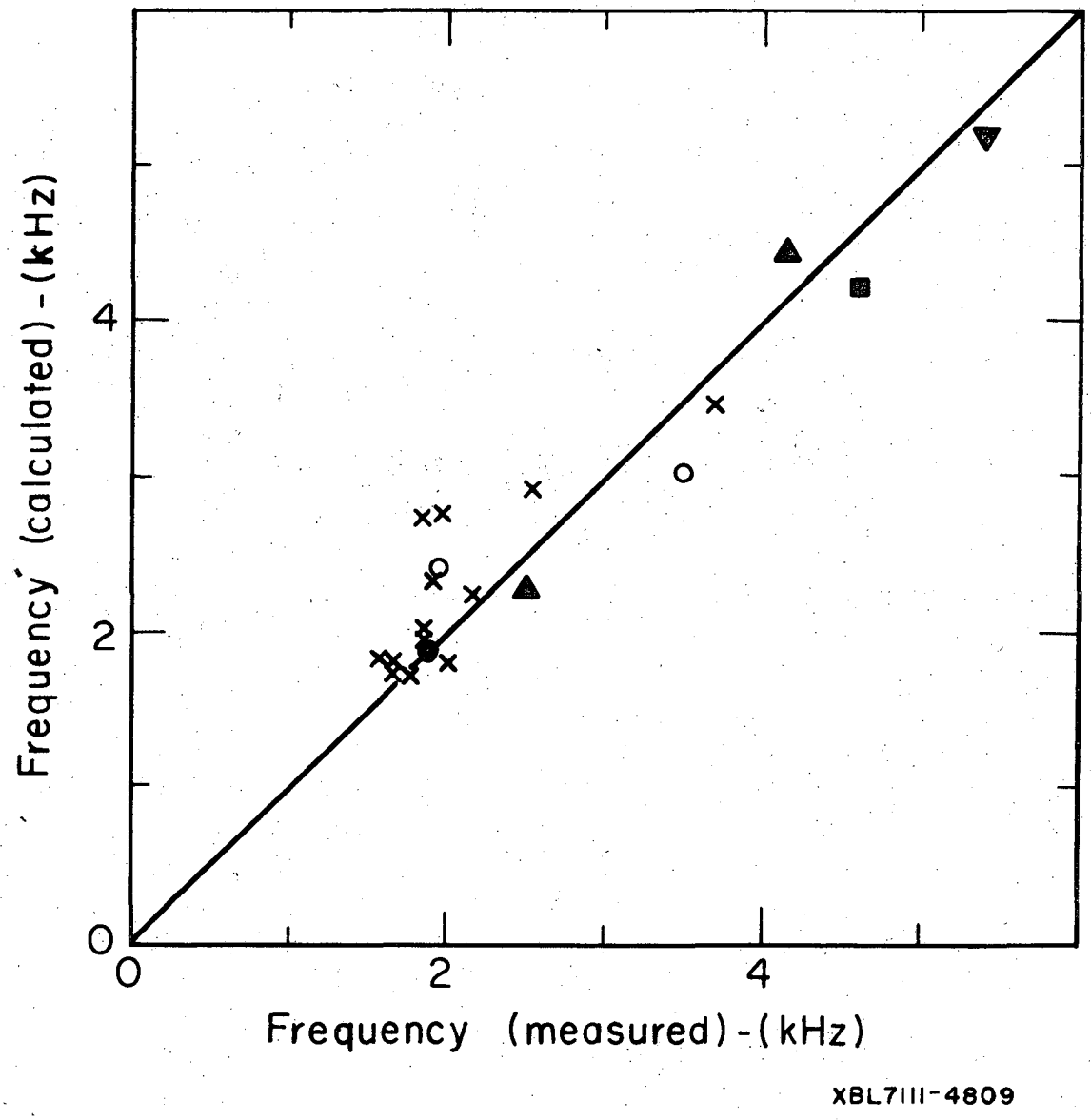

Fig. VI.12. Measured vs. calculated frequencies for the LF wave. ✕, argon, B = 580 G; ●, argon, B = 870 G; ○, argon, B = 1160 G; ▲, helium, B = 580 G; ▼, helium, B = 870 G; ■, helium, B = 1160 G.

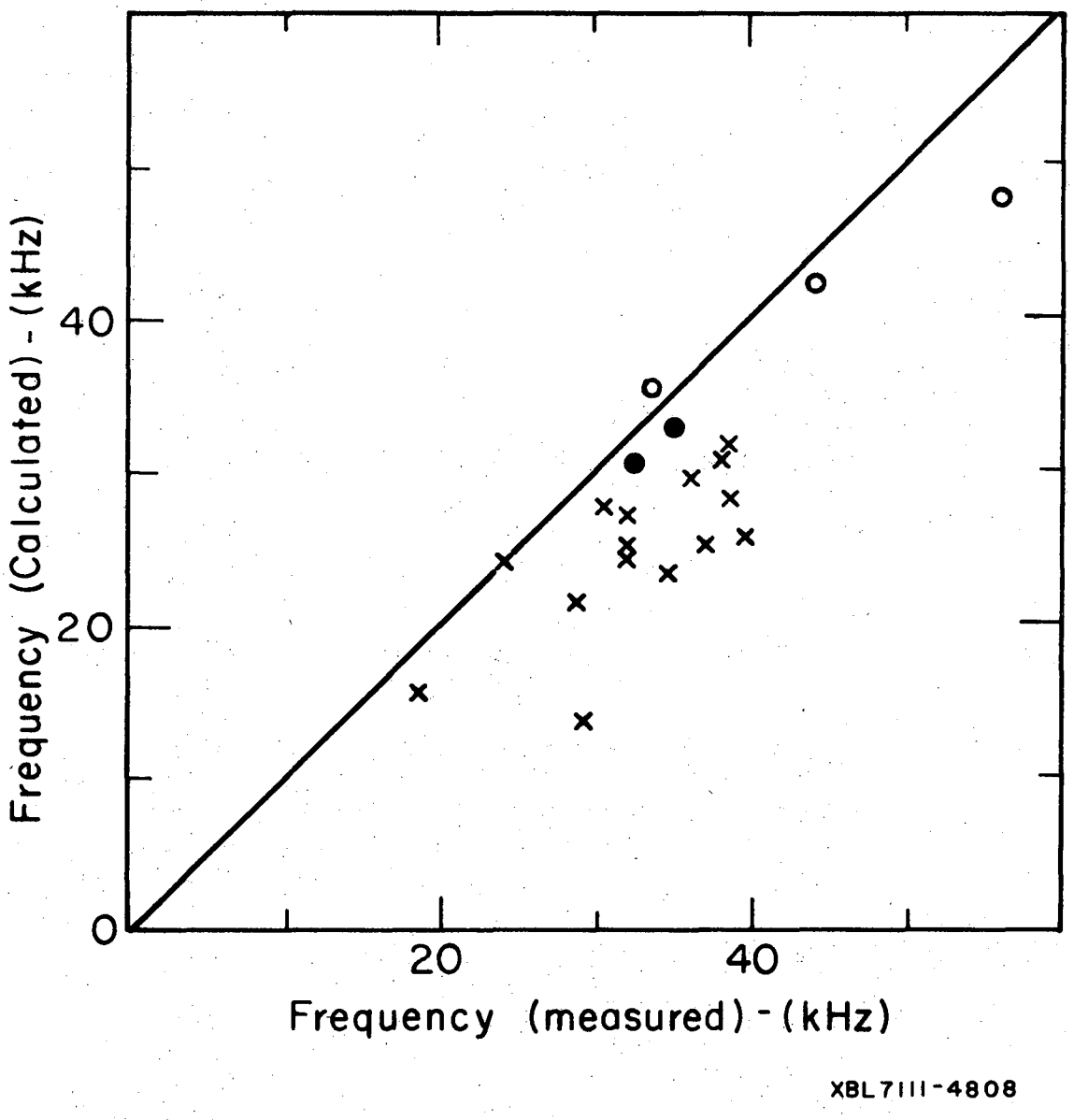

Fig. VI.13. Measured vs. calculated frequencies for the HF wave. ✕, argon, B = 580 G; ●, argon, B = 870 G; o, argon, B = 1160 G.

3. Direction of Propagation.

Phase measurements taken on Langmuir probes at three azimuths, separated by 90° each, show that the LF wave is an $m = 1$ mode which propagates in the ion-diamagnetic direction; while the HF wave is also an $m = 1$ mode which propagates in the electron-diamagnetic direction. Fig. VI. 14 shows the floating potential oscillations on the four quarters of the second end-ring electrode at the anode end. From the upper trace to the lower trace, the ring quarters increase 90° in azimuth in the ion-diamagnetic direction, I_D, indicating that the LF wave propagates in the ion-diamagnetic direction.

In fig. VI.11, we see that both the experimental HF wave frequency, indicated by the dashed line, and the Doppler shifted theoretical wave frequency, Ω_r , are large and positive at small radii, corresponding to propagation in the electron-diamagnetic direction. And similarly for the LF wave, both rotational theory and experiment agree on negative frequencies at large radii, corresponding to propagation in the ion-diamagnetic direction.

4. Parallel Wavelength, $\lambda_{\parallel}$.

We could find no experimental evidence to suggest either a travelling or a standing wave in the axial direction. Phase accuracy of the Princeton Applied Research Model HR-8 lock-in amplifier is specified as 5°. And, uncertainty in the azimuthal position of the stainless-steel axial probe is estimated to be $\sim 15^{\circ}$ for the worst case at small radii. But even with this kind of "worst case" accuracy, we can say $\lambda_{\parallel} \gtrsim 24$ L. In fig. VI.3, we observe that there is little evidence for a standing wave in the axial direction.

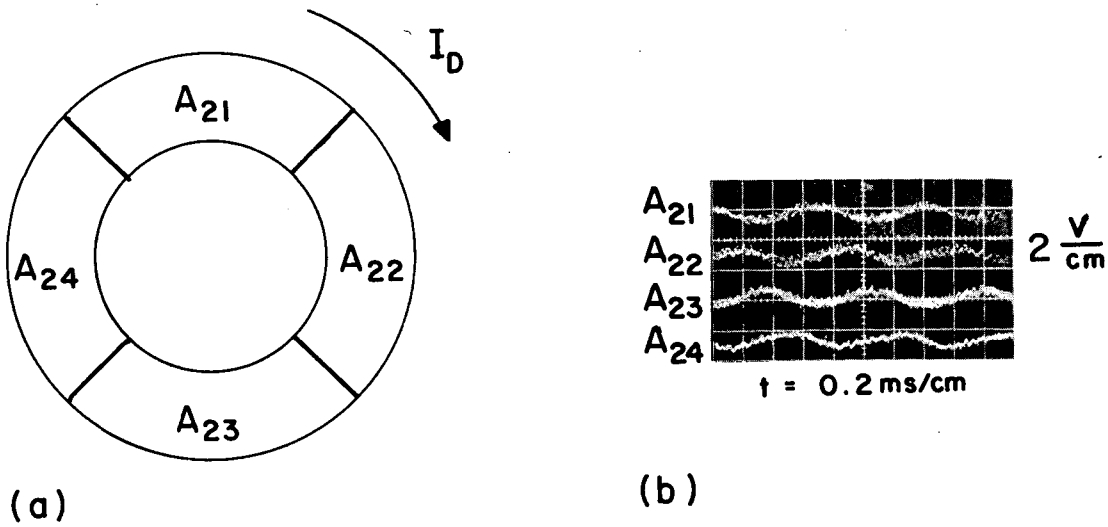

XBB 7112-6027

Fig. VI.14. Potential fluctuations on the quartered second end-ring at the anode end. (a) second anode end-ring, showing labels increasing in the ion-diamagnetic direction, I_D; (b) potential fluctuations on the four quarters, showing LF wave propagation in the ion-diamagnetic direction.

We would expect that if $\lambda_{||}$ were finite, then $\lambda_{||} >> L$ could only be maintained due to poor conductivity with the end-ring electrodes, through ion sheaths.[98] If, however, we positively bias the end-ring electrodes for better electron contact, we would expect $\lambda_{||}$ to be restricted to $\lambda_{||} \gtrsim 2L$, or at least changed observably. This was done, and finite $\lambda_{||}$ was not observed.

Hence, we rule out finite-$\lambda_{||}$ instabilities, and believe that both experimental waves are flutes.

5. Measured vs. Calculated Growth Rate, γ/Ω_r.

Two methods are discussed in section VI.G for measuring γ/Ω_r directly. Since we had no appreciable luck in stabilizing the HF wave, these methods cannot apply. However, a summary of the results of the two methods is presented for the LF wave in Table VI.2. Errors are discussed in section VI.G.

Table VI.2. Measured Vs. Calculated γ/Ω_r -Summary.

Stability Ratio	Azimuthal Growth Method	Temporal Growth Method
γ/Ω_r (measured)	0.54 ± 0.27	0.36 ± 0.36
γ/Ω_r (calculated)	0.43	0.34 ± 0.22

The calculated linear growth rate is obtained from the rotational instability dispersion relation, Eq.(5.18). Good agreement between theory and experiment is obtained using the azimuthal growth method for two reasons. First, the wave amplitudes can be measured

at different azimuths to ~15% accuracy. Also, the wave amplitude is reduced to ~20% of its non linear saturation value, where the linear growth rate is expected to be more valid.

Agreement is also obtained for the temporal growth method, although the accuracy is poor in this case. Accuracy is limited by out ability to determine how many wave periods are required for a given change in wave amplitude. In this experiment large growth rates, $\gamma/\Omega_r \sim 1$, imply that the wave amplitude can grow drastically in a single wave period. Therefore we estimate our uncertainty for the measured growth time as ~1 wave period (~100% uncertain). Better accuracy is predicted for lower growth rates, $\gamma/\Omega_r << 1$.

6. Wave Identification Conclusions.

We conclude that rotational instability theory and experiment agree on all five points of comparison. Therefore, both experimental waves are explained well by rotational flute theory.

C. Enhanced Transport and DC Stabilization

DC stabilization means the application of a constant "corrective" potential to any chosen end-ring electrode configuration. Two effects must be considered in this section. The first effect is that of DC stabilization on wave amplitude and the enhanced diffusion coefficient. The other effect is that of the enhanced diffusion coefficient on the density profile. The expression we use for the enhanced diffusion coefficient is $D_{enh} = (\tilde{n}\varphi_1 c/2BR\delta) \sin \Psi_{calc}$, as discussed in section VI.A.7.

The data presented in this section is summarized in Table VI.3 for convenience. Power for the case of floating electrodes is estimated as the floating voltage times the current when the electrode is grounded. No stabilization (NS) cases are for all end-ring electrodes and the tank grounded.

Table VI.3 DC Stabilization-Summary

Case	Figure	Suppressor (End-ring #)	Voltage (volts)	Power (watts)	Comment
(a)	VI.16	-	0	0	NS-reference
(b)	VI.17	3	+3	0.27	Floating
(c)	VI.18	3	+6	0.84	Floating
(d)	VI.19	1	-20	16.0	HF wave
(e)	VI.20	3	+5	4.5	LF wave stable
(f)	VI.21	3	+8	17.0	Excessive power

1. Effect of DC Stabilization on D_{enh}.

The wave spectra at R = 5 cm corresponding to cases (a), (b), (e) and (f) are shown in fig. VI.15. The last spectrum for power P = 17 watts, shows that by increasing feedback power greater than optimum, we can increase the amplitude of new modes.

The radial density profile and the enhanced diffusion coefficients due to the experimental waves appear in figs. VI.16 to VI.21. Also presented are the classical ion-neutral transverse diffusion coefficient and the Bohm diffusion coefficient, for comparison. The

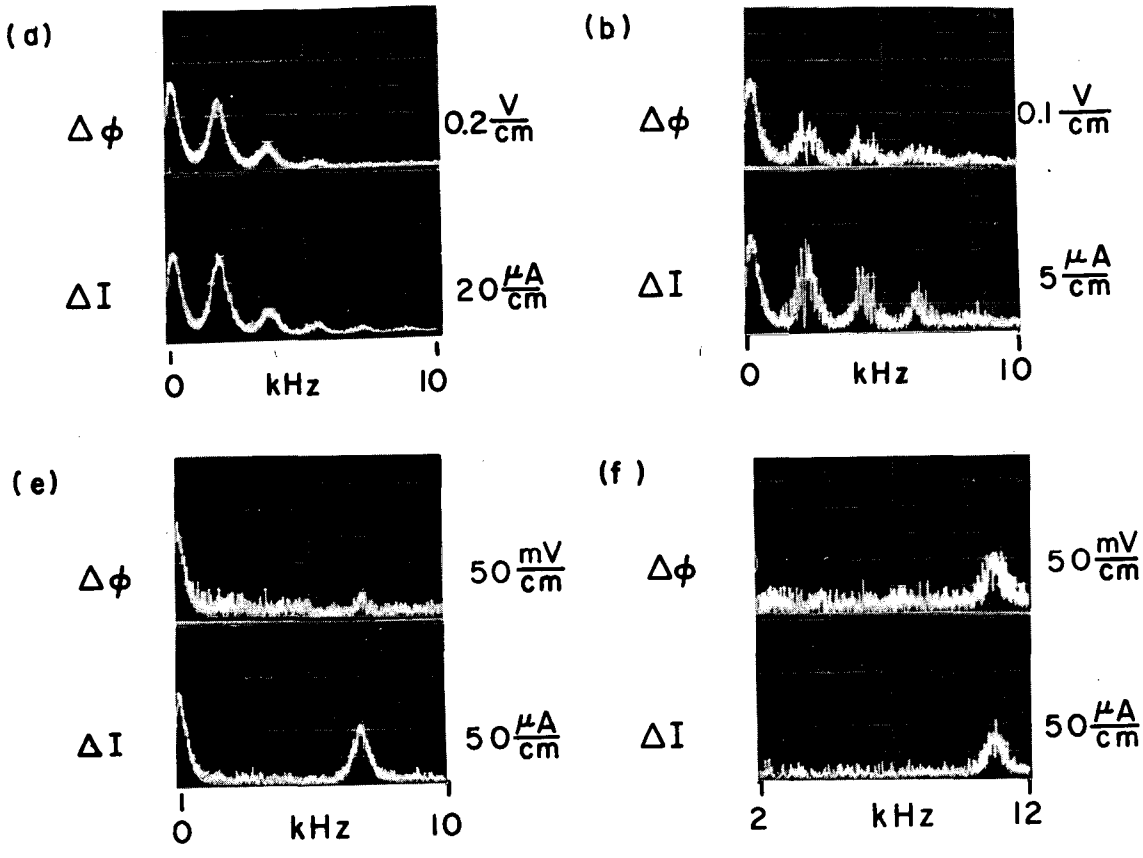

XBB 7112-6031

Fig. VI.15. DC stabilization wave spectra at R=5 cm. Upper trace shows potential fluctuation, $\Delta\phi$, while lower trace shows ion current fluctuation, ΔI. Case (a) all end-rings grounded; (b) third end-ring floated, showing LF wave amplitude reduction; cases (c) and (d) are not shown; (e) apply +5 volts to third end-ring, showing stabilization of LF wave at 2 kHz; and (f) apply +8 volts to third end-ring, showing excitation of "shear" mode at 11 kHz due to excessive potential.

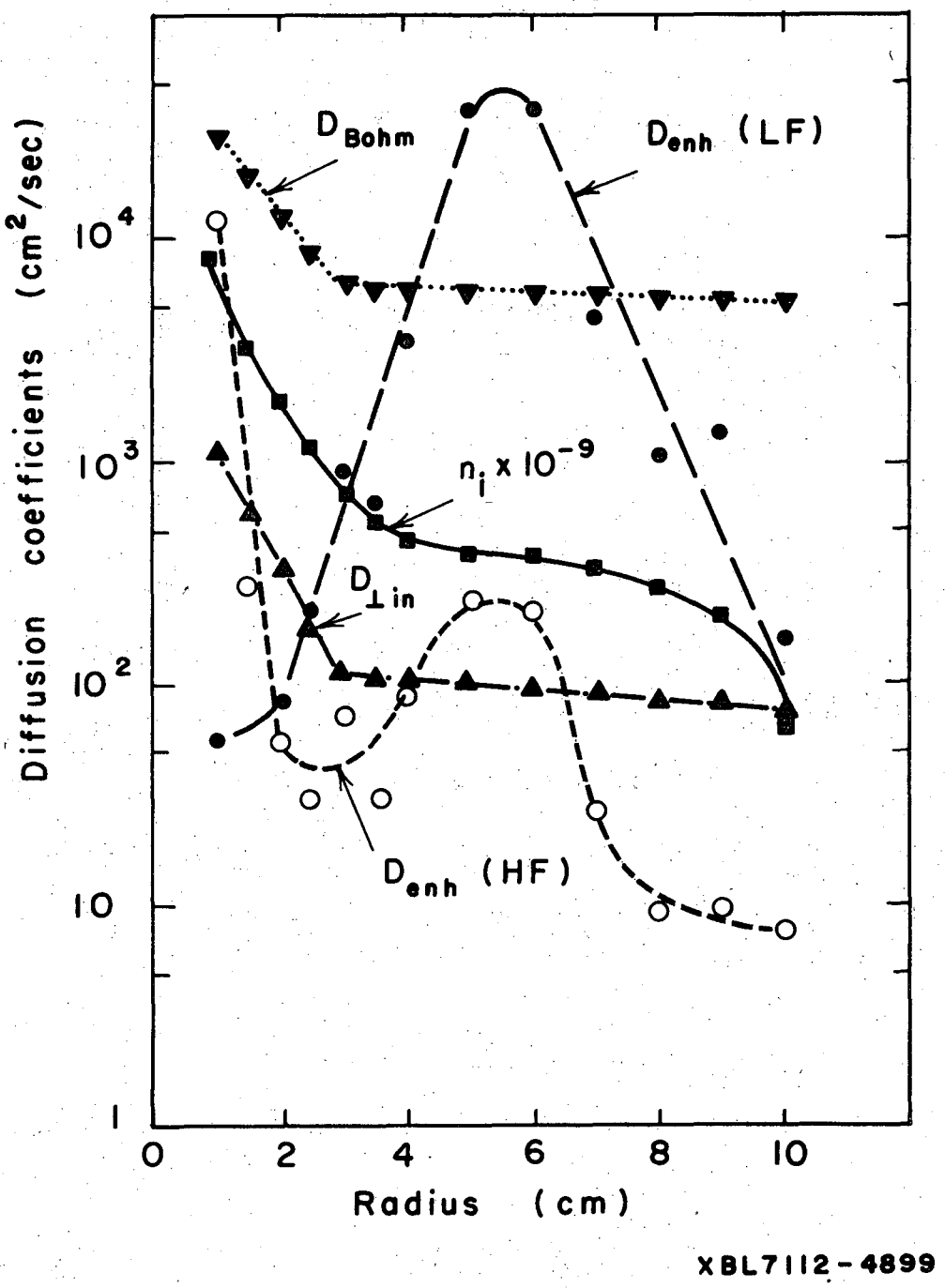

Fig. VI.16. Diffusion coefficients and density profile. No stabilization. ■, density, $n_i \times 10^{-9}$ cm^{-3}; ●, D_{enh} (LF wave); o, D_{enh} (HF wave); ▲, $D_{\perp in}$; and ▼, D_{Bohm}. Note flattening of density profile as D_{enh} (LF) becomes dominant. p_t = 0.25 mtorr Ar, B = 580 G, end-rings grounded.

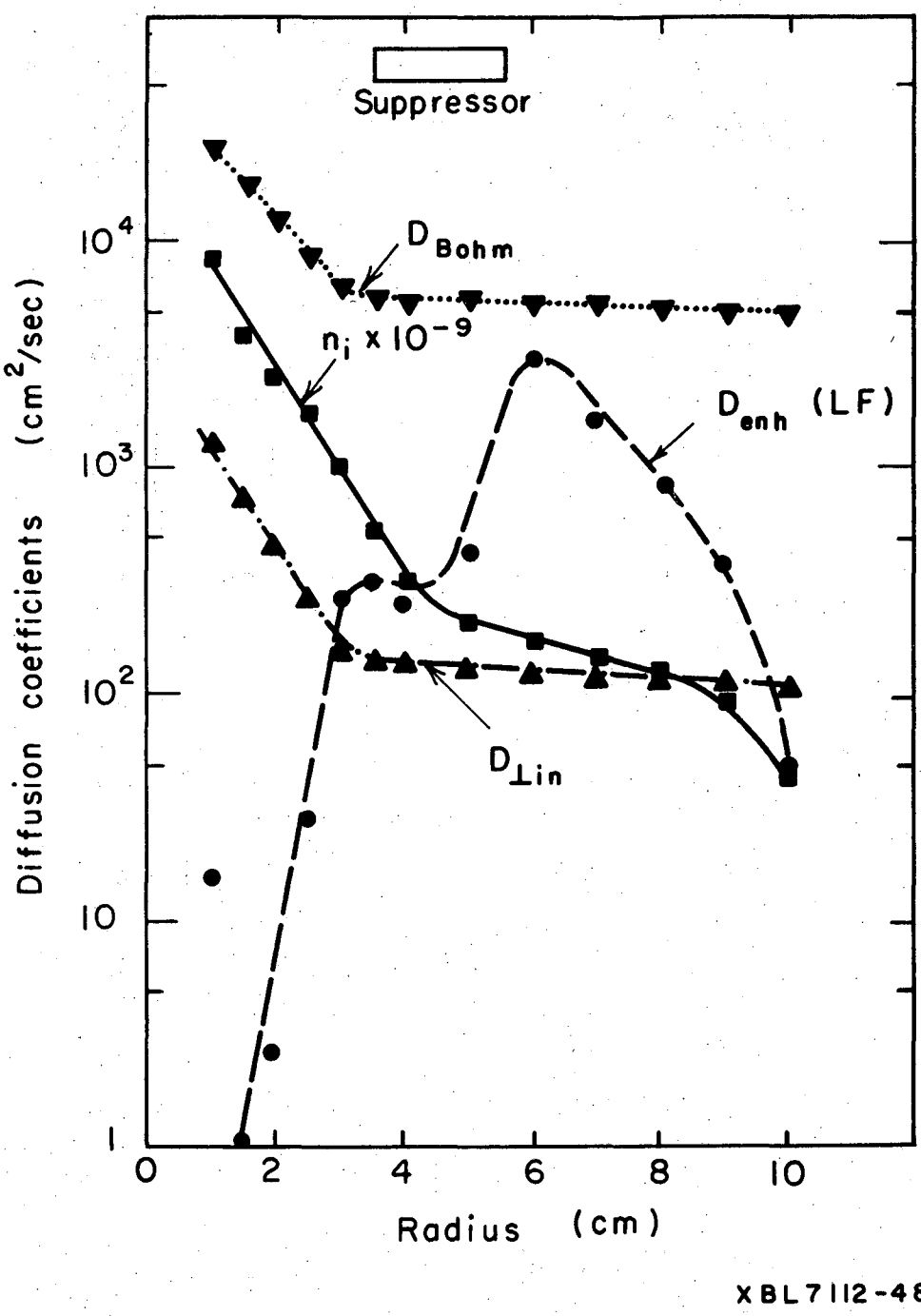

XBL7112-4897

Fig. VI.17. Diffusion coefficients and density profile. "Passive" DC stabilization. ■, density, $n_i \times 10^{-9}$ cm^{-3}; ●, D_{enh} (LF wave); ▲, $D_{\perp in}$; and ▼, D_{Bohm}. The third end-ring is floated electrically at +3 volts, power P = 0.27 watts. Radial suppressor position is indicated. p_t = 0.25 mtorr Ar, B = 580 G.

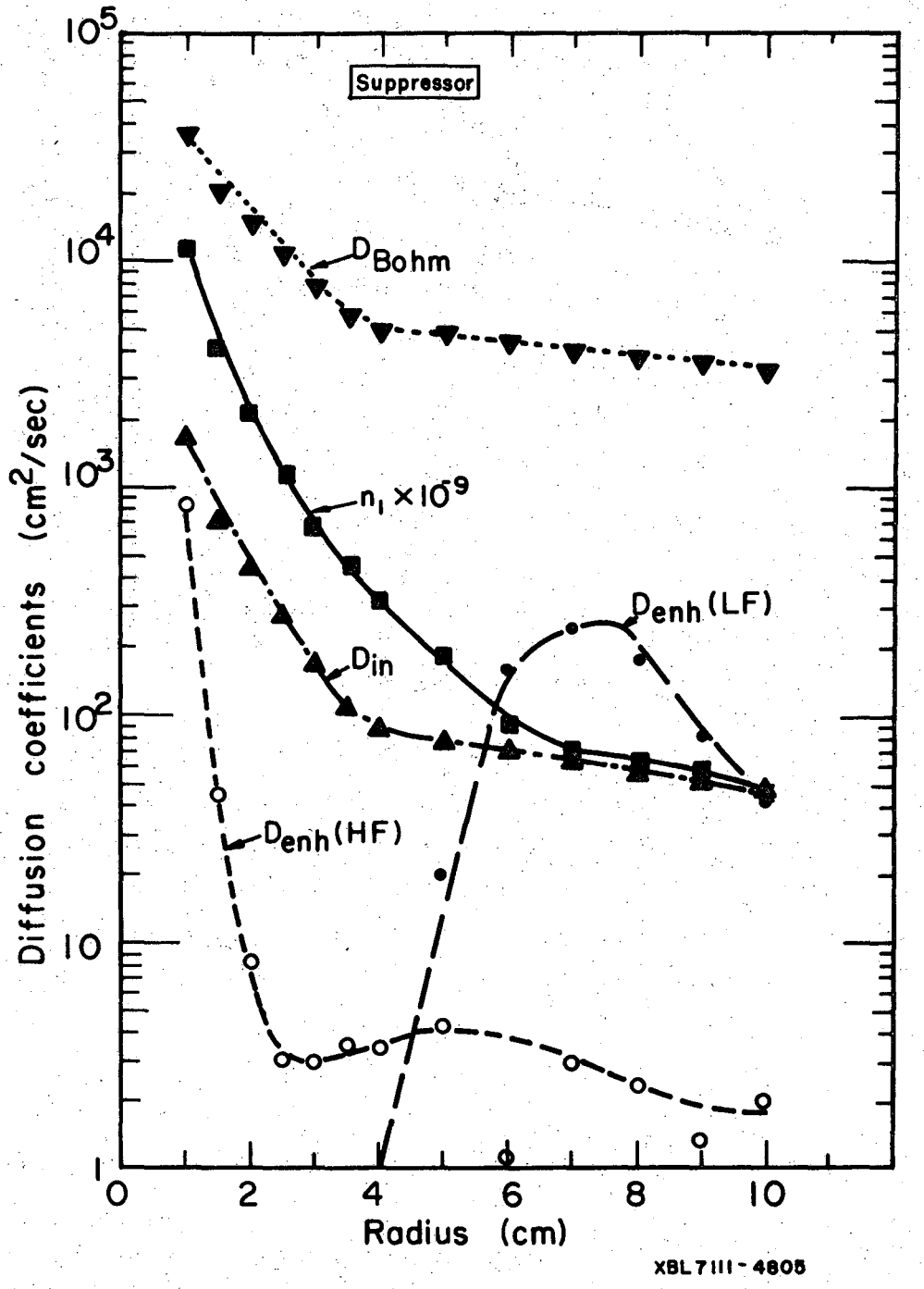

Fig. VI.18. Diffusion coefficients and density profile. "Passive" DC stabilization. ■, density, $n_i \times 10^{-9}$ cm^{-3}; ●, D_{enh} (LF wave); o, D_{enh} (HF wave); ▲, $D_{\perp in}$; and ▼, D_{Bohm}. Note steepening of the density profile and reduction of D_{enh} (LF) as the third end-ring is floated electrically, at +6 volts, power P = 0.84 watts. Radial suppressor position is indicated. p_t = 0.27 mtorr Ar, B = 580 G.

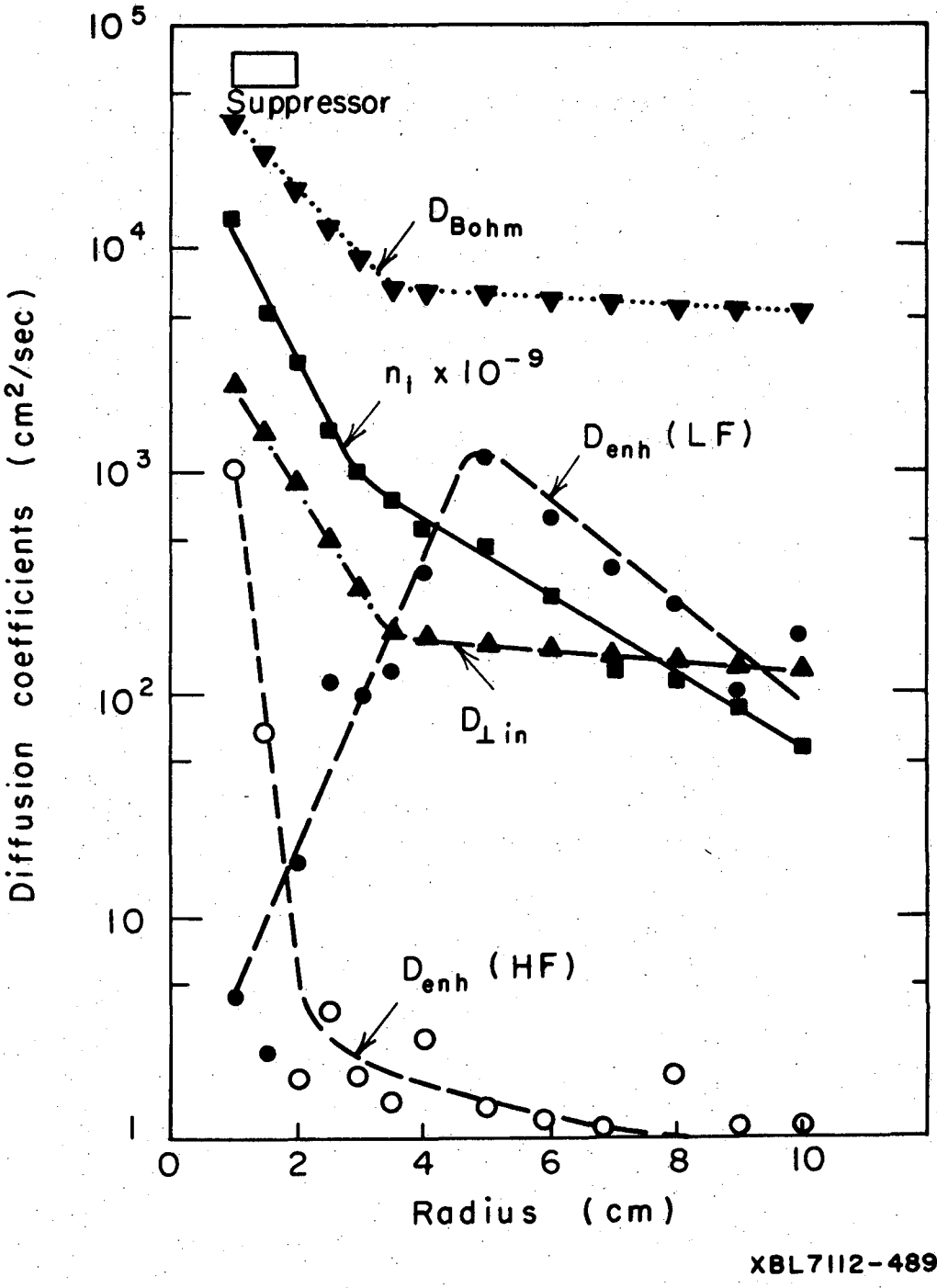

Fig. VI.19. Diffusion coefficients and density profile. DC stabilization. ■, density, $n_i \times 10^{-9}$ cm^{-3}; ●, D_{enh} (LF wave); o, D_{enh} (HF wave); ▲, $D_{\perp in}$; and ▼, D_{Bohm}. Note steepening of the density profile and reduction of D_{enh} (LF) as -20 volts is applied to the inner end-ring, indicated as suppressor. Power P = 16 watts. p_t = 0.38 mtorr Ar, B = 580 G.

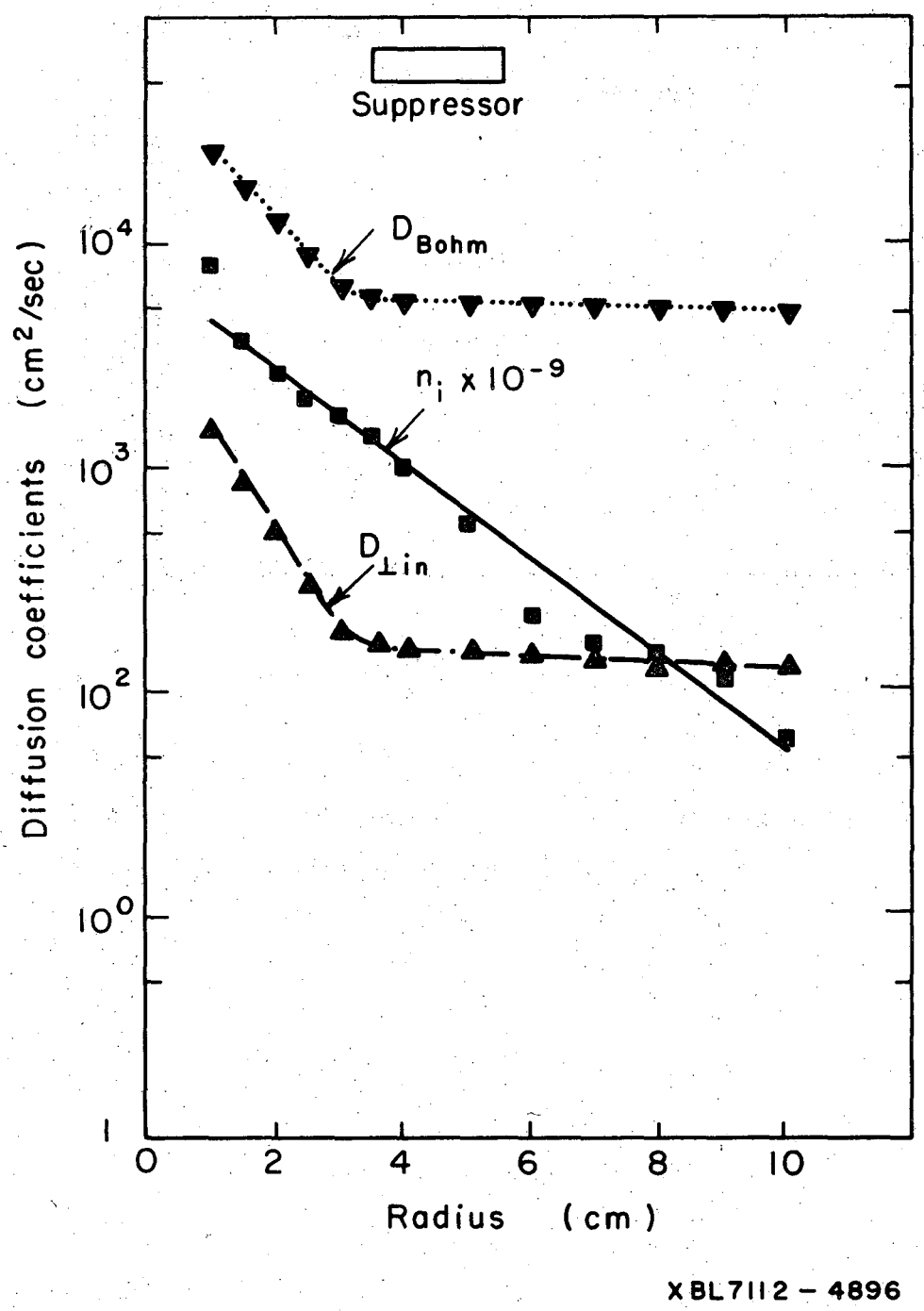

Fig. VI.20. Diffusion coefficients and density profile. DC stabilization. ■, density, $n_i \times 10^{-9}$ cm^{-3}; ▲, $D_{\perp in}$; and ▼, D_{Bohm}. The LF wave is stabilized by application of +5 volts, power P = 4.5 watts, to the third end-ring. Radial suppressor position is indicated. Note steep density profile. p_t = 0.40 mtorr Ar, B = 580 G.

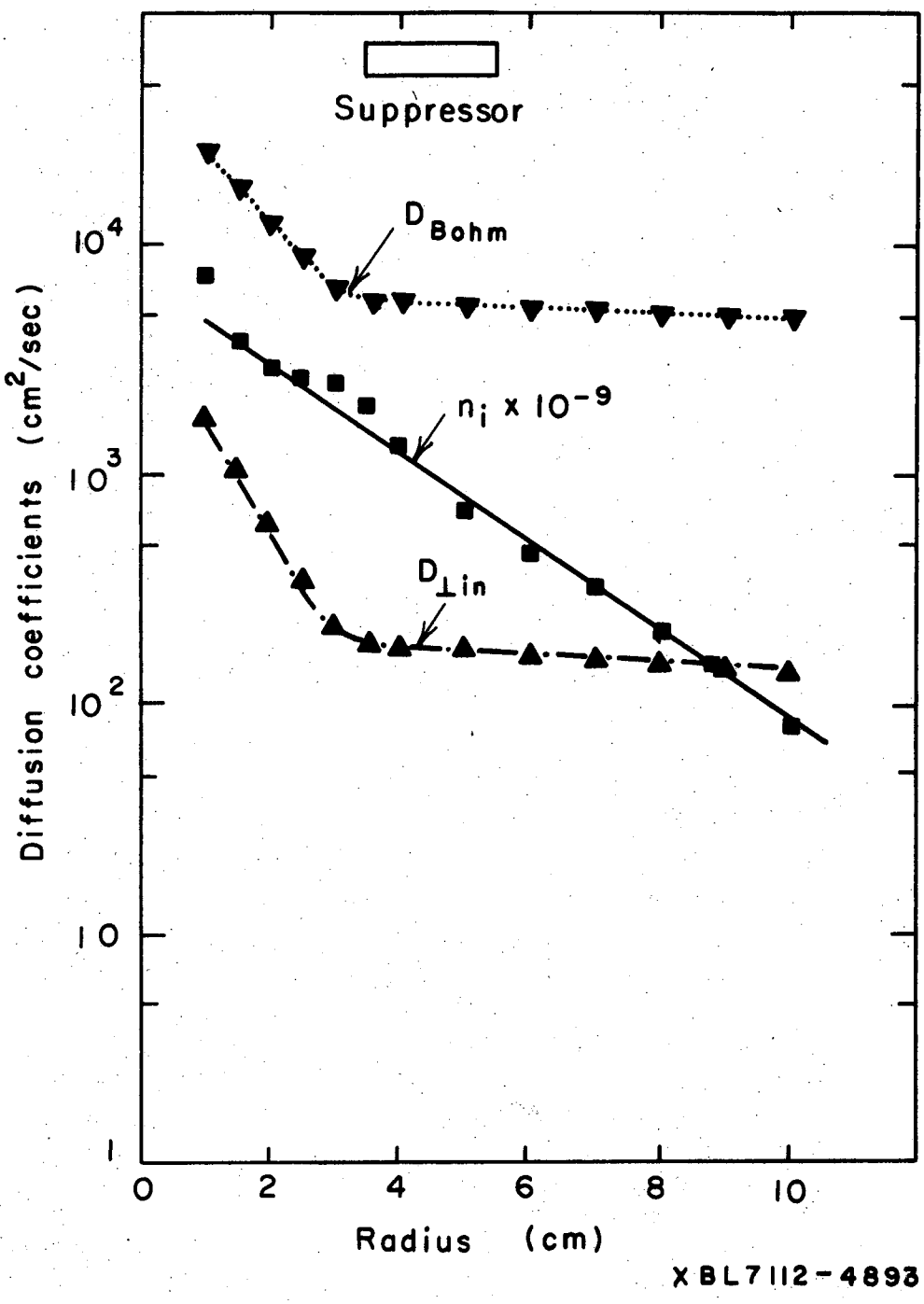

Fig. VI.21. Diffusion coefficients and density profile. DC stabilization. ■, density, $n_i \times 10^{-9}$ cm^{-3}; ▲, $D_{\perp in}$; and ▼, D_{Bohm}. Increasing the voltage to +8 volts, power P = 17 watts, applied to the third end-ring has little additional effect. Radial suppressor position is indicated. p_t = 0.47 mtorr Ar, B = 580 G.

position of the suppressor electrode is indicated in each figure. If the LF wave is stable ($\tilde{n} < 0.01$), then no D_{enh} (LF) appears. In figs. VI.17, VI.20, and VI.21, the HF wave was ignored in the interests of speedy data-taking, since this wave does not noticeably affect transport anyway, due to the fact that D_{enh} (HF) $\lesssim D_{\perp in}$. In addition, the HF wave is negligibly affected by all stabilization attempts.

A qualitative study of figs. VI.16 to VI.21 shows that DC voltage with power P ≈ 0.90 watts applied to the third end-ring is sufficient to stabilize or drastically reduce D_{enh} for the LF wave. Reduced D_{enh}(LF) is a direct consequence of reduced wave amplitude.

Fig. VI. 19 shows our best unsuccessful attempt to stabilize the HF wave, by applying DC voltage, V = -20 volts, and power P = 16 watts, to the inner end-ring electrode. Little effect on the HF wave is observed. (From fig. VI.22., we see that E_r is not significantly reduced near R = 1 cm. However, the DC stabilization does eliminate E_r at large radii, with the resulting LF wave amplitude reduction, as evidenced in fig. VI.19. Positive voltage applied to the inner end-ring has no favorable effect. Henceforth, DC stabilization is only discussed with respect to the LF wave, since we cannot stabilize the HF wave anyway. However, since enhanced diffusion is less than or comparable to classical diffusion, D_{enh}(HF) $\lesssim D_{\perp in}$, $D_{\perp ei}$, the effect on transport is negligible.

From figs. VI.17 and VI.18 we notice that D_{enh} (LF) can be reduced by 1 to 3 orders of magnitude by floating the third end-ring, thereby changing the radial boundary conditions at the end-rings. (The

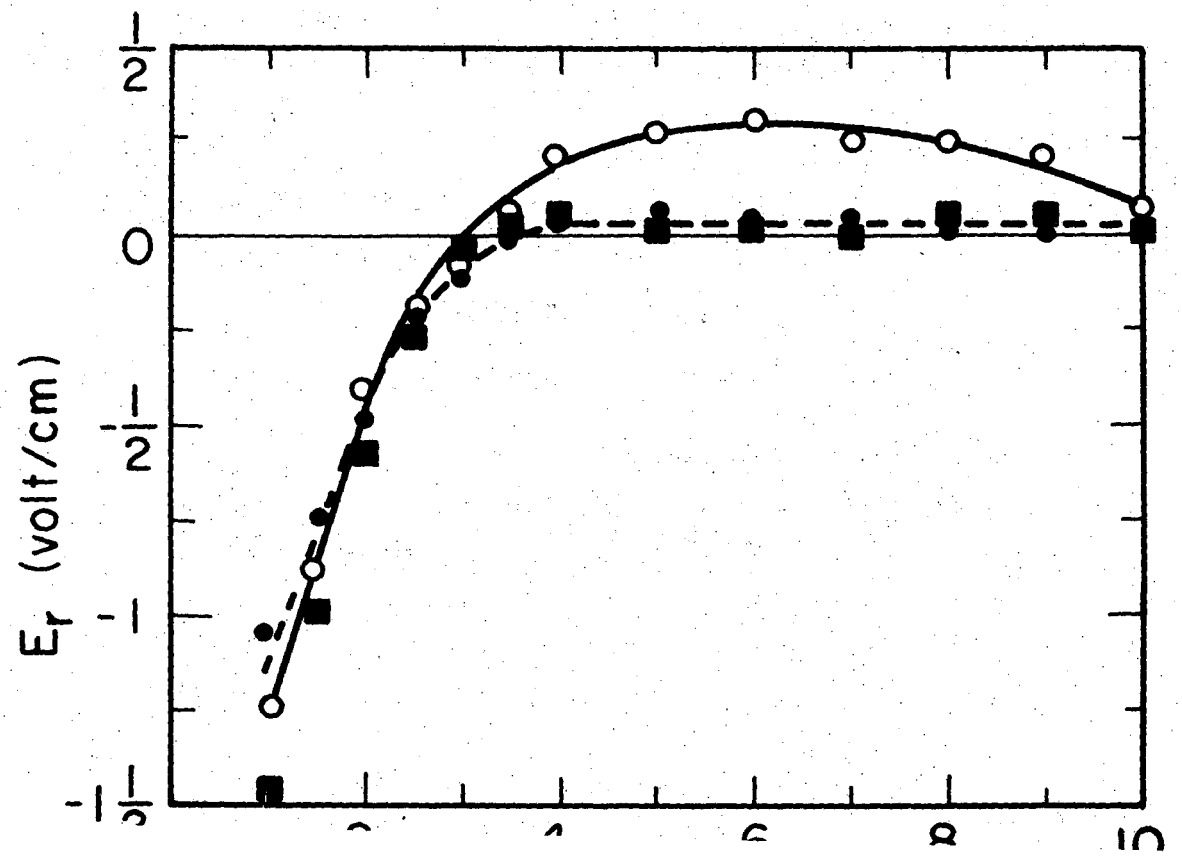

radial electric field corresponding to fig. VI.18 is shown in fig. VI.22, showing that E_r is eliminated at large radii by floating the third end-ring.) No external power is required, so we here report success of a passive stabilization technique.

Fig. VI.20 shows that power P = 4.5 watts is sufficient to completely stabilize the LF wave of fig. VI.16, whereas power P = .27 watts was not sufficient in fig. VI.17. We learn from fig. VI.21 that additional power, P = 17 watts, is unnecessary.

From fig. VI.22, one can infer that changing DC boundary conditions stabilizes the LF wave, in part at least, by reducing the radial electric field, which drives the rotational instability. We propose that this may be due to creating better electron contact with the axial boundary, which maintains the good electrical contact required to "short" the field.[98]

2. Semi-quantitative Effect of D_{enh} on the Density Profile.

Flattening of the radial density profile is often indicative of enhanced transport. Note qualitatively, from figs. VI.16 to VI.21, the flattening of the density profile near the radius at which $D_{enh}(LF)$ becomes larger than the classical ion-neutral diffusion coefficient, D_{lin}. When the LF wave is reduced in amplitude so that $D_{enh} \lesssim D_{in}$, we observe that the radial density profile does not flatten out, indicating improved plasma confinement.

The radial density scale length $q \equiv -(\nabla \ln n_i)^{-1}$, where $n_i \approx e^{-r/q}$, is a good parameter by which to characterize the shape of the density profile. As we calculate in Eq. (5.33),

q^* is a function of the magnitudes of the transport mechanisms, $q^* \equiv L_{eff}/\pi \left[D_{\perp eff} / (D_{\parallel in} (1+T_e/T_i)) \right]^{1/2}$ where $D_{\perp eff} = D_{\perp in} + D_{\perp ei} + D_{enh}(LF) + D_{enh}(HF)$, including enhanced diffusion. The measured q vs. the calculated q^* is shown in VI.23 for the case (a) of large amplitude waves. Note the density profile flattening near R = 5 cm indicated by the increase in scale length, which we propose is due to the LF wave presence. Fig. VI.24 is shown for the stable case (f) for comparison. No appreciable density profile flattening is observed or calculated.

The effect of enhanced transport on the density profile is to flatten the density profile when $D_{enh}(LF) \gtrsim D_{\perp in}, D_{\perp ei}$. This occurs at large radii ($R \gtrsim 4$cm) where the plasma density is approximately an order of magnitude below the density at small radii. Therefore, even an order of magnitude decrease in density at large radii, which we observe on wave stabilization, would only yield a corresponding increase in density of ~10% at small radii, due to improved confinement. For this reason we cannot reach any conclusions regarding density increases at small radii, due to wave stabilization at large radii.

Furthermore, one cannot exclude the possibility of altered axial particle currents, due to different axial boundary sheaths caused by the DC potentials. However, we observe small ($\lesssim 5\%$) or no changes in currents drawn to other end-rings when DC voltage is applied to a given end-ring electrode configuration. And when positive voltages are applied, only electrons are collected at the

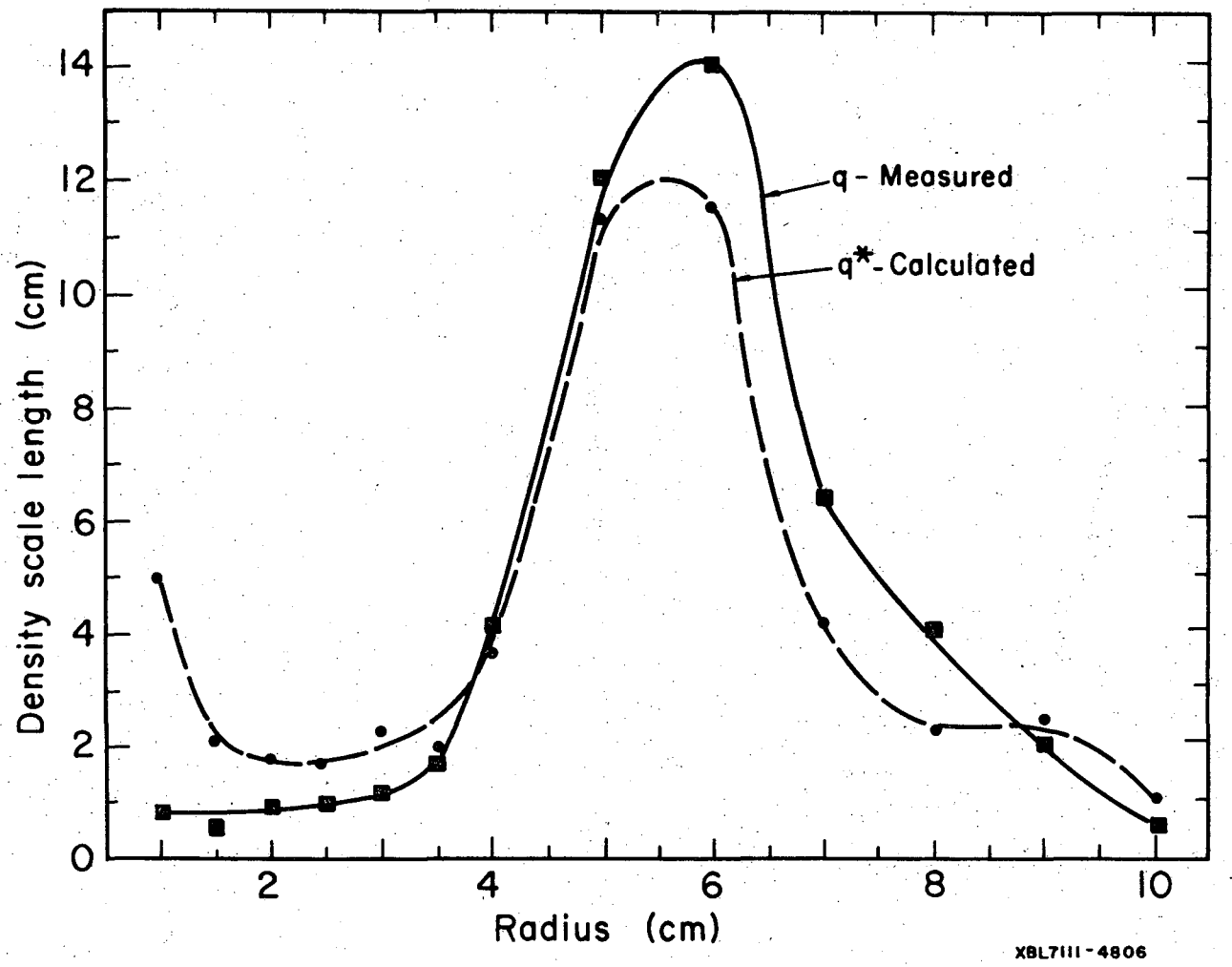

Fig. VI.23. Radial density scale length, q. Large amplitude LF wave present at large radii, corresponding to case (a). ■, measured q; ●, calculated q^*, showing significant flattening of density profile at large radii. p = 0.25 mtorr Ar, B = 580 G, end-rings grounded.

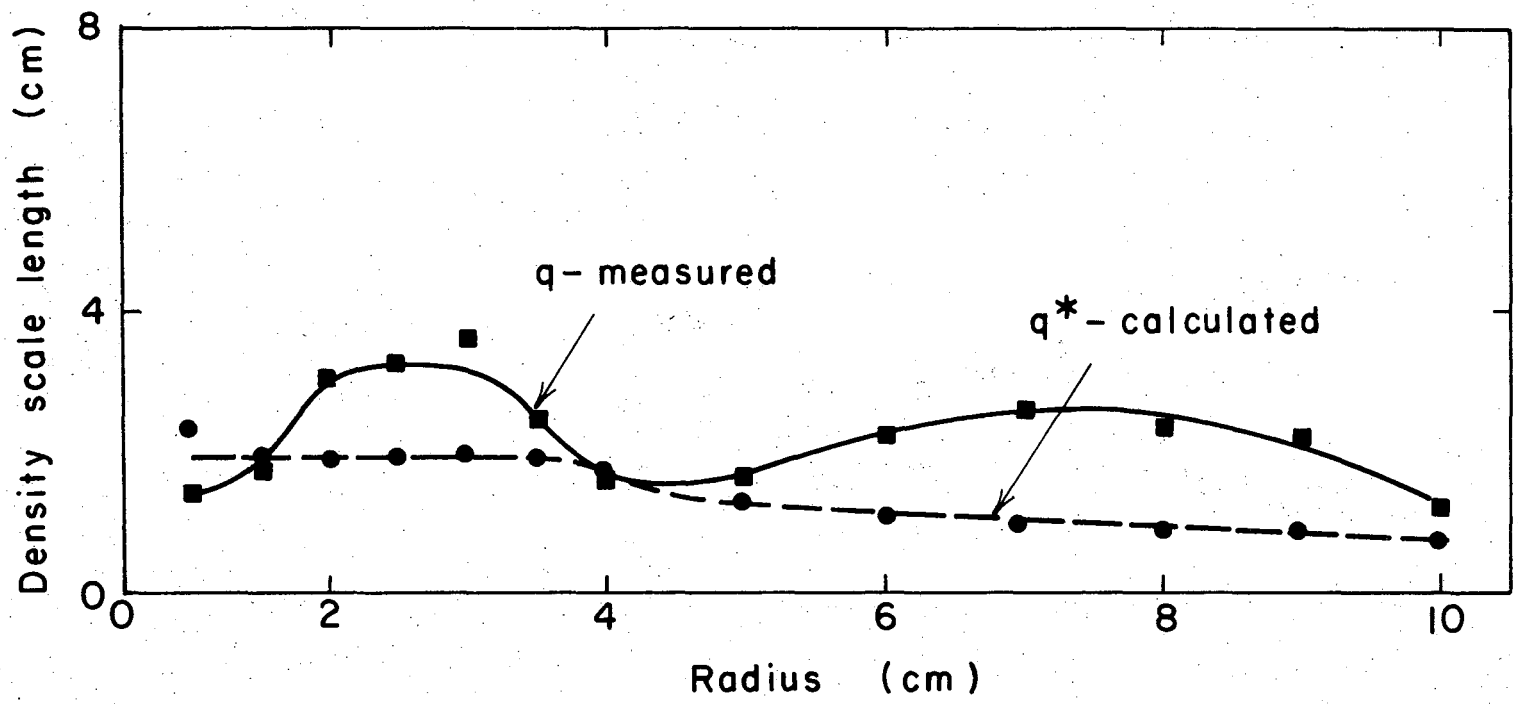

Fig. VI.24. Radial density scale length, q. LF wave stabilized corresponding to case (f). ■, measured q; ●, calculated q^*, showing steep density profile consistent with classical transport theory. p_t = 0.47 mtorr Ar, B = 580 G.

end-rings. The axial ion currents are still limited by axial ambipolar diffusion, Eq. (B.13).

We conclude that DC stabilization reduces enhanced transport due to the LF wave by more than two orders of magnitude, causing ion densities at large radii to decrease as much as an order of magnitude. In all cases, the shape of the radial density profile can be semi-quantitatively explained by including our expressions for D_{enh} in a simple diffusion theory.

D. Linear Feedback (F).

A linear feedback loop, as discussed in section III.D is employed. Linear feedback, F, is found to be more effective as a controlled electron sink when applied to the segmented end-ring electrodes (fig. III.2) than when applied to modified suppressor probes, 2-cm-long, .020 in. Tungsten wire electrodes, aligned along B. We propose that the increased effectiveness is due to the much larger area of the end-ring electrodes, Area = 6.0 cm^2. Only the inner two end-rings are quartered, unfortunately.

Linear feedback on any quarter of the inner end-ring is ineffective. Perhaps this can be explained by the fact that the wave power at small radii is too large. We estimate the wave power by considering the rate of electron collection to a feedback controlled sink, necessary for stabilization. The number of instability electrons in a feedback volume, V, is $n_1 V$, with an average energy, kT_e. If the instability were growing with the linear growth rate, γ, then wave energy would be increasing at the rate, 2γ. Using this model we estimate the power required to collect electrons

associated with the instability as, $P_{wave} = 2\gamma n_1 kT_e V$. The power in the HF wave corresponding to the inner end-ring is estimated to be ~30 watts. However, the power in the LF wave near the third end-ring is estimated to be ~0.1 watt, which can easily be supplied by the feedback loop.

The results of linear feedback on one quarter of the second end-ring will be presented. This suppressor segment extends from R = 2.0 cm to R = 3.5 cm, and subtends 90° in azimuth, $A_{suppressor} \approx 6.0\ cm^2$. "Negative" feedback (-F) occurs when the feedback voltage is in phase with the density fluctuations, hence supporting the theory of an electron sink.

When linear feedback is applied to any of the other quarters of the second end-ring, the phase of the feedback voltage with respect to the reference signal is shifted an amount appropriate to the azimuthal separation of the suppressor. The same phase relation between feedback voltage and density fluctuation is maintained.

The effect of different azimuthal separation of the suppressor probe with respect to the reference Langmuir probe monitoring the plasma is readily apparent. Since we measure and calculate $\gamma/\Omega_r \lesssim 1$ in section VI.G, the wave grows appreciably in one period. We observe the largest feedback effect on a probe located in the feedback region. Decreasing effect of feedback is observed 90°, 180°, and 270° downstream of the feedback, as the wave has time to grow or decay to its unperturbed amplitude. This is used

in section VI.G.1 to measure how fast the wave amplitude grows in a quarter period, 90^{o} downstream, from the feedback region.

Linear feedback parameters are summarized in Table VI.4.

Table VI.4. Linear feedback - Summary.

Case	Loop Gain, G	Volts (peak)	Power (watts)	Sink Term $\sigma \equiv \frac{S}{\rho_1}$ sec^{-1}	Comment
(a)	0	0	-----	0	NF - reference
(b)	-75	4.0	0.51	-1.25×10^{3}	Optimum -F
(c)	+75	5.0	0.88	$+1.66 \times 10^{3}$	+F
(d)	-25	2.5	0.088	-3.2×10^{2}	Intermediate gain
(e)	+25	3.0	0.11	$+3.1 \times 10^{2}$	Intermediate gain

1. Effect of Linear Feedback on Wave Amplitudes and Growth Rates.

We measure the effect of linear feedback on the wave amplitudes, and calculate the effect of linear feedback on the growth rate by including an ion sink term in the equation of continuity, Eq.(5.2). Quantitatively, when a sinusoidal feedback voltage, V_F, is applied to an end-ring electrode, an electron current, I_F, is drawn when V_F is sufficiently positive. We assume that a fraction, ($\tilde{n} = n_1/n_o$) of this current is coupled to the wave. Then for an effective ion sink over the feedback volume, V = Area(feedback electrode) x Length(system), we have (see section V.A.2), $S = I_F \rho_1/n_o ev = \sigma \rho_1$.

Fig. VI.25 shows the wave spectra for I_{si} on a Langmuir probe at R=3 cm, in the feedback region, for cases (a) to (e). We observe par-

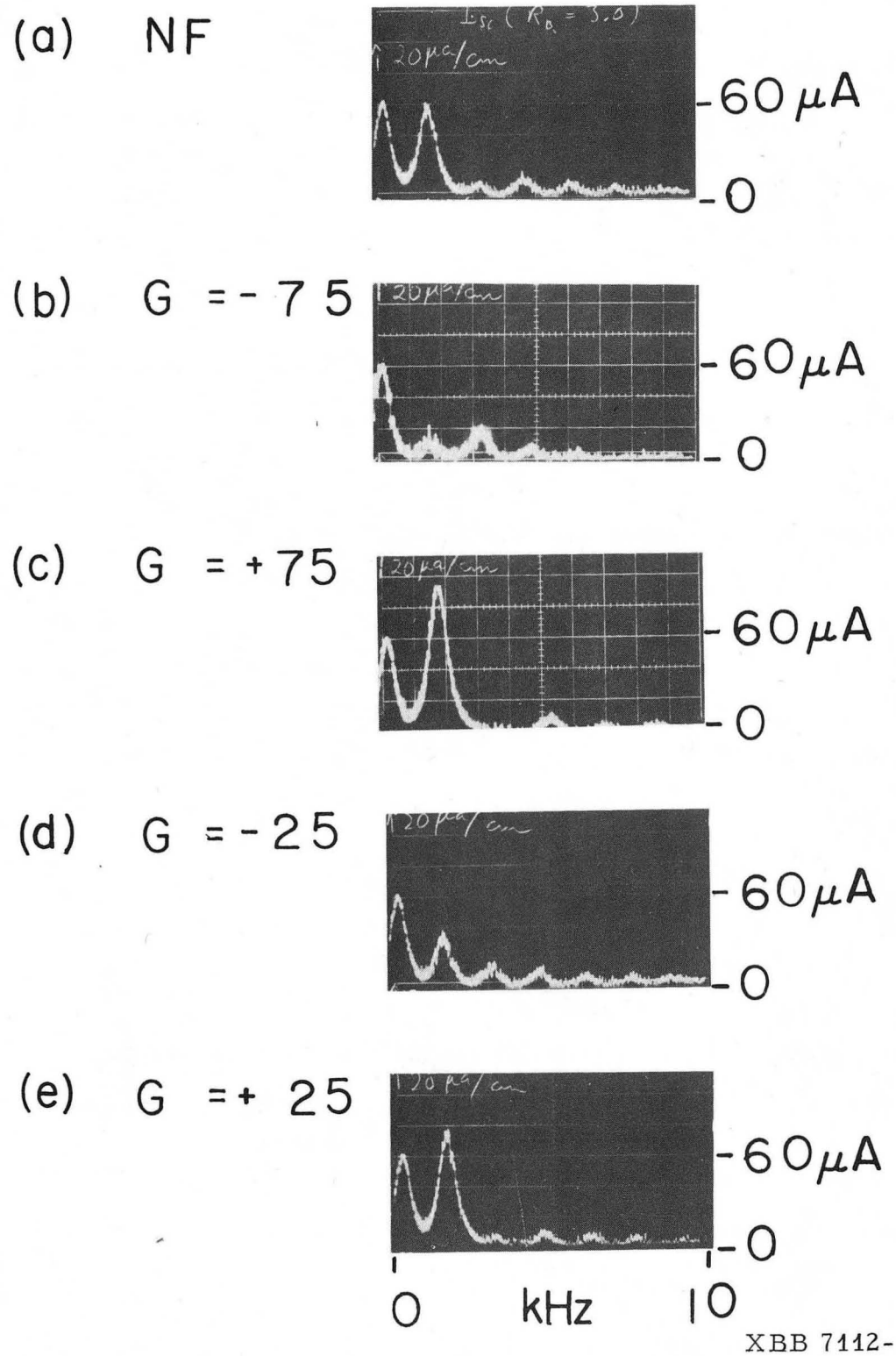

XBB 7112-6026

Fig. VI.25. Linear feedback wave spectra, ΔI, at R=3 cm. (a) No feedback, NF; (b) optimum negative feedback, gain G*= -75, showing near stabilization of LF≃1.8 kHz wave; (c) positive feedback, G= +75; (d) G= -25; and (e) G= +25. p_+=0.25 mtorr Ar, B=580 G.

tial reduction of wave amplitude, ΔI_{si}, at R=3 cm for small -F, case (d), and near stabilization for optimum -F, case (b). We observe corresponding increases in wave amplitude for +F, cases (c) and (e).

In figs. VI.26 to VI.28, the effect of linear feedback on the experimental wave amplitudes, and on the theoretical stability ratio, γ/Ω_r, is shown. Fig. VI.26, case (a), represents the case for no feedback, NF. Figs. VI.27, case (b), and VI.28, case (c), represent optimum negative and positive feedback, respectively. Optimum means maximum wave amplitude reduction, without enhancing the amplitude of higher azimuthal mode numbers. From fig. VI.27 we should observe that optimum -F reduces wave amplitude, while the wave is theoretically stabilized, $(\gamma/\Omega_r < 0)$. Positive feedback, fig. VI.28, increases the wave amplitude slightly, with a corresponding increase in γ/Ω_r.

Fig. VI.29, shows the effect of linear feedback on the normalized LF wave amplitude profile, $\tilde{n}$, as a function of loop gain, G, for cases (a) to (e). Only positive feedback, +F, and negative feedback, -F, will be considered since one cannot get much azimuthal phase resolution with a 90° suppressor. The calculated growth rate, section V.A.2, is shown in fig. VI.30, in the feedback region for cases (a) to (e).

From all the figures on wave amplitude and growth rate, we should notice that small -F, case (d), causes only small reductions in amplitudes and growth rates. Whereas optimum -F, case (b), causes order of magnitude reduction in wave amplitude and theore-

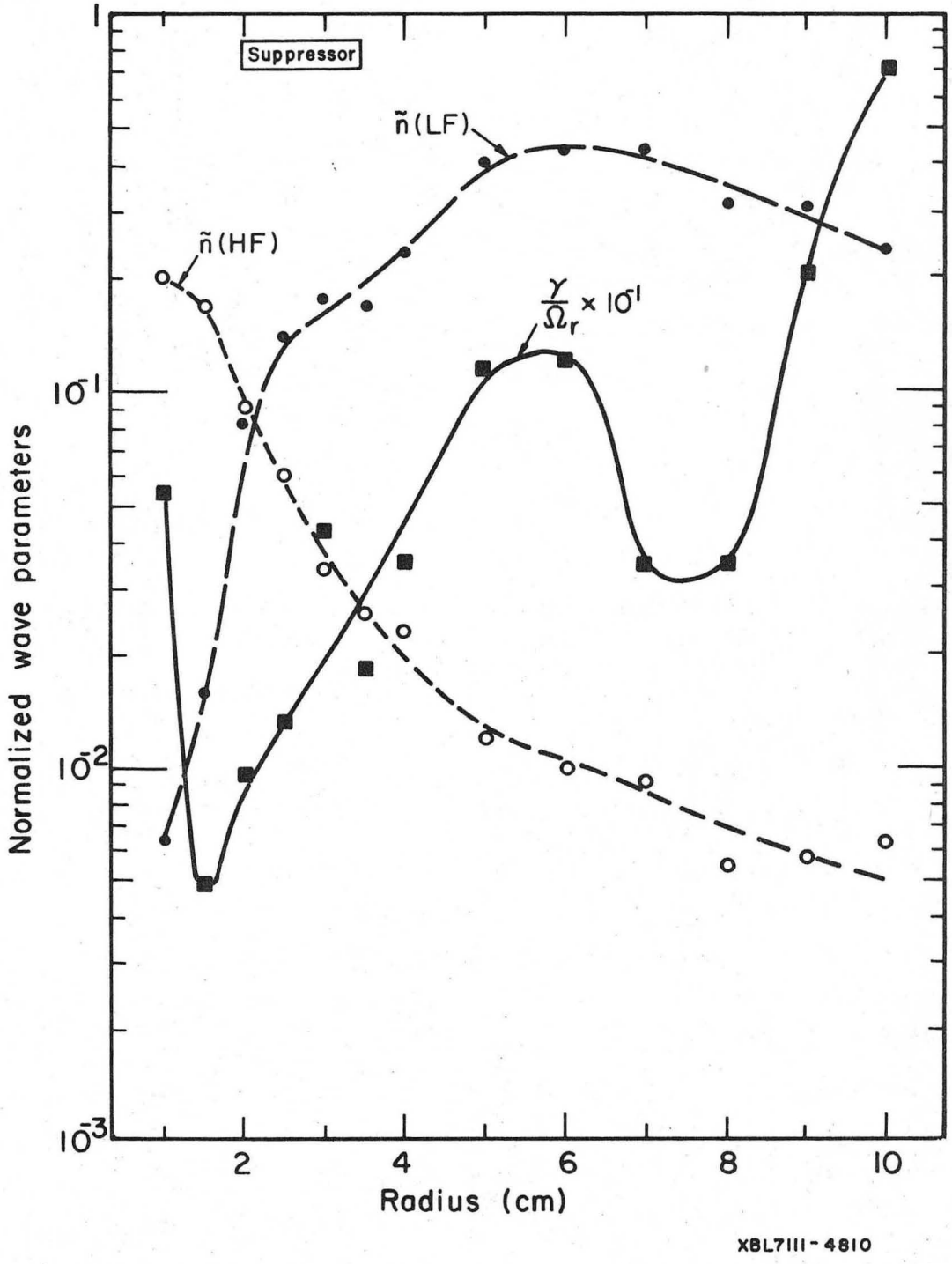

Fig. VI.26. Normalized wave parameters. No feedback. ■, stability ratio, $\gamma/\Omega_r \times 10^{-1}$; ●, $\tilde{n}$ (LF = 1.8 kHz); ◐, $\tilde{n}$ (HF = 36 kHz). p_t = 0.25 mtorr Ar, B = 580 G, end-rings grounded.

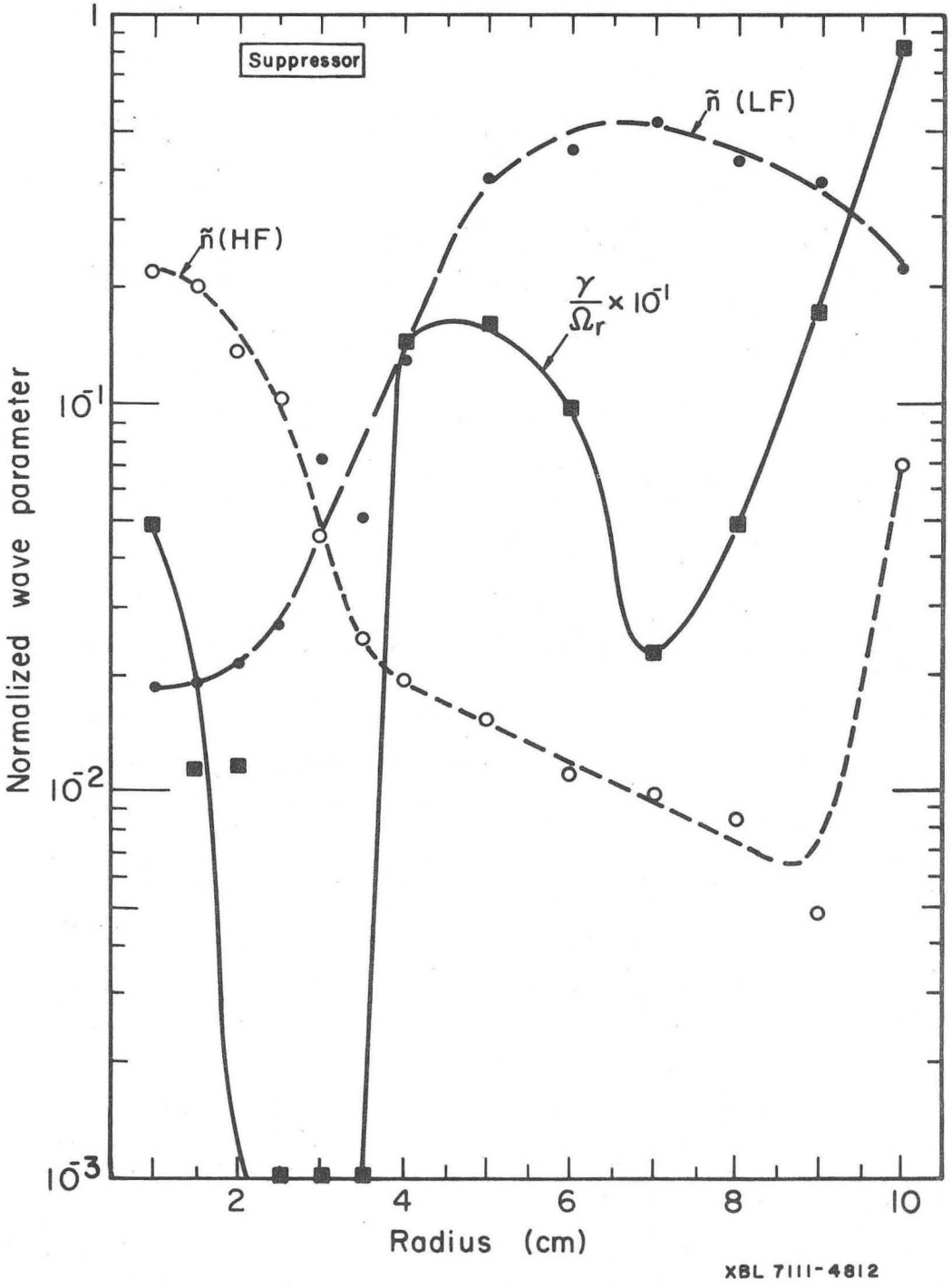

Fig. VI.27. Normalized wave parameters. Optimum negative feedback. ■, stability ratio, $\gamma/\Omega_r \times 10^{-1}$; ●, $\tilde{n}$ (LF); and ○, $\tilde{n}$ (HF). Feedback gain $G^* = -75$ and power $P_F = 0.51$ watts, showing LF wave amplitude reduction and theoretical stabilization, $\gamma/\Omega_r < 0$. Radial suppressor position is indicated. $p_t = 0.34$ mtorr Ar, B = 580 G.

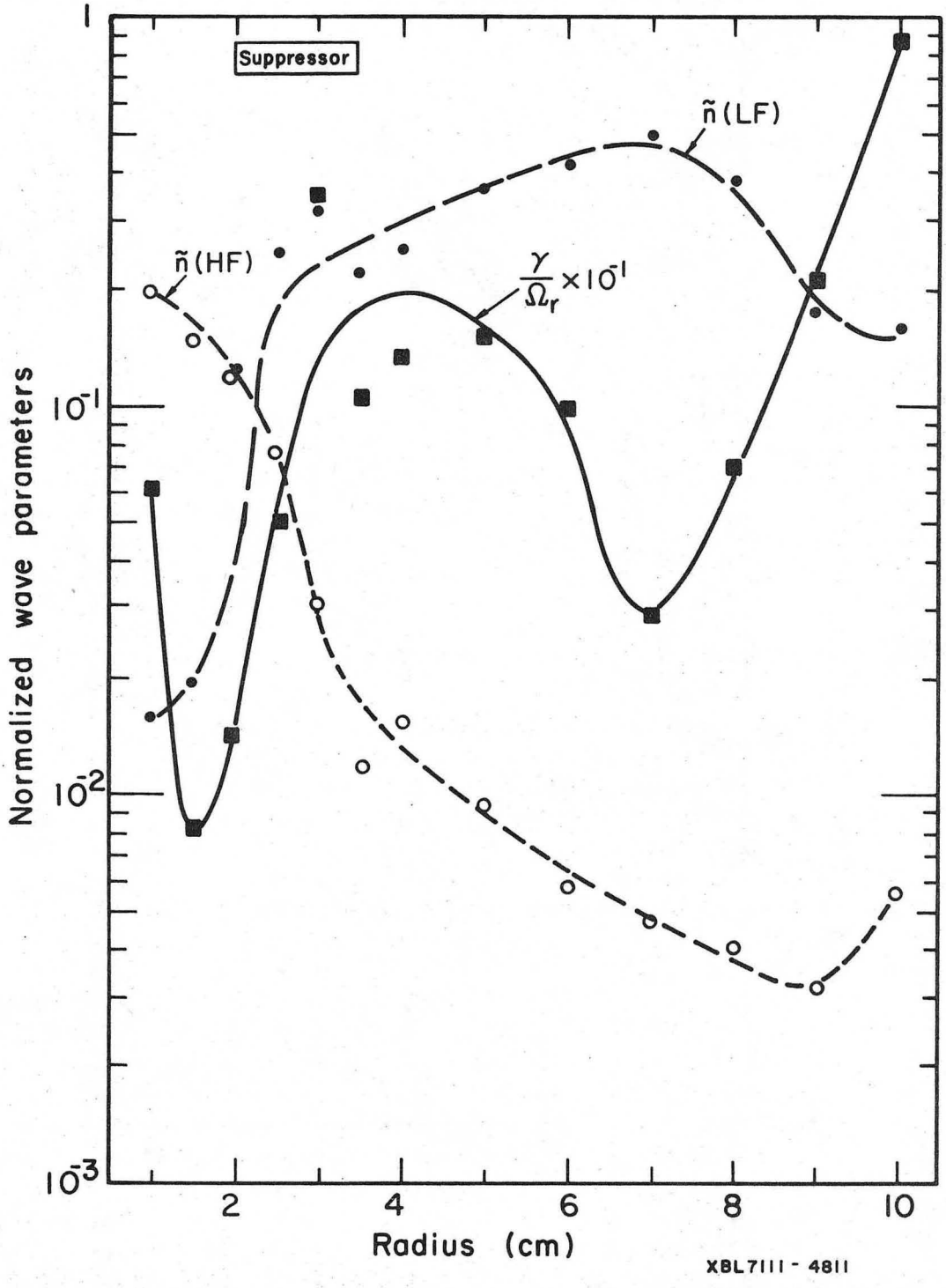

Fig. VI.28. Normalized wave parameters. Positive feedback. ■, stability ratio, γ/Ω_r x 10^{-1}; ●, $\tilde{n}$ (LF); and ○, $\tilde{n}$ (HF). Feedback gain G = +75 and power P_F = 0.88 watts, showing increased LF wave amplitude and growth rate. Radial suppressor position is indicated. p_t = 0.34 mtorr Ar, B = 580 G.

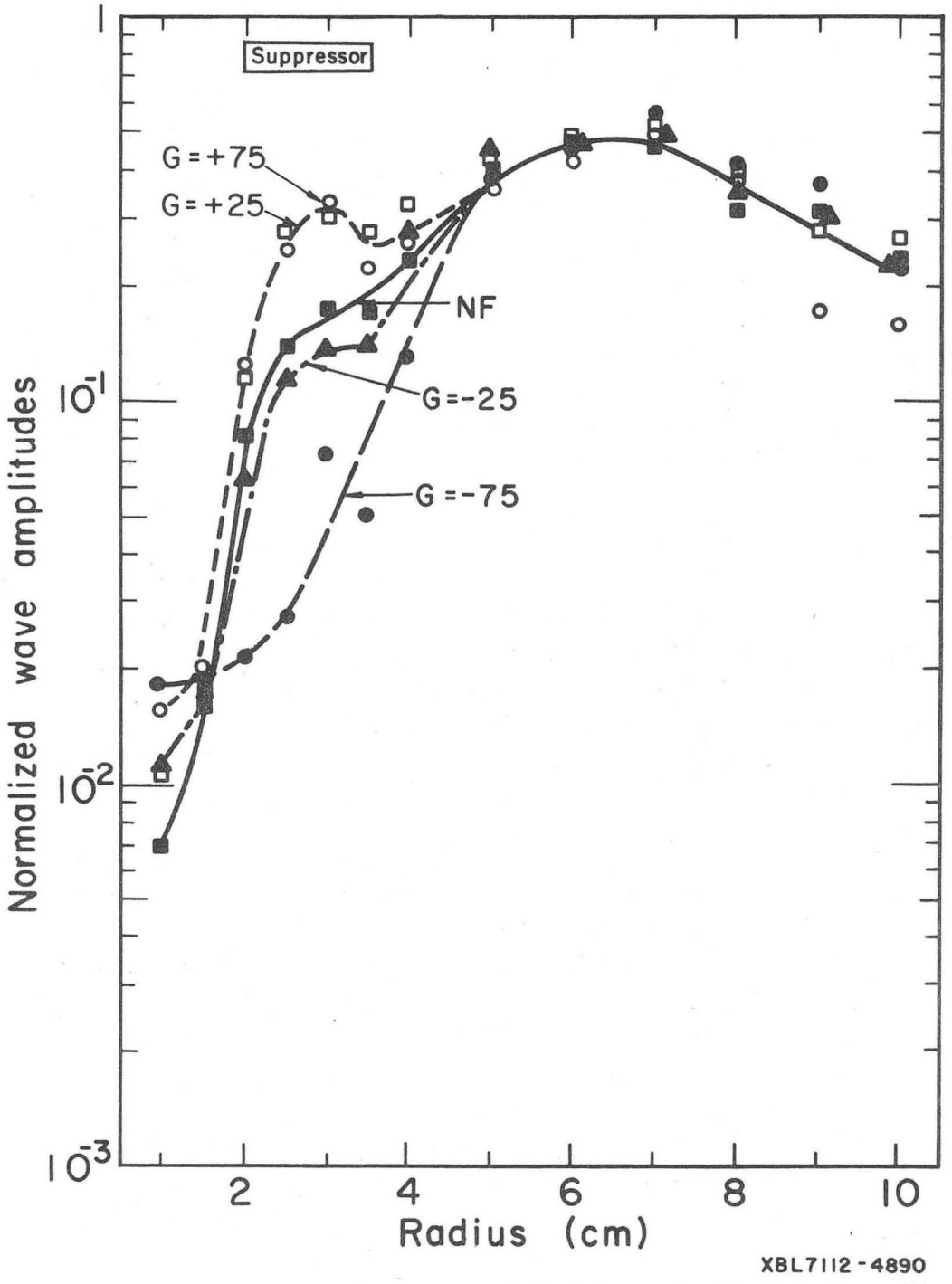

Fig. VI.29. Normalized LF wave amplitude vs. feedback gain. ■, No feedback, NF; ●, optimum negative feedback, gain G^{*} = -75, power P = 0.51 watts; ○, G = +75, P = 0.88 watts; ▲, G = -25, P = 0.088 watts; and □, G = +25, P = 0.11 watts. Note decreasing wave amplitude with increasing negative feedback power, and increasing amplitude for positive feedback. Radial suppressor position is indicated.

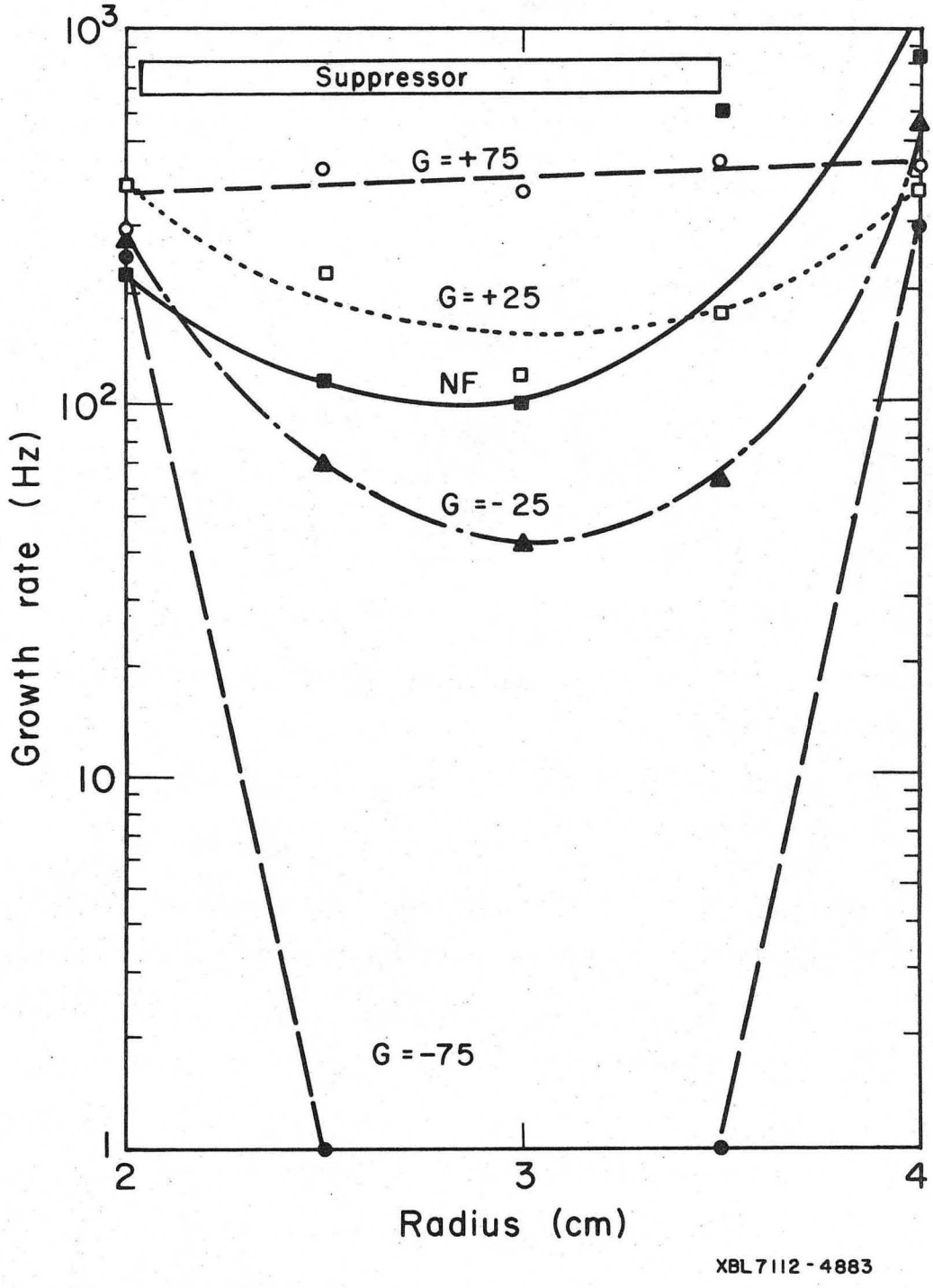

Fig. VI.30. Theoretical growth rate vs. feedback gain. ■, No feedback, NF; ●, optimum negative feedback, gain G*= -75, power P=0.51 watts; ○, G= +75, P=0.88 watts; ▲, G= -25, P=0.088 watts; □, G= +25, P=0.11 watts. Note theoretical stability, $\gamma<0$, for G*= -75, and increased growth rates for positive feedback. Radial suppressor position is indicated.

tical stabilization. Increasing amounts of -F drive the m = 2 mode unstable without further improvement for m = 1. Positive feedback seems to have similar effects for both cases (c) and (e) in increasing ΔI_{si} and γ .

2. Effect of Linear Feedback on Enhanced Transport and Density Profile.

The enhanced diffusion coefficients in the feedback region are presented in fig. VI.31. Observe that in the feedback region D_{enh} (LF) is on the order of classical diffusion. Hence, little or no effect is expected or observed on the radial density profile.

3. Linear Feedback Summary.

We have shown that quartered end-rings make very suitable suppressor electrodes for linear feedback loops. We have shown order of magnitude reductions in the LF wave amplitude, and wave enhanced convection. And we believe, as discussed in section VI.C.2, that wave enhanced convection explains semi-quantitatively the enhanced plasma loss associated with the flattening of the radial density profile. Further information regarding the effectiveness of feedback, or the effect of D_{enh} on n_i, is not expected to warrant setting up a linear feedback experiment at large radii.

E. AC Stabilization

AC stabilization means that a rectangular pulse signal is applied, the duration and frequency of which can be varied. AC stabilization can be applied to any end-ring electrode configuration by using the switching circuit discussed in section III.E. There is no phase relation between the wave signal and the AC pulse signal. We merely

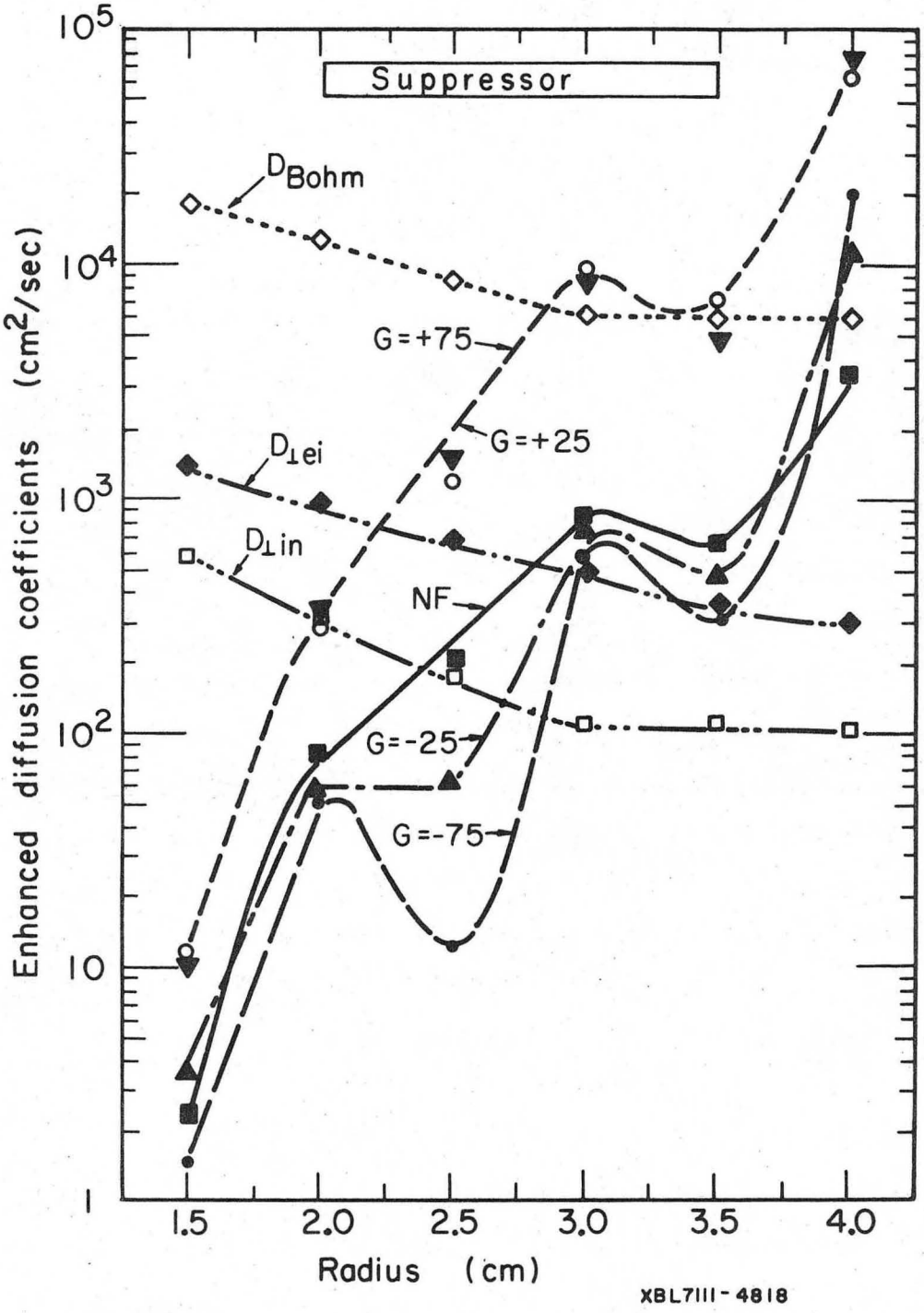

Fig. VI.31. Enhanced diffusion coefficients vs. feedback gain. ■, No feedback, NF; ●, G*= -75, P=0.51 watts; ○, G= +75, P=0.88 watts; ▲, G= -25, P=0.088 watts; ▼, G= +25, P=0.11 watts; □, $D_{\perp in}$; ◆, $D_{\perp ei}$; and ◇, D_{Bohm}. Note that in the suppressor region enhanced diffusion is comparable to classical diffusion.

wish to see if lower power levels might be required than for DC stabilization. For example, this might be the case if what is actually needed is a large enough voltage to draw electrons, but only for a time long enough to extract sufficient charge. We hope to change the plasma parameters, the electric field in particular, to a lesser extent than does DC stabilization.

AC stabilization will be labelled by the electrode voltage, V_{AC}, frequency, f_{AC}, duty ratio, DR, and power P_{AC}. (Suppressor voltages are shown in the lower oscilloscope traces of fig VI.36. The suppressor voltage is not equal to the power supply voltage due to a 10 ohm resistor, through which the current is measured).

1. Effect of AC Stabilization on Wave Amplitude, Enhanced Convection, and Density Profile.

The six cases of AC Stabilization to be studied are labelled and summarized in Table VI.5.

In case (e) the LF wave was reduced in amplitude sufficiently ($\tilde{n} \lesssim 0.01$) that it could not be reliably measured. End-rings 2 and 3 serve as suppressor electrodes here, extending from R = 2 cm to R = 5.5 cm, as indicated in figs. VI.33 and VI.34. Cases (a) to (f) are arranged in order of increasing power.

The wave spectra for the cases (a) to (f) are shown in VI.32, for 0 to 10 kHz. We observe that the LF (~2 kHz) wave amplitude decreases as we increase the power. The fact that the LF wave is

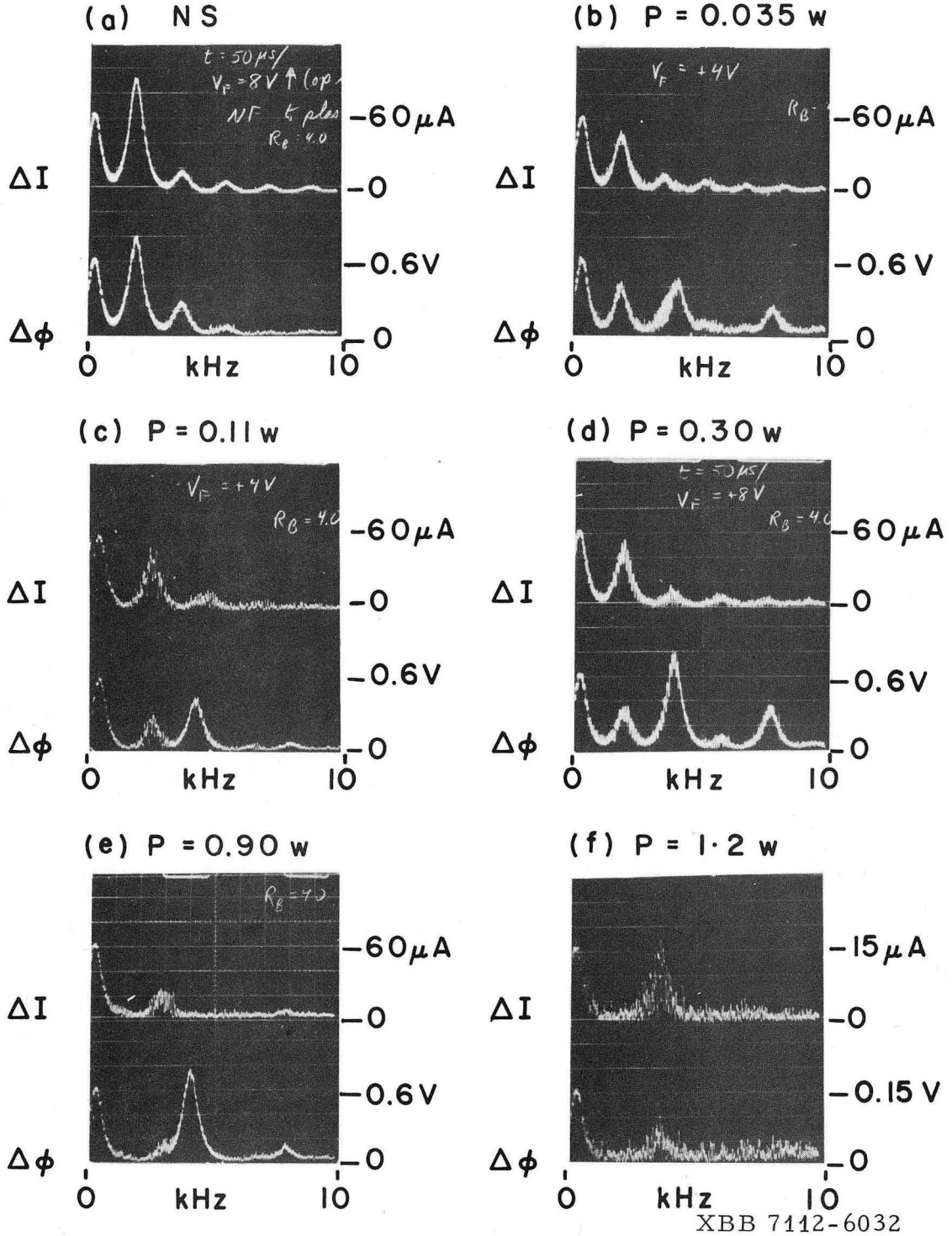

Fig. VI.32. AC stabilization wave spectra at R=4 cm. Upper trace shows rms ion current fluctuations, ΔI, while lower trace shows potential fluctuations, $\Delta\phi$. AC frequency f=4 kHz. (a) No stabilization, NS; (b) power P=0.035 watts; (c) P=0.11 watts; (d) P=0.30 watts, showing increasing potential fluctuation at f=4 kHz; (e) P=0.90 watts, which is sufficient to stabilize the LF wave; and (f) P=1.2 watts, showing DC stabilization for comparison.

Table VI.5. AC Stabilization - Summary

Case	Voltage, V_{AC}(volts)	Frequency, f_{AC}(kHz)	Duty Ratio, DR	Power P_{AC}(watts)	Comment
(a)	---	---	---	---	NS-reference
(b)	3.5	4.0	0.2	0.035	
(c)	3.5	4.0	0.6	0.11	
(d)	5.0	4.0	0.2	0.30	Increase V_{AC}
(e)	5.0	4.0	0.6	0.90	LF wave stable
(f)	5.8	---	1.0	1.2	DC feedback

not stabilized until case (e) shows that power $P \simeq 1$ watt is required. A potential oscillation at an arbitrary AC frequency ($f_{AC} = 4.0$ kHz) is observed to increase in amplitude with AC power. It is significant, however, that there is no measurable density fluctuation at f_{AC}, so that there is no externally induced contribution to enhanced convection.

The normalized LF wave amplitude profiles, $\tilde{n}$, are presented in fig. VI.33 for cases (a) through (f). Again we observe the wave amplitude decreasing as the power increases. The critical power level is $P_{AC} \approx 1$ watt, which is comparable to that required for linear feedback as well as for DC stabilization.

The effect of AC stabilization on the radial density profile can be seen in fig. VI.34 for cases (a) through (f). The density profile steepens with increasing power, indicating improved confinement. We observe that the density at large radii decreases by perhaps a factor of 2 to 3, as AC power ~1 watt is applied. As discussed in section VI.C.2, we venture no conclusions on density at small radii.

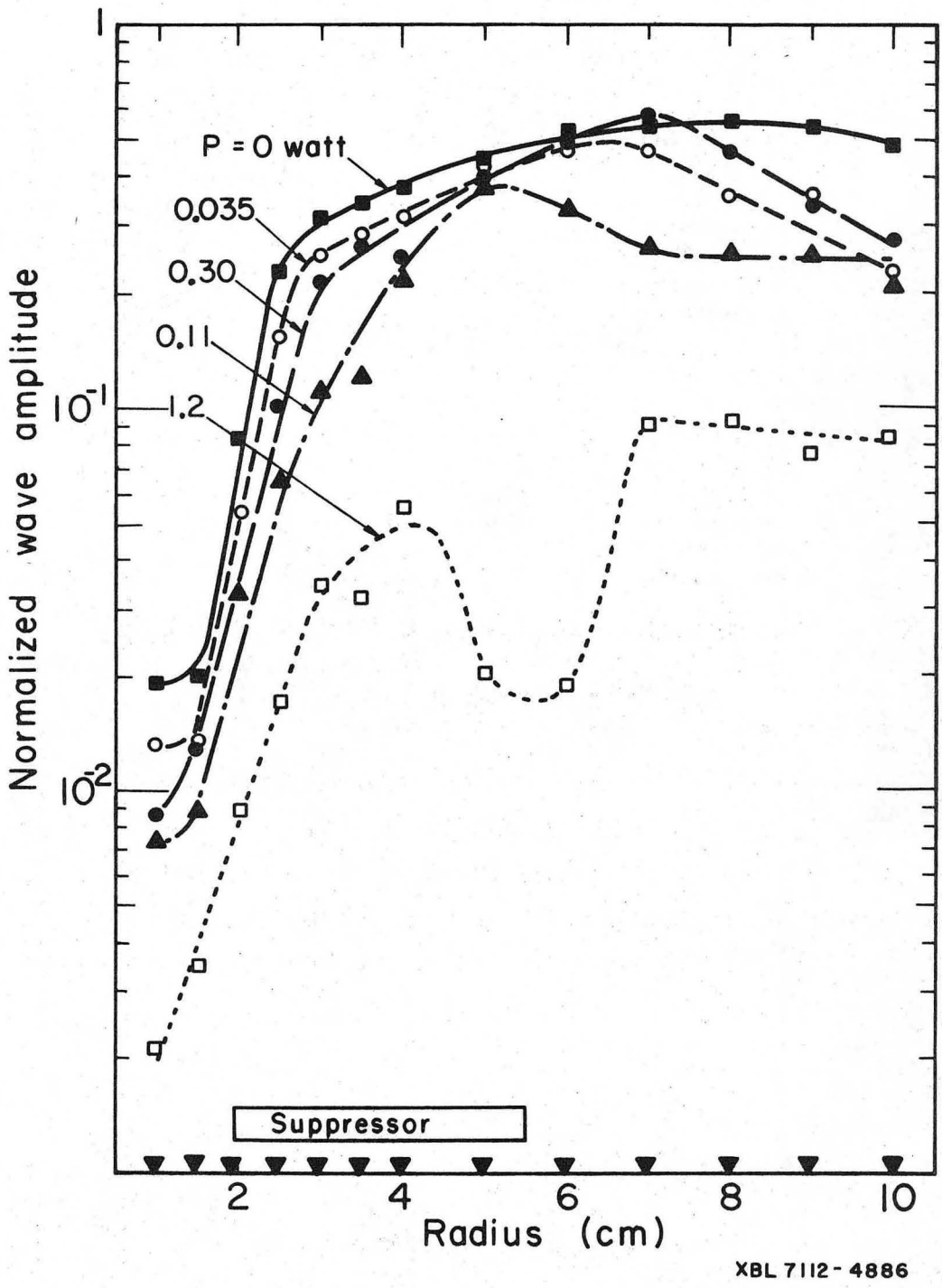

Fig. VI.33. Normalized wave amplitude vs. AC stabilization power for cases (a) thru (f). ■, No stabilization; ○, Power P_{AC}=0.035 watts; ▲, P_{AC}= 0.11 watts; ●, P_{AC}=0.30 watts; ▼, P_{AC}=0.90 watts, sufficient to stabilize the LF wave; and □, P_{DC}=1.2 watts, showing DC stabilization for comparison. Radial suppressor position is indicated.

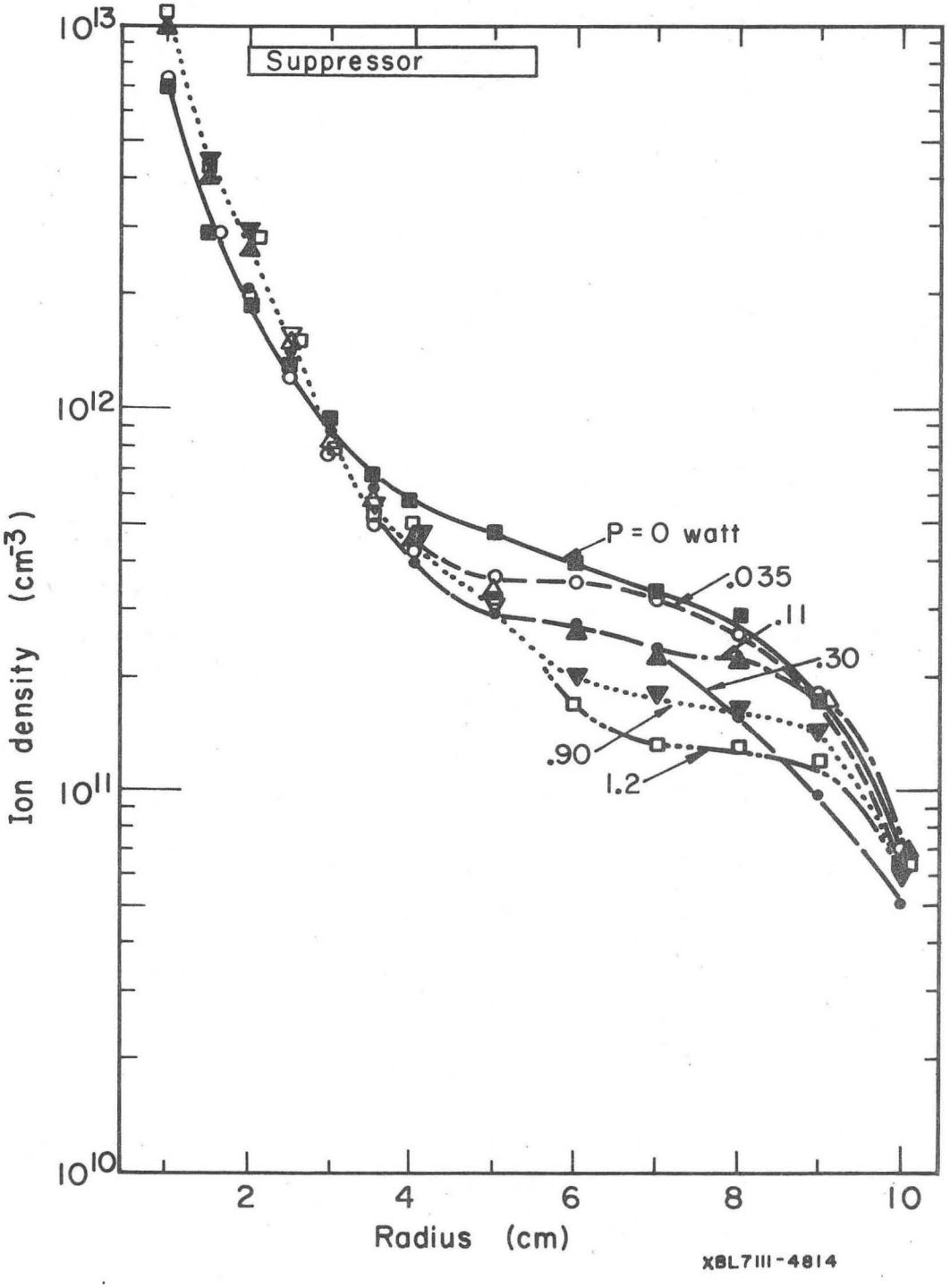

Fig. VI.34. Radial density profile vs. AC stabilization power for cases (a) thru (f). ■, No stabilization; ○, power P_{AC}=0.035 watts; ▲, P_{AC}=0.11 watts; ●, P_{AC}=0.30 watts; ▼, P_{AC}=0.90 watts; and □, P_{DC}=1.2 watts. Radial suppressor position is indicated. Note steepening of density profile with increasing power.

The density profile shape can be explained semi-quantitatively by the change in the enhanced diffusion coefficient (see section VI.C.2).

AC stabilization does not change the radial electric field so drastically as does DC stabilization. Changes in E_r due to AC stabilization were in fact small enough as to make any conclusive statements regarding the effect on E_r difficult, if not unjustifiable. The E_r profiles for cases (a) to (f) are presented in fig. VI.35, for the reader to draw his own conclusions.

2. AC Stabilization - A Pictorial Survey.

A more complete pictorial attempt is made to show the effects of AC power, P_{AC}, frequency, f_{AC}, and duty ratio, DR, on the wave amplitudes, ΔI_{si} and $\Delta\varphi_f$ at R = 4 cm. In the oscillographs presented in fig. VI.36, the upper two traces are the LF wave spectra from the I_{si} and φ_f probe signals, 0 to 10 kHz. The lower trace shows the AC voltage vs. time. No complete profiles were taken here. The cases presented in fig. VI.36 are summarized in Table VI.6.

We observe similar dependence of wave amplitude on power as in section VI.E.1. However, in fig. VI.36, case(g), we observe that excessive DC voltage can cause a new mode to destabilize as noted previously in section VI.C.1, case (f). This mode appears in regions of large electric field shear, caused by large changes in the radial potential profile.

Finally, comparison of cases (b), (h), and (i), all for power P_{AC} = 0.11 watts, shows us no significant change in stabilization effectiveness for AC frequencies from f_{AC} = 4 to 20 kHz.

3. AC Stabilization - Summary.

AC stabilization, described as application of a rectangular pulse

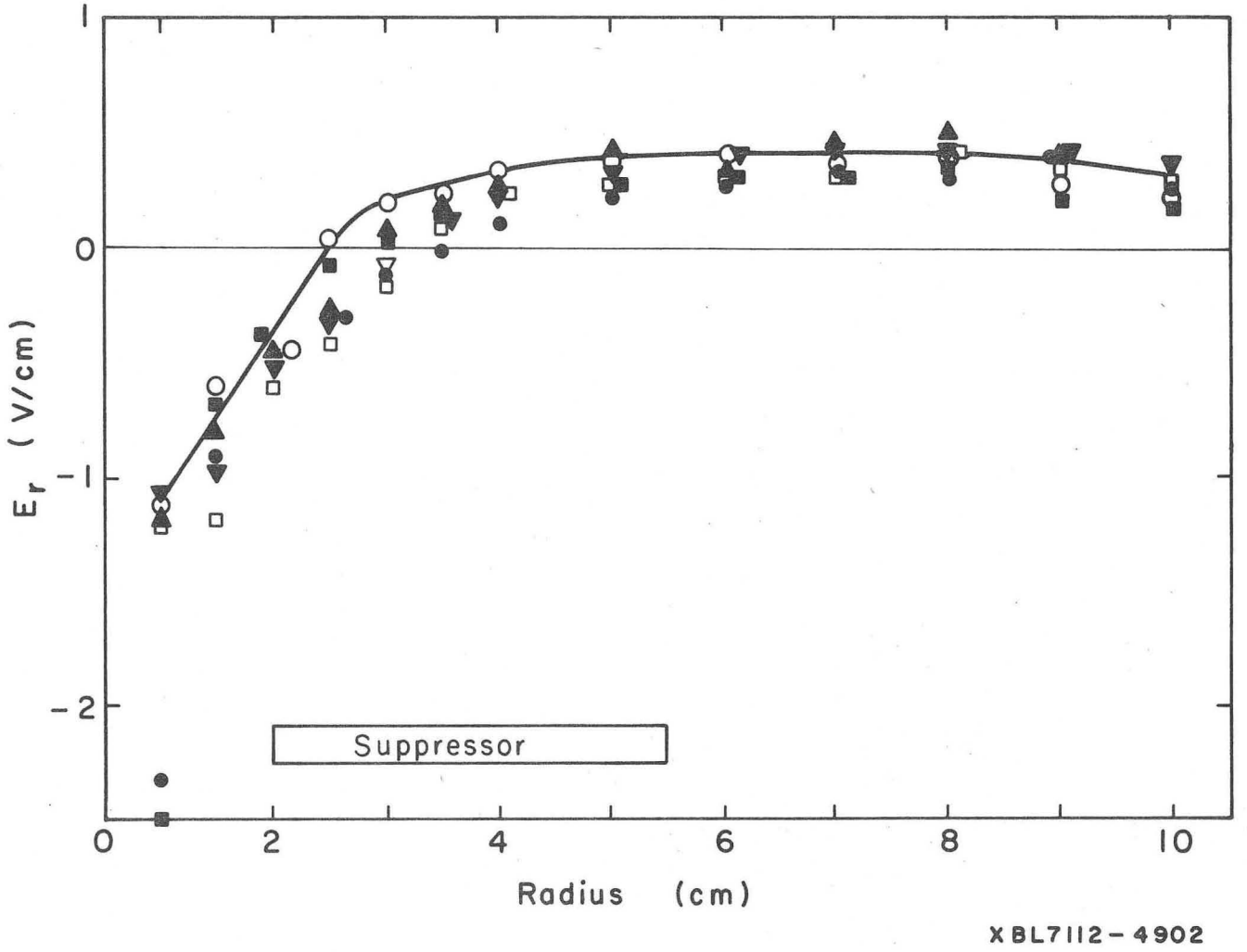

Fig. VI.35. Radial electric field vs. AC stabilization power. ■, No stabilization; ○, power P_{AC}=0.035 watts; ▲, P_{AC}=0.11 watts; ●, P_{AC}=0.30 watts; ▼, P_{AC}=0.90 watts; and □, P_{DC}=1.2 watts. Radial suppressor position is indicated.

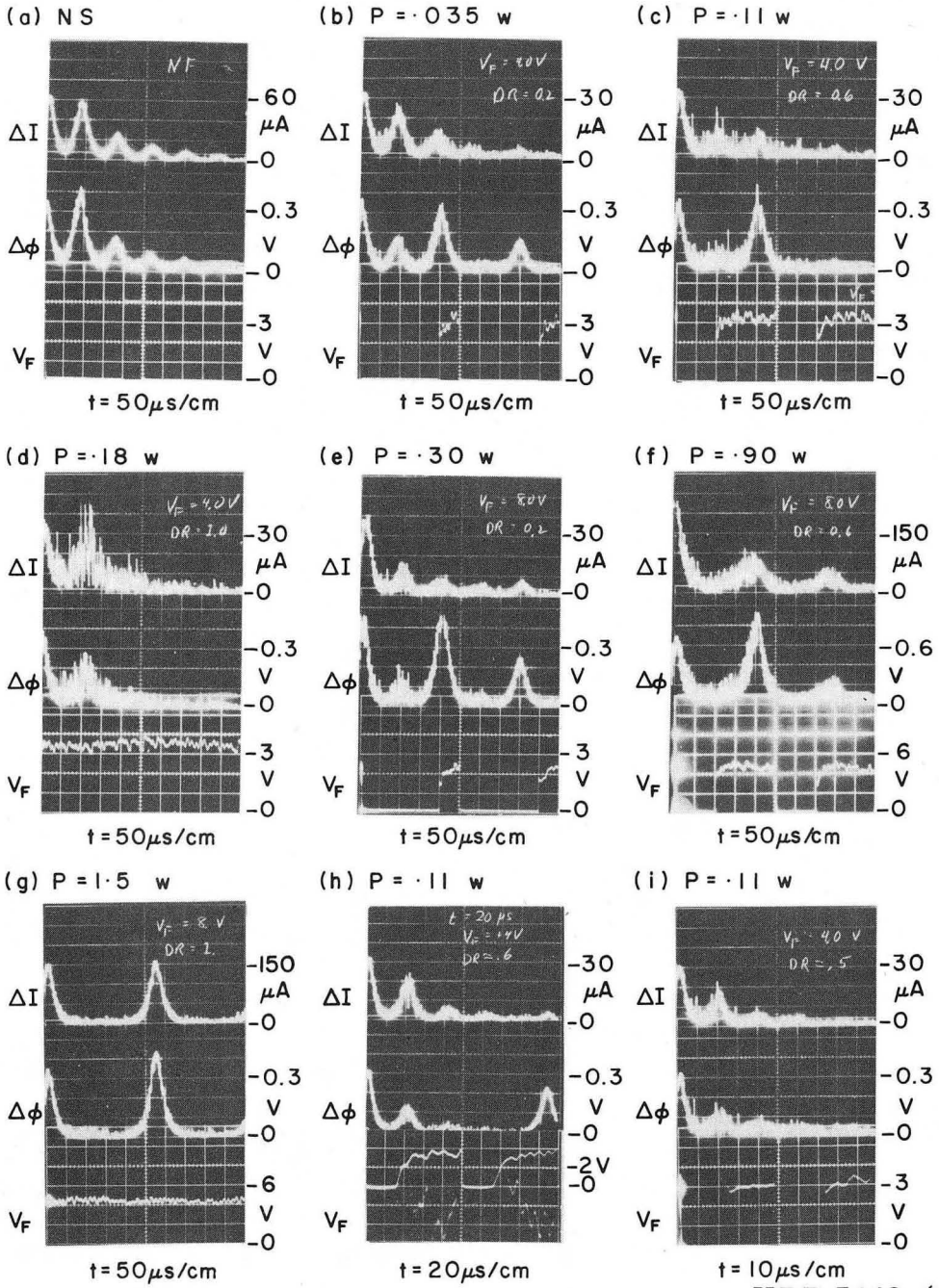

XBB 7112-6030

Fig. VI.36. AC stabilization wave spectra at R=4 cm. Upper trace is ion current fluctuation, ΔI, 0 to 10 kHz; middle trace is potential fluctuation, Δφ, 0 to 10 kHz; and the lower trace is the AC voltage signal on the indicated time scale. (a) No stabilization, NS; (b) power P=0.035 watts, AC frequency f=4 kHz; (c) P=0.11 watts, f=4 kHz; (d) P=0.18 watts, DC stabilization; (e) P=0.30 watts, f=4 kHz; (f) P=0.90 watts, f=4 kHz, sufficient to stabilize the LF wave; (g) P=1.5 watts, DC stabilization; (h) P=0.11 watts, f=9.4 kHz; and (i) P=0.11 watts, f=20 kHz.

Table VI.6. Effects of P_{AC}, DR, and f_{AC} on Wave Amplitudes.

Case	Voltage V_{AC}(volts)	Frequency, f_{AC}(kHz)	Duty Ratio DR	Power P_{AC}(watts)	Comment
(a)	---	----	---	-----	NS-reference
(b)	3.5	4.0	0.2	0.035	
(c)	3.5	4.0	0.6	0.11	
(d)	3.5	----	1.0	0.18	DC
(e)	5.0	4.0	0.2	0.30	
(f)	5.0	4.0	0.6	0.90	
(g)	5.0	----	1.0	1.5	DC
(h)	3.5	9.4	0.6	0.11	Increase f_{AC}
(i)	3.5	20.0	0.6	0.11	Increase f_{AC}

signal at a frequency $f_{AC} \tilde{>} \omega_r$, is effective in reducing the LF wave amplitude, which in turn leads to significant reduction of the enhanced diffusion coefficient. The resulting steepening of the radial density profile is observed with increasing power, indicating enhanced plasma confinement. Power levels of less than 1 watt are required for effective stabilization of the LF wave, with LF wave power in the region of the third end-ring estimated to be ~.1 watt.

AC stabilization was attempted to see if power requirements could be reduced from those of DC stabilization. The answer, so far as we can determine, would appear to be no; that power level, rather than voltage, duty ratio, or frequency is the critical parameter. Insufficient power leads to incomplete stabilization, while excessive power leads to increased potential fluctuations at the AC frequency, and possibly to velocity-shear instabilities.

We plot normalized wave amplitude vs. power for all three stabilization techniques in fig. VI.37 and observe that wave amplitude decreases with increasing power, and becomes stable in all cases for power levels $P \gtrsim 1$ watt. We explain this effect for linear feedback by means of a controlled electron sink. However, we are at a loss to explain why similar power levels are required for AC and DC stabilization techniques.

AC stabilization also has a much smaller effect on the radial electric field than does DC stabilization. Therefore, ion mobility in the radial electric field is still important, and the change in the shape of the radial density profile is more directly correlated with enhanced transport due to the LF wave.

AC stabilization will be shown to be a useful diagnostic method with which to measure the growth rate, γ/Ω_r, directly, in section VI.G.2.

F. Effect of Collisions on the Growth Rate.

1. Varying the Collision Frequency in the Dispersion Relation.

Collisions with neutrals have been included in the dispersion relation for the rotational instability, section V.A.2. By varying the collision frequency only, we can study the effect of collisions on the growth rate, γ. The effect of collsions on γ, as calculated from the dispersion relation, is presented in fig. VI.38, for 3 cases: (a) no collisions, $\nu_{in} = 0$; (b) normal collision frequency as calculated from the plasma parameters, $\nu_{in} = n_o \nu_{th}^i \sigma_{in}$; and (c) $\nu_{in} = 5 \times \nu_{in}$. The most important result to notice is that

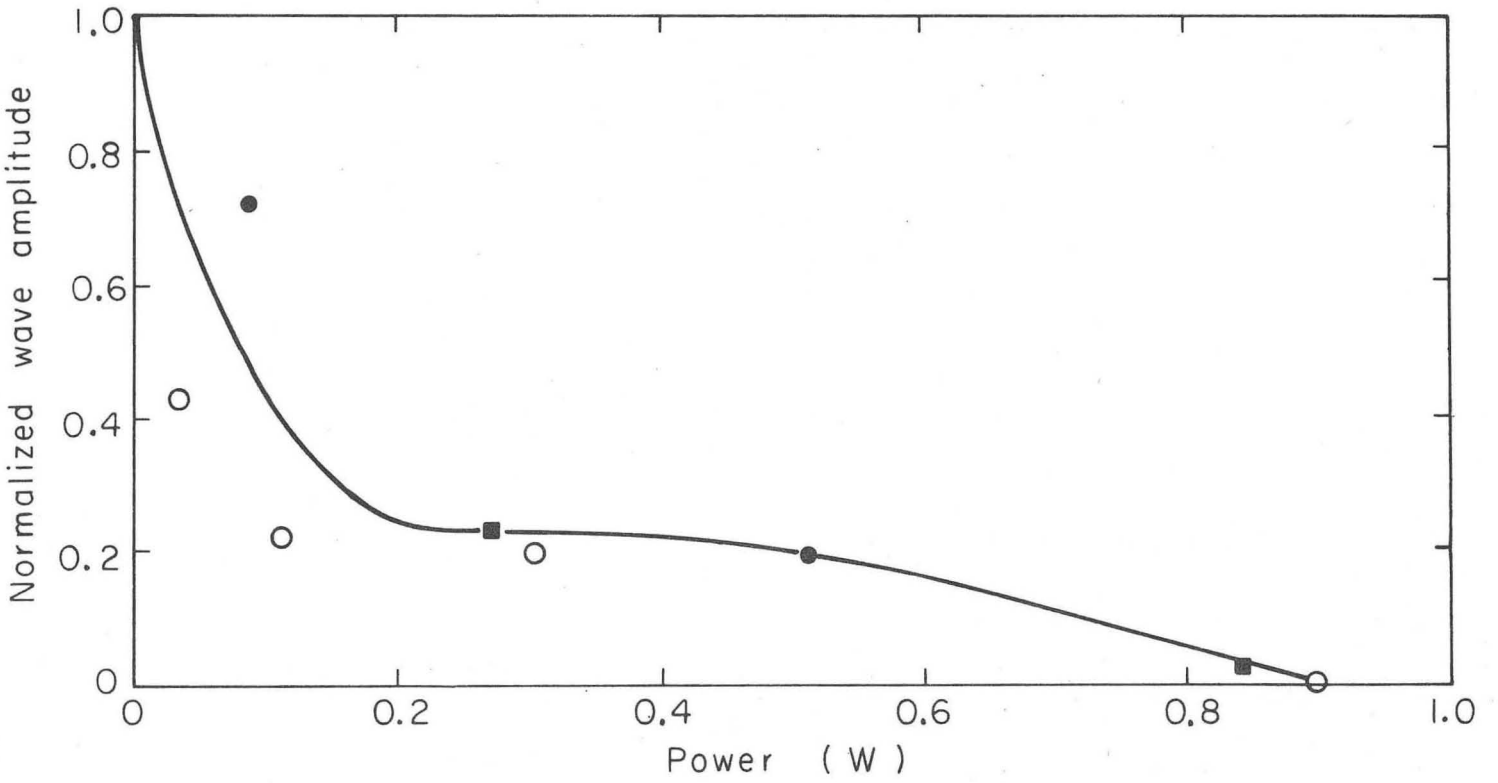

X BL 7112-4904

Fig. VI.37. Normalized ion current fluctuations vs. power. ■, DC stabilization; ●, linear feedback; and **O**, AC stabilization.

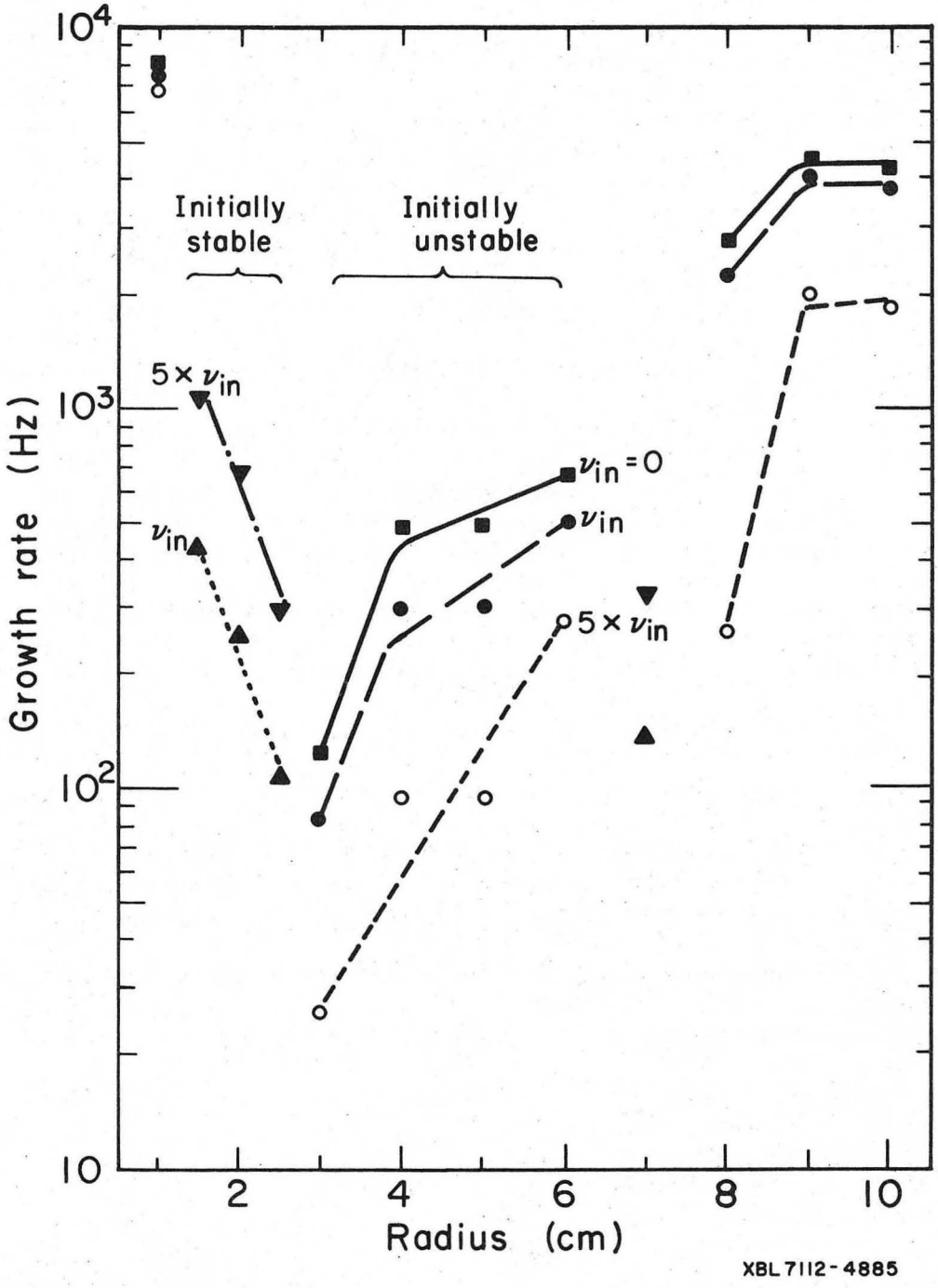

Fig. VI.38. Effect of neutral collision frequency in the dispersion relation [Eq. (5.18)] on the theoretical growth rate, γ. ■, No collisions, $\nu_{in}=0$, showing stability from R=1.5 to 2.5 cm; ●, ▲, collision frequency, $\nu_{in}=n_o v^i_{th\ in}\sigma$, and ○, ▼, $\nu_{in}=5 \times \nu_{in}$, increase the collision frequency by a factor of 5. Collisions are stabilizing for roots which are initially unstable. p_t=0.32 mtorr Ar, B=580 G.

collsions are stabilizing for roots which are initially unstable without collisions. We also observe that collisions are destabilizing for roots which are initially stable, in the absence of collisions.

2. Varying the Neutral Gas Pressure Experimentally.

We can experimentally study the effect of collisions on γ, by varying the neutral gas pressure in the tank, p_t. This has the effect of changing the plasma parameters, E_r in particular. The resulting theoretical growth rate, γ, calculated from the dispersion relation, Eq. (5.18), using experimental plasma profiles is shown in fig. VI.39 as a function of p_t. We observe that as the wave is stabilized, the theoretical growth rate fluctuates more as a function of radius. This is due to the fact that the wave stabilizing and destabilizing forces are more nearly balanced. Wave stability is therefore more sensitive to variations in plasma conditions, than when a single destabilizing mechanism dominates.

The LF wave near R = 5 cm is stabilized as the tank pressure is increased, whereas the HF wave near R = 1 cm is relatively unaffected. As previously mentioned, this stabilization can be in part attributed to the change in E_r with pressure. The E_r, corresponding to the three cases presented in fig. VI.39 for γ, are shown in fig. VI.40. We observe that E_r at small radii is only slightly decreased, while E_r at large radii can effectively be eliminated by collisions. This explains in part why the LF wave is more easily stabilized by collisions than the HF wave.

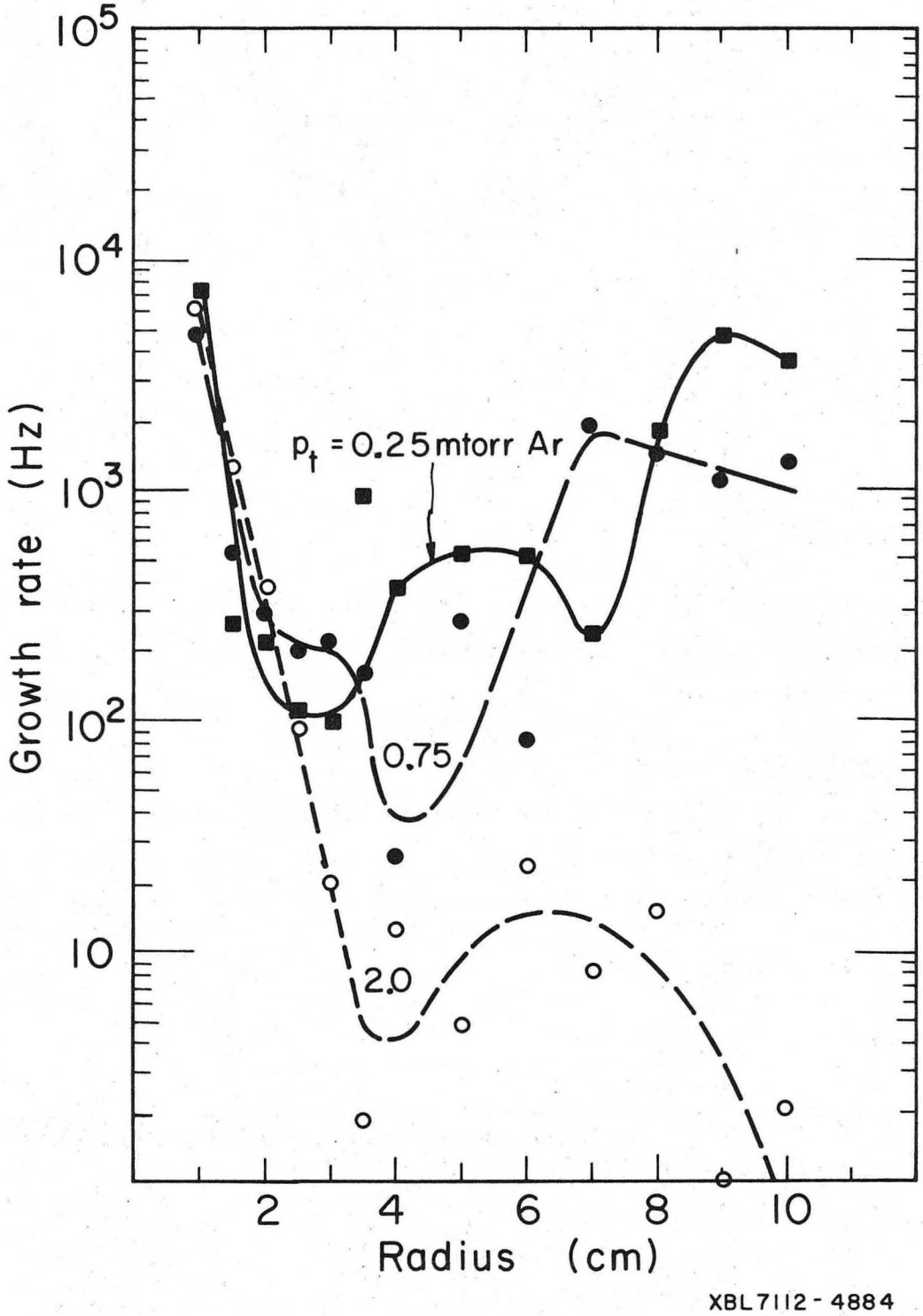

Fig. VI.39. Effect of neutral gas pressure in the tank, p_t, on the theoretical growth rate. ■, p_t=0.25 mtorr Ar; ●, p_t=0.75 mtorr Ar; and ○, p_t=2.0 mtorr Ar. Neutral gas pressure is stabilizing.

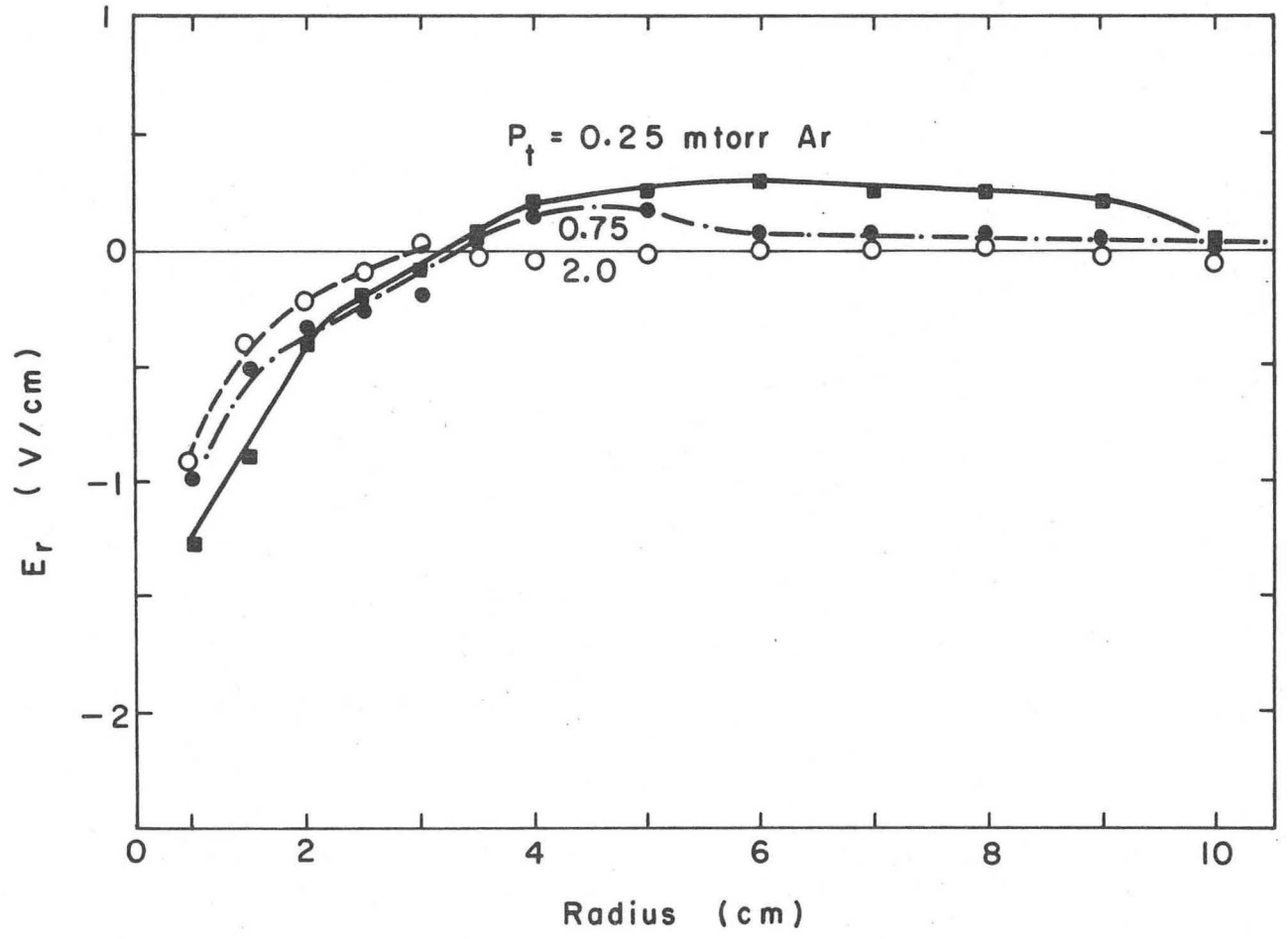

XBL7112-4901

Fig. VI.40. Effect of neutral gas pressure, p_t, on the radial electric field. ■, p_t=0.25 mtorr Ar; ●, p_t=0.75 mtorr Ar; and **o**, p_t=2.0 mtorr Ar. The radial electric field decreases with increasing neutral gas pressure.

G. Direct Measurement of Growth Rate, γ/Ω_r.

1. Azimuthal Growth Measurement.

Two methods are attempted to measure γ/Ω_r directly for the LF wave. The first method involves applying positive, +F, and negative, -F, linear feedback on the upper quarter of the second end-ring as a suppressor electrode, and then monitoring the wave amplitude on probes which are separated in azimuth by 90°. If -F is employed, we measure how large the wave has grown 90° azimuthally after feedback. And for +F, the decay rate is measured. In fig. VI.41, probe B is used as the reference, located in the center of the feedback region. Probe D is separated in azimuth by 90° in the direction of propagation. In all oscillographs, the wave spectrum, 0 to 10 kHz, for I_{si} or φ_f is shown at R = 3 cm. The upper trace represents no feedback, NF; the middle trace, negative feedback, -F; and the lower trace, positive feedback, +F. The cases presented in fig. VI.41 are summarized in Table VI.7.

Table VI.7. Azimuthal Growth Rate Summary

Case	Gain, G	Probe	Parameter
(a)	75	B	I_{si}
(b)	75	B	φ_f
(c)	75	D	I_{si}
(d)	75	D	φ_f
(e)	25	B	I_{si}
(f)	25	D	I_{si}

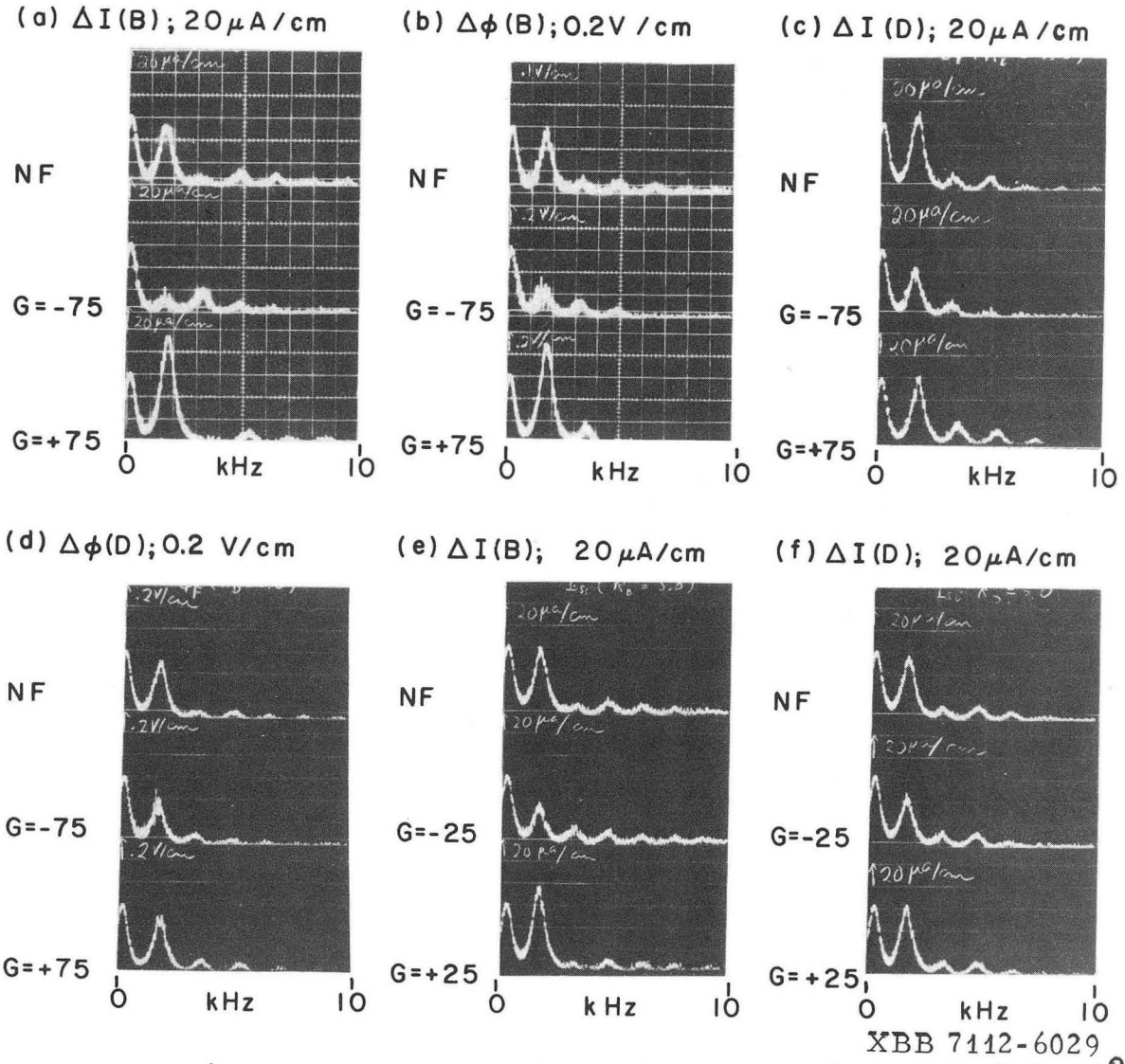

Fig. VI.41. Wave spectra on two probes separated in azimuth by 90° as a function of linear feedback loop gain, G. The upper trace is the reference case, for no feedback, NF. The middle trace is for negative feedback, -G, and the lower trace is for positive feedback, +G. (a) ΔI_{si}(probe B), gain G=75, located in the feedback region; (b) $\Delta\varphi_f$(probe B), G=75; (c) ΔI_{si}(probe D), G=75, located 90° downstream from feedback region; (d) $\Delta\varphi_f$(probe D), G=75; (e) ΔI_{si}(probe B), G=25; and (f) ΔI_{si}(probe D), G=25.

We now proceed to calculate γ/Ω_r using the spectra in fig. VI.41. The data is summarized in Table VI.8, where the tilde, ~ , implies that a quantity has been normalized to its unperturbed value, with no feedback, G = 0.

Table VI.8. Wave Amplitudes for Two Azimuths.

Probe	Gain, G	$I_{rms}(\mu A)$	$\varphi_{rms}(V)$	$\tilde{I}$	$\tilde{\varphi}$
B	0	52	0.6	probe B - reference	
B	-75	12	0.14	0.23	0.23
B	+75	92	0.9	1.8	1.5
D	0	66	0.5	probe D - reference	
D	-75	44	0.4	0.67	0.8
D	+75	60	0.5	0.91	0.1
B	-25	36	--	0.6	--
B	+25	76	--	1.3	--
D	-25	46	--	0.82	--
D	+25	64	--	1.1	--

We assume exponential growth and decay, $e^{\pm\gamma t}$. Since probes B and D are separated azimuthally by 90°, the time required to propagate the distance is $t = 1/4(2\pi/\Omega_r)$. Hence,

$\tilde{I}(\text{Probe D})/\tilde{I}(\text{Probe B}) = \exp\left[\pm\pi/2(\gamma/\Omega_r)\right]$ or inverting,

$$\gamma/\Omega_r = \pm\frac{2}{\pi}\ln\left[\tilde{I}(D)/\tilde{I}(B)\right] \qquad (6.1)$$

where the (-) sign is used for the decay rate.

If we now use the data of Table VI.8 in Eq. (6.1), we can summarize the results in Table VI.9 for γ/Ω_r.

Table VI.9. Measured Growth and Decay Rates, γ/Ω_r.

Variable I_{si} or φ_f	I_{si}	φ_f	I_{si}	φ_f	I_{si}	I_{si}	Calculated from Dispersion relation
Gain, G	-75	-75	+75	+75	-25	+25	
γ/Ω_r	0.68	0.80	0.43	0.26	0.12	0.067	0.43

Accuracy for this method is limited by our ability to measure the wave amplitudes at different azimuths, which we estimate as ~15% uncertain.

If we average all the growth and decay rates for G = 75, we get $\langle \gamma/\Omega_r \rangle_{G=75} = 0.54 \pm 0.27$, which includes measurement and statistical error. This agrees well with the value calculated from the linear dispersion relation, $\gamma/\Omega_r \Big|_{calc} = 0.43$. Note that for G = 75, the wave amplitudes are small, and we can expect linear theory to be more valid. However, for G = 25, the wave amplitudes are near nonlinear saturation, and linear theory should not be so valid. We observe that the measured growth rate falls off to $\langle \gamma/\Omega_r \rangle_{G=25} = 0.094 \pm 0.05$ as the wave approaches the nonlinear limit.

2. Temporal Growth Measurement.

The second method used to measure γ/Ω_r directly involves switching AC stabilization on or off, and watching the wave decay or

grow, respectively. We employ this technique by switching a rectangular pulse signal on end-rings 2 to 5, simultaneously. This experiment was already set up, because we could use the AC stabilization switching circuit of section III.E, but with a lower switching frequency, $f_{AC} = 4.0$ Hz. (The rise time of the switching circuit is much shorter than the wave period, as can be seen in fig. VI.36, case (i).)

Fig. VI.42, was taken using a Tektronix Model 555 oscilloscope, employing the delayed trigger for the lower sweep. The upper trace shows the applied electrode voltage, V_{AC}, on a time scale of 50 ms/cm. The lower trace shows the LF wave amplitude, ΔI_{si}, on probe B at radius R = 6 cm, in the region of maximum wave amplitude, on a magnified time scale, t = 0.5 ms/cm. Wave growth is observed when the stabilizing voltage is switched off, and decay is observed as the voltage is switched on.

This method is not so useful for accurate measurements of $\gamma/\Omega_r \lesssim 1$, since we would like to observe wave growth or decay over several periods. However, for lower growth rates, this technique should prove more useful.

We can still estimate the order of magnitude of γ/Ω_r. Let us estimate how many wave periods are required for the amplitude to change by an arbitrary factor of 10. The wave appears to grow or decay to full amplitude in approximately one period, with a large uncertainty estimated also to be ~ 1 period (100% uncertainty). We take $\tau \doteq (2\pi/\Omega_r)$, or 1 wave period as our estimate, and calculate γ/Ω_r from a formula discussed earlier, $\tilde{I}/\tilde{I}_o = e^{\gamma\tau}$. For $\tau = (2\pi/\Omega_r)$ and $\tilde{I}/\tilde{I}_o = 10$, we get $\gamma/\Omega_r = \ln(10)/2\pi = 0.36 \pm 0.36$. This agrees

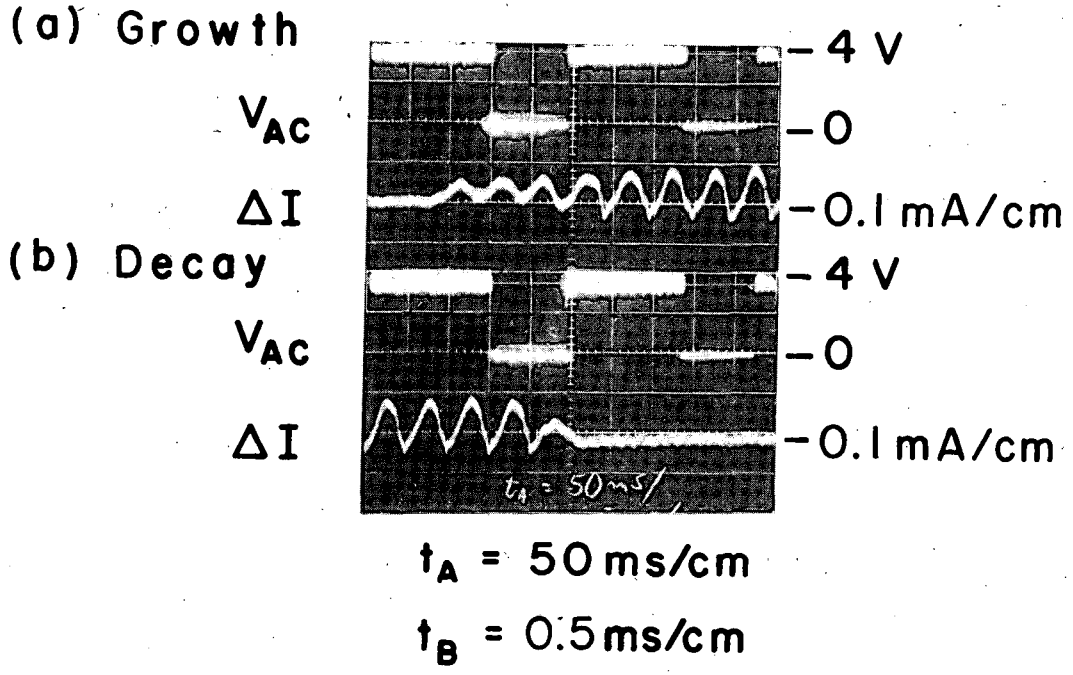

XBB 7112-6028

Fig. VI.42. Temporal wave growth and decay at R=6 cm, for the large amplitude LF wave. (a) Growth. The upper trace is the AC rectangular voltage pulse, V_{AC}, applied to the end-ring electrodes. t_A=50 msec/cm. The lower trace shows the ion current fluctuation, ΔI_{si}, grow on a delayed magnified time scale after the AC voltage is switched off. t_B=0.5 msec/cm. (b) Decay. I_{si} decays after V_{AC} is switched on.

well with the value calculated from the dispersion relation, averaged from R = 4 to 7 cm, where large wave amplitude exists, of $\gamma/\Omega_r \Big|_{calc} = 0.34 \pm 0.22$. The error is the standard deviation of the values from R = 4 to 7 cm.

3. Summary.

Both methods of direct measurement of γ/Ω_r show promise as a diagnostic tool. The azimuthal growth method, using linear feedback stabilization, gives good agreement with linear theory for large growth rates ($\gamma/\Omega_r \lesssim 1$). Accuracy is good, limited only by our ability to measure wave amplitudes at different azimuthal positions.

The temporal growth method is more useful for small growth rates ($\gamma/\Omega_r \ll 1$), since we would like to observe wave growth over several wave periods. Good agreement is obtained with linear theory, although a large error exists because the wave grows to full amplitude in about one wave period.

Agreement between theory and both experimental methods of measuring the growth rate supports the "identification" of the LF wave as the rotational flute instability.

7. Conclusion.

The properties of two low-frequency coherent waves, wave enhanced particle transport, and three methods of wave stabilization are studied in the secondary plasma of an HCD. Two techniques for direct measurement of the instability growth rate are also studied.

The present work adds new information regarding plasma stability based on simultaneous consideration of most of the effects considered important in an HCD. "Drift wave" theory seems inappropriate for experimental flute instabilities. And E x B neutral drag theory seems incomplete in not including diamagnetic and centrifugal gravity drifts.

We develop a single-fluid slab model for the "rotational instability", including the effects of density gradient, centrifugal and Coriolis forces due to plasma rotation in a radial electric field, collisions with cold neutrals, fluid compressiblity, finite gyroradius, and ion inertia. An effective ion sink term is also included in the equation of continuity, so that the effects of a linear feedback loop can be included theoretically. A cubic dispersion relation results, which we solve numerically, using Newton's method. In the low-frequency limit, $(\omega/\Omega_i \ll 1)$, the dispersion relation reduces to a quadratic expression which agrees with earlier work in the appropriate limits.

The solution of the dispersion relation explains the behavior of two low-frequency experimental waves on five points of comparison: (1) Spatial location---both waves are located in regions of large centrifugal and Coriolis effects, driven by plasma rotation in a radial electric field. The lower-frequency (LF $\tilde{}$ 2 kHz) wave is located at large radii in a region of large positive electric field.

The higher-frequency (HF ≈ 30 kHz) wave is located at small radii in a region of large negative electric field; (2) Frequency---- the measured frequencies are in good agreement with the calculated frequencies, when the Doppler shift due to plasma rotation is included; (3) Direction of propagation---the LF wave is predicted and observed to propagate in the ion-diamagnetic direction; while the HF wave propagates in the electron-diamagnetic direction; (4) Parallel wavelength---flute theory, and flutes observed; and (5) Growth rate, γ/Ω_r --- calculated growth rates, γ/Ω_r of the order unity, are in good agreement with directly measured values. Both low-frequency experimental waves are explained well by rotational flute theory.

Wave enhanced convection is estimated by measuring the correlation between the density, n_1, and potential, φ_1, fluctuations, $\langle n_1 v_{1r} \rangle_{conv} = (n_1 \varphi_1 \; c/\; 2Br) \sin\Psi$, where Ψ is the phase between the density and potential fluctuations. An effective "enhanced diffusion coefficient" is inferred, $-D_{enh} \nabla n \equiv \langle n_1 v_{1r} \rangle_{conv}$, which is used in a simple diffusion theory calculation. Enhanced diffusion due to the HF wave is less than or on the order of classical diffusion in a partially ionized plasma, and therefore is relatively unimportant. However, enhanced diffusion due to the LF wave at large radii is much larger than classical diffusion, and is comparable in magnitude to Bohm diffusion.

When enhanced diffusion is included in diffusion theory, we calculate a radial scale length, $q \equiv -(\nabla \ln n)^{-1}$, as a function of the transport coefficients, which explains semi-quantitatively the observed flattening of the density profile at large radii due to

enhanced diffusion. The LF wave is stabilized when a floating or positive DC bias is applied to the third concentric end-ring electrode. Again, the calculated scale length explains well the observed steepening of the density profile, in the absence of enhanced diffusion.

We do not claim that the change in the radial density profile is due solely to enhanced diffusion. We neglect ion mobility in the radial electric field, which is valid when the radial electric field is small, as often occurs for "DC stabilization." Furthermore, no detailed axial particle balance is attempted, since radial profiles at other axial positions are more difficult to obtain experimentally. However, axial profiles of floating potential and electron temperature indicate axial uniformity. We do observe that when positive stabilizing voltages are applied to a given end-ring configuration, ions are reflected and only electrons are drawn. Currents to the other end-rings are not significantly affected. We conclude that changes in the radial ion density are not due to axial losses through the end sheaths; and that the shape of the radial density profile can be explained semi-quantitatively by including enhanced radial diffusion in a simple diffusion theory.

All stabilization attempts on the HF wave at small radii were ineffective. We believe this is due to large wave power, estimated on the order of 30 watts, in the region of the inner end-ring. Also the large negative electric field at small radii, which drives the HF wave, seems characteristic of arc discharges, and is therefore difficult to suppress. Fortunately, enhanced transport due to the HF wave is negligible. All stabilization results refer to the LF wave at large radii.

A linear feedback loop, consisting of a bandpass filter, a 0° to 360° phase shifter, and a power amplifier, is terminated on one quarter of the second concentric end-ring as a suppressor electrode. Negative feedback power of ~.5 watt is required, drawing electrons only, to reduce the wave amplitude by an order of magnitude. Smaller feedback power causes less reduction in the wave amplitude, while increased power causes the m = 2 mode to grow. By including the feedback current in the continuity equation as an ion sink term, we were able to calculate reduced growth rates for smaller negative feedback power levels, and stabilization for optimum power (~.5 watt). Wave power in the feedback region is estimated as $\lesssim$ .1 watt.

Unfortunately, only the inner two end-rings were quartered in this experiment. Therefore, linear feedback could only be applied on end-ring suppressor electrodes for radii R < 3.5 cm, where enhanced diffusion is comparable to classical diffusion. No effect is expected or observed on the density profile. We conclude that linear feedback applied to segmented, concentric axial end-ring electrodes is an effective method of reducing wave amplitude and enhanced transport, and should be considered in the design of future experiments with conducting axial boundaries.

New information is also obtained in the present experiment by investigating wave stabilization and wave enhanced transport by controlling the axial boundaries which consist of five concentric, independently biasable, conducting rings.

"DC stabilization" is attempted by floating electrically, or DC biasing, a given end-ring electrode configuration. By merely floating the third end-ring at a positive voltage, the radial electric field can be reduced with no external power requirements. The LF wave is reduced or stabilized ($\tilde{n} < 0.01$), and the radial density profile steepens up in agreement with our calculations, which include enhanced diffusion. Increased positive voltage consistently stabilizes the LF wave, with power requirements ~1 watt.

Stabilization is in part due to the reduction of the radial electric field, which drives the LF wave. Increased electron contact with the axial boundary maintains the good electrical contact which may "short" the field. Again, we do not claim that the change of the radial density profile can be attributed entirely to enhanced transport.

We conclude that concentric end-rings are effective in controlling the radial electric field, and stabilizing electric field-driven instabilities, with small or no external power requirements. Wave enhanced transport does explain, at least semi-quantitatively, the shape of the radial density profile. In future experiments with conducting end plates, one should consider concentric end-rings.

An "AC stabilization" technique of applying a rectangular pulse signal is attempted to see if power requirements can be reduced from those of DC stabilization, and if a smaller perturbation on the radial electric field results. We find that the LF wave can be stabilized by similar power levels, ~1 watt, with corresponding steepening of the density profile. However, the radial electric

field is not so drastically reduced, and transverse ion mobility is still important at large radii. We conclude that the shape of the radial density profile can be explained consistently, by wave enhanced transport.

Two diagnostic techniques are used to measure the growth rate of the LF wave directly. In the first, the growth and decay rates are measured azimuthally as the wave propagates out of a region of linear feedback. This method is useful for measuring large growth rates ($\gamma/\Omega_r \gtrsim 1$), because the wave grows significantly in a single wave period and because experimental accuracy is good. We estimate our ability to measure wave amplitudes at different azimuths as ~15%. Good agreement is obtained between experiment and linear rotational instability theory.

In the second method, the growth and decay rates are measured temporally after a stabilizing voltage is switched off and on, respectively. This technique is more useful for small growth rates ($\gamma/\Omega_r \ll 1$), since we would like to observe wave growth over several wave periods. Accuracy is limited by our ability to determine wave amplitude changes during one or more periods. In the present experiment, large growth rates ($\gamma/\Omega_r \sim 1$) introduce large uncertainties (~100%), although good agreement is still obtained with linear theory.

The operation of a directional Langmuir probe (DLP) as a simple probe and as a tool to measure streaming velocities directly was checked experimentally. In particular, the streaming velocity was determined by measuring directional ion currents in a microwave plasma device, with a known streaming velocity. The streaming veloc-

ity was determined independently by measuring the difference in the propagation speeds of sound waves, launched in the upstream and downstream directions. Good agreement between the two methods is obtained.

The properties of two low-frequency instabilities are explained well by a rotational flute theory. Wave enhanced transport is included in a simple diffusion theory to explain semi-quantitatively the shape of the radial density profile. Three stabilization techniques, using quartered end-rings as suppressor electrodes, are shown to be effective in stabilizing one low-frequency instability, which contributes significantly to enhanced transport. And two methods of measuring the growth rate, γ/Ω_r, directly are found to agree with theory.

ACKNOWLEDGMENTS

The author wishes to express his special thanks to Dr. Robert V. Pyle for the inspiration and motivation which made this work possible, to Prof. Wulf B. Kunkel for much physical insight and encouragement, to Margaret Thomas for her patient help in editing and typing the manuscript, and to my friend, Leslie Redpath, for her patience and help throughout the long period of this work.

This work was supported by the National Science Foundation and the U.S. Atomic Energy Commision.

APPENDIX

APPENDIX

A. Basic parameters of an argon plasma.

1. Cross sections.

(a) Ion-neutral. The total ion-neutral collision cross section in argon is given by Gilbody and Hasted as $\sigma_{in}^{t} \simeq 6.0 \times 10^{-15}$ cm^2 for ion energy ~1 eV.[111] Cramer measured the total cross section as due to elastic scattering σ_{in}^{el} and charge exchange σ_{in}^{cx}.[112] He obtained for ion energy ~1 eV, $\sigma_{in}^{el} \simeq 3.5 \times 10^{-15}$ cm^2, $\sigma_{in}^{cx} \simeq 4.0 \times 10^{-15}$ cm^2, and $\sigma_{in}^{t} \simeq 7.5 \times 10^{-15} cm^2$.

There is some uncertainty involved in the extrapolation of the cross section to lower ion energies (~.1 eV) in this experiment, since the resonant charge exchange cross section increases as energy decreases. The cross section cannot be measured accurately at such low energies, however we can get an estimate from measurements of the ion mobility coefficient. The ion mobility at thermal energies is measured and calculated to be ~1.6 cm^2/volt-sec[113] at STP, from which the total cross section at thermal energies is estimated to be $\sigma_{in}^{t} \simeq 1.6 \times 10^{-14} cm^2$. And to good approximation, $\sigma_{in} \sim 1/v_{th}^{i}$,[113] so that for ion energies ~.1 eV, we estimate $\sigma_{in}^{t} \simeq 8 \times 10^{-15} cm^2$. We take $\sigma_{in}^{t} \simeq 6.0 \times 10^{-15} cm^2$, and estimate the uncertainty ~50%.

The major effects of ion-neutral cross section uncertainty on the experimental results would be to introduce a systematic error in the ion-neutral diffusion coefficient, and in the theoretical dispersion relation. Since we are primarily interested in enhanced diffusion coefficients several orders of magnitude larger than

classical, a small error in the ion-neutral diffusion coefficient would cause little problem. We observe in sections VI.A.6 and VI.F that order of magnitude error in σ_{in} is required for significant changes in the theoretical phase and growth rate, respectively, for the rotational instability.

(b) Electron-neutral. For elastic scattering of electrons from neutral argon atoms at electron energies $\sim$1 eV, we estimate $\sigma_{en} \simeq 1.0 \times 10^{-16}$ cm^2.[114,115] Electron collisions with neutrals are relatively unimportant in the present experiment, and electron-neutral collisional diffusion is negligible compared with electron-ion diffusion.

(c) Coulomb. We use the expression for the Coulomb collision frequency, as expressed in Rose and Clark, $\nu_{ei} = n_i \langle v_r \sigma_{ei}(v_r) \rangle$, averaged over a Maxwellian velocity distribution,[107]

$$\nu_{ei} = \frac{(4\pi)^2}{32\sqrt{2\pi}} \frac{n_i e^4}{\sqrt{m_e (kT_e)^3}} \ln \Lambda_D .$$

We use this relaxation frequency to define the Coulomb cross section, $\sigma_{ei} = \nu_{ei}/(n_i \sqrt{2kT_e/m_e})$, and take,

$$\sigma_{ei} = \frac{(4\pi)^{3/2}}{32} \frac{e^4}{(kT_e)^2} \ln \Lambda_D = \frac{2.89 \times 10^{-14}}{kT_e^2(\text{eV})} \ln \Lambda_D \text{ cm}^2 \quad \text{(A.1)}$$

where the Debye shielding parameter $\Lambda_D \equiv 12\pi n_i \lambda_{De}^3$, and the Debye length $\lambda_{De} \equiv \sqrt{kT_e/4\, n_i e^2}$.

2. Ionization.

The first three ionization potentials in argon are 15.8, 27.6, and 40.9 volts.[116] In order to estimate an ionization rate, we integrate the Maxwellian electron distribution from energies above

the first ionization threshold, E_1 = 15.8 volts. Rather than integrate over the ionization cross section, we take the worst case of uniform cross section at the maximum value, $\sigma_i(\max) \simeq 3.6 \times 10^{-16}$ cm^2.[117] We obtain a maximum ionization rate,

$$\beta_I \equiv \langle nv\sigma_i \rangle \lesssim n_o v_{th}^e \sigma_i(\max)\, e^{-E_1/kT_e}$$

This expression is used in section A.5 to show that ionization is negligible in the secondary plasma surrounding an HCD.

3. Recombination.

Several authors reported the dissociative recombination of Ar_2^+ molecular ion in thermal microwave argon plasmas.[118-120] Values of the volume dissociative recombination coefficient lie between $\alpha_{diss} = 10^{-6}$ and 10^{-8} cm^3/ion-sec. At electron temperatures of a few tenths of an eV in an argon arc discharge, the volume recombination coefficient is measured between $\alpha = 2 \times 10^{-10}$ and 4.2×10^{-10} cm^3/ion-sec.[120,121] These authors postulated possible creation of of the molecular ion Ar_2^+ as an explanation for the fact that their coefficients were still several orders of magnitude larger than expected for radiative recombination. Olsen and Huxford measured the radiative recombination coefficient by Stark broadening in a pulsed discharge, $\alpha_{rad} = 2.5 \times 10^{-13} cm^3$/ion-sec.[123] The electron temperature is T_e = .83 eV.

In the absence of evidence for molecular ions, as well as electron temperatures more compatible with ours, we take the radiative recombination coefficient $\alpha_{rad} = 2.5 \times 10^{-13} cm^3$/ion-sec. Radiative recombination is shown to be negligible in the present experiment in section A.5.

4. Plasma parameters at R=4 cm.

We now calculate some of the plasma and wave parameters for a typical argon plasma, in the presence of two large-amplitude, low-frequency waves. Results correspond to the typical data set discussed in section VI.A, but at R=4 cm. Pressure p_t=.25 mtorr Ar, and magnetic field B=580 G.

(a) Basic parameters.

Neutral density: $n_o = 8.8 \times 10^{12}$ cm^{-3}

Ion density: $n_i = 4.4 \times 10^{11}$ cm^{-3}

Electron temperature: $T_e = .50$ eV

Ion temperature: $T_i \approx T_e/10 = .05$ eV

Floating potential: $\varphi_f = 3.6$ volts

Plasma potential: $\varphi_p = 5.3$ volts

Radial electric field: $E_r = .21$ volts/cm

(b) Characteristic velocities.

Thermal:

$$V^e_{th} = \sqrt{2kT_e/m} = 5.93 \times 10^7 \sqrt{T_e(eV)} = 4.3 \times 10^7 \text{ cm/sec}$$

$$V^i_{th} = \sqrt{2kT_i/M_i} = 1.38 \times 10^6 \sqrt{T_i(eV)/A(amu)} = 4.9 \times 10^4 \text{ cm/sec}$$

Sound:

$$V_s = \sqrt{2kT_e/M_i} = 1.38 \times 10^6 \sqrt{T_e(eV)/A(amu)} = 1.5 \times 10^5 \text{ cm/sec}$$

Drift (DLP):

$$V^i_{d\theta} = \sqrt{(T_e/T_i)}\ (V_s/4)\ \Delta I_{si}/I_{si} = 4.2 \times 10^4 \text{ cm/sec}$$

(c) Characteristic frequencies.

Plasma:

$$\omega_{pe} = \sqrt{4\ ne^2/m} = 5.7 \times 10^4 \sqrt{n_i(cm^{-3})} = 3.8 \times 10^{10} \text{ sec}^{-1}$$

$$\omega_{pi} = \sqrt{4\ ne^2/M_i} = 1.32 \times 10^3 \sqrt{n_i(cm^{-3})/A(amu)} = 1.4 \times 10^8 \text{ sec}^{-1}$$

Cyclotron:

$$\Omega_e = eB/mc = 1.76 \times 10^7 \, B(G) = 10^{10} \, sec^{-1}$$

$$\Omega_i = eB/M_i c = 10^4 \, B(G)/ A(amu) = 1.4 \times 10^5 \, sec^{-1}$$

Collision: [107]

$$\nu_{in} = n_o v_{th}^i \sigma_{in} = 2.6 \times 10^3 \, sec^{-1}$$

$$\nu_{en} = n_o v_{th}^e \sigma_{en} = 3.7 \times 10^4 sec^{-1}$$

$$\nu_{ei} = 2.89 \times 10^{-14} n_i(cm^{-3}) \ln \Lambda_D / kT_e^{3/2}(ev) = 1.9 \times 10^7 \, sec^{-1}$$

$$\nu_{ee} = 2\sqrt{2}\nu_{ei} = 5.4 \times 10^7 sec^{-1}$$

Wave:

LF $\cong$ 1.8 kHz HF $\cong$ 36 kHz

Plasma rotation:

$$\Omega_o = V_{d\theta}^i / 2\pi R = 1.7 \text{ kHz}$$

Diamagnetic drift:

$$\omega_{De} = kT_e c\delta / 2\pi ReB = 0.83 \text{ kHz}$$

$$\omega_{Di} = kT_i c\delta / 2\pi ReB = 0.083 \text{ kHz}$$

Electric drift:

$$\omega_E = E_r / 2\pi RB = 1.5 \text{ kHz}$$

Centrifugal drift:

$$\omega_g = g / 2\pi R\Omega_i = \Omega_o^2 / 2\pi\Omega_i = 0.13 \text{ kHz}$$

(d) Characteristic lengths.

Density scale: $q_n = -(\nabla \ln n)^{-1} = 4.1$ cm

Temperature scale: $q_T = -(\nabla \ln T)^{-1} = 27$ cm

Debye:

$$\lambda_{De} = kT_e / 4\pi ne^2 = 740 \; kT_e(eV)/n_i(cm^{-3}) = 7.9 \times 10^{-4} \text{ cm}$$

Gyroradius:

$$a_i = V_{th}^i / \Omega_i = 0.35 \text{ cm}$$

$$a_e = V_{th}^e / \Omega_e = 4.2 \times 10^{-3} \text{ cm}$$

Mean-free-path:

$$\lambda_{in} = V^i_{th}/\nu_{in} = 19 \text{ cm}$$

$$\lambda_{en} = V^e_{th}/\nu_{en} = 1100 \text{ cm}$$

$$\lambda_{ei} = V^e_{th}/\nu_{ei} = 2.2 \text{ cm}$$

$$\lambda_{ee} = V^e_{th}/\nu_{ee} = 0.79 \text{ cm}$$

(e) Diffusion coefficients.

Ion-neutral:

$$D_{\parallel in} = \lambda_{in} V^i_{th}/3 = 3.1 \times 10^5 \text{cm}^2/\text{sec}$$

$$D_{\perp in} = D_{\parallel in}/(1+\Omega_i^2 \tau_{in}^2) = 1.1 \times 10^2 \text{cm}^2/\text{sec}$$

Electron-neutral:

$$D_{\parallel en} = \lambda_{en} V^e_{th}/3 = 1.6 \times 10^{10} \text{ cm}^2/\text{sec}$$

$$D_{\perp en} = D_{\parallel en}/(1+\Omega_e^2 \tau_{en}^2) = 0.21 \text{ cm}^2/\text{sec}$$

Fully-ionized:

$$D_{\perp ei} = 9.8 \times 10^{-5} \frac{n_i(\text{cm}^{-3})\ (kT_e + kT_i(\text{eV}))}{B^2(\text{G})\ kT_e^{3/2}} = 3.0 \times 10^2 \text{cm}^2/\text{sec}$$

Enhanced:

$$D_{\perp enh} = \frac{n_1 \phi_1 c}{2RBV n_i} \sin \psi$$

$$D_{\perp enh}(\text{LF}) = 3.4 \times 10^3 \text{cm}^2/\text{sec}$$

$$D_{\perp enh}(\text{HF}) = 87 \text{ cm}^2/\text{sec}$$

Bohm:

$$D_{\text{Bohm}} = (kT_e + kT_i)c/16eB = 5.9 \times 10^3 \text{ cm}^2/\text{ sec}$$

(f) Mobility.

$$\mu_{\perp in} = eD_{\perp in}/kT_i = 2.1 \times 10^3 \text{cm}^2/\text{volt-sec}$$

5. Ion accumulation rates.

The ion continuity equation can be written,

$$\frac{\partial n}{\partial t} + \nabla.(n\underline{v}) = -\alpha_R n^2 + \beta_I n \qquad \text{(A.2)}$$

We consider ion accumulation due to transport mechanisms, ionization, and recombination. The ion currents can be written,

$$nv_r = -D_{\perp in}\frac{\partial n}{\partial r} - D_{\perp ei}\frac{\partial n}{\partial r} - D_{enh}\frac{\partial n}{\partial r} + \mu_{\perp in} n E_r \qquad (A.3)$$

$$nv_z = -D_{\parallel in}(1 + T_e/T_i)\frac{\partial n}{\partial z} \qquad (A.4)$$

where the transport coefficients are defined in Appendix B. We estimate the accumulation rates from the Eqs. (A.2) to (A.4) and from the transport coefficients.

Ion-neutral diffusion:

$$D_{\perp in}/q^2 = 6.2 \text{ sec}^{-1}$$

$$D_{\parallel in}\frac{\pi^2}{L_{eff}^2}(1 + T_e/T_i) = 300 \text{ sec}^{-1}$$

Fully-ionized diffusion:

$$D_{ei}/q^2 = 18 \text{ sec}^{-1}$$

Enhanced diffusion:

$$D_{\perp enh}(LF)/q^2 = 200 \text{ sec}^{-1}$$

$$D_{\perp enh}(HF)/q^2 = 5.1 \text{ sec}^{-1}$$

Mobility:

$$\mu_{\perp in} E_r/q = 107 \text{ sec}^{-1}$$

Recombination:

$$\alpha_R n_i = 0.11 \text{ sec}^{-1}$$

Ionization:

$$\beta_I \lesssim 2.6 \times 10^{-9} \text{ sec}^{-1}$$

The dominant ion accumulation mechanisms at R=4 cm are enhanced convection due to the LF wave, and mobility in the radial electric field. These processes are larger than classical diffusion at R=4 cm. However, where the wave amplitude is small, or stabilized, and E_r is small, classical diffusion dominates.

Radiative recombination, collisional ionization, and enhanced transport due to the HF wave are negligible.

B. Transport theory.

The basic transport mechanisms to be considered here are weakly ionized diffusion, fully ionized diffusion, mobility in an electric field, and wave enhanced convection. Local production and recombination are estimated in Appendix A to be negligible in the secondary plasma of an HCD. The effects of a uniform axial magnetic field, B, are included.

1. Weakly ionized transport.

The diffusion coefficients in a weakly ionized plasma, where Coulomb collisions can be neglected, is given by Allis:[124]

$$\underline{D}_{\alpha n} = \frac{V_{th}^{\alpha 2}}{3\nu_{\alpha n}} \begin{bmatrix} \frac{1}{1 + \Omega_\alpha^2 \tau_{\alpha n}^2} & \frac{\Omega_\alpha \tau_{\alpha n}}{1 + \Omega_\alpha^2 \tau_{\alpha n}^2} & 0 \\ \frac{-\Omega_\alpha \tau_{\alpha n}}{1 + \Omega_\alpha^2 \tau_{\alpha n}^2} & \frac{1}{1 + \Omega_\alpha^2 \tau_{\alpha n}^2} & 0 \\ 0 & 0 & 1 \end{bmatrix} \qquad \text{(B.1)}$$

where $\tau_{\alpha n}$ is the collision time with neutrals, and V_{th}^{α} is the thermal velocity for species α. The mobility tensor can be expressed in terms of the diffusion tensor, by means of the Einstein relation:

$$\underline{\mu}_{\alpha n} = \frac{q_\alpha}{kT_\alpha} \underline{D}_{\alpha n} \qquad \text{(B.2)}$$

2. Fully ionized transport.

Kaufman calculates the fully ionized transverse diffusion coefficient for the case of unequal electron and ion temperatures:[125]

$$D_{\perp ei} = D_{\perp ie} = \eta_\perp \frac{n_o c^2}{B^2} (kT_e + kT_i) \qquad \text{(B.3)}$$

where the transverse resistivity $\eta_\perp = \frac{8}{3}\sqrt{\frac{\pi}{2}}\ \frac{m^{1/2}e^2}{kT_e^{3/2}}$.

Thermal gradients are neglected.

3. Enhanced convection.

Correlated density and velocity fluctuations can lead to net convection of plasma across $\underline{B}$. The two large amplitude, low-frequency waves present in the HCD are treated in this manner. The net time-averaged convection can be written:

$$\langle nv_r \rangle^\alpha_{conv} \equiv \frac{1}{2\tau}\int_{-\tau}^{+\tau} n_\alpha(t)\ v_r^\alpha(t)\ dt$$

Often the radial velocity, v_r, is due to a fluctuating azimuthal electric field, $E_{1\theta}$, so that $v_{1r} = E_{1\theta}c/B$. We linearize for the case of a coherent perturbation with the frequency, ω. The density $n = n_o + n_1 \cos \omega t$, and the radial velocity $v_r = v_{or} + v_{1r} \cos(\omega t + \Delta)$, where Δ is the phase angle between the density and velocity fluctuations. If we neglect the zero-order radial velocity, and take the time average, we get,

$$< n\ v_r >^\alpha_{conv} = \frac{n_1 v_{1r}}{2} \cos \Delta \qquad \text{(B.4)}$$

If we assume $v_{1r} = E_{1\theta}\ c/B$, and $E_{1\theta} = -ik_1\phi_1 = -i\ m\phi_1/r$, we have,

$$< n\ v_r >^\alpha_{conv} = \frac{n_1\ \phi_1 c}{2Br} \sin \psi \qquad \text{(B.5)}$$

where $\psi = \Delta \pm \pi/2$ is the phase angle between the density, n_1, and potential, ϕ_1, fluctuations.[11,12] From this expression, an effective enhanced diffusion coefficient will be inferred,

$$< n\ v_r >^\alpha_{conv} = -\ D^\alpha_{enh}\ \nabla n \qquad \text{(B.6)}$$

4. Bohm diffusion.

The expression we use is:

$$D_{Bohm} = \frac{c\,(kT_e + kT_i)}{16\,eB} \qquad (B.7)$$

Bohm diffusion will not be included in the diffusion equation, and will serve only as a reference with which to scale other transport mechanisms.

5. Ambipolar diffusion.

Ambipolar diffusion occurs when one charged particle species tries to diffuse faster than another, due to collisions with neutrals. An ambipolar electric field arises which equalizes the electron and ion currents, thus maintaining charge neutrality. Golant calculates the following expressions for the transverse ambipolar electric field and diffusion coefficient:[122]

$$E_{\perp amb} = \frac{D_{\perp in} - D_{\perp en}}{\mu_{\perp in} - \mu_{\perp en}} \frac{\nabla n}{n} \simeq \frac{kT_i}{e} \frac{\nabla n}{n} \qquad (B.8)$$

$$D_{\perp amb} = \frac{\mu_{\perp en} D_{\perp in} - \mu_{\perp in} D_{\perp en}}{\mu_{\perp en} - \mu_{\perp in}} \qquad (B.9)$$

Experimentally, the radial electric field is found to be much larger than the calculated ambipolar value. Schwirzke argued that this field arises due to transverse gradients in the electron temperature and currents to the end sheaths.[109] The temperature gradient is due to collisional cooling. The resulting plasma potential gradient arises for the grounded end-plate case because the potential drop across the end sheath is proportional to T_e. Changes in currents to the end sheaths can result in large potential

changes. Large nonambipolar electric fields are reported.[5-7]

6. Effect of temperature gradients.

Particle currents due to temperature gradients are of the order $D_\perp$ n $\nabla T/T$, as compared to $D_\perp$ $\nabla n/n$ due to density gradients.[127] The ratio of these terms is of order $\frac{\nabla \ln kT}{\nabla \ln n} \equiv q_n/q_T$. From data in Appendix A, at R=4 cm, $q_n/q_T \approx 0.16$. And near R=1 cm, in the region of large temperature and density gradients, $q_n/q_T \approx 0.58$.

The effect of temperature gradients is negligible at large radii, since the temperature profile is nearly flat. At small radii, in the region of large density and temperature gradients, the effect of temperature gradients is not negligible, however it is not so important as that of density gradient. Transport due to temperature gradients is neglected.

7. Diffusion equation.

The above transport mechanisms yield net particle currents, which must be balanced by the particle conservation equations:

$$\frac{\partial n_\alpha}{\partial t} + \nabla \cdot (n_\alpha \underline{v}_\alpha) = -\alpha_R n_\alpha^2 + \beta_I n_\alpha \qquad \text{(B.10)}$$

where α_R is the recombination rate, and β_I is the ionization rate. Recombination and ionization are found experimentally to be small in the secondary plasma of an HCD, and will be neglected.[5] (See Appendix A).

The particle currents for species α can be written down:

$$n v_r^\alpha = -(D_{\perp cn} + D_{\perp ei}) \frac{\partial n}{\partial r} + \mu_{\perp cn} n E_r + \langle n v_r \rangle_{conv}^\alpha \qquad \text{(B.11)}$$

$$nv_z^{\alpha} = - D_{\|in} \frac{\partial n}{\partial z} + \mu_{\|in} n E_z \qquad (B.12)$$

Cylindrical symmetry requires no net charge accumulation due to azimuthal drifts. The parallel electron-neutral mean-free-path λ_{en}, is larger than the system length, L, and most of the electrons are reflected by the large potential drops at the end sheaths. In addition, the mean-free-path for electron-electron collisions is small,[111] $\lambda_{ee} \approx 1$ cm. Hence, the electrons can be assumed to be in equilibrium along the field lines, $n(z) = n_o \exp(e\phi/kT_e)$.[2,4] The resulting axial electric field is $E_z = - (kT_e/e)(1/n\ \partial n/\partial z)$. The axial electron current vanishes to lowest order, and the ion current can be written:

$$nv_z^{i} = - D_{\|in} (1 + T_e/T_i)\ \partial n/\partial z \qquad (B.13)$$

In order to solve the above system of equations for the ion density, $n(r,z)$, we make the following assumptions: (1) Steady state, $\partial n_\alpha/\partial t = 0$; (2) $n(r,z) = n(r) \cos(\pi z/L_{eff})$, where L_{eff} is the effective length of the diffusion region; (3) Radial convection can be expressed in terms of an effective enhanced diffusion coefficient, $D_{enh} \nabla n \equiv - \langle nv_r \rangle^{\alpha}_{conv}$, which is reasonable for sufficiently small radial variations; and (4) Mobility in the radial electric field, E_r, can be neglected. Assumption (2) is shown to be a good approximation in section VI.A.2. L_{eff} is the effective length of neutron transport theory, required by the boundary conditions of zero density and zero return current.[128] We assume that the parallel ion-neutral transport mean-free-path is increased by the factor $(1 + T_e/T_i)$, $\lambda_{eff} = \lambda_{in}(1 + T_e/T_i)$, similar to the axial ion current Eq.(B.12), due to E_z. Therefore $L_{eff} = L + \frac{4}{3}\lambda_{eff}$.

Assumption (4) is perhaps the worst. In Appendix A we found that when a large radial electric field is present, radial ion mobility is important. In this case no analytic solution can be obtained for the ion density, $n(r,z)$, without specific assumptions about E_r. However, if the radial electric field is small, as is often the case when dc or floating potentials are applied to the conducting end-rings, then an analytic expression for the ion density profile can readily be obtained.

With assumptions (1) thru (4), the ion continuity equation can be written:

$$\frac{\partial n_i}{\partial t} = \frac{1}{r}\frac{\partial}{\partial r} r D^i_{\perp eff}\frac{\partial n_i}{\partial r} + \frac{\partial}{\partial z} D^i_{\parallel in}(1 + T_e/T_i)\frac{\partial n_i}{\partial z} = 0$$

where $D_{\perp eff} = D_{\perp in} + D_{\perp ei} + D_{enh}$. Using assumption (2), this reduces to:

$$\frac{1}{r}\frac{\partial}{\partial r} r \frac{\partial n(r)}{\partial r} - \frac{n(r)}{q^2} = 0$$

where,

$$q = \frac{L_{eff}}{\pi}\left[\frac{D_{\perp eff}}{D_{\parallel in}(1 + T_e/T_i)}\right]^{1/2} \qquad (B.14)$$

The resulting Bessel equation has the solution,

$$n(r) = A\, K_o(r/q) + B\, I_o(r/q) \qquad (B.15)$$

For $q \ll r$, which is reasonably vadid in an HCD for large radii ($r \gtrsim 3$ cm), where the density gradient is not so steep, the Bessel functions of imaginary arguments can be approximated,

$$K_o(r/q) \simeq \left(\frac{\pi q}{2r}\right)^{1/2} e^{-r/q} \qquad (B.16)$$

$$I_o(r/q) \simeq \left(\frac{q}{2\pi r}\right)^{1/2} e^{r/q}$$

When $q << r$, a nearly exponential radial density variation is predicted, with radial scale length q. Observations of the magnitude and parametric dependence of q may yield information on the magnitude and type of diffusion mechanisms present.[9,32]

In the present experiment, the measured scale length will be compared with a calculated value in an effort to show the importance of wave enhanced convection.

C. Langmuir probe theory.

A Langmuir probe is a small metal electrode which is immersed in the plasma. When a probe is connected to an external biasing circuit, one finds that much useful information can be obtained from the magnitude and shape of the resulting probe characteristic--- i.e., probe current vs. probe voltage. For example, we can determine the plasma density, potential, and electron temperature in the vicinity of the probe tip. In this manner one can readily obtain a spatially resolved profile of plasma paramters.

1. Simple probe theory.

Classical probe theory[3] is based on the following assumptions:

(1) $T_i << T_e$

(2) $\lambda_{De} << R_p$

(3) $\lambda_{in} >> R_p$

(4) $B = 0$

(5) $v_d << v_s$

(6) **Fluctuations negligible**

Assumption (1), $T_i << T_e$, is necessary in order to solve the Langmuir-Child space-charge formulation in the "sheath" region. Incomplete shielding of the probe is implied.

Assumption (2), $\lambda_{De} << R_p$, requires that the sheath thickness be much less than the probe radius. The probe collection area can then be approximated by the geometrical area of the probe tip. The electric field due to the probe extends only a few Debye lengths,

λ_{De}, into the plasma, and is a function of probe voltage. Assumption (2) also requires small change in collection area with probe voltage, hence the electron and ion currents should saturate in the large probe voltage limits, in the absence of magnetic fields.

Assumption (3), $\lambda_{in} >> R_p$, states that the probe presence does not appreciably perturb the plasma. Ions are replaced by random collisions as fast as they are lost to the probe.

Assumption (4), $B = 0$, implies we can neglect magnetic effects for now, and discuss them later.

Assumption (5), $v_d << v_s$, requires that the plasma drift velocity be sufficiently small, so that particle collection is negligibly affected. Probe theory in a drifting plasma is discussed further in Appendix D.

Assumption (6), regarding the effect of fluctuations, will be discussed in a later section.

With these assumptions, Bohm, Burhop, and Massey[3] derived an expression for the saturated ion current to a negatively biased probe. The ions are accelerated to the sound speed when they reach the sheath, $V_s = \sqrt{2kT_e/M_i}$. This is known as the Bohm sheath criterion, and is a necessary condition for a stable solution of the space charge equations. The resulting expression for the saturated ion current is:

$$I_{si} = Cn_i e(2kT_e/M_i)^{1/2} A_{probe}$$

where the factor C is determined by space charge and geometrical effects. $C = 0.40$ is obtained for a spherical probe, which we will take as a good estimate for a cylindrical probe. Solving for the ion density,

$$n_i = 1.13 \times 10^{12} \quad \frac{I_{si}(ma)}{A_{probe}(mm^2)} \sqrt{\frac{A(amu)}{kT_e(eV)}} \quad cm^{-3} \qquad (C.1)$$

The electron temperature can be calculated from the probe character-istic, if we assume that the electrons are reasonably Maxwellian. Then as we increase the probe voltage from the ion saturation region, we begin to collect electrons. In this case we calculate,

$$e/kT_e = d/dV \ \ln \left[I(V) - I_{si} \right] \qquad (C.2)$$

Experimentally, the electron temperature can be determined from the slope of a semi-log plot of the probe characteristic, [I(V) vs. V].

Hall calculated the relationship between the plasma potential and the floating potential.[101] At the plasma potential, ϕ_p, a probe is at the same potential as the plasma. There are no electric fields due to the probe, and particles are collected due to thermal and drift motions. The floating potential, ϕ_f, is defined as that potential for which the probe currents for the two species balance, and no net current is drawn. If we balance the ion and electron currents at ϕ_f, and assume that only electrons with sufficient energy to get up the potential barrier will be collected, we obtain,

$$\phi_p = \phi_f + kT_e/2e \ \ln(kT_e M_i/m_e kT_i) \cong \phi_f + \gamma kT_e/e \qquad (C.3)$$

If we assume that ions are collected at the electron temperature, due to the electric field penetrating the plasma, we write,

$$\gamma = 1/2 \ \ln (M_i/m_e) \qquad (C.4)$$

For argon, $\gamma = 5.6$, in agreement with the theory of Laframboise, which includes the effects of finite sheath thickness and trapped particle orbits.[106]

2. Effect of magnetic field.

A magnetic field reduces the transverse mean-free-path to the gyroradius. If the ion gyroradius $a_i >> R_p$, then the collection of ions is relatively unaffected. However, in general $a_e \lesssim R_p$, and electron collection is strongly affected.

Chen derived expressions for the reduced electron currents, when electron collection is diffusion limited.[102,103] However, he claimed that I_{si} is negligibly affected, if $a_i/R_p \gtrsim 7$. Hudis verified experimentally that no effect on I_{si} is observed if $a_i/R_p \gtrsim 2$.

Brown, Compher, and Kunkel[104] studied the experimental effects of a strong magnetic field in hydrogen, for $0.4 \lesssim a_i/R_p \lesssim 10$. They claim B has small effect on the shape of the probe characteristic, and hence the electron temperature derived from the slope seems to agree with the temperature measured with a three-grid energy analyzer. **However, the electron current to a floating probe may be affected so that the expression for the plasma potential [Eqs. (C.3) and (C.4)] may be modified by strong B. They also report an empirical expression for the reduction of I_{si} as a function of a_i/R_p. Reduction in hydrogen is less than 30% for $a_i/R_p \approx 10$.**

For the characteristic parameters presented in Appendix A, we calculate $a_i/R_p \approx 13.5$. Magnetic effects will be ignored here.

3. Effect of fluctuations.

Fluctuations on I_{si} and ϕ_f can be integrated out. However, fluctuations in n_i, ϕ_f, and T_e do introduce uncertainty into the measurement of T_e. The Langmuir probe sweep chassis, fig. III.4, has been designed to minimize stray capacitance, in order to get accurate probe characteristics.

Warren[5] studied the effects of low-frequency coherent fluctuations on the probe characteristic. The envelope of the fluctuations on the probe characteristic changes shape due to the changing plasma impedance, determined from the slope of the V - I probe characteristic. Warren studied the resulting T_e obtained from the maximum and minimum of the envelope, as well as from the four characteristics obtained by enhancing an oscilloscope trace 0°, 90°, 180°, and 270° after the peak of a reference signal. All values for T_e are reported to lie within those obtained from the maximum and minimum of the envelop, with a spread of ~ 30%.

We measure the probe characteristic by integrating out the fluctuations, and realize that the result may be uncertain to ± 25%. Temperature fluctuations are ignored.

4. Perturbation of plasma by a probe.

Ecker, Masterson, and McClure note that the presence of a probe in a plasma such as the positive column of a glow discharge may introduce errors by perturbing the plasma in the vicinity of the probe.[129] However, in this experiment the plasma potential is determined by the currents to the conducting end-ring sheaths. The electron-neutral mean-free-path along the magnetic field lines is long compared to the system length. Therefore, the plasma potential is dominated by the axial boundary sheaths. A Langmuir probe is a small perturbation compared with the conducting end-rings.

In practice, the presence of one probe causes negligible effect on a reference probe signal, except for the following conditions: (1) the probe is inserted at radii less than 1 cm, near the primary arc column; (2) the probe is drawing large electron

currents; and (3) the probe is on the same axial magnetic field line. Typical probe measurements are observed to have no effect on a reference probe. Care was taken to withdraw probes beyond the plasma edge when not being used, so as to minimize the chance of extraneous perturbations.

5. Validity of simple probe theory.

We show the validity of simple probe theory, based on the satisfaction of assumptions (1) to (6).

In 1954, Allen and Thonemann replaced the probe radius, R_p, with the sheath transition radius, R_t, in order to calculate the collection area more precisely.[105] They reported that the improvement in results was bounded by a factor of 2 if $R_p/\lambda_{De} \gtrsim 30$. Using the characteristic parameters presented in Appendix A, we calculate $R_p/\lambda_{De} \simeq 33$.

Laframboise employed numerical analysis for a Maxwellian ion distribution.[106] He considered orbital angular momentum, and showed that trapped orbits can reduce I_{si}, and that the effect of angular momentum can be parametrized by the ratios T_i/T_e and R_p/λ_{De}. For $T_i/T_e \lesssim 0.1$ and $R_p/\lambda_{De} > 1$, this effect can be ignored. Our calculations yield $T_i/T_e \lesssim 0.1$, and $R_p/\lambda_{De} \simeq 33 > 1$. The effects of trapped orbits are negligible.

We calculate $\lambda_{in}/R_p \simeq 730$, and $a_i/R_p \simeq 13.5$ from Appendix A. Hence the probe tip does not significantly perturb the plasma.

Chen[102,103] claimed that the effect of B on I_{si} could be neglected if $a_i/R_p \gtrsim 7$. Hudis[6,10] studied this result experimentally, observing negligible effect on I_{si} for $a_i/R_p \gtrsim 2$. The effects of

B on I_{si} are neglected. We also neglect the effect of B on T_e.[104]

The secondary plasma of the HCD in argon satisfies the requirements for simple probe theory to give a good estimate of n_i, T_e, and ϕ_p. Hence, the simple expressions presented here will be employed.

D. Directional Langmuir probe theory.

The directional Langmuir probe (DLP) can be used to measure particle currents directly and easily. Directional means that the probe tip is shielded, so that particles strike the probe from a restricted solid angle only. We will use a model presented by Hudis and Lidsky to express the ion drift velocity as a function of the directional ion currents, measured using a DLP.[6,10]

In 1964, Brundin considered the validity of a Langmuir probe in a streaming plasma.[130] He claimed that for drift velocities much greater than the ion thermal velocity, $V_d^i >> V_{th}^i$, ions are collected only by streaming directly into the probe. No ions are collected in the wake. In this case, he wrote down an expression for the saturated ion current to a cylindrical probe,

$$I_{si} = n_o e V_d^i (\pi R_t L),$$

where L is the length of the probe tip, and R_t is the sheath radius. Validity was predicted for Mach numbers, $M \gtrsim 4$. Experiments in the wind tunnel of the University of California Aeronautical Sciences Laboratory[131] for M = 6, 9, and 12, verified that the ion density could accurately be determined by a measurement of the saturated ion current in a plasma streaming at a known velocity.

In 1970, Hudis and Lidsky[6,10] improved on Brundin's model, and investigated the experimental characteristics of the DLP for lower drift velocities, $V_d^i \lesssim V_s$. Their results will be summarized and modified here. We consider a DLP, as in fig. III.5, designed to measure I_{si} in a preferred direction through a 1K resistor. Simple

probe theory applies and all the same conditions (Appendix C) are satisfied.

Consider a uniformly drifting plasma, with the drift velocity less than the sound speed, $V_d^i \lesssim V_s$. Shielding of the probe is incomplete, and the ion is accelerated to V_s at the sheath edge. The sheath itself should be unperturbed for $V_d^i \lesssim V_s$, However, the penetration of the probe potential into the plasma is changed, depending on the direction of streaming. This effects the density at the sheath edge, through the Boltzmann factor, e^{-eV/kT_e}, so that the particle flux to the probe is shifted. The degree to which we can measure this change in I_{si} determines the effectiveness of this method.

Hudis and Lidsky calculated the density change at the transition edge,

$$\begin{aligned} n_i(R_t) &= n_\infty e^{-1/2} \exp\left[-(V_{th}^i \pm V_d^i)^2/V_s^2\right] \\ &= n_\infty e^{-1/2} \exp\left[-(V_{th}^{i2} + V_d^{i2})/V_s^2 \pm 2V_d^i V_{th}^i/V_s^2\right] \end{aligned} \tag{D.1}$$

where n_∞ is the unperturbed density away form the probe, and $\pm V_d^i$ represents ion streaming toward or away from the probe. The factor, $\exp\left[-(V_{th}^{i2} + V_d^{i2})/V_s^2\right]$, will be neglected, since in our case, $V_{th}^{i2}, V_d^{i2} \ll V_s^2$, and more importantly, this factor is independent of the direction of streaming. They noted that the thermal velocity must be included, or only particles streaming directly into the probe would be collected, as in Brundin's model.

If ΔI_{si} is defined as the difference in I_{si} when the particles are streaming toward the probe, and when they are streaming away, $\Delta I_{si} \equiv I_+ - I_-$, they get

$$\Delta I_{si} = I_{si}[\exp(2V_d^i V_{th}^i / V_s^2) - \exp(-2V_d^i V_{th}^i / V_s^2)]$$

$$= 4I_{si} V_d^i V_{th}^i / V_s^2$$

using the fact that $V_d^i V_{th}^i << V_s^2$ to expand the exponentials. Rewriting,

$$V_d^i = \left(\frac{T_e}{T_i}\right)^{\frac{1}{2}} \frac{V_s}{4} \frac{\Delta I_{si}}{I_{si}} \qquad (D.2)$$

where $I_{si} = 1/2(I_+ + I_-)$. This expression will be used to express the drift velocity in terms of measurable quantities.

We now calculate an expression for the radial electric field, E_r, as a function of the observables. The ion equation of motion can be written,

$$M_i n_i \dot{\underline{v}}_i = n_i e(\underline{E} + \underline{v}_i/c \times \underline{B}) - \nabla p_i + M_i n_i \underline{g} + 2M_i n_i \underline{v}_i \times \underline{\Omega}_o - M_i n_i \nu_{in} \underline{v}_i \qquad (D.3)$$

where $\Omega_o = v_\theta / R$ is the rotation frequency determined by the measured azimuthal drift $v_\theta = v_{d\theta}^j$(DLP). The centrifugal gravity $g = \Omega_o^2 R$, and ν_{in} is the ion-neutral collision frequency. We define $\Lambda \equiv 1 + 2\Omega_o / \Omega_i$, $B^* \equiv B\Lambda$, and $\Omega^* \equiv \Omega_i \Lambda$. Then solving for the steady state drift velocity,

$$v_{d\theta}^i \left(1 + \frac{\nu_{in}^2}{\Omega^{*2}}\right) + \frac{E_r c}{B^*} - \frac{kT_i c}{eB^*} \frac{\nabla n_i}{n_i} + \frac{g}{\Omega^*} = 0$$

We see here that the azimuthal drift velocity is the sum of the electric, ion-diamagnetic, and gravitational drifts. If we examine fig. VI.11, we see that the electric drift is in fact the dominant ion drift at large radii and our results to lowest order are similar to those of Hudis and Lidsky, who include only the electric

drift and collisions with neutrals. However, at small radii, the gravity drift and ion-diamagnetic drift become comparable to the electric drift and should be included. The expression we use for the electric field is,

$$E_r = -\frac{B^*}{c} V^i_{d\theta}\left(1 + \frac{\nu^2_{in}}{\Omega^{*2}}\right) + \frac{g}{\Omega^*} - \frac{kT_i c}{eB^*}\frac{\nabla n_i}{n_i} \qquad (D.4)$$

We now question the experimental validity of the DLP on six counts.

First, we check to see if the DLP is operating correctly as a simple probe. When two values of $I_{si} = 1/2\ (I_+ + I_-)$ are obtained by averaging the directional ion currents in the axial, $I_{si}(z) = \frac{1}{2}(I_{z+} + I_{z-})$, and azimuthal, $I_{si}(\theta) = \frac{1}{2}(I_{\theta+} + I_{\theta-})$, directions, the two values agree to better than 10%. This shows that our model applies to particles collected parallel and perpendicular to B, that the collection process is not affected by B.

Second, we check to see if the averaged directional ion currents to a DLP give the same ion density profile as a cylindrical probe. The DLP has a collection area, $A_{DLP} = 3.56\ mm^2$, including the semi-circles at each end of the slot, while cylindrical probe B has an area $A_B = 3.4\ mm^2$. We would expect the ratio of the ion currents to be $I_{si}(B)/I_{si}(DLP) = A_B/A_{DLP} = 0.96$. If we average this ratio over the profile for the typical data case, section VI.A, we get $I_{si}(B)/I_{si}(DLP) = 0.96 \pm 0.20$, in agreement with the predicted value.

Third, we check the shape of the probe characteristics, (V-I plots), for directional currents in the axial and azimuthal

directions. The probe characteristics are shown in fig. D.1, where I_D and E_D refer to azimuthal streaming in the ion- and electron-diamagnetic directions, and C and A refer to axial streaming from the cathode and anode directions, respectively. All probe curves yield the same electron temperature from a semi-log plot of the characteristics, in agreement with the electron temperature obtained from a cylindirical probe.

Fourth, we would like a direct experimental check that the streaming velocity, calculated in Eq. (D.2), is accurate. To do this we measure directional ion currents in a plasma device with a known streaming velocity.

Brown et. al. reported on such a device at the Lawrence Berkeley Laboratory called COMPLEX, for "Cold Microwave Plasma Experiment".[132] Microwave power is coupled to the electron gyroresonance using a "Lisitano Coil"[133] The plasma then streams the 1.5 meter length of the system along an axial magnetic field of B = 1 to 10 kG. The plasma flow velocity is determined by measuring the difference in the upstream and downstream propagation speeds of acoustic waves. Ion-acoustic waves are launched using grids immersed in the plasma, and by pulsing the microwave power.

We measure directional currents in the COMPLEX device in argon, krypton, and neon. For lighter gases, and possibly even neon, the gyroradius is too small for simple probe theory to be valid. Density was varied between $n_i = 1.6 \times 10^{11}$ and 9.4×10^{12} cm^{-3}, in an axial magnetic field of B = 2.34 to 4.68 kilogauss. The electron temperature was measured to be T_e = 3.3 to 4.6 eV,

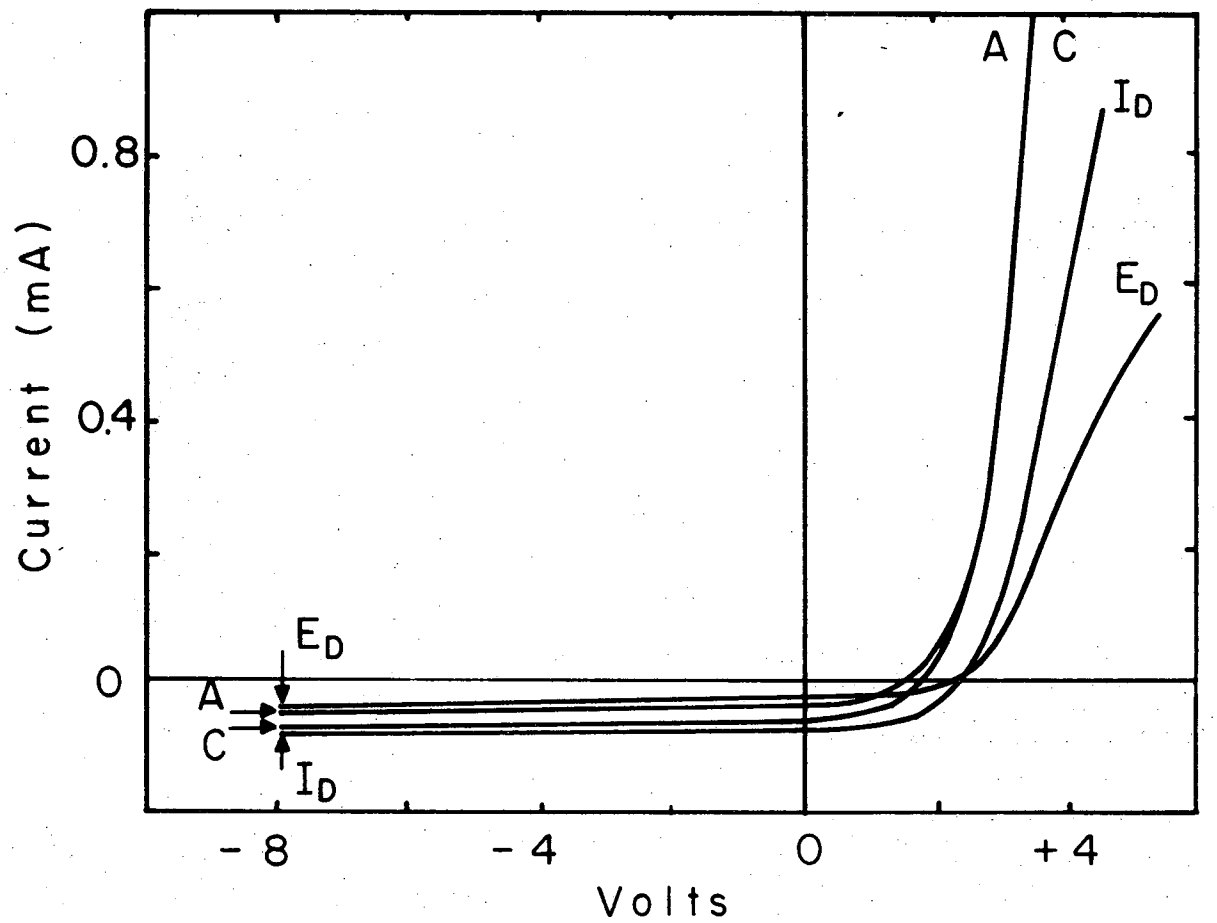

XBL 7112-1821

Fig. D.1. Directional Langmuir probe characteristics at R=5 cm. Axial characteristics are obtained when the probe is facing the cathode, C, and the anode, A. Azimuthal characteristics are obtained facing the ion-diamagnetic, I_D, and electron-diamagnetic, E_D, directions. Semi-log plots yield the same electron temperature, in agreement with the value obtained using a cylindrical probe.

while the ion temperature was assumed to be $T_i \approx 0.1$ The DLP radius is $R_{DLP} = 0.51$ mm. Recombining these numbers, the DLP was tested over the following ranges: (1) $T_i/T_e \gtrsim 0.1$; (2) gyroradius, $a_i/R_{DLP} = 0.82$ to 2.78; and (3) Debye length, $R_{DLP}/\lambda_{De} = 12.9$ to 31.3. Briefly, we expect simple probe theory to be valid for $T_i/T_e \gtrsim 0.1$, $a_i/R_p \lesssim 2$, and $R_{DLP}/\lambda_{De} \lesssim 30$.

Brown et. al. reported that the drift speed, measured by the propagation of ion-acoustic waves, is always slower than the sound speed, and tends to be in the neighborhood of $v_d/v_s \gtrsim 0.5$ in the noble gases.[132] We measured the directional axial ion currents in argon, krypton, and neon using the DLP, and employ Eq. (D.2) to infer a drift velocity. Comparison of the two methods is shown in fig. D.2. Error bars for the DLP determination are statistical over several measurements, while errors in the sound speed determination represent uncertainties in the measurement of the propagation speeds. Good agreement is observed for argon and krypton, but not so good for neon. We suggest that magnetic field effects are more important in neon due to its smaller mass, since for neon, $a_i/R_p = 0.82$ to 1.4. We conclude that the DLP correctly measures plasma drifting, using Eq. (D.2), if the conditions of validity for simple probe theory are satisfied.

Fifth, we would like experimental verification that we can determine an accurate value for the radial electric field, E_r. The DLP is used to measure the azimuthal drift velocity used in Eq. (D.4). An independent determination of E_r by taking the gradient of the plasma potential, $\phi_p = \phi_f + 5.6\ kT_e/e$, is presented in

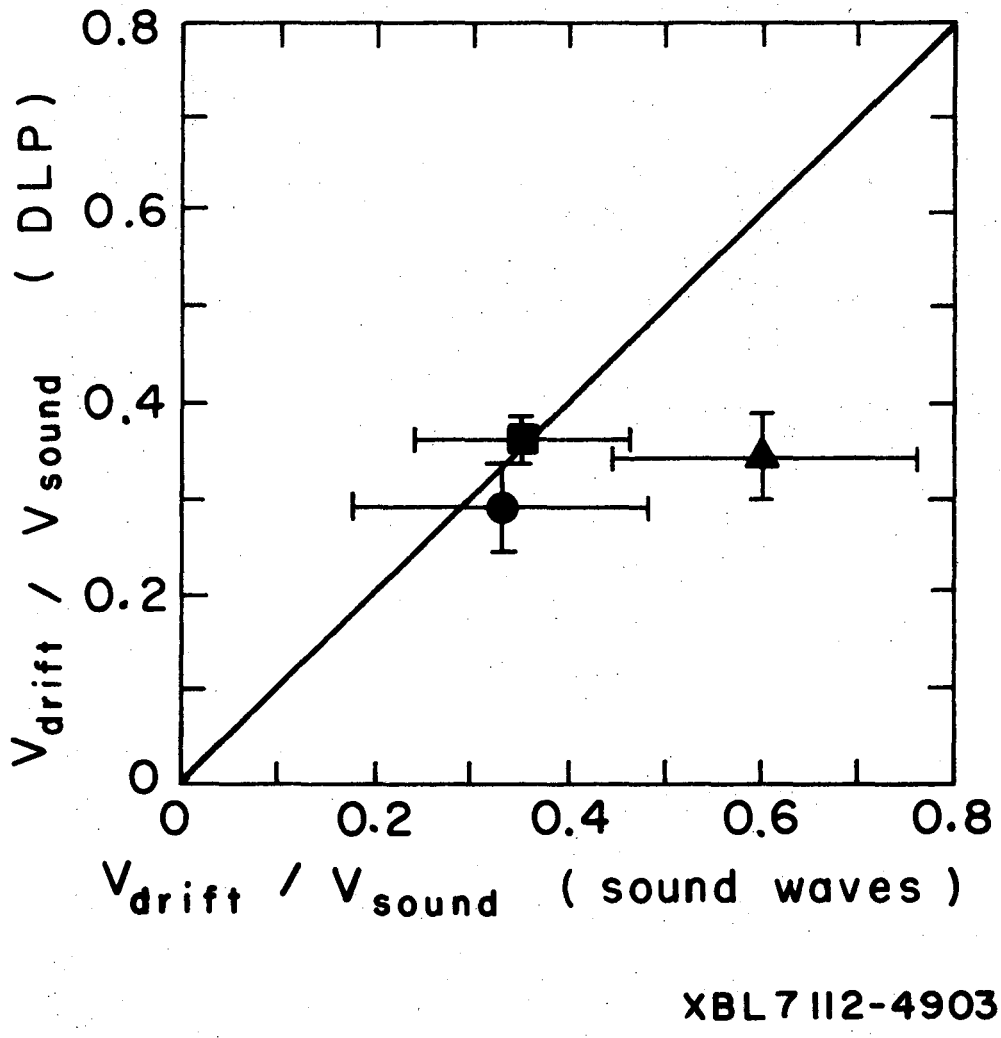

Fig. D.2. Normalized streaming velocities in the "COMPLEX" device, comparing measurements made using a DLP with an independent determination based on the propagation of sound waves. ■, argon; ●, krypton; and ▲, neon.

fig. VI.4 for comparison. Good agreement supports the validity of both techniques.

Finally, Hudis and Lidsky considered the effect of slot width, w, (fig. III.5), on the normalized I_{si} profile. It was shown experimentally that for $w/a_i \lesssim 0.25$, there is negligible effect on the normalized I_{si} profile. We do not verify this directly, but design the probe with $w/a_i \simeq 0.75$ at B = 580 G in argon.

We believe the DLP to give valid and reliable results, based on the theoretical inequalities satisfied, and on our six experimental verifications.

The DLP was aligned as in fig. III.3, probe E, along a radius, so that we could only measure streaming in the axial and azimuthal directions. Typically $\Delta I_{si}/I_{si} \simeq$ 10 to 50 %, and could be easily measured using a digital voltmeter.

Enhanced radial streaming velocities are estimated to be an order of magnitude lower than the measured azimuthal rotation velocities, and therefore could not be measured reliably in this experiment.

E. List of symbols and abbreviations.

a_α	gyroradius for species α
A	atomic mass number
A_I, A_{II}	anodes I and II
A_x	area of surface x
Ar	argon
AC	alternating current, sinusoidal or rectangular
$\underline{B}$, B	magnetic field strength in gauss
B*	B x Λ
c	speed of light
c_A	Alfven speed
D_{Bohm}	Bohm diffusion coefficient
D_{eff}	effective diffusion coefficient
D_{enh}	enhanced diffusion coefficient
$D_{\alpha\beta}$	classical diffusion coefficient for species α due to species β
DC	direct current
DLP	directional Langmuir probe
DP	diffusion pump
DR	duty ratio
e	electron charge, electron species
eV	electron-volt, energy unit

$\underline{E}$	electric field
E_I , E_{II}	electrode E_I , E_{II}
f	frequency
F	linear feedback
$\pm F$	positive or negative linear feedback
FGR	finite gyroradius
FGRE	finite gyroradius effects
$\underline{g}$	gravity
He	helium
HCD	hollow cathode discharge
HF	higher-frequency experimental wave
i	ion species, or $\sqrt{-1}$
I	electric current
I_{CI}	arc discharge current
I_D	ion-diamagnetic direction
I_o	Bessel function of imaginary argument
$\underline{j}$	current density
J	Richardson number
$\underline{k}$	wave number
k	Boltzmann constant

K_o	Bessel function of imaginary argument
K-H	Kelvin-Helmholtz instability
L	system length
L_{eff}	effective system length as seen by the plasma
L_n	density scale length
L_v	velocity scale length
LF	lower-frequency experimental wave
m	azimuthal mode number, electron mass
m_e	electron mass
M_i	ion mass
n	plasma density, neutral species
n_α	density for species α
n_o	neutral gas density
n_1 , Δn	first-order density perturbation
$\tilde{n}$	normalized first-order density perturbation
$\langle n\underline{v} \rangle^{\alpha}_{conv}$	time-averaged convection for species α
NF	no linear feedback
NS	no stabilization, AC or DC
p	scalar plasma pressure
p_t	neutral pressure in the diffusion tank
p_α	scalar pressure for species α
P	power
$\underline{\underline{P}}$	collisionless pressure tensor

q	radial density scale length
q_α	charge for species α
r, R	radius
rf	radio frequency
rms	root-mean-square
R_x	tip radius of probe x
R-T	Rayleigh-Taylor instability
S	controlled electron sink term
STP	standard temperature and pressure
t	time
T_α	temperature for species α
$\underline{v}$	velocity
$\underline{v}_d^\alpha$	drift velocity for species α
$v_{D\alpha}$	diamagnetic drift velocity for species α
v_{th}^α	thermal speed for species α
v_s	sound speed
V	voltage with respect to system ground, or volume
w	slot width of directional Langmuir probe

α	species type α = i, e, n (for ion, electron, and neutral)
α_R	volume recombination coefficient
β	ratio of plasma to magnetic pressure
β_I	ionization rate
γ	instability growth rate
δ	inverse density scale length
Δ	phase between density and radial velocity fluctuations
η	plasma resistivity
θ_α	thermal energy for species α
$\underline{\lambda}$	force due to the divergence of the collisionless pressure tensor
λ_{eff}	effective mean-free-path, $\lambda_{in}\ (1 + T_e/T_i)$
λ_{De}	Debye length
$\lambda_{\alpha\beta}$	mean-free-path for collisions between species α and β
Λ	Coriolis force term $= 1 + 2\Omega_o/\Omega_i$
Λ_D	Debye shielding parameter
$\underline{\mu}_{\alpha n}$	mobility tensor for species α due to neutral collisions
ν	collisionless viscosity
$\nu_{\alpha\beta}$	collision frequency for species α with species β

ρ	mass density
ρ_e	charge density
ρ_1	first-order mass density fluctuation
$\tilde{\rho}$	normalized first-order mass density fluctuation
σ	controlled electron sink collection frequency
σ'	$\sigma + i\ \nu_{in}$
$\sigma_{\alpha\beta}$	cross section for species α colliding with species β
τ	wave period
$\tau_{\alpha\beta}$	collision time for species α with species β
φ_f	Langmuir probe floating potential with respect to system ground
φ_p	plasma potential with respect to ground
φ_1 , $\Delta\varphi_f$	first-order potential fluctuation
$\tilde{\varphi}$	normalized first-order potential fluctuation
ψ	phase between density and potential fluctuations
ψ_{calc}	calculated phase, ψ
ω	complex wave frequency
ω'	$\omega + i\ \nu_{in}$
$\omega_{p\alpha}$	plasma frequency for species α
Ω_o	plasma rotation frequency
Ω_r	wave frequency, real part
Ω_α	gyrofrequency for species α
Ω^*	$\Omega_i \times \Lambda$

REFERENCES

1. K. H. Berkner, R. V. Pyle, H. F. Rugge, J. W. Stearns, and J. Winocur, Diffusion from a Line Source in a Magnetic Field, in VI Conference Internationale sur les Phenomenes d'Ionisation dans les Gas, 8-13 July 1963 (SERMA, Paris, 1965), Vol. 1, p. 389.

2. A. Simon and R. V. Neidigh, Diffusion of Ions in a Plasma Across a Magnetic Field, Oak Ridge National Laboratory report ORNL-1890, July 11, 1955 (unpublished).

3. D. Bohm, E. H. S. Burhop, and H. S. W. Massey, The Use of Probes for Plasma Exploration in Strong Magnetic Fields, in The Characteristics of Electrical Discharges in Magnetic Fields, A. Guthrie and R. K. Wakerling, eds. (McGraw-Hill Book Co., New York, 1949), Chap. 2.

4. F. Schwirzke, Diffusion eines Plasmas in Abhängigkeit von Magnetfeld und Druck und von der Längs-ausdehnung in Magnetfeldrichtung, Z. Naturforsch 18A, 889 (1963).

5. L. Warren, Transport of a Partially Ionized Plasma Across a Magnetic Field, (Ph.D. Thesis), Lawrence Radiation Laboratory report UCRL-17601, Sept. 30, 1968 (unpublished).

6. M. Hudis, Particle Flux Measurements in a Hollow Cathode Arc (Ph.D. Thesis), Department of Nuclear Engineering, Massachusetts Institute of Technology, November 1969 (unpublished).

7. M. Hudis and L. M. Lidsky, Low-Frequency Instabilities in a Nonuniformly Rotating Plasma, to be published in The Physics of Fluids.

8. J. H. Noon, H. A. Schmidt, and E. H. Holt, Connection Between Self-Excited Low Frequency Oscillations and Anomalous Plasma Diffusion, Plasma Phys. 12, 477 (1970).

9. S. Yoshikawa and D. J. Rose, Anomalous Diffusion of a Plasma Across a Magnetic Field, Phys. Fluids 5, 334 (1962).

10. M. Hudis and L. M. Lidsky, Directional Langmuir Probe, J. Appl. Phys. 41, 5011 (1970).

11. T. K. Chu, H. W. Hendel, and P. A. Politzer, Measurements of Enhanced Plasma Losses Caused by Collisional Drift Waves, Phys. Rev. Letters 19, 1110 (1967).

12. H. W. Hendel, T. K. Chu, and P. A. Politzer, Collisional Drift Waves--Identification, Stabilization, and Enhanced Plasma Transport, Phys. Fluids 11, 2426 (1968).

13. T. K. Chu, B. Coppi, H. W. Hendel, and F. W. Perkins, Drift Instabilities in a Uniformly Rotating Plasma Cylinder, Phys. Fluids 12, 203 (1969).

14. F. F. Chen,"Univeral" Overstability of a Resistive, Inhomogeneous Plasma, Phys. Fluids 8, 1323 (1965).

15. A. Simon, Instability of a Partially Ionized Plasma in Crossed Electric and Magnetic Fields, Phys. Fluids 6, 382 (1963).

16. F. C. Hoh, Instability of Penning-Type Discharges, Phys. Fluids 6, 1184 (1963).

17. David L. Morse, Plasma Rotation in a Hollow-Cathode Discharge, Phys. Fluids 8, 516 (1965); Low-Frequency Instability of Partially Ionized Plasma, Phys. Fluids 8, 1339 (1965).

18. K. V. Roberts and J. B. Taylor, Magnetohydrodynamic Equations for Finite Larmor Radius, Phys. Rev. Letters 8, 197 (1962).

19. B. Lehnert, Gravitational Instability of a Magnetized Plasma, Phys. Rev. Letters 7, 440 (1961).

20. H. K. Hans, Larmor Radius and Collisional Effects on the Combined Taylor and Kelvin Instabilities in a Composite Medium, Nucl. Fusion 8, 89 (1968).

21. F. F. Chen, Microinstability and Shear Stabilization of a Low-β, Rotating, Resistive Plasma, Phys. Fluids 9, 965 (1966).

22. B. Lehnert, Stabilization of Flute Disturbances by the Coriolis Force, Phys. Fluids 5, 740 (1962).

23. G. I. Kent, N. C. Jen, and F. F. Chen, Transverse Kelvin-Helmholtz Instability in a Rotating Plasma, Phys. Fluids 12, 2140 (1969).

24. T. E. Stringer and G. Schmidt, Flute Instability in the Presence of Nonuniform Electric Fields, Plasma Phys. 9, 53 (1967).

25. S. Chandrasekhar, Hydrodynamic and Hydromagnetic Stability (Clarendon Press, Oxford, 1961), Chaps. X, XI.

26. F. W. Perkins and D. L. Jassby, Velocity Shear and Low-Frequency Plasma Instabilities, Phys. Fluids 14, 102 (1971); D. L. Jassby and F. W. Perkins, Transverse Kelvin-Helmholtz Instability in a Q-Machine Plasma, Phys. Rev. Letters 24, 256 (1970).

27. A. Simon, Ambipolar Diffusion in a Magnetic Field, Phys. Rev. 98, 317 (1955).

28. A. V. Zharinov, The Diffusion of Electrons in a Magnetic Field, J. Nucl. Energy: Pt. C 1, 271 (1960).

29. L. Tonks, Diffusion Through a Finite Plasma in a Uniform Magnetic Field, Phys. Fluids 3, 758 (1960).

30. F. C. Hoh, Low Temperature Plasma Diffusion in a Magnetic Field, Revs. Mod. Phys. 34, 267 (1962).

31. F. Boeschoten, Review of Experiments on the Diffusion of Plasma Across a Magnetic Field, J. Nucl. Energy: Pt. C 6, 339 (1964).

32. Fred Schwirzke, Diffusion of Charged Particles Across a Magnetic Field in "Short Circuiting Geometry," Phys. Fluids 7, 311 (1964).

33. T. C. Simonen, T. K. Chu, and H. W. Hendel, Feedback Control of Collisional Drift Waves by Modulated Parallel-Electron-Current Sink--Experiment and Interpretation, Phys. Rev. Letters 23, 568 (1969).

34. N. E. Lindgren and C. K. Birdsall, Feedback Suppression of Collisionless, Multimode Drift Waves in a Mirror Confined Plasma, Phys. Rev. Letters 24, 1159 (1970).

35. H. P. Furth and P. H. Rutherford, Feedback Stabilization of Drift Waves by Modulated Electron Sources, Phys. Fluids 12, 2638 (1969).

36. D. Bohm, E. H. S. Burhop, H. S. W. Massey, and R. M. Williams, A Study of the Arc Plasma, in The Characteristics of Electrical Discharges in Magnetic Fields, A. Guthrie and R. K. Wakerling, eds. (McGraw-Hill Book Co., New York, 1949), Chap. 9.

37. S. D. Rothleder, Charged Particle Diffusion and Energy Transport in a Highly Ionized Magnetically Confined Plasma (Ph.D. Thesis), Nuclear Engineering Dept., Massachusetts Institute of Technology, August 1962 (unpublished).

38. J. A. Byers, Confined and Nonconfined Interchange Instabilities Obtained from Nonlinear Computer Models, Phys. Fluids 9, 1038 (1966); Large Amplitude Stabilization of Flute Growth, Phys. Fluids 10, 2235 (1967).

39. K. I. Thomassen, Feedback Stabilization in Plasmas, Nucl. Fusion 11, 175 (1971).

40. A. R. Millner and R. R. Parker, Nonlinear Stabilization of a Continuum, in Feedback and Dynamic Control of Plasmas, T. K. Chu and H. W. Hendel, eds. (Am. Inst. of Phys., New York, 1970), No. 1, p. 54.

41. J. R. Melcher, Feedback Stabilization of Hydromagnetic Continua: Review and Prospects, in Feedback and Dynamic Control of Plasmas, T. K. Chu and H. W. Hendel, eds. (Am. Inst. of Phys., New York, 1970), No. 1, p. 38.

42. H. W. Hendel and T. K. Chu, paper CN-28/b-14, IAEA 4th Conf. on Plasma Physics and Controlled Nuclear Fusion Research, Madison, Wisc., June 1971.

43. V. V. Arsenin and V. A. Chuyanov, A Possible Stabilization of Trough-Shaped Plasma Instability Through a Feedback System, Soviet Phys.-Doklady 13, 570 (1968); V. V. Arsenin, Possibility of Suppressing Flute Instability of a Dense Plasma, JETP Letters 11, 173 (1970).

44. V. V. Arsenin, V. A. Zhilitsov, and V. A. Chuyanov, Suppression of Flute Instability of a Plasma by Means of a Feedback System, in Proceedings of the Conference on Plasma Physics and Controlled Nuclear Fusion Research, Novosibirsk, 1-7 August 1968 (IAEA, Vienna, 1969), Vol. 2, p. 515.

45. V. A. Chuyanov, Experimental Results on the Suppression of the Flute Instability by a Feedback System on Phoenix II, Culham Laboratory report CTO/598, March 1969 (translated from Russian).

46. V. V. Arsenin and V. A. Chuyanov, Possibility of Suppressing Drift Instability in a Nonuniform Plasma by Feedback Systems, Soviet Atomic Energy 24, 407 (1968).

47. Alfred Y. Wong, Dan R. Baker, and Newell Booth, Efficient Modulation Coupling between Electron and Ion Resonances in Magnetoactive Plasmas, Phys. Rev. Letters 24, 804 (1970).

48. R. Prater, Interchange Stabilization by Electron Beam Feedback, Bull. Am. Phys. Soc. 16, 1298 (1971).

49. H. W. Hendel, T. K. Chu, F. W. Perkins, and T. C. Simonen, Remote Feedback Stabilization of Collisional Drift Instability by Modulated Microwave Energy Source, Phys. Rev. Letters 24, 90 (1970).

50. F. F. Chen and H. P. Furth, Low-Frequency Plasma Stabilization of Feedback Controlled Neutral Beams, Nucl. Fusion 9, 364 (1969).

51. F. F. Chen, Plasma Control with Infrared Lasers, in Feedback and Dynamic Control of Plasmas, T. K. Chu and W. W. Hendel, eds. (Am. Inst. of Phys., New York, 1970), No. 1, p. 33.

52. Francis F. Chen, The Double-Resonance Effect, Bull. Am. Phys. Soc. 16, 1274 (1971).

53. R. R. Parker and K. I. Thomassen, Feedback Stabilization of a Drift-Type Instability, Phys. Rev. Letters 22, 1171 (1969).

54. B. E. Keen and R. V. Aldridge, Suppression of a Drift-Type Instability in a Magnetoplasma by a Feedback Technique, Phys. Rev. Letters 22, 1358 (1969).

55. R. V. Aldridge and B. E. Keen, Rotationally Convected Drift Wave Instability in an Inhomogeneous Plasma Column, Plasma Phys. 12, 1 (1970).

56. B. E. Keen, Interpretation of Experiments on Feedback Control of a "Drift-Type" Instability, Phys. Rev. Letters 24, 259 (1970).

57. B. E. Keen and P. E. Scott, Experimental Study of Drift Wave Stabilization, paper CN-28/B-13, IAEA 4th Conf. on Plasma Physics and Controlled Nuclear Fusion Research, Madison, Wisc., June 1971.

58. J. Stufflebeam, R. E. Reinovsky, J. H. Noon, and W. C. Jennings, Feedback Stabilization of the Drift Instability in a Hollow Cathode Arc, Bull. Am. Phys. Soc. 16, 1244 (1971).

59. H. F. Rugge, Instability of an Alternating-Current Positive Column in a Magnetic Field (Ph.D. Thesis), Lawrence Radiation Laboratory report UCRL-10698, April 22, 1963 (unpublished).

60. B. B. Kadomtsev and A. V. Nedospasov, Instability of the Positive Column in a Magnetic Field and the "Anomalous" Diffusion Effect, J. Nucl. Energy: Part C 1, 230 (1960).

61. M. W. Alcock and B. E. Keen, Experimental Observation of the Drift-Dissipativ Instability in Afterglow Plasmas, J. Phys. 3A, L21 (1970).

62. Alfred Y. Wong and Francis Hai, Direct Measurements of Linear Growth Rates and Nonlinear Saturation Coefficients of Instabilities, Phys. Rev. Letters 23, 163 (1969).

63. H. W. Hendel, T. K. Chu, and T. C. Simonen, Measurement of Nonlinear Growth Rate of Drive Wave Decay Mode, Bull. Am. Phys. Soc. 15, 1424 (1970).

64. P. E. Scott, P. F. Little, and J. Burt, Collisionless Drift Waves in a Thermionic Plasma, in Proceedings of the 3rd European Conference on Controlled Fusion and Plasma Physics (Wolters-Noordhoff, Groningen, The Netherlands, 1969), p. 125.

65. C. W. Hartman, H. W. Hendel, and R. H. Munger, Feedback Control of Collisional Drift Waves in a Toroidal Stellarator, in Feedback and Dynamic Control of Plasmas, T. K. Chu and H. W. Hendel, eds. (Am. Inst. of Phys., New York, 1970), No. 1, p. 170.

66. F. F. Chen and K. C. Rogers, Minimum-B Stabilization of Drift Waves in a Q-Machine, Plasma Phys. 12, 253 (1970).

67. T. K. Chu, H. W. Hendel, D. L. Jassby, and T. C. Simonen, Feedback Stabilization of the Transverse Kelvin-Helmholtz Instability--Experiment and Theory, in Feedback and Dynamic Control of Plasmas, T. K. Chu and H. W. Hendel, eds. (Am. Inst. of Phys., New York, 1970), No. 1, p. 142.

68. V. V. Arsenin, V. A. Zhiltsov, V. Kh. Likhtenshtein, and V. A. Chulnov, Suppression of Cyclotron Instability of a Rarefied Plasma with the Aid of a Feedback System, JETP Letters 8, 41 (1968).

69. B. E. Keen and W. H. W. Fletcher, Remote Feedback Stabilization of the Ion-Sound Instability by a Modulated Source at the Electron-Cyclotron Resonance Frequency, Phys. Rev. Letters 25, 350 (1970).

70. A. Garscadden and P. Bletzinger, Feedback Experiments on Multimode Ionization Waves, in Feedback and Dynamic Control

of Plasmas, T. K. Chu and H. W. Hendel, eds. (Am. Inst. of Phys., New York, 1970), No. 1, p. 149.

71. E. L. Lindman, Generalized Boundary Conditions of Plasma Feedback Systems, in Feedback and Dynamic Control of Plasmas, T. K. Chu and H. W. Hendel, eds. (Am. Inst. of Phys., New York, 1970), No. 1, p. 17.

72. David C. Carlyle, Passive Feedback Stabilization, in Feedback and Dynamic Control of Plasmas, T. K. Chu and H. W. Hendel, eds. (Am. Inst. of Phys., New York, 1970), No. 1, p. 138.

73. M. Hudis, K. Chung, and D. J. Rose, Ion Temperature, Charge Exchange, and Coulomb Collisions in an Argon Plasma Column, J. Appl. Phys. 39, 3297 (1968).

74. L. M. Lidsky, S. D. Rothleder, D. J. Rose, S. Yoshikawa, C. Michelson, and R. J. Mackin, Jr., Highly Ionized Hollow Cathod Discharge, J. Appl. Phys. 33, 2490 (1962).

75. K. Chung and D. J. Rose, Interpretation of the Fluctuations in the Discharge Arc Column, Bull. Am. Phys. Soc. 12, 694 (1967); Appl. Phys. Letters 11, 247 (1967).

76. R. L. Gunshor, J. H. Noon, and E. H. Holt, Correlation Measurements of Ion-Acoustic Waves in a Hihgly Ionized Plasma, Phys. Fluids 11, 1763 (1968).

77. G. X. Kambic, J. H. Noon, and W. C. Jennings, Phase Properties of a Drift Wave in a Hollow Cathode Arc, Bull. Am. Phys. Soc. 16, 1236 (1971).

78. M. N. Rosenbluth and A. Simon, Finite Larmor Radius Equations with Nonuniform Electric Fields and Velocities, Phys. Fluids

8, 1300 (1965).

79. B. Lehnert, Experimental Evidence of Plasma Instabilities, Plasma Phys. 9, 301 (1967).

80. R. H. Levy, Diocotron Instability in a Cylindrical Geometry, Phys. Fluids 8, 1288 (1965).

81. T. H. Stix, The Theory of Plasma Waves (McGraw-Hill Book Co., New York, 1962), p. 41.

82. H. W. Hendel, B. Coppi, F. W. Perkins, and P. A. Politzer, Collisional Effects in Plasmas--Drift Wave Experiments and Interpretation, Phys. Rev. Letters 18, 439 (1967).

83. B. B. Kadomtsev, Plasma Turbulence (Academic Press, New York, 1965), Chap. IV.

84. N. A. Krall, Drift Waves, in Advances in Plasma Physics (Intersciences Publishers, New York, 1968), p. 172.

85. A. B. Mikhailovskii and A. V. Timofeev, Theory of Cyclotron Instability in a Nonuniform Plasma, Soviet Physics JETP 17, 626 (1963).

86. C. C. Damm, J. H. Foote, A. H. Futch, Jr., A. L. Gardner, F. J. Gordon, A. L. Hunt, and R. F. Post, Cooperative Effects in a Tenuous Energetic Plasma Contained by a Magnetic Mirror Field, Phys. Fluids 8, 1472 (1965).

87. L. Enriques, A. M. Levine, and G. B. Righetti, Experimental Study of the Effect of Radial Electric Fields on the Stability of a Magnetically Confined Plasma, in Proceedings of a Conference on Plasma Physics and Controlled Thermonuclear Fusion Research, Novosibirsk, U.S.S.R., 1968 (IAEA, Vienna, 1969), Vol. 1, p. 641.

88. M. N. Rosenbluth and C. L. Longmire, Stability of Plasma Confined by Magnetic Fields, Ann. Phys. 1, 120 (1957).

89. M. Kruskal and M. Schwarzschild, Some Instabilities of a Completely Ionized Plasma, Proc. Royal Soc. (London) 223, 348 (1954).

90. B. Lehnert, Stability of an inhomogeneous Plasma in a Magnetic Field, Phys. Fluids, 4, 525 (1961); Stability of a Plasma Boundary in a Magnetic Field, Phys. Fluids 4, 847 (1961).

91. M. N. Rosenbluth, N. A. Krall, and N. A. Rostoker, Finite Larmor Radius Stabilization of "Weakly" Unstable Confined Plasmas, in Proceedings of the Conference on Plasma Physics and Controlled Nuclear Fusion Research 4-9 September 1961, Salzburg, Austria, Nucl. Fusion Suppl., Part 1, 143 (1962).

92. E. T. Whittaker and G. N. Watson, A Course of Modern Analysis, (Cambridge University Press, Cambridge, 1952) 4th ed., p. 337.

93. W. B. Thompson, The Dynamics of High Temperature Plasmas, in Reports on Progress in Physics (The Physical Society, London, 1961), Vol. 24, p. 363.

94. G. F. Bogdanov, I. N. Golovin, Y. A. Kucheryaev, and D. A. Panov, Properties of a Plasma Formed by the Injection into Ogra of a Beam of Fast Molecular Hydrogen Ions, in Proceedings of the Conference on Plasma Physics and Controlled Nuclear Fusion Research, 4-9 September 1961, Salzburg, Austria, Nucl. Fusion Suppl., Part 1, 215 (1962), in Russian.

95. F. F. Chen, Resistive Overstabilities and Anomalous "Diffusion", Phys. Fluids 8, 912 (1965).

96. P. K. Bhatia, Collisional Effects of the Rayleigh-Taylor Instability in a Composite Medium, Nucl. Fusion 10, 383 (1970).

97. P. D. Ariel and P. K. Bhatia, Rayleight-Taylor Instability of a Rotating Plasma, Nucl. Fusion 10, 141 (1970).

98. F. F. Chen, Effect of Sheaths on Drift Instabilities in Thermionic Plasmas, Phys. Fluids 8, 752 (1965).

99. Ronald Prater, Interchange Destabilization by Incomplete Line-tying, Bull. Am. Phys. Soc. 16, 1254(1971).

100. W. B. Kunkel and J. U. Guillory, Interchange Stabilization by Incomplete Line-tying, in Proceedings of the Seventh International Conference on Ionization Phenomena in Ionized Gases, (Gradevinska Knjiga, Beograd, Yugoslavia, 1966), p. 702.

101. L. S. Hall, Probes and Magnetic Pumping in Plasma, Lawrence Radiation Laboratory report UCRL-6535, July 19, 1961 (unpublished).

102. F. F. Chen, Electric Probes, in Plasma Diagnostic Techniques, R. H. Huddlestone and S. L. Leonard, eds. (Academic Press, New York, 1965).

103. F. F. Chen, C. Etievant, and D. Mosher, Measurement of Low Plasma Densities in a Magnetic Field, Phys. Fluids 11, 811 (1968).

104. I. G. Brown, A. B. Compher, and W. B. Kunkel, Response of a Langmuir Probe in a Strong Magnetic Field, Phys. Fluids 14, 1377 (1971).

105. J. E. Allen and P. C. Thonemann, Current Limitation in the Low-Pressure Mercury Arc, Proc. Phys. Soc. (London) 67B, 768 (1954).

106. J. G. Laframboise, Theory of Spherical and Cylindrical Langmuir Probes in Collisionless, Maxwellian Plasma at Rest, University of Toronto, Institute for Aerospace Studies report UTIAS-100, June 1966.

107. D. J. Rose and M. Clark, Jr., Plasmas and Controlled Fusion, (The MIT Press, Cambridge, Mass., 1961), pp. 165-172.

108. A. N. Kaufman, Dissipative Effects, in Plasma Physics in Theory and Application, Wulf B. Kunkel, ed. (McGraw-Hill Book Col, New York, 1966), p. 108.

109. Fred Schwirzke, Electric Fields Caused by the Diffusion of Charged Particles Across a Magnetic Field, Phys. Fluids 9, 2244 (1966).

110. J. H. Noon and W. C. Jennings, Instabilities and Turbulence in Highly Ionized Plasmas in a Magnetic Field, Rensselaer Polytechnic Institute, Plasma Dynamics Laboratory, Technical Report 71-3, Nov. 1971 (unpublished); G. X. Kambic, J. H. Noon, and W. C. Jennings, Phase Properties of a Drift Wave in a Hollow Cathode Arc, Bull. Am. Phys. Soc. 16, 1236 (1971).

111. H. B. Gilbody and J. B. Hasted, Anomalies in the Adiabatic Interpretation of Charge-Transfer Collisions, Proc. Royal Soc. (London) A238, 334 (1956).

112. W. H. Cramer, Elastic and Inelastic Scattering of Low-Velocity Ions: Ne^+ in A, A^+ in Ne, and A^+ in A, J. Chem. Phys. 30, 641 (1959).

113. Earl W. McDaniel, Collision Phenomena in Ionized Gases (John Wiley and Sons, Inc., New York, 1964), p. 466.

114. Ibid., pp. 116-124.

115. R. A. Brode, Quantiative Study of the Collisions of Electrons with Atoms, Revs. Mod. Phys. 5, 259 (1933).

116. Earl W. McDaniel, op. cit., p. 732.

117. Earl W. McDaniel, op. cit., p. 184.

118. A. Redfield and R. B. Holt, Electron Removal in Argon Afterglows, Phys. Rev. 82, 874 (1951).

119. M. A. Biondi, Concerning the Mechanism of Electron-Ion Recombination, Phys. Rev. 83, 1078 (1951).

120. Manfred A. Biondi and Sanborn C. Brown, Measurements of Ambipolar Diffusion in Helium, Phys. Rev. 75, 1700 (1949); Measurement of Electron-Ion Recombination, Phys. Rev. 76, 1697 (1949).

121. Carl Kenty, The Recombination of Argon Ions and Electrons, Phys. Rev. 32, 624 (1928).

122. J. Sayers, cited by L. B. Loeb, The Recombination of Ions, in Handbuch der Physik, S. Flugge, ed. (Springer-Verlag, Berlin, 1956), p. 491.

123. H. N. Olsen and W. S. Huxford, Dynamic Characteristics of the Plasma in Discharges through Rare Gases, Phys. Rev. 87, 922 (1952).

124. W. P. Allis, Motions of Ions and Electrons, in Handbuch der

Physik, Vol. XXI (Springer-Verlag, Berlin, 1956), p. 383.

125. Allan N. Kaufman, Plasma Transport Theory, in La Theorie des Gaz Neutres et Ionises, C. DeWitt and J. F. Detoeuf, eds. (John Wiley and Sons, Inc., New York, 1960), p. 331.

126. V. E. Golant, Diffusion of Charged Particles in a Plasma in a Magnetic Field, Sov. Phys. Uspekhi 6, 161 (1963); Usp. Fiz. Nauk. 79, 377 (1963).

127. M. N. Rosenbluth and A. N. Kaufman, Plasma Diffusion in a Magnetic Field, Phys. Rev. 109, 1 (1958).

128. R. V. Meghreblian and D. K. Holmes, Reactor Analysis (McGraw-Hill Book Co., New York, 1960), p. 179.

129. G. Ecker, K. S. Masterson, and J. J. McClure, Probe Theory in a Dense Plasma, Lawrence Radiation Laboratory report, UCRL-10128, March 21, 1962.

130. Clark L. Brundin, The Application of Langmuir Probe Techniques to Flowing Ionized Gases, Inst. of Engineering Research, University of California, Berkeley, Report A4-64-9, June 15, 1964.

131. F. S. Sherman and L. Talbot, Diagnostic Studies of a Low-Density Arc-Heated Wind Tunnel Stream, in Hypersonic Flow Research, F. R. Ridell, ed. (Academic Press, New York, 1962), p. 581.

132. I. G. Brown, A. B. Compher, K. W. Ehlers, D. B. Hopkins, W. B. Kunkel, and P. S. Rostler, Feedback-Controlled Stead-State Plasma, Plasma Phys. 13, 47 (1971).

133. G. Lisitano, R. A. Ellis, Jr., W. M. Hooke, and T. H. Stix, Production of Quiescent Discharge with High Electron Temperatures, Rev. Sci. Instr. 39, 295 (1968).

TECHNICAL INFORMATION DIVISION
LAWRENCE BERKELEY LABORATORY
UNIVERSITY OF CALIFORNIA
BERKELEY, CALIFORNIA 94720